MEASUREMENTS OF IDENTIFIED HADRONS IN Au+Au AND d+Au COLLISIONS AT $\sqrt{s_{NN}}$ = 200 GeV

By

Ronald John Belmont III

Dissertation

Submitted to the Faculty of the

Graduate School of Vanderbilt University

in partial fulfillment of the requirements

for the degree of

DOCTOR OF PHILOSOPHY

in

PHYSICS

December, 2012

Nashville, Tennessee

Approved:

Professor Julia Velkovska

Professor Charles F. Maguire

Professor J. Kelly Holley-Bockelmann

Professor David J. Ernst

Professor Will E. Johns

This dissertation is dedicated in loving memory to my Grandmother, Josephine Hayes
(née Johanna Cussen),
27 September 1926 - 15 March 2010.

ACKNOWLEDGEMENTS

I would like to express my sincere gratitude to my advisor, Dr. Julia Velkovska, for her guidance, mentorship, and support over the years. I would also like to thank the members of my PhD committee, Dr. Charles Maguire, Dr. Will Johns, Dr. David Ernst, and Dr. Kelly Holley-Bockelman for always being supportive and attentive.

I am deeply indebted to Dr. Shengli Huang, Dr. Michael Issah, and Dr. Hugo Valle for their invaluable contributions to my graduate education. I am very grateful to have had the opportunity to work and travel with Dillon Roach, who is always up for a trip from Upton to Mastic for some gyros. I am very grateful to Dr. Carla Vale and Dr. Christine Aidala for many helpful conversations and especially for their friendship.

I thank my dear friends Dr. Saurav Dhital, Dr. Manodeep Sinha, Jennifer Piscionere, and most especially Dr. Jillian Bellovary for always believing in me.

I thank Anthony Cusmano for the kind of friendship that can only be described as brotherhood. I thank my mom, Alma Hayes-Belmont, my brother, Andrew Belmont, and my sister-cousin, Stephanie Johnson, for being the best family anyone could ever have.

Finally, and most importantly, I thank my study buddy, best friend, life partner, and wife, Dr. Alicia Aarnio, whose love and support have carried me through the best and worst of days.

TABLE OF CONTENTS

LIST OF TABLES

LIST OF FIGURES

CHAPTER I

INTRODUCTION AND PHYSICS MOTIVATION

1.1 Historical Perspective

Humanity's greatest achievements have always stemmed from our desire to learn more about the nature of the world around us.[a] The pinnacle of this drive for knowledge is physics. While physics was more or less formally established in 1687 with the publication of Isaac Newton's *Philosophiae Naturalis Principia Mathematica*, the origins of physics can be traced back to the 4^{th} century BCE, when Democritus hypothesized the existence of atoms ($\alpha\tau o\mu\alpha$, atoma; singular: $\alpha\tau o\mu o\varsigma$, atomos). While atoms as we now know them are not the most fundamental, indivisible units of matter, we do believe in the pursuit of this reductionist view of nature and, further, that there do exist fundamental, indivisible units of matter. Ultimately this quest for Democritus's atoms has given us the Standard Model of particle physics. With the advent of modern physics, we know now that nature is much cleverer than we, and every new discovery demonstrates that nature is richer and more complex that we had previously imagined could be possible.

The Standard Model of particle physics describes all known particles and their interactions, excluding gravity. The Standard Model is, in its mathematical formulation, a quantum field theory. The Standard Model is a marriage of three unique components, each corresponding to one of the fundamental forces of the universe. Each component can eas-

[a] This section is a conglomeration of the historical perspectives offered by [1–4], see also [5–7].

ily be identified in the Standard Model gauge group, which is $SU(3) \times SU(2) \times U(1)$. The first, $SU(3)$, corresponds to the strong interaction; the second, $SU(2)$, corresponds to the weak interaction; the third, $U(1)$, corresponds to the electromagnetic interaction. It is this first one, the strong interaction, which concerns us in this thesis. It is worthwhile to note that attempts to incorporate gravity for a unified field theory of all the known forces have lead to many and various new ideas about the new physics, much of which may be accessible at the Large Hadron Collider (LHC) at CERN. The three main branches of this approach are Loop Quantum Gravity, Warped Geometry, and String Theory.

It is now well known that the correct quantum field theory describing the strong interaction is Quantum Chromodynamics (QCD). Quantum Chromodynamics has its origins in the Quark Model, developed in the 1960s to explain the so-called "particle zoo," the seemingly innumerable hadron states. As more and more particles were discovered, it seemed less and less likely that they were all fundamental. This led to many and various ideas about how to describe these particles not as fundamental, but rather as bound states or excitations of something else. A few early ideas failed, but the Quark Model put forward by Murray Gell-Mann and George Zweig in 1963 proved to be both descriptive and predictive. Ultimately, a few underlying issues with the Quark Model led to the idea that Quark Model was not fundamental, but that a deeper symmetry was at work. This was largely motivated by the Δ^{++} baryon. The Quark Model correctly predicted its mass, spin, and internal parity. It required that this particle be composed of three up quarks with spin up and vanishing orbital angular momentum. However, this was in direct conflict with the Pauli Exclusion Principle, which precludes any two fermions being in the same state. It was therefore proposed by Moo-Young Han and Yoichiro Nambu in 1965 that there were

in fact three triplets of quarks. By 1973, this was understood to be equivalent to each quark having an extra degree of freedom, color, which had three possible states (red, green, and blue). The terms "color" and "Quantum Chromodynamics" were put forth by Gell-Mann at the 16^{th} International Conference on High Energy Physics in 1972.

One of the greatest criticisms of the Quark Model was that quarks were never found in isolation. At the time, a fundamental particle was believed to be a physical observable, and so Gell-Mann himself often said that quarks were convenient mathematical constructs and not actual particles. Richard Feynman disagreed, believing that the diffusion of quark momentum explained diffractive scattering. James Bjorken derived inelastic scattering structure functions and a new scaling relation (now known as Bjorken scaling) for deep inelastic scattering under the assumption that, at arbitrarily small distances (or, equivalently, arbitrarily large momenta), the quarks were point-like. His predictions were verified at SLAC in 1969, the same year in which Gell-Mann was awarded the Nobel Prize in physics for his work on the Quark Model. For their pioneering work on these experiments, Jerome Friedman, Henry Kendall, and Richard Taylor were awarded the 1990 Nobel Prize in Physics. Bjorken's idea that at the smallest distances the quarks were point-like and freely moving motivated the work leading to the discovery of the mathematical formulation of asymptotic freedom in 1973, for which Frank Wilczek, David Gross, and H. David Politzer were awarded the 2004 Nobel Prize in Physics. One of the great injustices in the history of physics is that despite these and many other pioneering contributions, James Bjorken has never been awarded a Nobel Prize.

By the mid 1970's, the mathematical framework being used more or less resembled the QCD we know today. At that time, it also seemed that QCD might be used to prove

confinement, which can be thought of as related to but the opposite of asymptotic freedom; confinement refers to the confinement of quarks within hadrons. Since quarks had been proven to be real, but still had not been isolated in nature, it was assumed that there was some physical mechanism that forced them to be unobservable. It was postulated that physical observables had to be color neutral, and therefore the colored quarks could only exist within color neutral hadrons and never be found isolated. However, there was no mathematical justification for it, and one was sought. In fact, to this day, confinement has not been demonstrated analytically. However, with the advent of super computers and lattice gauge theory (specifically lattice QCD in this case), confinement has been unambiguously confirmed as a feature of QCD. The analytical solution to this problem is related to the mathematical proof of the existence of Yang-Mills fields and of the mass-gap, for which the Clay Mathematics Institute will award a Millennium Prize.

As already stated, QCD is a quantum field theory. More specifically, it is a Yang-Mills non-Abelian gauge field theory. Chen Ning Yang and Robert Mills first put forward the idea of non-Abelian gauge theories in 1954. The term non-Abelian comes from the fact that the mathematical group describing the gauge symmetry is a non-Abelian group. The non-commutativity of the generators of the gauge symmetry group has the profound physical consequence that the gauge bosons, the interaction particles that mediate the force, interact with themselves. Non-Abelian gauge field theories were first successfully quantized by Ludvig Faddeev in 1967, and were shown to be renormalizable by Gerardus 't Hooft and Martinus Veltman in 1971. For their successful formulation of a renormalization scheme for non-Abelian gauge field theories (known as dimensional regularization), 't Hooft and Veltman were awarded the 1999 Nobel Prize in Physics.

An important aspect of QCD is the coupling constant. While all coupling constants have been known to run since the invention of the Renormalization Group by Ernst Stueckelberg and Andre Peterman in 1953, the running of the QCD coupling constant, α_s, is much more dramatic than in the unified electroweak theory and, moreover, runs inversely to those of the electroweak interaction. The weak and electromagnetic coupling constants are small at zero energy and increase with increasing energy, whereas α_s is divergent at zero energy and decreases with increasing energy. This is a crucial aspect of asymptotic freedom and confinement. It has also been key in the development of methods for calculating physical observables in QCD. At arbitrarily large energies, the coupling constant is small enough that perturbative expansions can be used. However, not all interesting physical processes take place at sufficiently high energies. This necessitated the development of lattice gauge theory, where space and time are discretized and observables are calculated on a computer using numerical techniques and approximations. Using this method, even physical phenomena where the coupling constant is large can be studied. Lattice QCD has been especially important in the understanding of quantum field theories at finite temperature and density.

Finite temperature field theory (that is, quantum field theory as applied to a statistical ensemble) was first formulated by Takeo Matsubara in 1955, and by 1957, Murray Gell-Mann and Keith Brueckner formulated a theory of a QED plasma. Drawing on this work, John Collins and Malcolm Perry put forward the first theory of a QCD plasma in 1975. In the same year, Aleksandr Polyakov discovered non-perturbative topological fluctuations in the QCD vacuum, and later work demonstrated that these fluctuations are responsible for phase transitions in QCD. In a now famous review by Edward Shuryak in 1980, the

term “quark gluon plasma” (QGP) was coined to described the QCD plasma and the first vastly influential prescription for a relativistic nucleus-nucleus collision program to study this plasma and the associated phase transition was given.

Interestingly, the first heavy ion program predated this prescription by 8 years, even predating the prediction of a QCD plasma. The heavy ion program at the Bevalac at LBNL started in 1972 with the goal of understanding the equation of state (EOS) of dense hadronic matter. However, after the aforementioned theoretical discoveries, it was clear that heavy ion facilities could be used to study the QGP and the phase transitions of QCD matter. The Bevalac program continued through to the mid 1980s, passing the torch along to the SIS at GSI in Darmstadt, Germany. After the early work at the Bevalac and GSI/SIS, the AGS at BNL and the SPS at CERN began their heavy ion program in the 1990s. In 2000, operations began at the RHIC at BNL began. While its beam energies are actually lower than those at CERN/SPS, the center of mass energy per nucleon ($\sqrt{s_{NN}}$) is greater by more than a factor of ten, owing to the fact that it is an intersecting storage ring collider and not a fixed target accelerator. Finally, while the main thrust of the LHC program at CERN is particle physics (especially topics such as the search for the Higgs boson and supersymmetric particles), there is additionally a heavy ion program that will run for a few weeks of the year. The first successful run of the LHC particle physics program began in November of 2009 with a commissioning run of p+p collisions starting at $\sqrt{s} = 900$ GeV and ramping upwards. A few months later, in March of 2010, research operations began with p+p collisions at $\sqrt{s} = 7$ TeV. Beginning on 8 November 2010 and ending on 6 December 2010 was the first heavy ion run of Pb+Pb collisions at $\sqrt{s_{NN}} = 2.76$ TeV.

1.2 The Evolution of a Heavy Ion Collision

The evolution of a heavy ion collision can be summarized, in brevis, in the following way: 1) the preconditions, which are various physical properties of the highly Lorentz contracted nucleus; 2) the impact, which is described by such fundamental parameters as collision centrality, which is a proxy for the impact parameter; 3) equilibration, during which the quark-gluon plasma develops; 4) chemical freeze-out, when particle production via inelastic scattering ceases; and 5) kinetic freeze-out, when all particle interactions cease and the distribution of particles is in its final state. Figure 1.1 gives a nice, simple pictorial representation of this evolution.

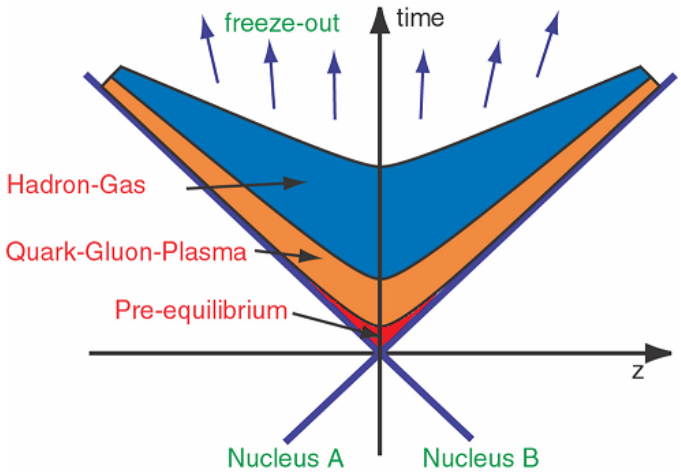

Figure 1.1: Evolution of a Heavy Ion Collision.

1.3 Initial Conditions

1.3.1 Preconditions

In any experiment, it is important to have an understanding of the initial conditions and their affects on the final state. Because the energies involved in ultra-relativistic heavy ion collisions are several orders of magnitude larger than the binding energies of atomic nuclei, the details of nuclear structure physics are largely inconsequential, although basic properties like spatial density distributions are important at any collision energy [6]. The parton distribution functions in nuclei are modified from those in free nucleons [8]. At high energy and low longitudinal momentum fraction, gluon saturation occurs [9]. This saturation can be modeled, in certain regimes, with an effective theory called Colored Glass Condensate [10]. We study d+Au collisions in order to understand these cold nuclear matter (CNM) effects [11]. Because there is a highly Lorentz contracted nucleus, the physics of cold nuclear matter is relevant; because there is only one, there are far too few participants for large scale thermalization and the consequent QGP formation, therefore the CNM effects can be studied in isolation. The CGC was proposed as a possible mechanism for the apparent particle suppression in Au+Au collisions [12]. This mechanism would also produce particle suppression in d+Au collisions, as argued above, but experimental results indicate that there is no particle suppression in d+Au collisions at mid-rapidity [13].

As long ago as 1974, it was observed by James Cronin and collaborators that in nucleon-nucleus (typically denoted as p+A) collisions the yield of particles exhibits a modification relative to the yield of particles in p+p collisions [14]. The ratio of these spectra, normalized to the number of binary nucleon-nucleon collisions that takes place in the p+A

collision, is sometimes called the Cronin ratio. At very low transverse momentum p_T, the yield is reduced, and the Cronin ratio is less than one; in the intermediate p_T region ($2GeV/c < p_T < 6GeV/c$) the yield is enhanced and so the ratio is greater than one; and at sufficiently high p_T ($p_T > 6GeV/c$) the yield becomes unmodified and the ratio is equal to one. The enhancement at intermediate p_T is called the Cronin enhancement. It was not long after the measurement by Cronin et al. that the enhancement was measured with identified particles, and the enhancement was found to depend on the particle species [15]. Traditional explanations of this effect involve the multiple scattering by soft partons in the target nucleus of hard partons from the projectile [16]. This naturally explains the deficit at low p_T and enhancement at intermediate p_T, but does not account for the particle species dependence. Relatively recently, in 2004, a very different approach, based on final state rather than initial state interactions, was put forward [17]. This model naturally explains the particle species dependence of the Cronin enhancement. This model is based on parton recombination, which will be discussed in further detail later on.

1.3.2 Impact

Physical parameters such as the impact parameter are collected under the heading of impact. In heavy ion collisions, the impact parameter is defined in the same way as it is in classical mechanics, see Figure 1.2. One can define the number of participants, N_{part}, as the number of nucleons in the overlap region. The centrality of a collision is defined in such a way that that each bin, expressed as a percentage of the total inelastic nucleus+nucleus cross section, has the same probability as every other bin and so the centrality distribu-

tion is thusly flat by definition. Figure 1.3 show the energy deposited in the zero degree calorimeters (ZDC) vs the total charge induced in the beam-beam counters (BBC). The details of the BBC and ZDC will be described in the next chapter. The distribution is divided into equality probability percentiles. The ZDC measures the energy of spectator neutrons, of which there are more in peripheral collisions. Conversely, more charged particles are produced in more central collisions, and therefore the total charge induced in the BBC is greater. Collisions with vanishing impact parameter, that is where there is total overlap, are called the "most central;" collisions where the impact parameter is nearly equal to the nuclear radius, that is where there is almost no overlap, are called the "most peripheral." By definition, then, the most central collisions have the largest N_{part}, and the most peripheral have the smallest. By convention, the centrality is 0% for the most central, and 100% for the most peripheral. The most peripheral collisions produce too low of a signal for the event to pass the minimum bias trigger requirement, so not all events can be collected. In PHENIX, for example, only events with centrality 0% through 92% can be recorded for Au+Au collisions. In d+Au collisions, only 0–88% can be recorded.

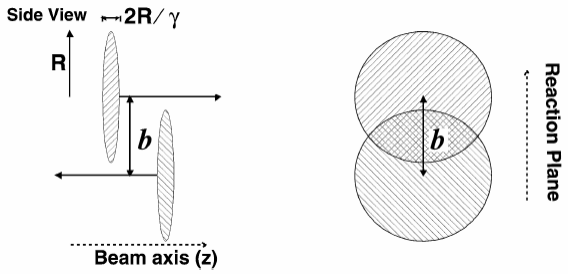

Figure 1.2: Schematic drawing of two colliding nuclei, indicating the definition of impact parameter in nuclear interactions.

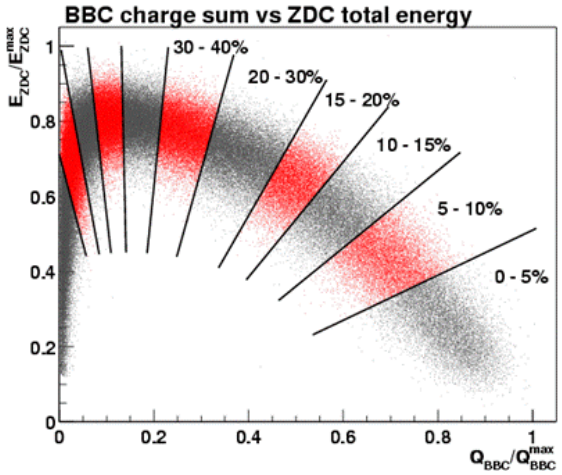

Figure 1.3: Plot of correlation between charge collected in BBC and energy deposited in ZDC, partitioned into segments of equal probability, defining centrality.

The number of binary collisions, N_{coll}, is calculated using the Glauber model [18, 19]. This is an important quantity for the classification of any observable produced in hard processes. By hard processes we mean interactions in which there is a large momentum transfer between the constituent partons in the nucleon. In the absence of any nuclear medium

effects, hard processes would be expected to scale with the total number of individual nucleon+nucleon collisions, since each nucleon+nucleon has its own collection of partons and thus, in the aggregate, the same probability for a hard scattering. For a comparison of N_{part} to N_{coll}, see Figure 1.4 and Table 1.1. In the most central Au+Au collisions, N_{coll} exceeds N_{part} by nearly a factor of three. In peripheral Au+Au and in d+Au collisions they have similar values and in peripheral d+Au collisions N_{part} is slightly greater than N_{coll}. This can be understood intuitively as for a single nucleon-nucleon collision $N_{coll} = 1$ and $N_{part} = 2$. For the Run8 d+Au, the uncertainties of N_{part} have not been evaluated and are estimated based on Run3 results.

Of particular note are nuclear modification factors, which are quantitative measures of medium affects on particle production More specifically, R_{AA} is the ratio of yields in nucleus+nucleus (A+A) collisions to the yields in proton on proton (p+p) collisions, normalized to the number of binary collisions; R_{dA} is the ratio of yields in deuteron+nucleus (d+A) collisions to the yields in p+p collisions, normalized to the number of binary collisions; and R_{CP} is the ratio of yields in central collisions to the yields in peripheral collisions, scaled by the ratio of the respective numbers of binary collisions, and is defined the same way for both deuteron+nucleus and nucleus+nucleus collisions. These quantities are defined as follows:

$$R_{AA} = \frac{Yield^{A+A}}{N_{coll}^{A+A} Yield^{pp}}, \quad R_{dA} = \frac{Yield^{d+A}}{N_{coll}^{d+A} Yield^{pp}}, \quad R_{CP} = \frac{Yield^{central}}{Yield^{peripheral}} \frac{N_{coll}^{peripheral}}{N_{coll}^{central}}. \tag{1.1}$$

Table 1.1: Average $\langle N_{part} \rangle$ and $\langle N_{coll} \rangle$ for Various Centralities in Au+Au and d+Au at $\sqrt{s_{NN}} = 200$ GeV

Centrality	$\langle N_{coll} \rangle$	$\langle N_{part} \rangle$
Au+Au		
0-10%	960.2 $\pm$ 96.1	325.8 $\pm$ 3.8
10-20%	609.5 $\pm$ 59.8	236.1 $\pm$ 5.5
20-40%	300.8 $\pm$ 29.6	141.5 $\pm$ 5.8
40-60%	94.2 $\pm$ 12.0	61.6 $\pm$ 5.1
60-92%	14.8 $\pm$ 3.0	14.7 $\pm$ 2.9
d+Au		
0-20%	15.1 $\pm$ 1.0	15.2 $\pm$ (0.9)
20-40%	10.2 $\pm$ 0.7	10.8 $\pm$ (0.6)
0-100%	7.6 $\pm$ 0.4	8.4 $\pm$ (0.4)
40-60%	6.6 $\pm$ 0.4	7.5 $\pm$ (0.4)
60-88%	3.1 $\pm$ 0.2	4.3 $\pm$ (0.2)
p+p	$\equiv 1$	$\equiv 2$

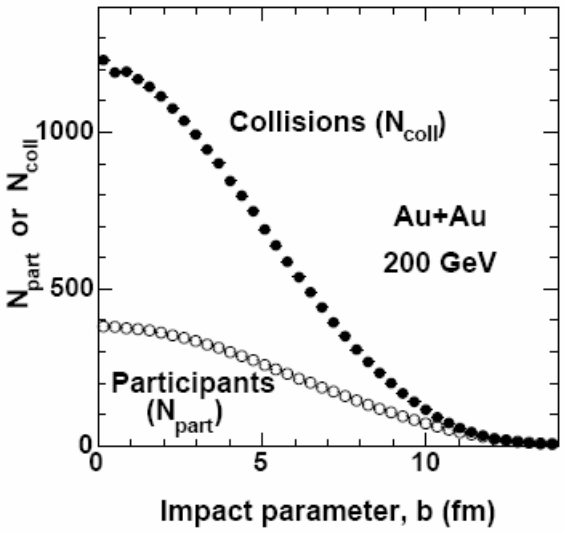

Figure 1.4: N_{part} and N_{coll} for Au+Au collisions at $\sqrt{s_{NN}} = 200$ GeV as a function of impact parameter b as determined using the Glauber Model.

There are two physical pictures for what happens at impact: the Landau picture and the Bjorken picture. In the Landau picture [20, 21], the two nuclei hit dead on and stop, known as nuclear stopping. In this picture, the rapidity distribution of net baryons, which is defined as the difference between the total number of baryon and the total number of antibaryons, is Gaussian. In the Bjorken picture [22], the two nuclei pass through each other, exciting the region of vacuum they sweep out in the process. The distribution of net baryons is zero at mid rapidity with peaks at forward and backward rapidity. Various heavy ion experiments have shown that the Landau picture dominates particle production in lower energy collisions, and that the Bjorken picture dominates particle production in higher energy collisions. In [23] the BRAHMS collaboration summarizes the situation nicely, concluding that the Bjorken picture dominates at RHIC energies; see Figure 1.5.

In [22] Bjorken gives a prescription for estimating the energy density:

$$\varepsilon = \frac{1}{\tau_0 A_T} \frac{dE_T}{dy}, \tag{1.2}$$

where τ_0 is the characteristic time, usually taken to have a typical value of 1 fm, and A_T is the overlap area, such that the product gives the equilibration volume; and dE_T/dy is the rapidity density of the total transverse energy. In fact, Bjorken introduced an erroneous factor of two in his calculation [4]; here I have written it correctly.

In [24, 25] by the PHENIX collaboration, this method is used to estimate the energy density in Au+Au collisions at various collision energies. As stated therein, these energy densities, between 4.5 and 5.5 GeV/fm^3, are well above the expected critical energy density for QGP formation, estimated to be approximately 1 GeV/fm^3 [3, 4, 26, 27]. Although

this is far from a definitive identification of the QGP, it was an important first step in the qualification and quantification of the hot dense matter produced at RHIC.

The issue of determining the characteristic time should not be trivialized. Historically, it has simply been assumed to be 1 fm, which was nothing more than an ad-hoc order of magnitude guess by Bjorken in [22]. One can in fact use somewhat more sophisticated ideas to make a more physical estimate, as outlined in §2 of the PHENIX White Paper [4]. The shortest time for which the Bjorken formula can be considered valid is the crossing time, which is the time it takes for the two nuclei to pass through each other. This is simply the sum of the radii of each nucleus in the center of mass frame, so for symmetric collision species we have $\tau_{\text{crossing}} = 2r/\gamma$. Table 1.2 shows the crossing times for Au+Au nuclei at various collision energies.

The shortest time is, of course, not necessarily the correct time. A realistic characteristic time might be the time required for particle formation. This can be estimated using the Heisenberg uncertainty principle. Taking from $\Delta E \Delta t \geq 1$, one can make the analogy that $\langle m_T \rangle \tau_{\text{formation}} \geq 1$, and so we take $\tau_{\text{formation}} = 1/\langle m_T \rangle$. This yields a formation time of about 0.35 fm for the 200 GeV data. Another possibility for the characteristic time is the thermalization time. This can be taken from hydrodynamics models, which require a thermalization time between 0.6 and 1.0 fm to adequately reproduce the 200 GeV data on collective anisotropy [4, 28].

Putting all these ideas together, we get a broad range of possible characteristic times and thus a broad range of possible energy densities, and each of these is well in excess of the critical energy density for QGP formation; see Figure 1.6.

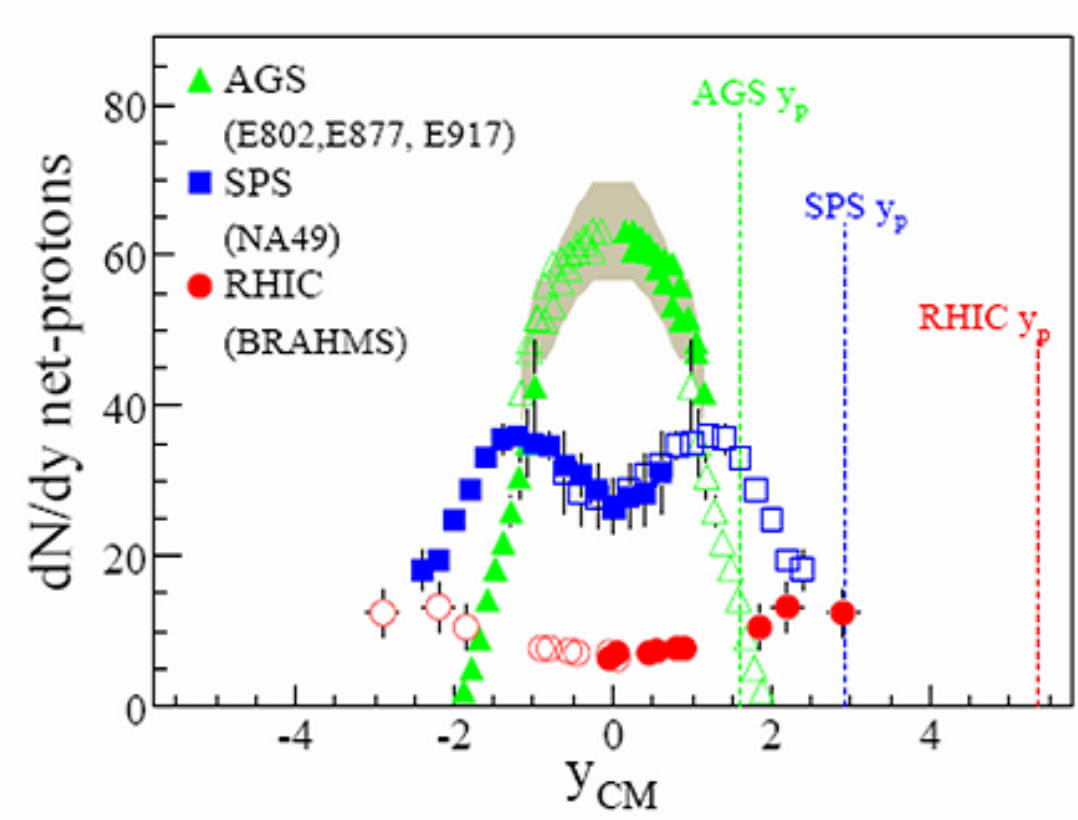

Figure 1.5: dN/dy for net protons [23]. For AGS data, $\sqrt{s_{NN}} = 4.7$ GeV. For SPS data, $\sqrt{s_{NN}} = 17.3$ GeV. For RHIC data, $\sqrt{s_{NN}} = 200$ GeV.

Table 1.2: Crossing Times for Various Collision Energies.

$\sqrt{s_{NN}}$ (GeV)	E_{beam} (GeV)	γ	τ_{crossing} (fm)
200.00	100.00	106.38	0.13
100.00	50.00	53.19	0.26
62.40	31.20	33.19	0.42
27.40	13.70	14.57	0.96
17.20	8.60	9.15	1.53
12.30	6.15	6.54	2.13
8.80	4.40	4.68	2.98
7.60	3.80	4.04	3.45
6.30	3.15	3.35	4.17
5.00	2.50	2.66	5.25

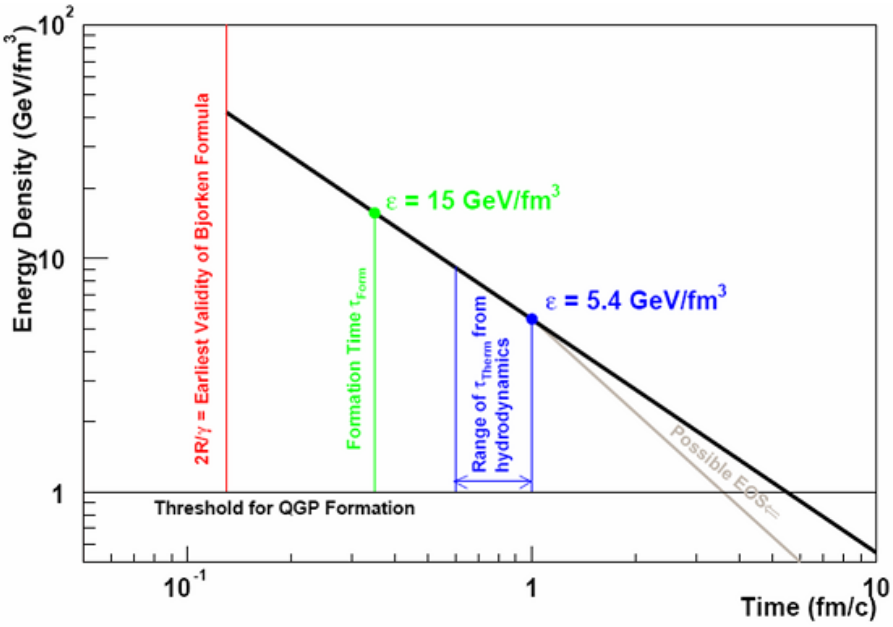

Figure 1.6: Energy density estimations based on various assumptions, as presented in [4].

1.4 Thermalization

As discussed previously, there exists a phase boundary between ordinary nuclear matter and the quark gluon plasma. This phase transition and the properties of the QGP are often studied theoretically using lattice QCD. Lattice calculations have unequivocally identified the phase transition, and can also determine the critical temperature, the temperature of the phase transition, at vanishing baryon chemical potential. The critical temperature, as well as the energy density and pressure at arbitrary temperature, have been studied extensively, see e.g. [26, 27]. To extrapolate to non-vanishing baryon chemical potential, models need to be employed. One of the most successful theoretical models from the earlier days of heavy ion physics is the thermal model [29]. It is essentially a grand canonical ensemble applied to a partonic system. A grand canonical ensemble is usually defined as a system with global conservation of particle number and energy conservation, but no local conservation. Therefore, the system can exchange energy and particles with the surroundings. One can extend this formalism to include other conserved quantities. For thermal models dealing with heavy ion collisions, there is the usual conservation of 4-momentum, and the conservation of particle number is extend to conservation of charge, baryon number, and strangeness [30]. The approach is simple but powerful, and has been met with great success [29, 31, 32]. It very accurately predicts a wide variety of particle abundances (see Figures 1.7 and 1.8), which demonstrates thermalization. However, this alone is not enough to determine at which phase of the evolution of the system that thermalization occurs. The two free parameters in the fits to the data are the chemical freeze-out temperature and baryon chemical potential, which describe the location of the system at chemical freezeout on the

QCD phase diagram (see Figures 1.9 and 1.10). Karsch [33] and Braun-Munzinger [34] provide excellent reviews on lattice results and on the thermal model, respectively.

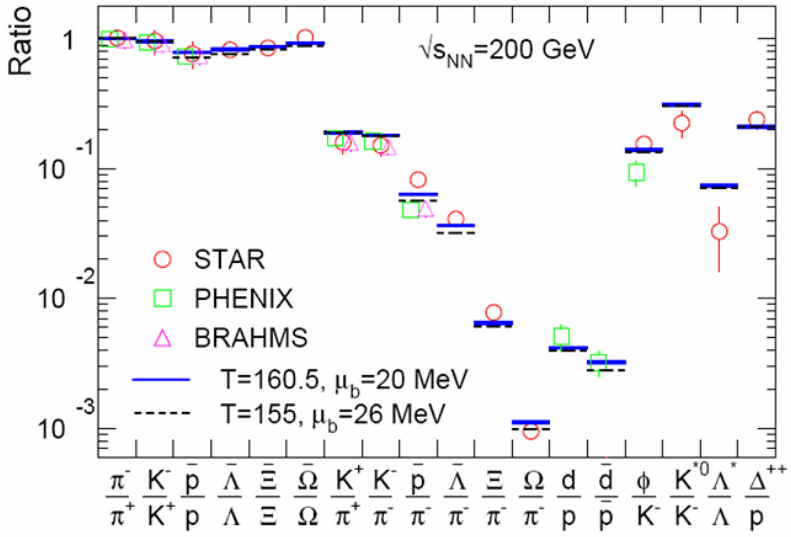

Figure 1.7: Comparison of particle ratios from theoretical calculations and experimental measurements [29]. This model assumes full strangess saturation, $\gamma_s = 1$.

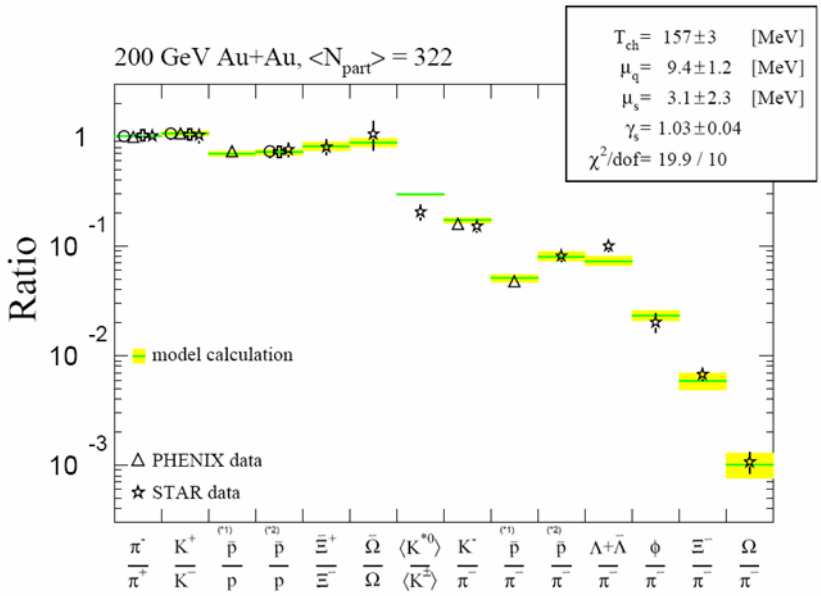

Figure 1.8: Comparison of particle ratios from theoretical calculations and experimental measurements [32]. This model has strangeness saturation as a free parameter, with the result $\gamma_s = 1.03 \pm 0.04$.

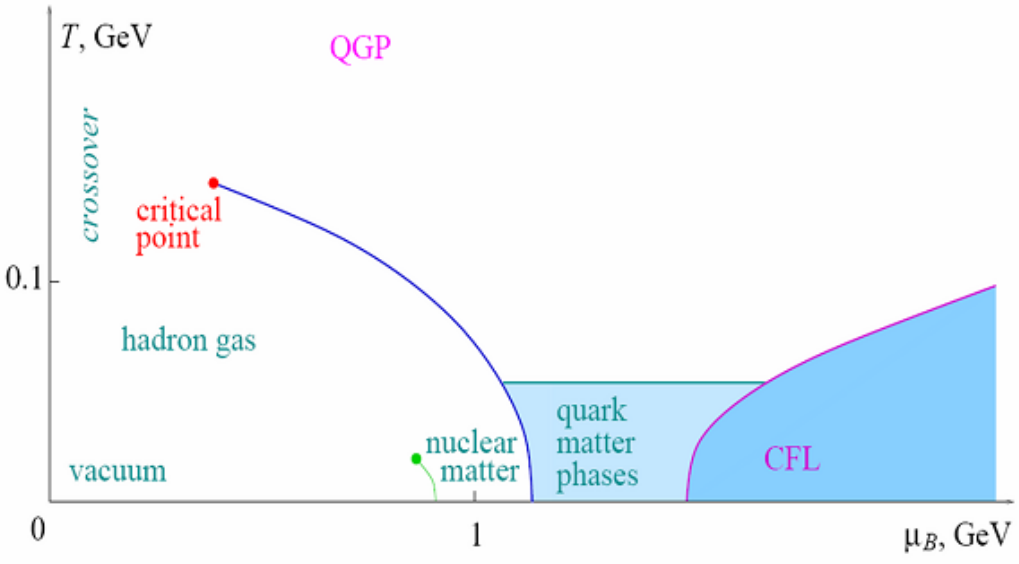

Figure 1.9: QCD Phase Diagram [35] of temperature T vs. baryon chemical potential μ_B. Shown schematically are the various regions of the phase diagram along with the phase boundaries.

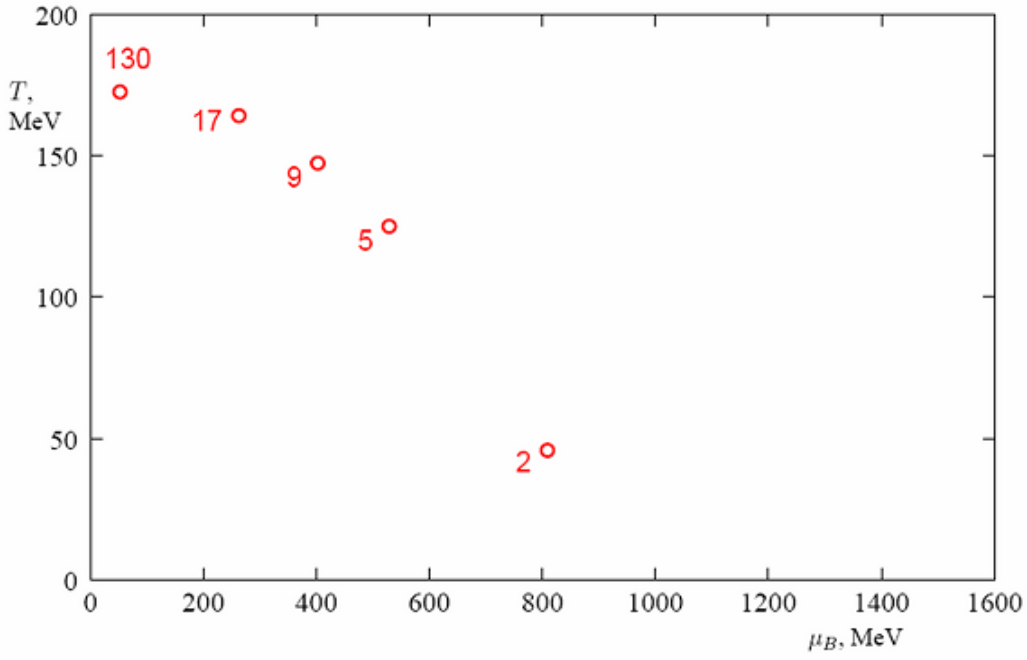

Figure 1.10: QCD Phase Diagram [35] of temperature T vs. baryon chemical potential μ_B. Shown as data points are the locations of T and μ_B as determined from thermal model fits to data on integrated particle yields.

A crucial aspect of thermalization is the degree of strangeness equilibration. In a QGP, the quark masses are reduced to their bare Higgs masses [36]; see Figure 1.11. The Higgs mass of the strange quark is approximately 150 MeV, on the same order as the critical temperature. This means that strange quarks would be produced thermally and would equilibrate in a similar way that the much lighter up and down quarks would. As seen in the aforementioned references and figures, this is in fact observed, as even multi-strange particles are produced in thermal abundances. Another insight into this is to look at the K/π ratios as a function of N_{part}, see Figure 1.12. There is a clear rise of the K/π ratio as a function of N_{part} up to about $N_{part} = 100$, where it mostly levels off. This may be an indication that as the number of particles in the system increases, strangeness equilibration increases, until reaching a certain value at which full strangeness equilibration is achieved. To fully justify the idea strangeness saturation increasing with increasing N_{part}, one needs to also consider multi-strange particles [31, 32, 37] Figure 1.13 shows the stragness equilibration parameter γ_s as a function of N_{part}.

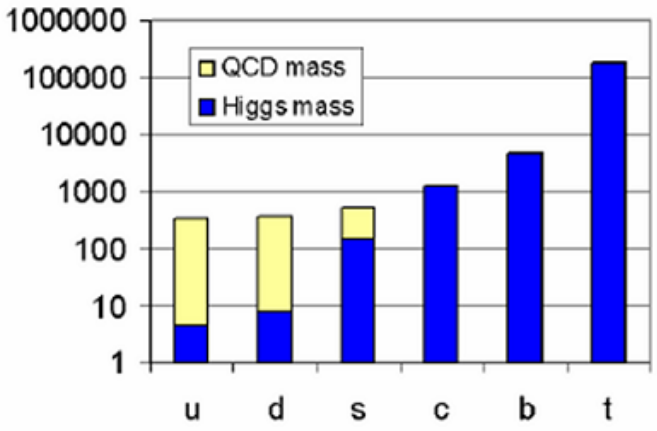

Figure 1.11: QCD and Higgs contribution to quark masses [36].

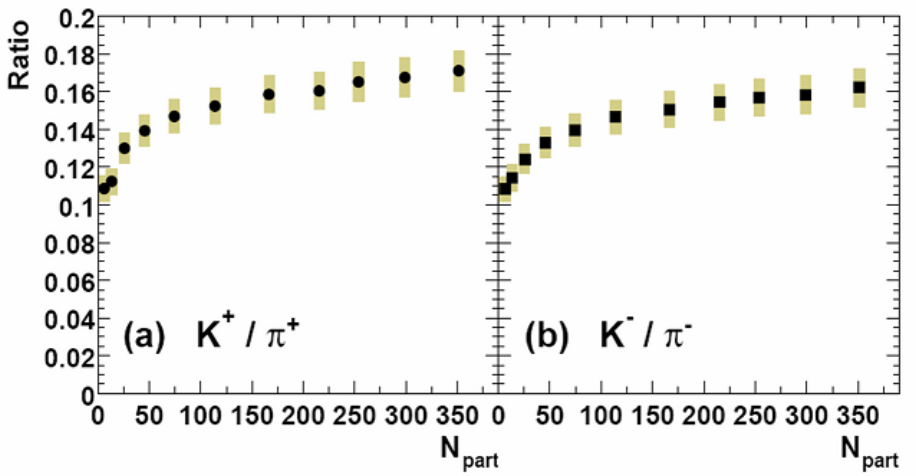

Figure 1.12: K/π as a function of N_{part} [38].

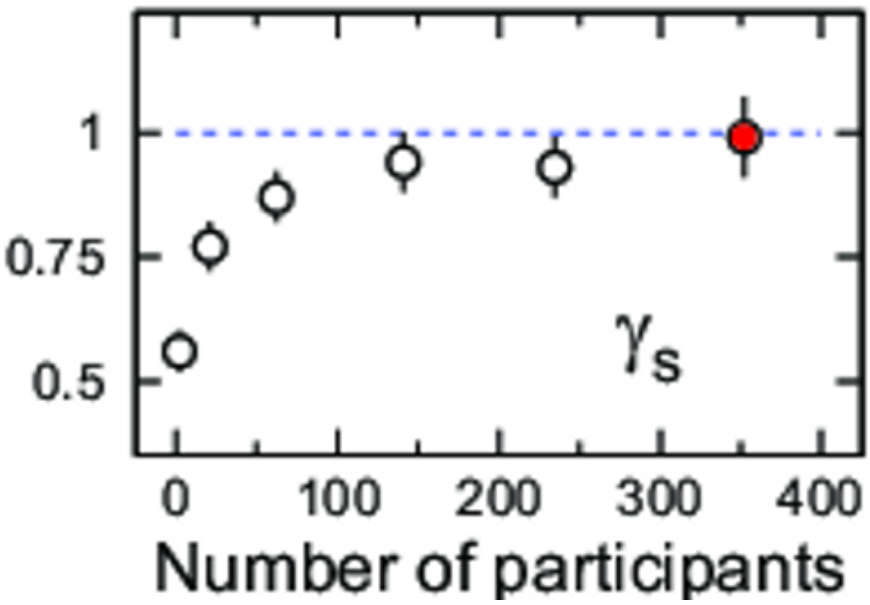

Figure 1.13: Strangeness equilibtation parameter γ_s as a function of N_{part} [37].

1.5 Radial and Elliptic Flow

One of the most important aspects of the hot dense medium produced at RHIC is the fact that it flows. Quite surprisingly, early results indicated that the matter is very well described by relativistic hydrodynamics with no viscosity. The deep insight provided by flow measurements stems from the fact that the flow builds up early during the evolution of the system and self-quenches, and can thusly reveal information about the early stages of the fireball and various aspects of thermalization. The latter is because the hydrodynamics models require at least local thermal equilibrium, and so one can conclude that the success of the hydrodynamics description of the flow data indicate some degree of thermalization in the medium. Moreover, the flow models are highly dependent on the relevant degrees of freedom; thusly, flow measurements can provide insight into which types of particles, e.g. whether they be hadrons or partons, are the ones that are flowing [39, 40].

The essence of relativistic hydrodynamics can be very succinctly summarized with a few basic equations [21, 22, 28]. The stress energy tensor is defined as

$$T^{\mu\nu}(x) = (\varepsilon(x) + p(x))u^{\mu}(x)u^{\nu}(x) + p(x)g^{\mu\nu}, \tag{1.3}$$

where ε is the energy density, p is the pressure, $u^{\mu}(x) = \gamma(1, v_x, v_y, v_z)$ is the four-velocity and $\gamma = 1/\sqrt{1 - v_x^2 - v_y^2 - v_z^2}$ is the usual Lorentz factor, and $g^{\mu\nu}$ is the metric tensor. The conserved currents are $j_i^{\mu}(x) = n_i(x)u^{\mu}(x)$, where $n_i(x)$ are the number densities of the conserved quantities (usually charge, baryon number, and strangeness). The conservation laws

$$\partial_{\mu}T^{\mu\nu}(x) = 0, \qquad \partial_{\mu}j_i^{\mu}(x) = 0 \tag{1.4}$$

define the equations of motion. For k conserved quantities, we have 2+k equations with 3+k unknowns, meaning one more equation is needed to solve for the unknowns. The missing equation is the equation of state, which relates the the energy density, pressure, and number density of the conserved quantities. The equation of state cannot be determined a priori. Usually the equation of state is taken as an input from lattice QCD calculations. By comparing hydrodynamics calculations to the data, we hope to be able to determine the equation of state experimentally.

The flow of the matter manifests itself in two distinct ways: radial flow and elliptic flow. Radial flow is very simply the expansion of the matter in all directions. The data support the idea that the matter expands through all stages of the fireball evolution with a common flow velocity for all hadrons. This is ascertained from the scaling relations of transverse mass spectra [39]. Essentially, the transverse mass spectrum for soft particle production is proportional to the exponential of the transverse mass normalized to an effective temperature, called the inverse slope parameter:

$$\frac{d^2N}{m_T dm_T} \propto e^{-m_T/T}, \tag{1.5}$$

where T is the inverse slope parameter, defined as

$$T = T_{thermal} + m\langle\beta_T\rangle^2, \tag{1.6}$$

where β_T is the collective flow velocity in the transverse plane.

Elliptic flow can be understood as stemming from pressure gradients in the matter.

These pressure gradients exist only in the transverse plane. Elliptic flow is measured using angular correlations in the transverse plane. When one orients the transverse plane in such a way that the reaction plane defines the x-axis, the strongest pressure gradients point in the $\pm$ x-direction. One can easily see that the matter below the reaction plane is identical to the matter above it, and so the x-axis defines a symmetry of the system. Clearly, then, the function describing the correlation is symmetric about the x-axis, and therefore an even function. Further, the y-axis is also clearly a symmetry axis, since the matter on the left side is clearly the same as on the right side, and so the pressure gradients are necessarily of equal strength on either side. Using these two points, we can conclude that the Fourier expansion includes only cosine terms (because of the x-axis symmetry) and only even-numbered coefficients (because of the y-axis symmetry). The former is true at all rapidities, the latter however is only true at mid-rapidity. At forward and backward rapidity, there exists also directed flow. This can be understood as a deformation of the overlap region as the spectator part of the nucleus drags the edge of the overlap region a bit with it as it passes by. Therefore, the sign of the directed flow is different at forward and backward rapidity. Which sign is ascribed to which rapidity is of course totally arbitrary, but the fact that the two regions are opposite is very important. See Figure 1.14 to see how directed flow changes as a function of rapidity.

It is interesting to note that in the case of asymmetric collisions species, e.g. Cu+Au, the aforementioned y-axis symmetry is broken and so there are non-zero odd-numbered coefficients even at mid-rapidity. Additionally, the above discussion holds for a continuous distribution of matter. However, the discrete nature of the nucleons in the nuclei allows for statistical fluctuations, which can lead to some surprising results. Recent work, both

theoretical [41, 42] and experimental [43], has shown that initial state fluctuations lead to non-negligible third-order coefficients with respect to a randomly distributed (with respect to the reaction plane) third-order event plane. The addition of non-negligible v_3 to a distribution of particles has some significant consequences, forcing a serious reconsideration of many observed phenomena in heavy ion collisions [41, 42].

One of the most striking results from elliptic flow measurements is the constituent quark scaling. As seen in Figure 1.15, baryons and mesons of many different types tend to group together. However, when the axes are rescaled by the number of quarks, all the curves line up. This is a strong indication that in the stage during which elliptic flow builds up the relevant degrees are partonic since this has been predicted by parton recombination models, see e.g. [36]. Furthermore, since the hydrodynamics models require thermal equilibrium, and the success of the thermal model indicates that there is indeed thermalization (although it doesn't specifically indicate where), the combination of these results is strongly suggestive of a system of thermalized quarks and gluons.

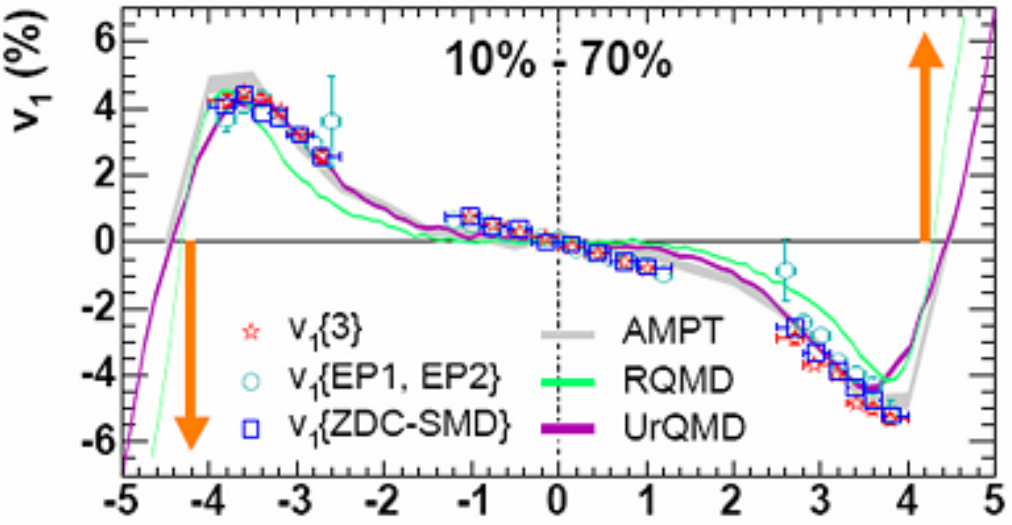

Figure 1.14: Directed flow as a function of rapidity [44].

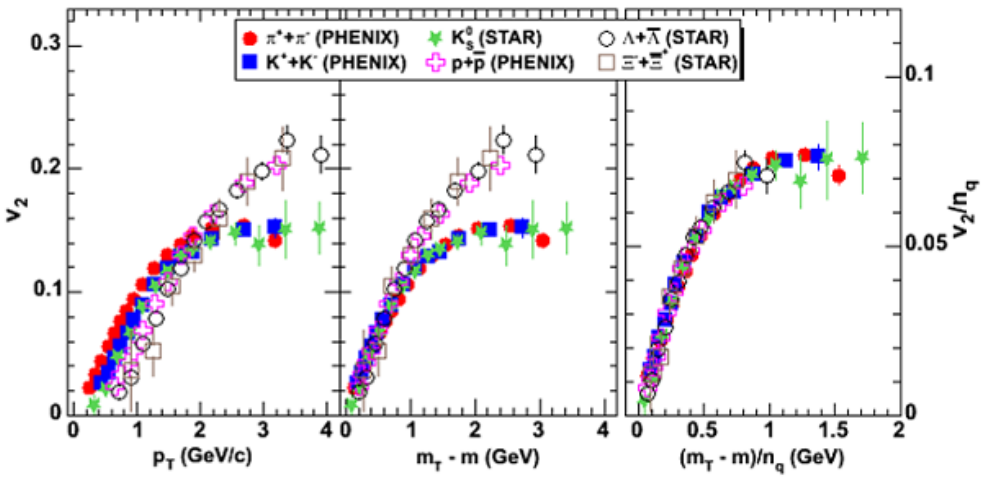

Figure 1.15: Elliptic flow scaling [45].

1.6 Hadronization in the QGP

Prior to the many discoveries made in the RHIC era, it was thought that fragmentation was the only mode of hadronization. It was predicted that all particles would be roughly equally suppressed [46] (particle suppression occurs because the partons traversing the medium will lose energy; see the next section for details). However, this in fact is not the case: while mesons are indeed suppressed at all momenta, Baryons are not suppressed at all at intermediate momentum, see Figure 1.16. One of the most important discoveries at RHIC is this so-called "Baryon Anomaly," which was first observed experimentally in [47] and studied theoretically in [48]. Since then it has has been studied extensively, see e.g. [38, 49–52]. It was a strong indication that there was more to hadronization in the QGP that had been previously postulated. Hwa and Yang [53] put forward the quark recombination model in an attempt to explain the data. This powerful model was based on the very simple idea that quarks in the same region of phase space will simply coalesce into a bound state; in fact this idea is not new [54, 55]. The cartoon in Figure 1.17 displays the basic concept nicely. Hwa is a vigorous proponent of the model, see e.g. [56]. Others have also made significant contributions to the recombination model in heavy ion collisions, see also the work of the Duke [36, 57, 58] and Texas A&M [59, 60] groups.

It is noteworthy that the apparent non-suppression of protons could have in fact been simply an effect of the mass. Because of the radial flow the particles move with a common expansion velocity, and protons being the heaviest get the largest momentum boost. This has been seen in earlier eras, see e.g. [39]. However, as Figure 1.16 shows, even mesons with a mass as heavy as the proton, e.g. the ϕ meson shown, are suppressed, which rules

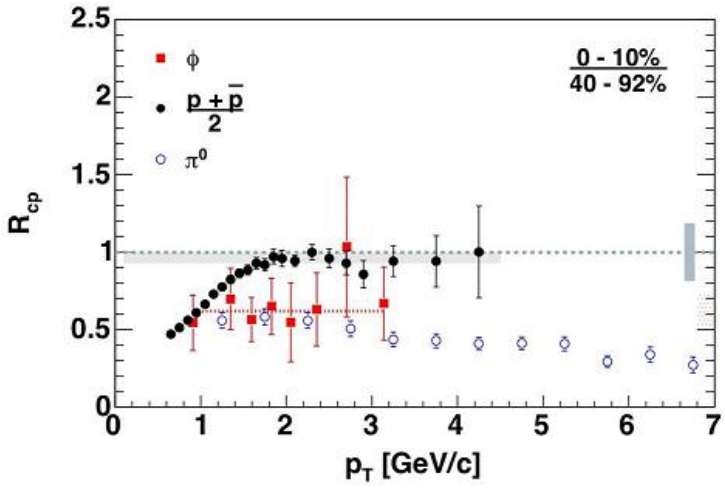

Figure 1.16: Nuclear Modification for Various Hadrons [51].

out radial flow and supports recombination as an explanation for this effect [51].

1.6.1 A Brief Comparison of Fragmentation and Recombination

Pictorially, the differences are summarized nicely in Figure 1.18. In words, the differences between the above two modes can be outlined as below:

Fragmentation

1. Inclusive process
2. Slower fall-off (power law)
3. Hadron momentum less than parton momentum
4. Many more mesons than baryons produced

Recombination

1. Exclusive process
2. Faster fall-off (exponential)
3. Hadron momentum greater than parton momentum
4. Roughly equal numbers of mesons and baryons produced

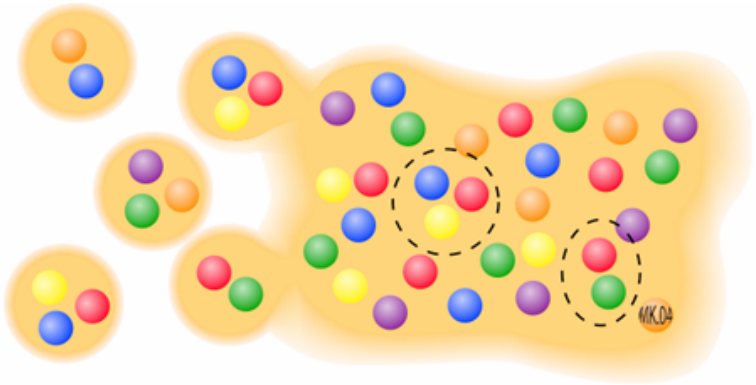

Figure 1.17: Recombination Cartoon [61]

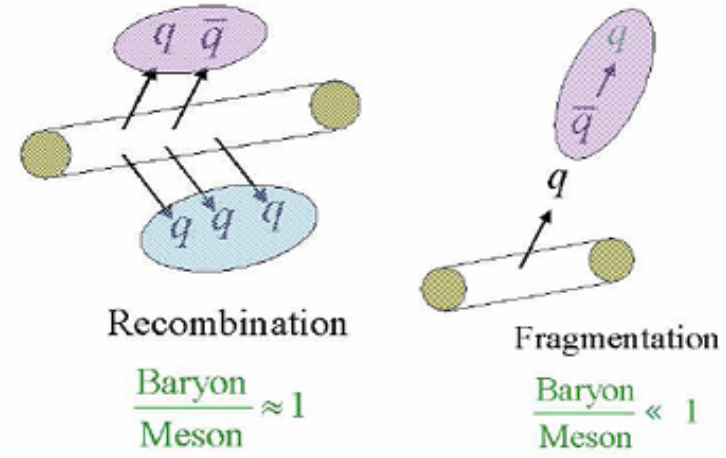

Figure 1.18: Cartoon Comparing Recombination and Fragmentation [36].

Fragmentation is inclusive because any parton can fragment to produce more partons and ultimately hadrons, whereas recombination requires that they be in a similar region of phase space. The momentum spectrum predicted by fragmentation has a slower fall off compared to that of recombination. Fragmentation greatly favors meson production, because fragmentation is much more likely to produce a quark-antiquark pair than it is to produce a diquark [4]; recombination favors them roughly equally.

1.6.2 Theoretical Calculations of Momentum Spectra

It is useful to compare the theoretical formulae for the momentum spectra predicted by these models. They can be written in various equivalent ways, I present them here as in [36, 57, 58]. For fragmentation, the momentum spectrum is

$$E\frac{d^3N_h}{d^3p} = \int d\Sigma \frac{P\cdot u}{(2\pi)^3}\sum_\alpha \int dz z^{-3} w_\alpha(P/z) D_{\alpha\to h}(z), \tag{1.7}$$

where Σ is the chemical freeze out hypersurface, P^μ is the hadron momentum, u^μ is the collective expansion velocity, w are the quark phase space distributions, α represents the various parton degrees of freedom, z is the momentum fraction, and $D(z)$ is the fragmentation function. The fragmentation function cannot be calculated analytically, it always reconstructed using fits to data. For recombination, the momentum spectrum is either

$$E\frac{d^3N^{(M)}}{d^3p} = \int d\Sigma \frac{P\cdot u}{(2\pi)^3}\sum_{\alpha\beta} \int dx w_\alpha(xP)\bar{w}_\beta((1-x)P)|\phi^{(M)}_{\alpha\beta}(x)|^2, \tag{1.8}$$

for mesons, or

$$E\frac{d^3N^{(B)}}{d^3p} = \int d\Sigma \frac{P\cdot u}{(2\pi)^3}\sum_{\alpha\beta\gamma}\iint dxdx' w_\alpha(xP)w_\beta(x'P)w_\gamma((1-x-x')P)|\phi^{(B)}_{\alpha\beta\gamma}(x,x')|^2, \tag{1.9}$$

for baryons, where x and x' are momentum fractions and ϕ are the hadron wave functions. For a thermal distribution of partons, the phase space distribution is $w(p) = e^{p\cdot u/T}$, but at sufficiently high momentum the phase space distribution is a power law.

1.6.3 Regimes of Applicability for Fragmentation and Recombination

As stated above, recombination has a faster fall-off than fragmentation. Therefore, one might expect that recombination dominates at lower momentum and that fragmentation takes over at sufficiently high momentum. Indeed, this seems to be the case. This is seen quite clearly in Figures 1.19 and 1.21, which show theory curves for the π^0 spectrum overlayed with experimental data from PHENIX; in Figure 1.20, which shows the theory curves for the unidentified hadron spectrum overlayed with PHENIX data; and in Figure 1.22, which shows theory curves and PHENIX data for $\bar{p}$. The Duke group originally argued for purely thermal recombination together with fragmentation. Hwa and Yang and Greco et al. have argued for recombination of partons in both similar and dissimilar momentum space in all momentum ranges. It is clear both of these approaches can reproduce the spectrum.

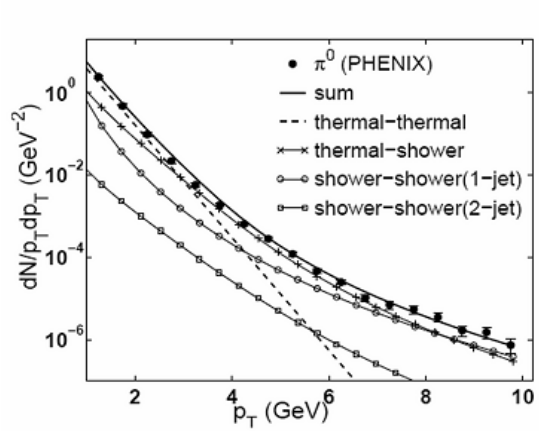

Figure 1.19: Recombination prediction for momentum spectrum of π^0 shown with experimental data from PHENIX [56].

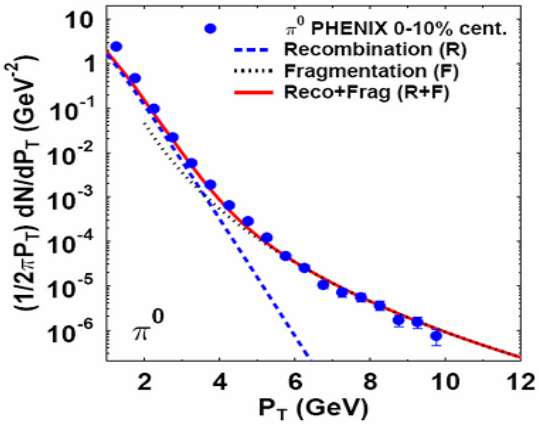

Figure 1.20: Recombination prediction for momentum spectrum of π^0 shown with experimental data from PHENIX [57].

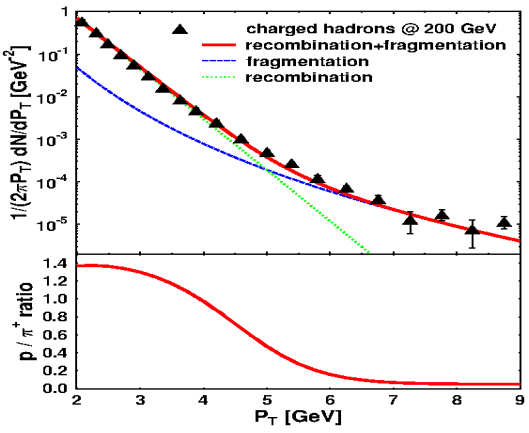

Figure 1.21: Recombination prediction for momentum spectrum of unidentified hadrons with experimental data from PHENIX [58].

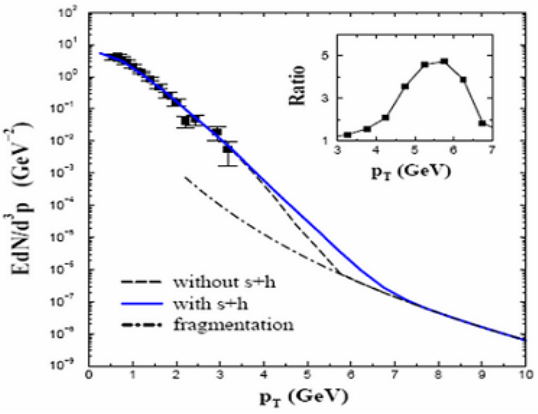

Figure 1.22: Recombination prediction for momentum spectrum of $\bar{p}$ shown with experimental data from PHENIX [60].

1.6.4 Recombination and Elliptic Flow

As mentioned very briefly in the previous section, the scaling of v_2 with the number of constituent quarks is a prediction of the recombination models. This was first observed theoretically in [62] and experimentally in [63]. The original formulation relied on a simplified version where the partons are thermal and co-moving. However, what happens in a more general formulation where partons in different momentum space can coalesce into a a bound state, e.g. in the formulation used by Hwa and collaborators? Additional considerations of the nature of this dynamical quark coalescence suggest that the constituent quark scaling should eventually break, as the production mechanism transitions from strictly thermal recombination (TT for mesons and TTT for baryons) to thermal+shower recombination (TS for mesons and TTS and TSS for baryons), and the breaking point of the scaling is expected to shift as a function of centrality [64]. Very nice recent experimental results [65] demonstrate this scaling breaking as a function centrality quite clearly.

In fact, even under the most favorable assumptions, this scaling is only approximate because it ignores higher order terms [62, 66, 67]. Additionally, the inclusion of higher Fock states also modifies the scaling, although not by an inordinate amount [68].

1.7 Partonic Energy Loss in the QGP

It is a well-known phenomenon that charged particles traveling through electromagnetic fields lose energy by radiating photons. This process is usually called bremsstrahlung, although in some cases, such as in astrophysics, this term is reserved for the more narrow definition of the process by which electrons radiate photons in the presence of the electric

field of ions or nuclei. Such a definition is convenient for distinguishing the astrophysical sources for various features of photon spectra, but I use the term in its broader sense. Analogously to the electromagnetic case, color-charged particles will lose energy by radiating gluons when traveling through chromo-electromagnetic fields. In a large system of deconfined partons, strong chromoelectric and chromomagnetic fields are present on a (relatively) large scale, and so this is a relevant process. Because of the obvious and immediate analogy with electromagnetism, this process is called gluon bremsstrahlung. The energy loss of high energy partons as a probe of the medium was first proposed in [69].

1.7.1 Brief Survey of Energy Loss Models

Majumder [70] and Wiedemann [71] give excellent reviews of energy loss schemes. Additionally Bass and collaborators [72, 73], also give an excellent review of energy loss approaches, in the context of a systematic comparison using a single set of assumptions about the bulk properties of the medium to ensure a fair comparison of the physical observables. Finally, Horowitz and Cole [74] give a brief but very good review while going to in excellent depth and detail about the underlying assumptions and their associated uncertainties. In this section we give a very brief overview of the various energy loss schemes using the preceding references as a guide.

Baier et al. [75, 76] put forward the first calculation of parton energy loss that correctly took into account the rescattering of the parton and of the emitted gluon. Zakharov [77] put forward an alternative approach, which was later shown to be equivalent. This approach is now known as the BDMPS or BDMPS-Z approach. Wiedemann [78], along with Sal-

gado [79] and Armesto [80], extended the work of Baier et al. to account for arbitrary medium opacity. This arbitrary opacity version of BDMPS-Z is called ASW or sometimes BDMPS-Z/ASW.

The GLV approach [81, 82], named for the authors Gyulassy, Levai, and Vitev, was developed from the older Gyulassy-Wang model with the improvement of accounting for the rescattering of the emitted gluon. Like ASW, GLV accounts for arbitrary opacity. However, the formalism is quite different and the two approaches are not equivalent (although they are equivalent at first order in opacity).

The higher twist (HT) approach [83] is based on calculating higher twist corrections to the total cross sections in deep inelastic scattering (DIS). While generally higher twist terms are suppressed by the powers of $1/q^2$, they are enhanced by the medium length and thus can contribute significantly. The observables calculated in this approach, while derived in DIS, are readily generalized to the kinematics of the medium.

The method put forward by Arnold, Moore, and Yaffe [84–86], called AMY, is an approach using finite temperature field theory and is only one that is completely model independent. In fact, because of this model independence, the regime of validity is greatly limited and therefore phenomenological applications require significant extrapolations beyond the strict limits of validity.

Obviously, gluon radiation is not the only possible source of energy loss. As far back as 1982, Bjorken anticipated parton energy loss when traversing the medium, but his work was based on collisional energy loss [87]. Elastic energy loss was reintroduced to examine its effect on heavy quark energy loss, since radiative energy loss alone is not enough to explain the observed open heavy flavor suppression as measured by single electron nuclear

modification factors [88–90]. Note however that the effect of collisional energy loss on light quarks and gluons is small.

We can attempt to measure energy loss in several different ways: single particle measurements, such as π^0 spectra [91–93] and π^0 spectra with respect to the reaction plane [94, 95]; and two particle correlation measurements, such as dihadron [96–99] and dihadron with respect to the reaction plane [100], π^0 triggered correlations with hadrons [101], and photon-hadron correlations [102].

1.7.2 Flavor Dependence of Energy Loss

In QED photons only lose energy through elastic collisions, i.e. Compton scattering. Because a photon is chargeless, each vertex can have only one photon, and therefore a photon cannot lose energy through the emission of a photon. This is not the case in QCD. Because gluons carry color charge, multiple gluons can share a vertex and therefore a gluon can directly emit a gluon, making it possible for gluons to lose energy through gluon bremsstrahlung. In fact, gluons not only have color charge but they have more color charge than quarks by the ratio of Casimirs $C_A/C_F = 9/4$. Therefore, not only do gluons lose energy through gluon emission, they lose more energy than quarks do. This is a fundamental feature of the theory (see for example [1, 2, 5–7, 103]).

Since gluons are expected to lose more energy than light quarks, particles created from gluon fragmentation should exhibit a stronger suppression pattern than those created from quark fragmentation. Therefore, if one could measure the nuclear modification factors of particles coming from gluons and quarks separately, one should be able to see this effect

in the data. Heuristically speaking, we may indeed have access to particles coming from quarks and gluons separately. Determination of fragmentation functions from fits to the data [104–108] show that at high p_T the production of light mesons (like pions) is dominated by quark fragmentation while the production of baryons (like protons) is dominated by gluon fragmentation. Therefore, the protons should exhibit a stronger suppression pattern than the pions, meaning the R_{AA} or R_{CP} of protons should be lower than that of pions.

Any number of other effects could wash out this effect. For example, the differences between the fragmentation functions could be smaller than is assumed. Another possible effect is jet flavor conversions [109, 110], where elastic scattering changes the flavor of the leading parton of the jet. Depending on the cross section for the particular scattering process, the color charge effect could be completely washed out by this mechanism. Regardless, this effect should not at all be considered any kind of constraint on the fundamentals of QCD. The ratio $C_A/C_F = 9/4$ is fundamental to $SU(3)$, which is already well established as the correct gauge group for strong interactions.

CHAPTER II

EXPERIMENTAL APPARATUS

2.1 The Relativistic Heavy Ion Collider

The Relativistic Heavy Ion Collider is an intersecting storage ring collider, and the first of such a type to collide nuclei. The principle advantage of such an accelerator is that for a given beam energy, the center of mass energy is much higher than that for a fixed target accelerator. In an ISR collider, two beams are collided head on. Conversely, in a fixed target accelerator, a single beam is directed onto a stationary target. The advantage of an ISR in terms of $\sqrt{s}$ is striking. At CERN/SPS, $E_{\rm beam}$ = 158 GeV/u, but $\sqrt{s_{NN}}$ = 17.6 GeV. On the other hand, at BNL/RHIC $E_{\rm beam}$ = 100 GeV/u, but $\sqrt{s_{NN}}$ = 200 GeV.

The RHIC complex can be seen in Figure 2.1. At RHIC [111], the ions are first created in a pulsed sputter ion source, with a charge state Q = -1. They are then electrostatically accelerated in the Tandem Van de Graaff accelerator, passing through stripping foils and leaving the Tandem with an energy of 1 MeV/u and charge state Q = +32. They next go into the Booster synchrotron, where they are accelerated to 95 MeV/u and then passed through another stripping foil taking them to the charge state Q = +77. The next and penultimate step in their journey is the Alternating Gradient Synchrotron, where they are accelerated to 8.86 GeV/u and then passed through one last stripping foil, bringing them to the Q = +79 state, i.e. the bare nucleus. Finally, they are transferred to RHIC where they are accelerated from 8.86 GeV/u to 100 GeV/u in under two minutes.

When RHIC began operations in 2000, there were four experiments. The two large ones, PHENIX (see [112]) and STAR (see [113]); and the two small ones, PHOBOS (see [114]) and BRAHMS (see [115]). At the conclusion the fifth period of RHIC operations in the summer of 2005 (known as Run5), PHOBOS and BRAHMS had completed their physics goals and were consequently decommissioned. Presently, PHENIX and STAR are still active and are intended to continue their physics programs well into the future. For a complete list of RHIC beam energies and species, see Table 2.1.

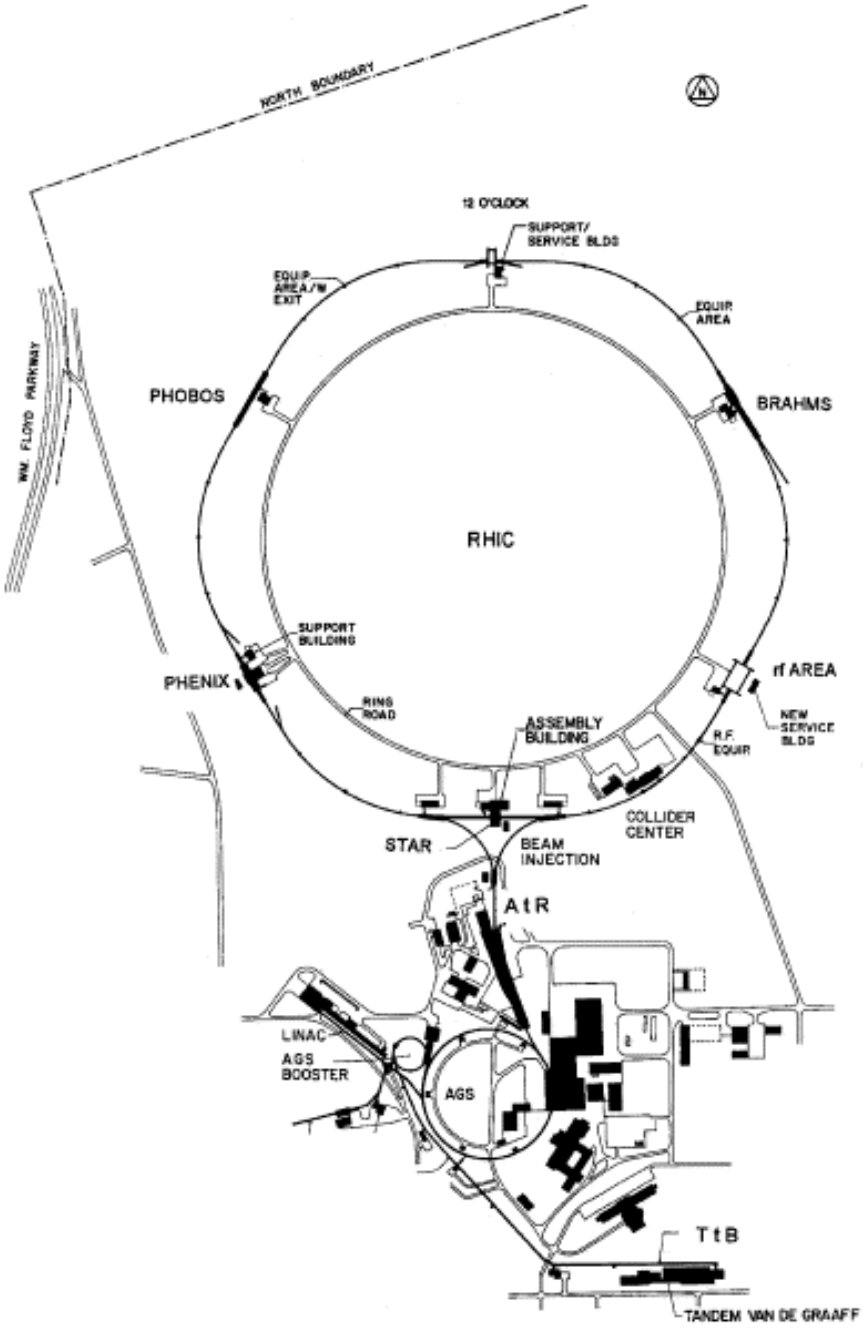

Figure 2.1: The RHIC Complex [111]

Table 2.1: RHIC Collision Species and Energies.

RHIC Run Number	Operational Period	Collision Species	$\sqrt{s_{NN}}$
01	2000	Au+Au	130 GeV
		Au+Au	56.0 GeV
02	2001-2002	Au+Au	200 GeV
		Au+Au	19.6 GeV
		p+p	200 GeV
03	2002-2003	d+Au	200 GeV
		p+p	200 GeV
04	2003-2004	Au+Au	200 GeV
		Au+Au	62.4 GeV
05	2004-2005	Cu+Cu	200 GeV
		Cu+Cu	62.4 GeV
		Cu+Cu	22.5 GeV
		p+p	200 GeV
06	2006	p+p	200 GeV
		p+p	62.4 GeV
07	2007	Au+Au	200 GeV
08	2007-2008	d+Au	200 GeV
		p+p	200 GeV
		Au+Au	9.2 GeV
09	2008-2009	p+p	500 GeV
		p+p	200 GeV
10	2010	Au+Au	200 GeV
		Au+Au	62.4 GeV
		Au+Au	39.0 GeV
		Au+Au	7.7 GeV
		Au+Au	5.0 GeV
		Au+Au	11.5 GeV
11	2011	p+p	500 GeV
		Au+Au	19.6 GeV
		Au+Au	200 GeV
		Au+Au	27.0 GeV
12	2012	p+p	510 GeV
		p+p	200 GeV
		U+U	192 GeV
		Cu+Au	200 GeV
		Au+Au	5.0 GeV

2.2 The Pioneering High Energy Nuclear Interaction Experiment

The PHENIX collaboration over 500 members from 68 institutions around the world. The PHENIX spectrometer [112] consists of global event characterization detectors [116]; two central arms [117–119], covering the central rapidity region; and two muon arms [120], covering forward and backward rapidity. Although PHENIX distinctly lacks both full azimuthal and full rapidity coverage, it has by far the most various and sophisticated detector subsystems of all the RHIC experiments. It also has one of the fastest data acquisition systems [121] in the world.

The PHENIX coordinate system (see Figure 2.2) defines the z-coordinate pointing exactly along the beam pipe, roughly northward. The xy-plane is the plane normal to the beam pipe with the y-coordinate pointing straight up and the x-coordinate pointing parallel to the ground in a roughly westward direction. The azimuthal angle ϕ is the angle with respect to the x-coordinate in the xy-plane and the zenith angle θ is the angle with respect to the z-coordinate. The origin of the coordinate system is defined as being exactly at the center of the central arms on the z-axis and exactly at the center of the beam pipe along the xy-plane.

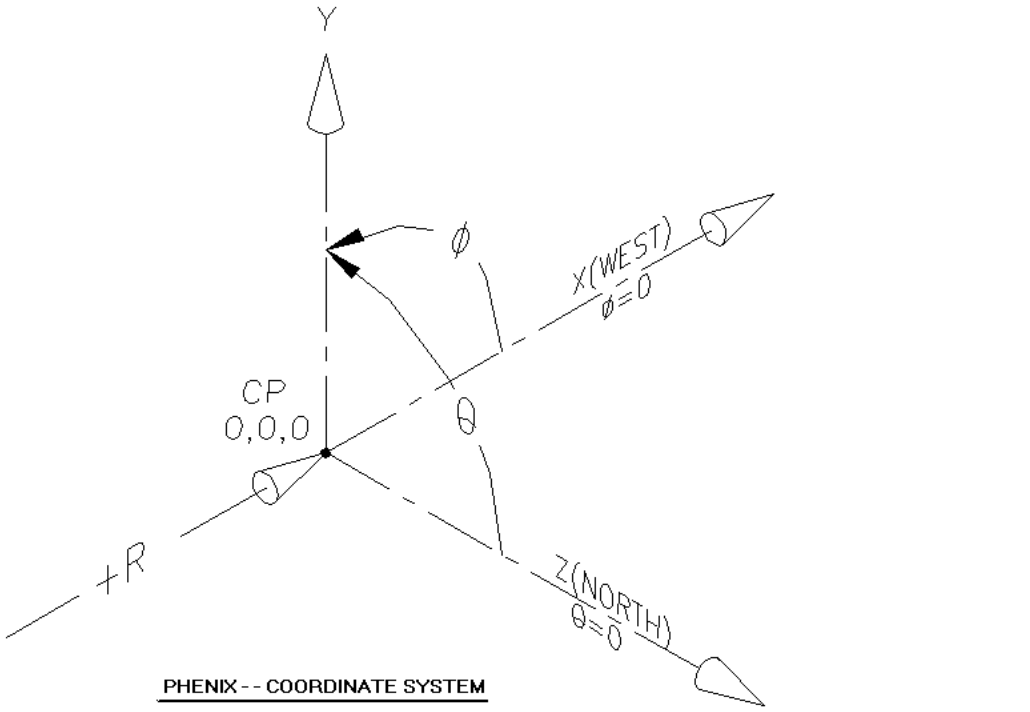

Figure 2.2: The PHENIX coordinate system.

2.3 Magnet System

The PHENIX magnet system [122] has three main components, muon magnets north and south, and the central magnet. The muon magnets each have a tapered piston at their center through which the beam pipe passes. Each magnet has two coils at the back of the piston. The north magnet has two coils with 51 turns each an an operational current of 2941 A. The south magnet has two coils, the outer having 57 turns and the inner having 114 turns, with an operation current of 2300 A. The central magnet rests at the very center of PHENIX with the beam pipe running right through it, and the central arms on each side of it. It is 7.900 m tall, 4.840 m long, and weighs roughly 421 metric tons. It is comprised of two sets of matched coils centered, both azimuthally and longitudinally, at the origin of the PHENIX coordinate system. The first pair of coils has an average radius of 0.657 m at a distance of 0.600 m from the origin, and the second pair has an average radius of 1.732 m at a distance of 1.000 m from the origin. The inner coils have 120 turns and an operational current of 2442 A, and the outer coils have 144 turns and an operational current of 1719 A.

The current in each central magnet coil pair can be run in either direction (forward and reverse) and the pairs can be run together ($++$ and $--$), opposed ($+-$ and $-+$), and with the interior coil off ($+0$ and -0). When run together, the maximum achieved field strength is 0.90 T at $R = 0$ and the field integral is 1.15 T-m. When run with the interior coil off, the maximum achieved field strength is 0.50 T at $R = 0$ and the field integral is 0.78 T-m. When run opposed, the maximum achieved field strength is 0.35 T at $R = 1.0$ m and the field integral is 0.43 T-m. All three configurations have the same field strengths at distances of 1 m and greater from the origin. Figure 2.3 shows the field lines in the magnet system for

the combined configuration in the left panel and reversed configuration in the right panel.

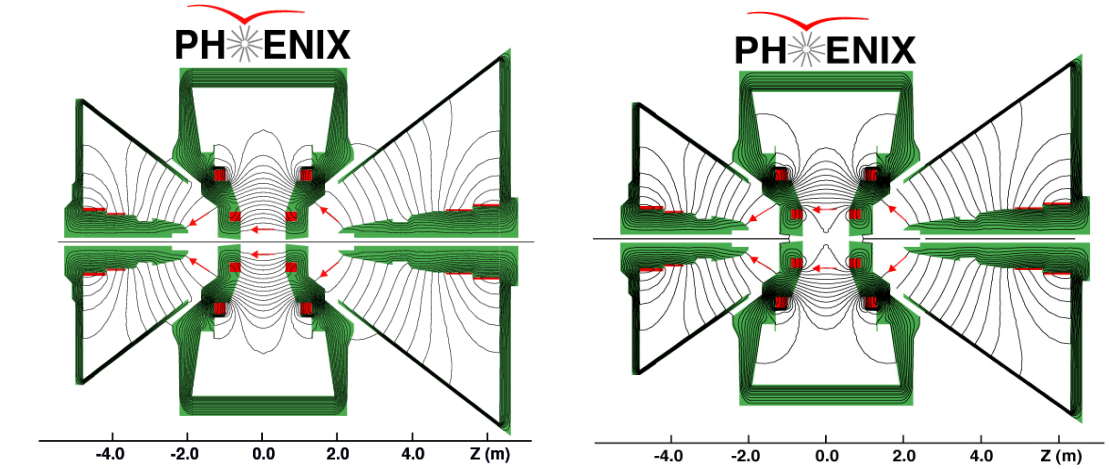

Magnetic field lines for the two Central Magnet coils in combined (++) mode Magnetic field lines for the two Central Magnet coils in reversed (±) mode

Figure 2.3: Magnetic field lines in the PHENIX Magnet system. Left panel shows combined ($++$) configuration, right panel shows reversed ($+-$) configuration.

2.4 Global Detectors

The main event characterization detectors are the Beam-Beam Counters and the Zero-Degree Calorimeters. These two detectors were once used in concert to measure the centrality and the event vertex, although more recently those two quantities have been measured using the BBC alone. The BBC are also used to determine the reaction plane and the initial time for the event (collision). This start time t_0 is used as the start time for time-of-flight measurements, with the time measured in the time-of-flight detector as the stop time. Since the publication of [116], one detector subsystem (the Multiplicity Vertex Detector or MVD) has been decommissioned and two other have been added: the aptly named Reaction Plane detector (RXNP), which is used to determine the reaction plane; and the Forward Calorimeters, which can be used to determine the centrality in d+Au collisions.

2.4.1 Beam-Beam Counters

The Beam-Beam Counters [116, 123] are small, simple, and highly effective. The BBC are two separate units, one at the North side of PHENIX, and one at the South side (forward and backward rapidity, respectively), the beam pipe passing through the center of each. They cover full azimuth and a pseudorapidity range of $3.0 < |\eta| < 3.9$ and are located 1.44 m from the interaction point, mounted on the far side of the central magnet frame. Each BBC is an array of 64 identical hexagonal detector elements. Each element is a simple Cherenkov[a] radiation counter. The radiator and photomultiplier tube are constructed

[a]Cherenkov is sometimes written as Čerenkov. Pavel Alekseevich Cherenkov was Russian, therefore his name is most properly written in the Cyrillic alphabet Павел Алексеевич Черенков. Since transliteration from one writing system to another is somewhat arbitrary, I prefer to use the standard transliteration of "Ch". Use of the monograph "Č" is a result of the influence of Western-Slavic languages that are written in the Latin alphabet. If you're still reading this, send me an email with subject "Cherenkov" and I'll buy you a beer.

as a single piece. A hexagonally shaped fused quartz crystal, 3 cm thick and inscribing a 1" circle, serves as both the radiator and the window for the PMT. The PMT has a 1" diameter tube and has a 15 stage fine-mesh dynode and is designed to be capable of operating in high magnetic fields, which is a necessary feature because the field strength can be as high as 0.3 T in the region around the BBC.

2.4 (a)

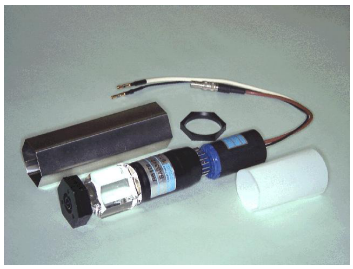

2.4 (b)

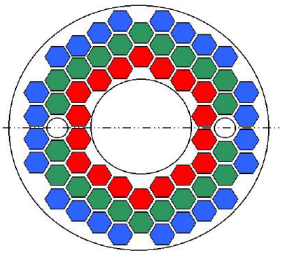

2.4 (c)

Figure 2.4: (a) Photograph of a BBC assembly. (b) Photograph of an individual BBC detector element. (c) Schematic drawing of a BBC, indicating the layout of the individual elements.

2.4.2 Zero-Degree Calorimeters

Like the BBC, the Zero-Degree Calorimeters [124] are small, simple, and highly effective. Like the BBC, the ZDC are two separate units, one to the North and one to the South. Unlike the BBC however, the ZDC are not in the experiment hall of PHENIX but rather are much further out, in the beam tunnel, a full 18 m from the interaction point, and cover a zenith angle of $\pm$ 0.23°, compared to the 2.4-5.7° covered by the BBC. They are behind the dipole magnets that steer the beams into the interaction region. The charged remnants (protons) from a collision will be swept into the beam pipe along with the beam itself, while the

neutral remnants (neutrons) will continue along a straight path, which is where the ZDC is placed. Since the purpose is to measure the neutron remnants, the ZDC is a hadronic calorimeter. It is a relatively simple design with 3 longitudinal segments and no transverse segmentation. Each segment has a 5 mm ($2\lambda_I$) thick tungsten absorber and poly(methyl methacrylate) optical fiber bundle sampler with a 12 stage general purpose PMT. The ZDC is a parallelepiped, with the cross section along the beam line being roughly square and the face and back swept at 45° so that the incidence angle with respect to the fibers is roughly equal to the Cherenkov angle.

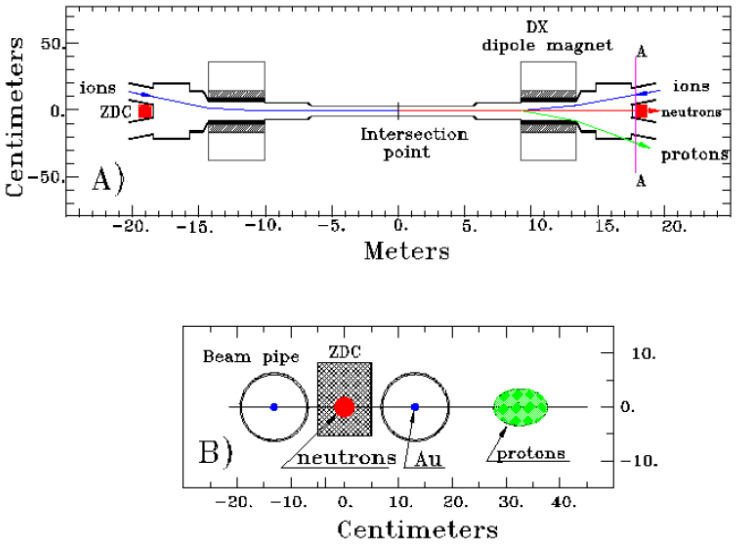

Figure 2.5: Top: view of the ZDC layout from above. Bottom: view of the ZDC layout from the back.

2.5 Central Arm Spectrometers

The central arms have both excellent particle tracking and particle identification. Each arm covers 90° in azimuth and -0.35 $< \eta <$ 0.35 in pseudorapidity. The Drift Chamber (DC) determines the momentum by measuring the particle deflection in the central magnetic field. Married to the DC is the first layer of Pad Chambers (PC1), which measures the position upon exit of the drift chamber. The other main tracking detector is the third layer of Pad Chambers (PC3). Unique to the west arm is the second layer of Pad Chambers (PC2). Particle identification is performed with various subsystems for various types of particles. The Electromagnetic Calorimeter (EMC or EMCal) is used principally for photons, and also electrons. The Ring Imaging Cherenkov detector (RICH) is use for identification of electrons. There are two time-of-flight detectors, one in each arm; the primary purpose for these subsystems is the identification of charged hadrons. The time of flight west (TOFW), which began operation in PHENIX during Run7, was a major contribution from the group at Vanderbilt University. The time of flight east (TOF or TOFE) has been in PHENIX since its inception. See Figure 2.6 for a schematic drawing of the Run12 (present day) configuration of PHENIX. In the succeeding sections, I will discuss the relevant detector subsystems in greater detail.

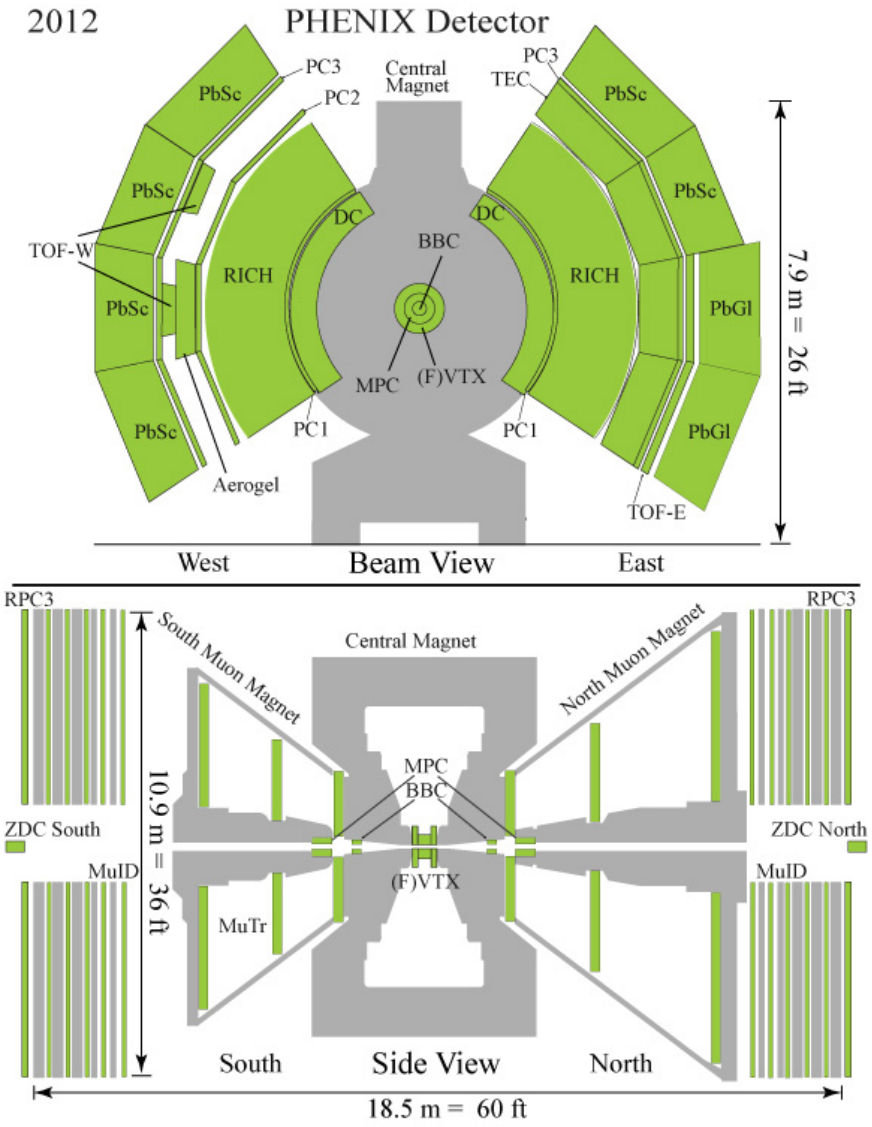

Figure 2.6: Schematic of the PHENIX spectrometer.

2.5.1 Drift Chambers

The drift chambers [117, 125] are a controlled drift geometry type drift chamber. In addition to the cathode and anode wires, there are potential wires, gate wires, and back wires. The potential wires decouple adjacent anode wires, the gate wires limit the drift length, and the back wires prevent charge from passing a certain region. The anode wires serve as the sense wires and are isolated at the middle so they can be read out on both sides. Each DC has a titanium frame that defines the fiducial volume azimuthally and longitudinally, and mylar windows define the fiducial volume radially. The frame has a single 2" diameter carboplastic support strut at the azimuthal center. The DC are cylindrically shaped, 2.5 m in length along the beam pipe, and have an inner radius of 2.02 m and an outer radius of 2.46 m. The active area covers 90° in azimuth for each arm (east and west) and 1.8 m along the beam pipe (-0.35 $< \eta <$ 0.35 in pseudorapidity). Each DC has 20 identical segments in azimuth, called keystones, each 4.5° and having a central support strut made of 100 micron-thick kapton at $z = 0$ to isolate the sense wires. There are six series of wire modules in the DC: X1, U1, V1, X2, U2, V2. The X wires are strung parallel to the beam pipe and are used to measure position in the xy-plane. The U/V wires are strung at small angles with respect to the beam pipe and measure the position on the z-axis. The angles are 5.376°, 5.512°, 5.900°, 6.040° for U1, V1, U2, V2, respectively, and are chosen to match the z-coordinate resolution of the pad chambers.

The X wire nets each contain 12 wires and the U/V wire nets contain 4 wires. The nets are mounted in aluminum cages, which are bolted to the frame. There are 8 nets per cage, and 1 cage for each wire series. Each keystone contains 3 cages, one for each wire series,

and has a total of 160 sense wires. There are 20 keystones for each arm, meaning 3200 sense wires per arm and 6400 sense wires total. There are readouts on either end of the sense wires for a total of 12,800 readouts. This number is reduced to 12,544 due to the fact that U/V wires can't be mounted at the azimuthal extremes as well as the presence of the central support struts.

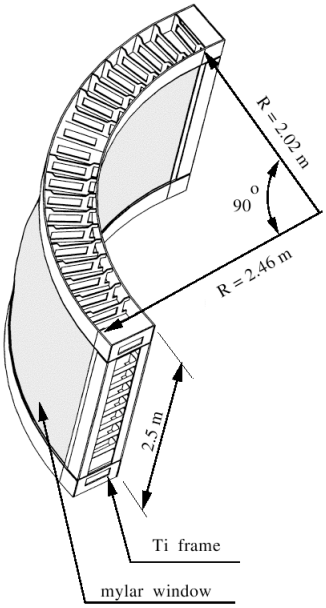

2.7 (a)

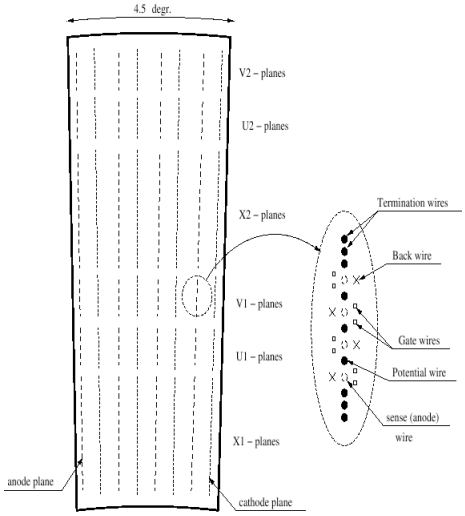

2.7 (b)

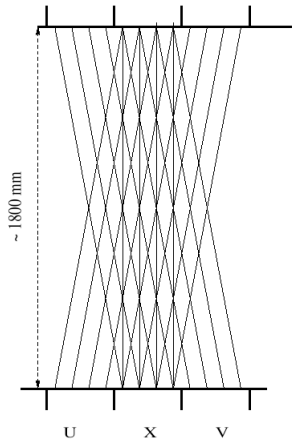

2.7 (c)

Figure 2.7: (a) Schematic of one arm of the drift chamber. (b) Wire position within one sector and inside the anode plane. (c) Top view of the stereo wire orientation.

2.5.2 Pad Chambers

The pad chambers [117, 126] are multi-wire proportional chambers. While early designs intended there to be 3 layers in each arm, the final design has 3 layers in west arm and 2 layers in the east arm. The first layer of pad chambers, PC1, are mated directly to the DC and are at a radius of 2.49 m; the second layer of pad chambers, PC2, is at a radius of 4.19 m; and the third layer of pad chambers, PC3, are at a radius of 4.89 m. Each layer has an active volume covering 90° in azimuth for each arm and lengths of 1.8 m for PC1, 3.2 m for PC2, and 3.6 m for PC3, covering -0.35 $< \eta <$ 0.35 in pseudorapidity. Each layer is segmented into 8 individual chambers. In PC1, there are 8 azimuthal segments, while in PC2 and PC3, there are 4 azimuthal segments and 2 z-direction segments. The PC1 has no structural frame while the PC2 and PC3 have a fiberglass structure surrounding the chambers. Each individual chamber consists of single plane of anode and field wires surrounded on either side by solid cathode planes, which define the gas volume. Each cathode plane is segmented into an array of pixels, and the basic readout element is a "pad" of 9 pixels.

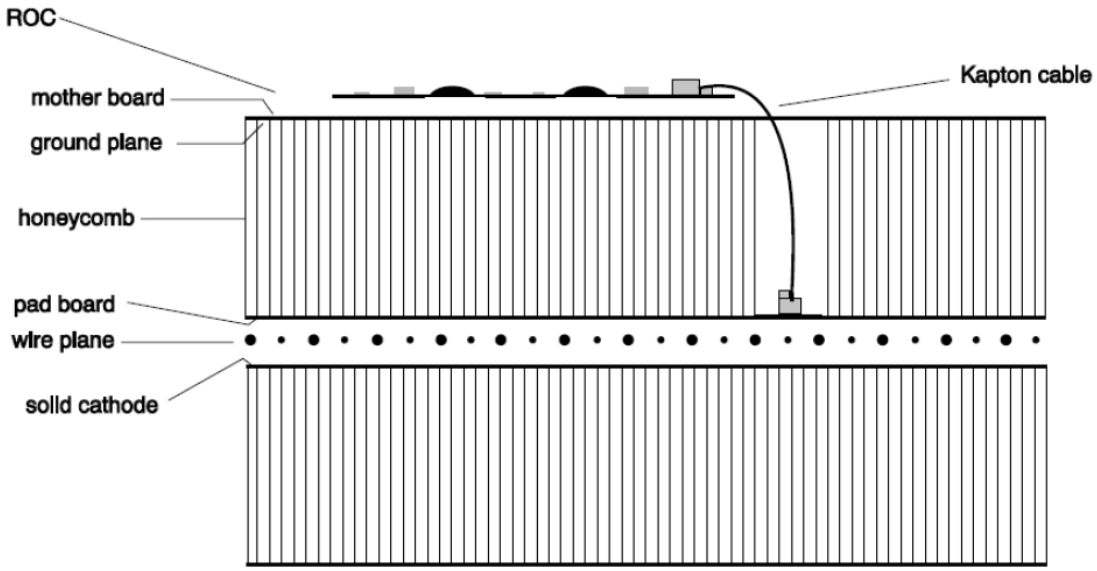

Figure 2.8: Schematic of a Pad Chamber.

2.5.3 Time-of-Flight West

The TOFW [127] is a time-of-flight detector based on multi-gap resistive plate chamber (MRPC) technology. It is composed of four boxes, two in sector W1 and two in sector W2. In each sector, one box is on the north side and one box is on the south side. Each box contains two rows (top and bottom) and two layers (front and back) of MRPCs, for a total of 4 separate HV busses, each powering 8 MRPCs for a total of 32 MRPCs per box (128 MRPCs in all). At the heart of each MRPC are 7 glass plates with 6 gaps with a thickness of 230 microns. On either side of the glass are two HV electrodes, one held at positive voltage, and one at negative voltage. Standard operation is $\pm$ 7 kV for a total operating voltage of 14 kV. During the commissioning run in 2007 (Run7), the gas mixture was 95% R134a (1,1,1,2-Tetrafluoroethane, CF_3CFH_2) and 5% isobutane(2-Methylpropane, $CH_3CHCH_3CH_3$). In the 2008 operational period (Run8) the gas mixture was changed to 95% R134a, 4.5% isobutane, and 0.5% sulfur hexafluoride (SF_6). Starting in the operational period in 2011 (Run11), The gas mixture was changed to 92% R134a, 5% isobutane, and 3% SF_6.

Each MRPC has 4 copper strips on either side, front and back. Each strip is 37 cm $\times$ 2.8 cm. Each strip on one side is wired to its partner on the opposite side, so the 8 strips function as 4 strips. Each strip pair has a readout on each end, top and bottom. This gives a total of 8 readouts per chamber, 1024 readouts in all. The ionization caused by a fast particle traversing the gas is imaged in the strip. The on-board Front End Electronics (FEE) process the signal pulse height and time and convert the pulse current into voltage. The FEEs also provide impedance matching and amplification for the signal. After processing in the FEE, the signal is transmitted via 25 ft. of cable to the Front End Modules (FEM).

The FEMs split the signal for simultaneous processing of time (TVC) and pulse height (QVC) measurements and perform the analog to digital conversions, giving time as a TDC value and pulse height as an ADC value.

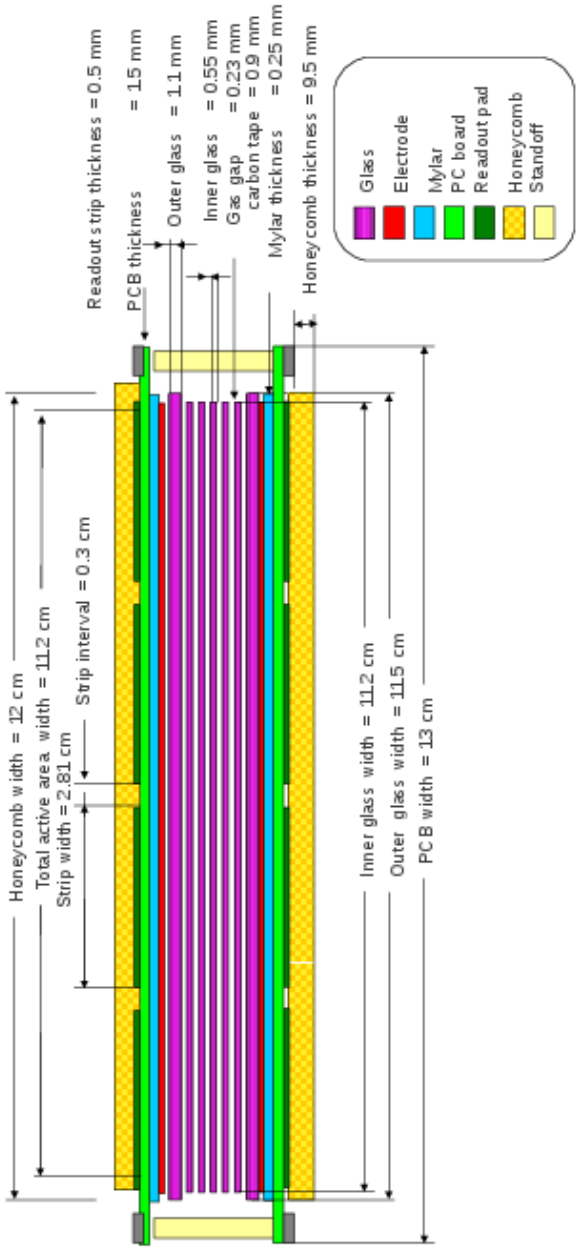

Figure 2.9: Schematic of an MRPC from the TOFW.

CHAPTER III

METHODS AND DETAILS OF THE ANALYSIS

3.1 Data Selection

3.1.1 Run Selection

A total of 933 runs were produced for the Run7 data set, Au+Au collisions at $\sqrt{s_{NN}} =$ 200 GeV. Of these, a range of 865-871 are available on the Analysis Train, which is the internal PHENIX collaboration framework for accessing the full data sets. Exactly how many runs are available at any given time is dependent on specific conditions when the train is running. For this analysis, we base our run list off of the list of 869 runs that were available for Analysis Train 160. There are several ways to go about determining a good run list. In this analysis, we consider two different ways and compare the results. One approach is to use the data from the train and analyze certain basic quantities. We looked at the ratio of charged tracks as well as the mean per-event multiplicity as a function of runnumber. The charge ratio analysis yields 27 problematic runs and the multiplicity analysis yields 28 problematic runs. There are 18 runs of overlap in these two analyses for a total of 38 bad runs. The results of this approach can be seen in Figure 3.1. The second approach is to examine the online monitoring plots and determine which runs exhibit unfavorable detector performance. Using this method, 32 runs were found to be problematic for the TOFW. For the drift chamber, 324 runs were found to have issues. Because this number is much larger than can be regarded as reasonable, the criteria must be stricter than merely having found

a problem. In one case, 113 runs were found to have dead X2 high voltage in keystone number 10 on the North and South sides, but to have no other problems; these runs were kept. In another case, 96 runs were found to indicate too many dead channels and/or too low of a hit rate, but indicated no other problems; these runs were kept. Of the 324 runs, 115 remain to be excluded. Of course, not all of the runs in the online monitoring are in the actual Taxi160 run list. Of the 32 runs found to be bad for the TOFW, 17 are found in the run list, and of the 115 runs found to be bad for the DC, 94 are found in the run list. Of these, a mere 2 runs overlap, for a total of 109 runs to be excluded. Quite surprisingly, we find that in spite of all our efforts towards making a good runs list, the spectra are virtually identical regardless of which run-by-run QA is applied or even whether any is applied at all. We performed a very similar analysis for the Run8 d+Au data with essentially identical results. In the final analysis, the only runs that are excluded are the small set of runs in Run7 where the magnetic field was briefly operated with the coils together instead of opposed.

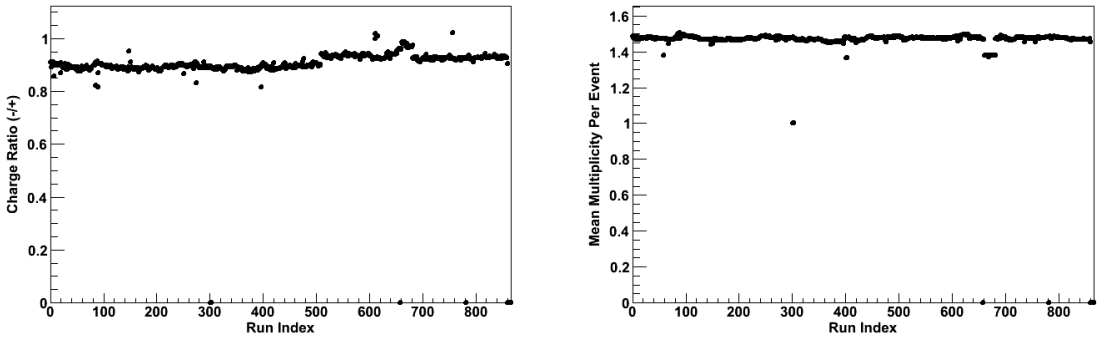

Figure 3.1: Run-by-run Quality Assurance. Left panel: charged track ratio as a function of run index. Right panel: mean multiplicity per-event as a function of run index.

3.1.2 Event Selection

For both the Run7 Au+Au and Run8 d+Au we select events that pass the minimum bias (MB) trigger, which is defined as a coincidence in both the North and South BBCs, meaning at least one PMT fired (produced one or more photoelectrons) in each BBC. In Au+Au collisions, this trigger measures 92% of the total inelastic cross section; in d+Au collisions, it measures 88% of the total inelastic cross section. We have an additional requirement that the collision vertex is within $|z_{vertex}| < 30$ cm of the nominal origin of the coordinate system. Collisions beyond this range are too far off-center for reliable analysis and are therefore excluded from the analysis. This is generally the standard event vertex cut in PHENIX, except in a few special cases where a tighter vertex cut is needed.

In both Run7 Au+Au and Run8 d+Au the centrality is determined by the BBC percentile method. In Au+Au, the centrality is measured by taking the sum of the charge in the north BBC and in the south BBC and dividing the charge distribution into equally probable percentiles. In d+Au, the charge distribution in only the south BBC, the Au-going side, is used and again divided into equally probable percentiles. Glauber Monte Carlo simulations are done to determine the number of binary nucleon-nucleon collisions N_{coll} and the number of participating nucleons N_{part}. The Run7 Au+Au Glauber results are presented in AN768 [128] and the Run8 d+Au Glauber results are presented in AN900 [129]. A table of the Glauber values relevant for this analysis is given in Table 1.1.

3.1.3 Track Selection

The detector subsystems we use are the drift chamber (DC), the first layer of the pad chambers (PC1), and the third layer of the pad chambers (PC3) for momentum reconstruction and tracking; and the time of flight detector in the west arm (TOFW) for particle identification.

Charged track reconstruction in the DC is based on a combinatorial Hough transform, which gives the angle α in the main bend plane ($r - \phi$) and thus p_T; that is, $\alpha \propto 1/p_T$. The PC1 is used to determine the hit position in the longitudinal (z) direction and thus p_z/p_T. We require the longitudinal position to be 3 cm $< |z| <$ 70 cm, where the lower bound cuts out the vertical support strut and the upper bound cuts out the edges on either side. Only tracks with valid information in both the DC and PC1 are used in this analysis. Specifically, we use tracks with DC/PC1 quality either 31 or 63. Table 3.1 shows the bit information of a track and what the different bits mean.

Table 3.1: DC track quality bit information

Bit position	Numerical value	Meaning
0	1	X1 used
1	2	X2 used
2	4	UV found
3	8	UV unique
4	16	PC1 found
5	32	PC1 unique

Since the z-coordinate information is based on the PC1 and then matched to the DC, the lowest possible sequence is 100010. The sequence is used to determine the numerical

value of the track quality: $100010 \rightarrow 1\times1+0\times2+0\times4+0\times8+1\times16+0\times32=17$. The best case scenario is the highest possible sequence: $111111 \rightarrow 1\times1+1\times2+1\times4+1\times8+1\times16+1\times32=63$. The second best case scenario is not in fact the second highest numbered sequence, but rather a found/ambiguous PC1 hit with a best choice of UV hit and both X wires firing: $111110 \rightarrow 1\times1+1\times2+1\times4+1\times8+1\times16+0\times32=31$.

A summary of the different possible DC track qualities can be seen in table 3.2 (sorted by z-coordinate information) and table 3.3 (sorted by momentum information).

Table 3.2: DC track quality summary, by z-coordinate information

Quality	PC1 found	PC1 unique	UV found	UV unique
17,18,19	1	0	0	0
21,22,23	1	0	1	0
29,30,31	1	0	1	1
49,50,51	1	1	1	0
61,62,63	1	1	1	1

Table 3.3: DC track quality summary, by momentum information

Quality	X1 used	X2 used
17,21,29,49,61	1	0
18,22,30,50,62	0	1
19,23,31,51,63	1	1

Tracks in DC/PC1 are projected to the outer detectors, such as PC3 and TOFW, and matched with hits in those detectors with the minimum distance between the projection and the hit position. The distribution of differences between hits and projections which is called

the track matching residual distiribution (residual for short) is approximately Gaussian, with an additional underlying background caused by random associations. Only tracks with a difference of less than two standard deviations in both the azimuthal and longitudinal directions in both the PC3 and the TOFW are selected, so as to minimize background contamination. For analysis, these track matching residual distributions are normalized in such a way that the standard deviation of the distribution is one and the mean is zero. These normalized residual distributions are often called the "sigmalized residuals" in the PHENIX jargon. The analysis variable for a particular residual has the name of the detector and the coordinate variable. For example, the residual distribution in the z direction in the TOFW is called $tofwdz$ and the sigmalized residual is $tofwsdz$. In the same way, the TOFW ϕ residual is $tofwdphi$ and the sigmalized residual is $tofwsdphi$. The PC3 variables are $pc3dz$, $pc3dphi$, $pc3sdz$, and $pc3sdphi$. In this analysis we require the track matching residuals to be less than two standard deviations from the mean in both the ϕ and z directions in both the PC3 and the TOFW, so as to minimize background contamination.

In the Run7 Au+Au data, for $p_T > 5.0$ GeV/c we require an additional cut to further reduce background. This cut is $ecore/p_T > 0.2$, where ecore is the core energy in the electromagnet calorimiter (EMCal). This cut removes low momentum particles that are falsely reconstructed as high p_T tracks. For the Run8 d+Au data, we only measure up to $p_T = 5.0$ GeV/c and therefore this cut is not applied.

Finally, we have additional cuts for the TOFW. We require the ADC value to be 60 $< qtofw <$ 600, and we also remove poorly performing strips. Most of these (32) are from a dead HV buss, and a few others (9) have weak signals.

The analysis cuts and their values are presented in table 3.4.

Table 3.4: Analysis Cuts

Cut	Value
Trigger	Minimum Bias
Event Vertex	$\lvert z_{\rm vertex}\rvert < 30$ cm
Track Quality	DC quality number 63 or 31
DC Zed	3 cm $< \lvert z_{\rm DC}\rvert < 70$ cm
Fiducial Cuts	
DC	2D cuts in $\alpha_{\rm DC}$–$\phi_{\rm DC}$ space
PC1	2D cuts in $z_{\rm PC1}$–$\phi_{\rm PC1}$ space
PC3	2D cuts in $z_{\rm PC3}$–$\phi_{\rm PC3}$ space
Track Matching	
PC3	2σ cuts on both z and ϕ residuals
TOFW	2σ cuts on both z and ϕ residuals
EMCal cut	$ecore/p_T > 0.2$ (for $p_T > 5.0$ GeV/c)
TOFW specific	
Strip ID	1 dead HV buss (32 strips) and 9 additional poorly performing strips
ADC	$60 < q_{\rm tofw} < 600$
PID	2σ on m^2 with 2σ veto on other particle types

3.1.4 Particle Identification

The TOFW uses multi-gap resistive plate chamber technology to achieve an intrinsic timing resolution of $\sigma_t \approx 75$ ps, enabling excellent particle identification (PID) capabilities. Using the TOFW, charged pions and kaons can be identified separately up to a transverse momentum of $p_T \approx 2.8$ GeV/c, and charged kaons and protons separated up to $p_T \approx 4$ GeV/c using the traditional method of a m^2 window cut of two standard deviations from the mean as a function of p_T. Using more advanced PID methods, higher p_T can be reached. In this analysis, we use asymmetric cuts, where in addition to requiring a 2σ m^2 cut, we further require the exclusion of the 2σ m^2 region of the other particles. Figure 3.2 illustrates the effect of this cut clearly. The left panel shows a 2-d scatter plot of the m^2 vs charge $\times p_T$ distribution with the PID functions superimposed, and the right plot shows the same with all the PID cuts applied. In principle, this PID method allows charged pions and protons to be identified up to infinite momentum. In practice, this allows pion and proton identification up to 5-6 GeV/c, beyond which things like background contamination and the uncertainty in the m^2 distributions are too large for reliable PID and yield extraction. The PID of kaons is limited by the merge of the pion and proton m^2 distributions, which happens between 3.5 and 4 GeV/c.

The procedure to determine the PID functions for each particle is the same for Run7 and Run8 (and in principle any Run). However, there can be differences in the functions across Runs due to differences in BBC timing performance. For example, the lower multiplicity in d+Au collisions results in poorer timing resolution, thereby making the timing resolution and, consequentially the m^2 resolution, worse in the TOFW.

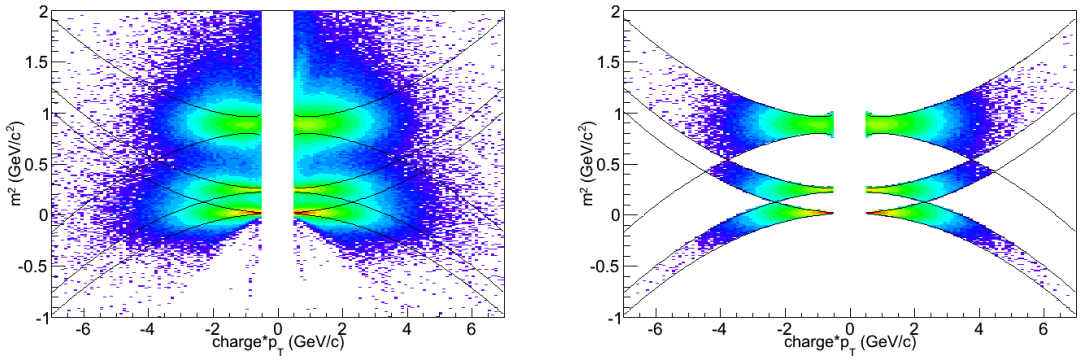

Figure 3.2: Two dimensional scatter plot of the m^2 distribution as a function of charge $\times p_T$, with the PID functions superimposed. Left panel: full distribution. Right panel: distribution with PID cuts applied. Run7 Au+Au data shown, Run8 d+Au data very similar.

To determine the PID functions for each particle, a 2-d histogram is filled with the m^2 as measured in the tofw as a function of p_T. Then, each peak is fit independently with a Gaussian distribution. In the case of the pion and kaon, the peaks begin to merge at $p_T \approx$ 2.5 GeV/c, so a double Gaussian is employed to reduce the uncertainty of the individual fits. Figures 3.3 and 3.4 show examples of the 1-d fits in Run7, and Figures 3.5 and 3.6 show the same examples in Run8. Next, the mean and standard deviation of each particle as a function of p_T are fitted with a function of the form

$$f(x) = p_0 + p_1/x + p_2/x^2 + p_3 e^{\sqrt{x}} + p_4\sqrt{x} \tag{3.1}$$

and the parameters from the fit are used to define the final PID function for each particle. Figures 3.7–3.12 show the functional fits in Run7, and Figures 3.7–3.12 show them in Run8.

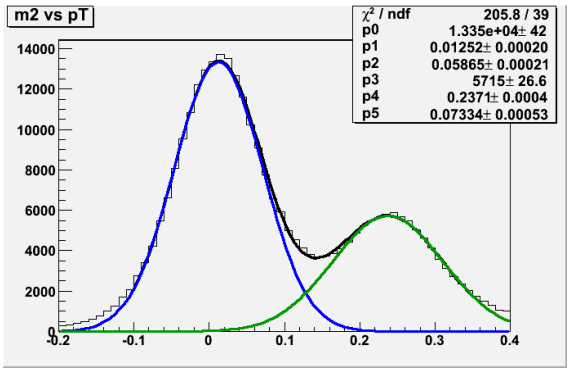

Figure 3.3: 1-d m^2 distribution of pions and kaons for 2.5 GeV/c $< p_T <$ 2.6 GeV/c, Run7 data set.

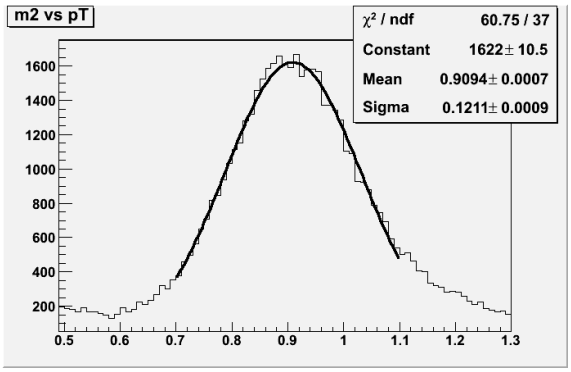

Figure 3.4: 1-d m^2 distribution of protons for 3.0 GeV/c $< p_T <$ 3.1 GeV/c, Run7 data set.

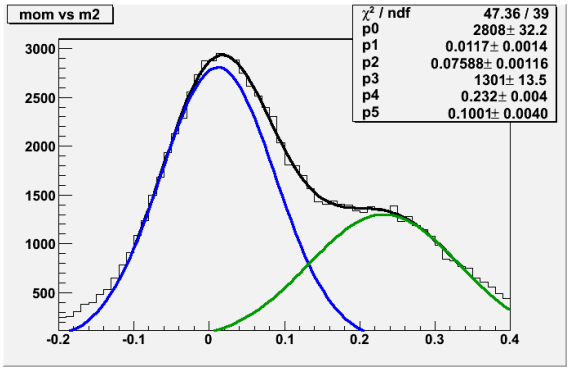

Figure 3.5: 1-d m^2 distribution of pions and kaons for 2.5 GeV/c $< p_T <$ 2.6 GeV/c, Run8 data set.

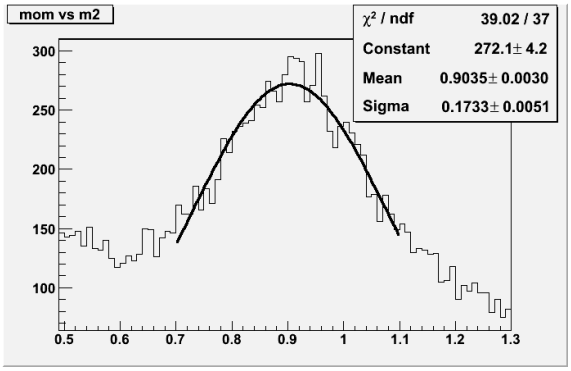

Figure 3.6: 1-d m^2 distribution of protons for 3.0 GeV/c $< p_T <$ 3.1 GeV/c, Run8 data set.

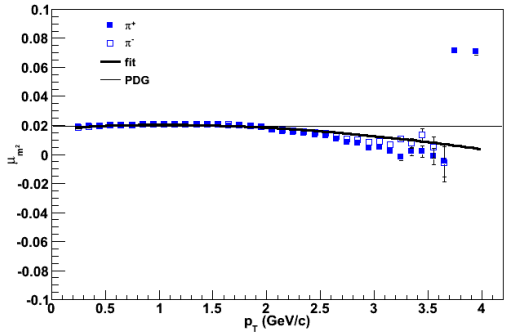

Figure 3.7: The mean of the m^2 distribution for $\pi^{\pm}$ as a function of p_T, Run7.

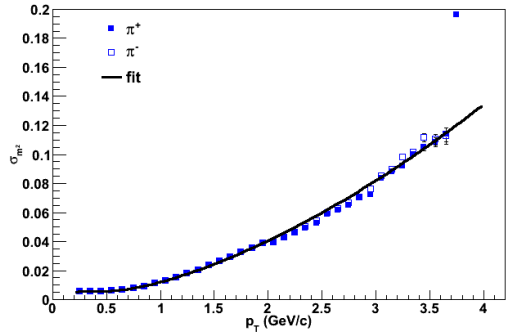

Figure 3.8: The standard deviation of the m^2 distribution for $\pi^{\pm}$ as a function of p_T, Run7.

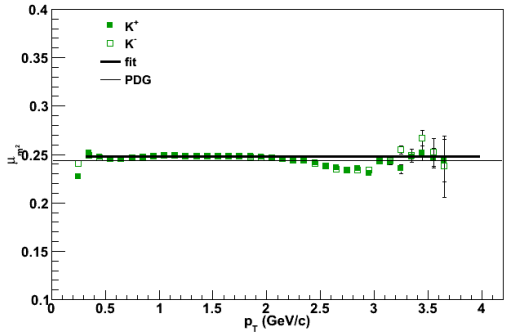

Figure 3.9: The mean of the m^2 distribution for $K^{\pm}$ as a function of p_T, Run7.

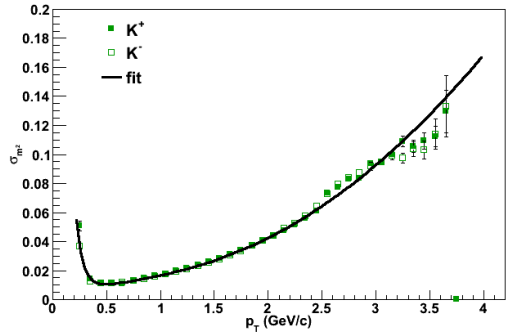

Figure 3.10: The standard deviation of the m^2 distribution for $K^{\pm}$ as a function of p_T, Run7.

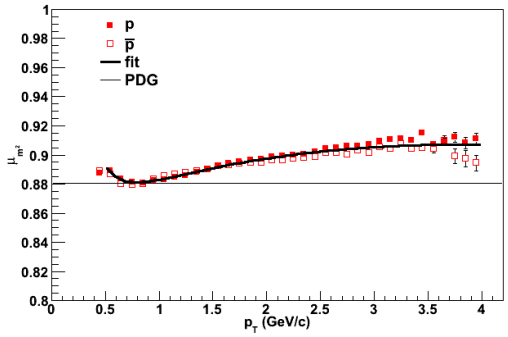

Figure 3.11: The mean of the m^2 distribution for p and $\bar{p}$ as a function of p_T, Run7.

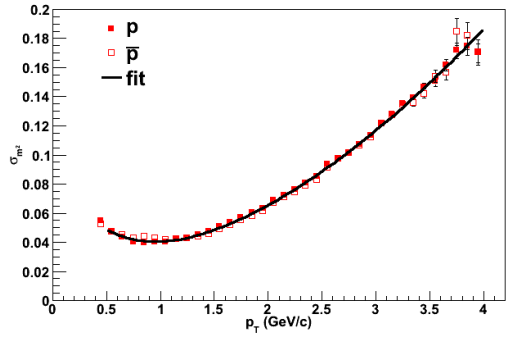

Figure 3.12: The standard deviation of the m^2 distribution for p and $\bar{p}$ as a function of p_T, Run7.

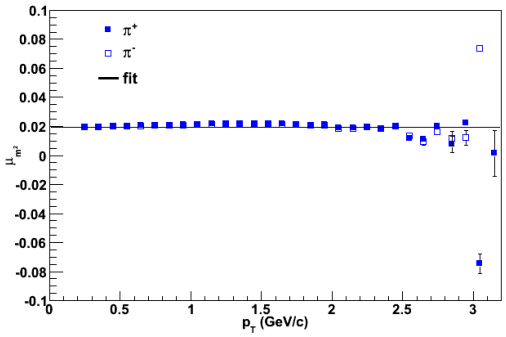

Figure 3.13: The mean of the m^2 distribution for $\pi^{\pm}$ as a function of p_T, Run8.

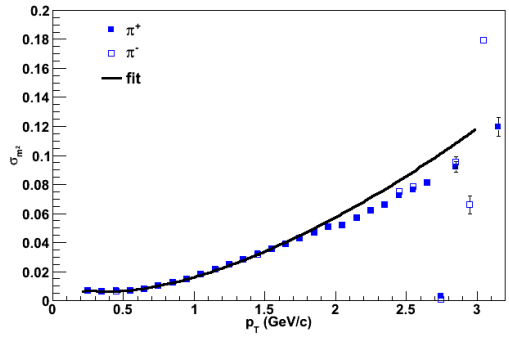

Figure 3.14: The standard deviation of the m^2 distribution for $\pi^{\pm}$ as a function of p_T, Run8.

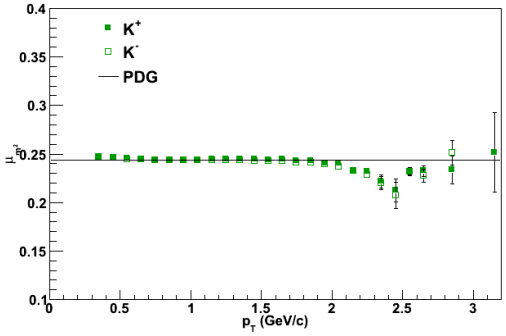

Figure 3.15: The mean of the m^2 distribution for $K^{\pm}$ as a function of p_T, Run8.

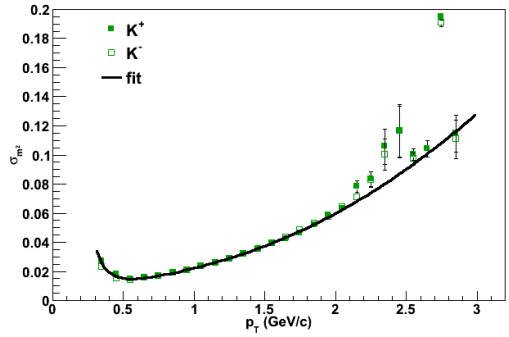

Figure 3.16: The standard deviation of the m^2 distribution for $K^{\pm}$ as a function of p_T, Run8.

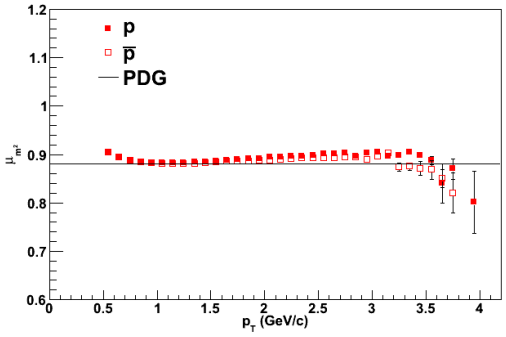

Figure 3.17: The mean of the m^2 distribution for p and $\bar{p}$ as a function of p_T, Run8.

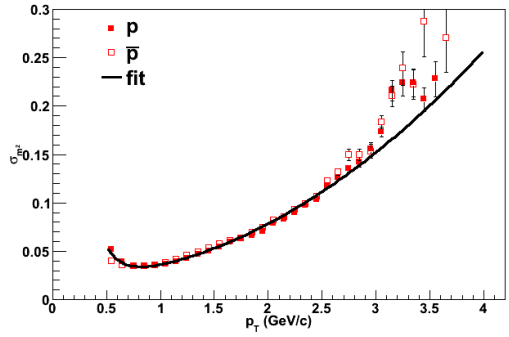

Figure 3.18: The standard deviation of the m^2 distribution for p and $\bar{p}$ as a function of p_T, Run8.

Now we compare the functional fit the analytic parametrization used in previous analyses (AN187 [130] for PPG015 [50] and PPG026 [38], AN231 [131] for PPG030 [132], and AN776 [133] for PPG101 [134]). The standard deviation of the m^2 distribution can be parametrized by the angular resolution σ_α of the DC, the multiple scattering term σ_{ms}, and the timing resolution σ_t:

$$\sigma^2_{m^2} = \frac{\sigma^2_\alpha}{K_1^2}\left(4m^4p^2\right) + \frac{\sigma^2_{ms}}{K_1^2}\left(4m^4\left(1+\frac{m^2}{p^2}\right)\right) + \frac{\sigma_t^2c^2}{L^2}\left(4p^2\left(m^2+p^2\right)\right), \tag{3.2}$$

where K_1 is the field integral (104 mrad GeV for the $++$ and $--$ field configurations as in Run8, 75 mrad GeV for the $+-$ and $-+$ field configurations as in Run7) and L is the distance from the collision vertex to the TOFW (495 cm).

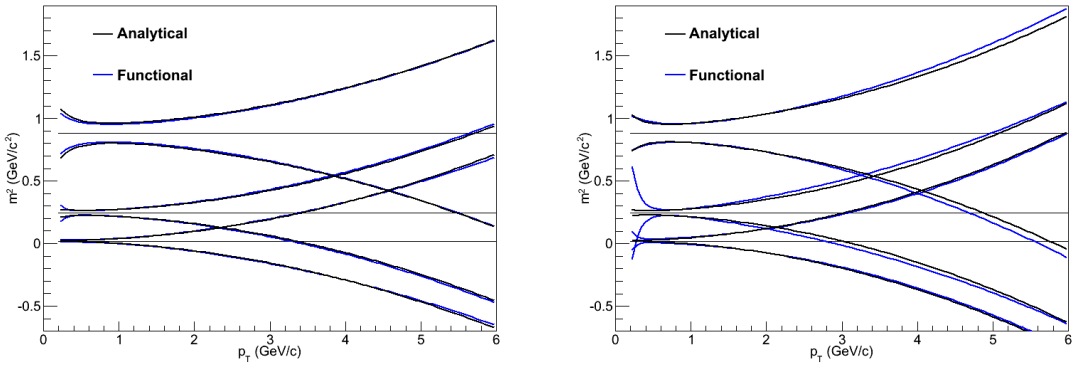

Figure 3.19: The 2σ PID functions based on the functional and analytical forms for all particles as a function of p_T. Left panel Run7, right panel Run8.

As can be seen, with the two types of PID functions show nearly identical behavior. The parameters in equation 3.2 were determined from a simultaneous fit performed for the TOFW NIM paper. In this analysis we adjust the timing resolution to be slightly wider

to match it to the known performance from the timing recalibration, and compare to the parameters from the fit to estimate the systematic uncertainty. The "Alternate" set of parameters is an additional set for the evaluation of systematic uncertainties.

Table 3.5: PID function parameters

	Run7		
Parameter	From Fit	Expected	Alternate
σ_α	0.896 mrad	0.9 mrad	1.0 mrad
σ_{ms}	0.992 mrad GeV	1.0 mrad GeV	1.0 mrad GeV
σ_t	74 ps	84 ps	80 ps
	Run8		
Parameter	From Fit	Expected	Alternate
σ_α	1.5 mrad	1.0 mrad	1.0 mrad
σ_{ms}	1.0 mrad GeV	1.0 mrad GeV	1.0 mrad GeV
σ_t	100 ps	90 ps	95 ps

3.2 Corrections to the Raw Data

3.2.1 Correction Factors From Single Particle Monte Carlo Simulations

Most of the corrections that need to be made to raw measurements, such as those of geometrical acceptance and track reconstruction efficiency, can be evaluated using single particle Monte Carlo (SPMC) simulations. These simulations are also be used to correct for the various tracking cuts used. The basic steps of the simulation chain are:

1. Single particle Monte Carlo event generation (Exodus)
2. Evaluation of material interactions and secondary particle generation (PISA)
3. Track reconstruction from PISA hits in detector volumes (pisaToDST)
4. Analysis of simulated tracks
5. Calculation of correction factors

The correction factors are determined by comparing the Exodus input to the final output of the analyzed simulated tracks. The efficiency can be determined by the following relation:

$$\frac{dN_{output}/dp_T}{dN_{input}/dp_T} = \epsilon_{\text{acceptance}}\epsilon_{\text{efficiency}}\epsilon_{\text{cuts}}; \tag{3.3}$$

the correction factor is merely the inverse of this quantity:

$$F_C(p_T) = \frac{dN_{output}/dp_T}{dN_{input}/dp_T}. \tag{3.4}$$

The corrected spectrum then is simply

$$\frac{dN_{corrected}}{dp_T} = \frac{dN_{raw}}{dp_T}F_C(p_T). \tag{3.5}$$

The parameters we use to run Exodus are summarized in Table 3.6.

Table 3.6: Exodus input parameters

Parameter	Value
Event type	single particle
p_T distribution	flat
p_T range	0.0 GeV/c $< p_T <$ 10.0 GeV/c
rapidity range	-0.6 $< y <$ 0.6
z-vertex range	-30 cm $< z <$ 30 cm
azimuth range	$-\pi/2 < \phi < \pi/2$

3.2.1.1 Plots of the SPMC correction factors for Run7

Here we plot both charges of pions in each magnetic field together, and additionally represent the correction factors both with the asymmetric m^2 cut used in the analysis as well as a symmetric only m^2 cut to represent the overall efficiency.

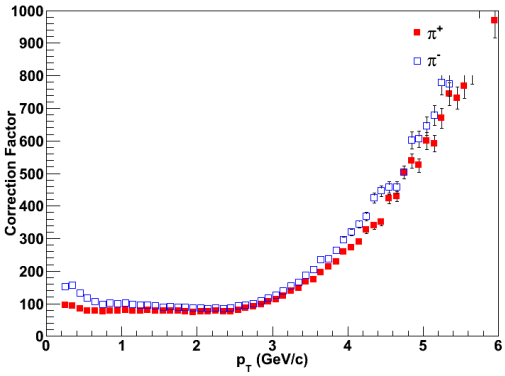

Figure 3.20: The correction factors of π in the $+-$ field as a function of p_T.

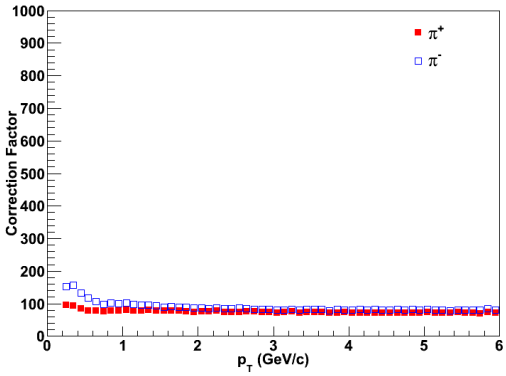

Figure 3.21: The correction factors with symmetric m^2 cut only of π in the $+-$ field as a function of p_T.

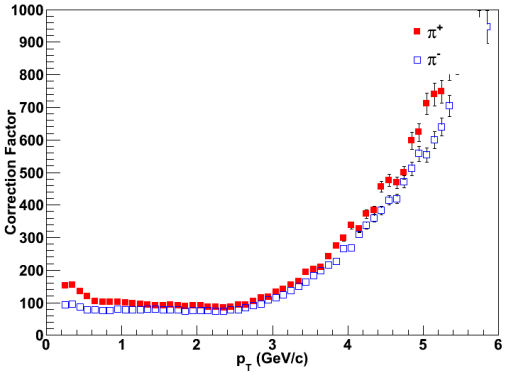

Figure 3.22: The correction factors of π in the $-+$ field as a function of p_T.

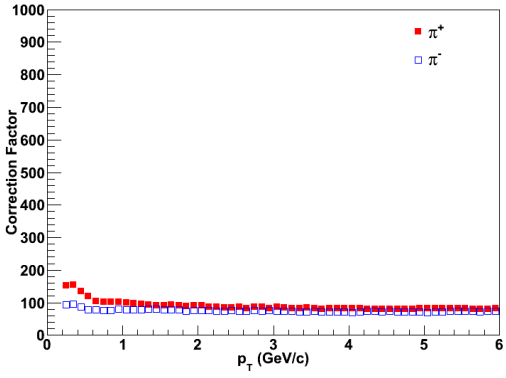

Figure 3.23: The correction factors with symmetric m^2 cut only of π in the $-+$ field as a function of p_T.

Here we plot both charges of pions for each DC alpha value field together, which highlights the uniformity of the acceptance when mixing fields in order to sample the same fiducial region of the DC. As before, we include the correction factors both with the asymmetric m^2 cut used in the analysis as well as a symmetric only m^2 cut to represent the overall efficiency.

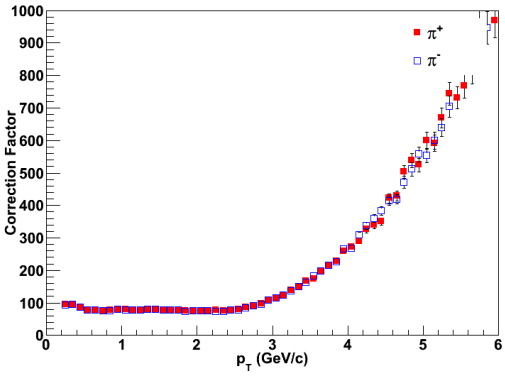

Figure 3.24: The correction factors of π with $\alpha < 0$ as a function of p_T.

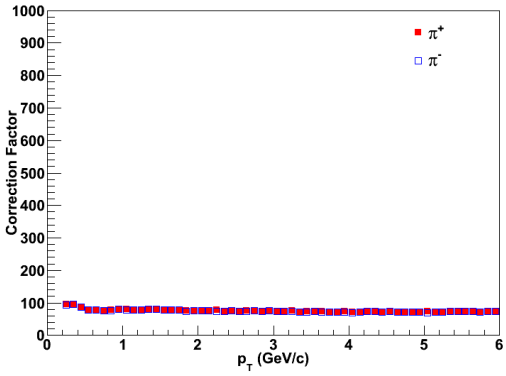

Figure 3.25: The correction factors with symmetric m^2 cut only of π with $\alpha < 0$ as a function of p_T.

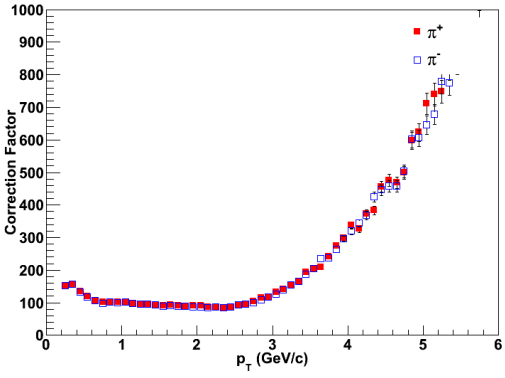

Figure 3.26: The correction factors of π with $\alpha > 0$ as a function of p_T.

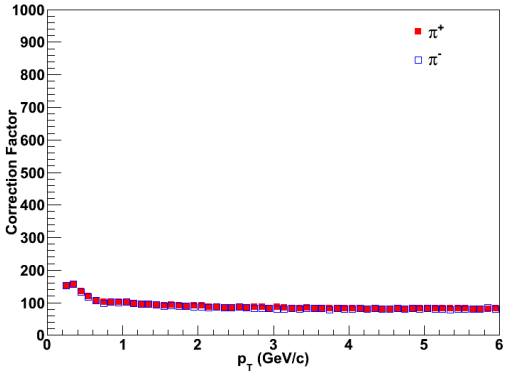

Figure 3.27: The correction factors with symmetric m^2 cut only of π with $\alpha > 0$ as a function of p_T.

In the proceeding 4 pages, we reiterate the above process for kaons on the next two pages protons for the two pages following that.

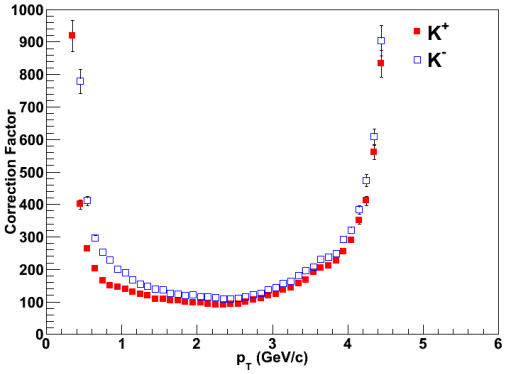

Figure 3.28: The correction factors of K in the $+-$ field as a function of p_T.

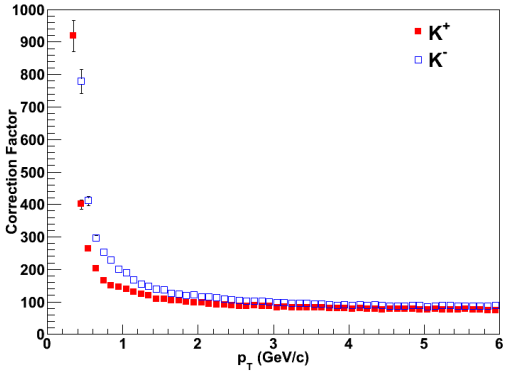

Figure 3.29: The correction factors with symmetric m^2 cut only of K in the $+-$ field as a function of p_T.

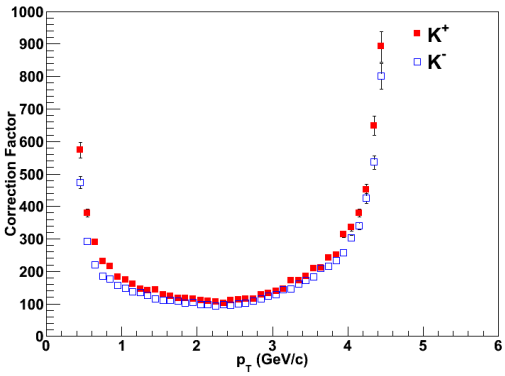

Figure 3.30: The correction factors of K in the $-+$ field as a function of p_T.

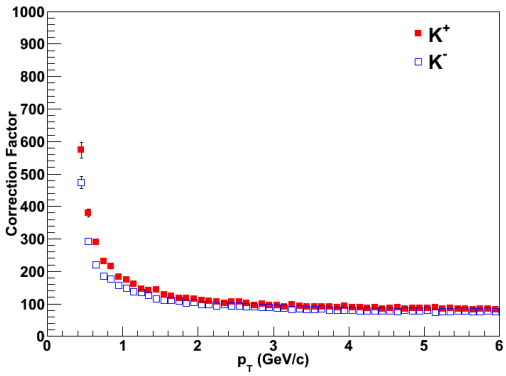

Figure 3.31: The correction factors with symmetric m^2 cut only of K in the $-+$ field as a function of p_T.

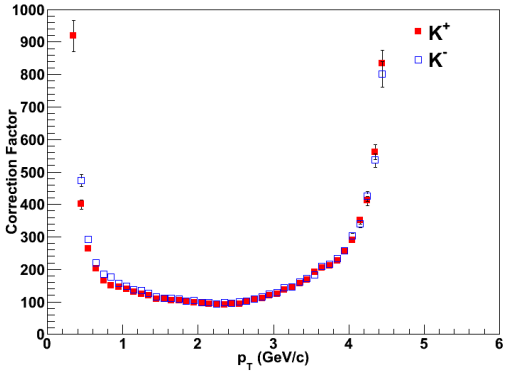

Figure 3.32: The correction factors of K with $\alpha < 0$ as a function of p_T.

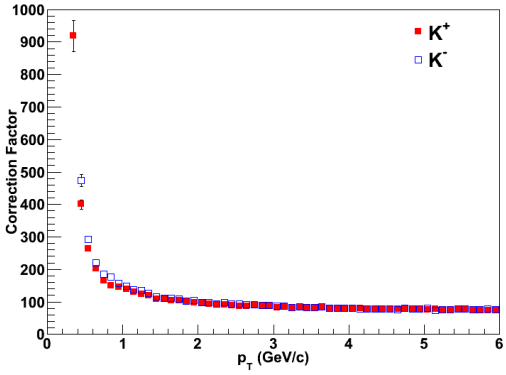

Figure 3.33: The correction factors with symmetric m^2 cut only of K with $\alpha < 0$ as a function of p_T.

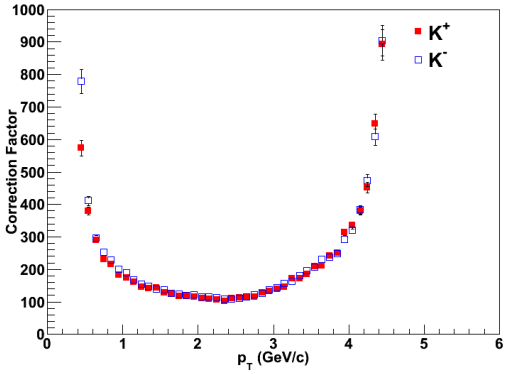

Figure 3.34: The correction factors of K with $\alpha > 0$ as a function of p_T.

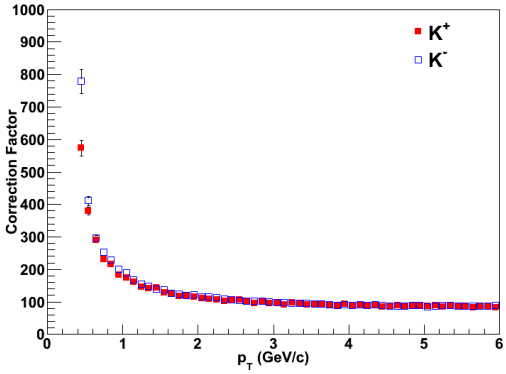

Figure 3.35: The correction factors with symmetric m^2 cut only of K with $\alpha > 0$ as a function of p_T.

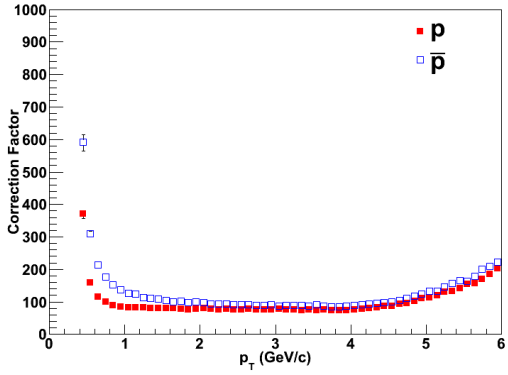

Figure 3.36: The correction factors of p and $\bar{p}$ in the $+-$ field as a function of p_T.

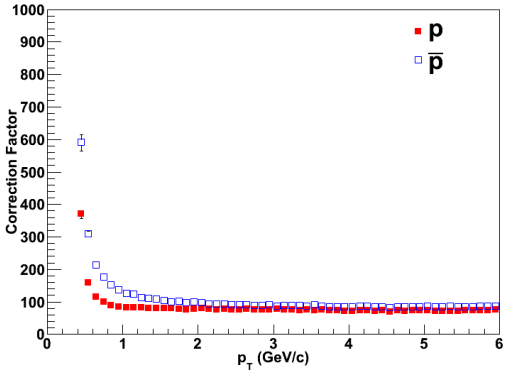

Figure 3.37: The correction factors with symmetric m^2 cut only of p and $\bar{p}$ in the $+-$ field as a function of p_T.

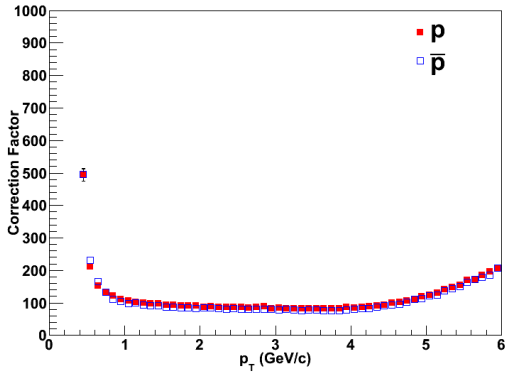

Figure 3.38: The correction factors of p and $\bar{p}$ in the $-+$ field as a function of p_T.

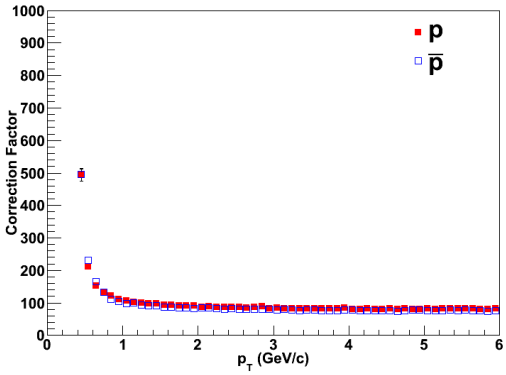

Figure 3.39: The correction factors with symmetric m^2 cut only of p and $\bar{p}$ in the $-+$ field as a function of p_T.

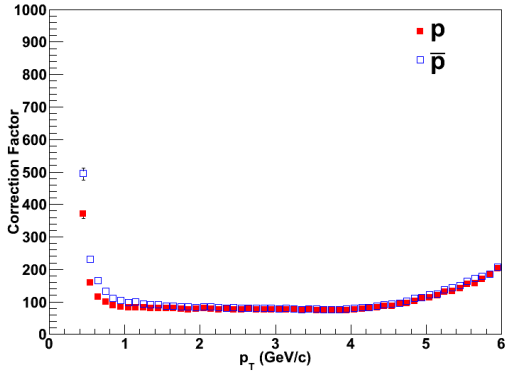

Figure 3.40: The correction factors of p and $\bar{p}$ with $\alpha < 0$ as a function of p_T.

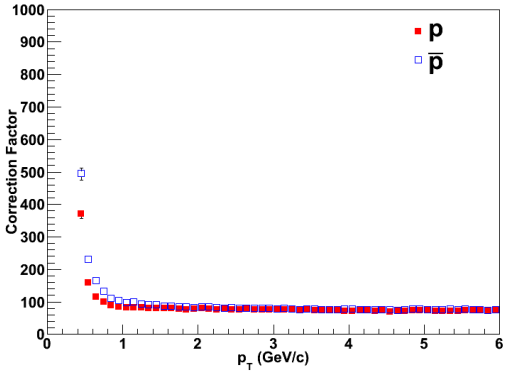

Figure 3.41: The correction factors with symmetric m^2 cut only of p and $\bar{p}$ with $\alpha < 0$ as a function of p_T.

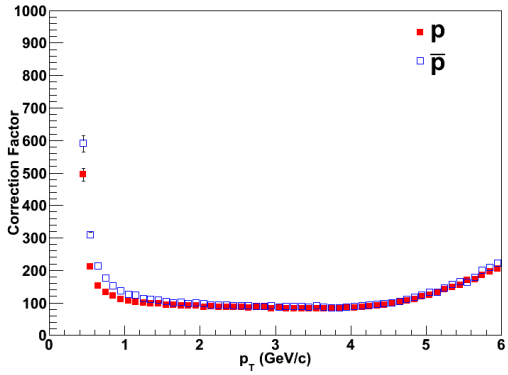

Figure 3.42: The correction factors of p and $\bar{p}$ with $\alpha > 0$ as a function of p_T.

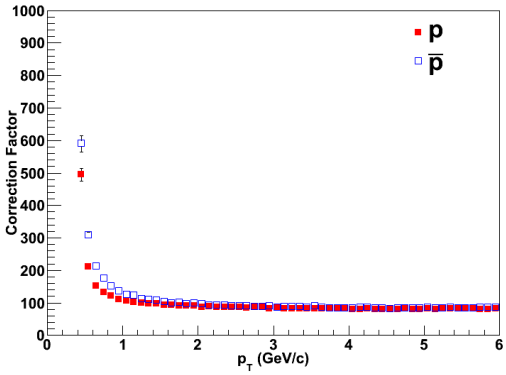

Figure 3.43: The correction factors with symmetric m^2 cut only of p and $\bar{p}$ with $\alpha > 0$ as a function of p_T.

3.2.1.2 Plots of the SPMC correction factors for Run8

Here we reiterate the previous section for the Run8 corrections.

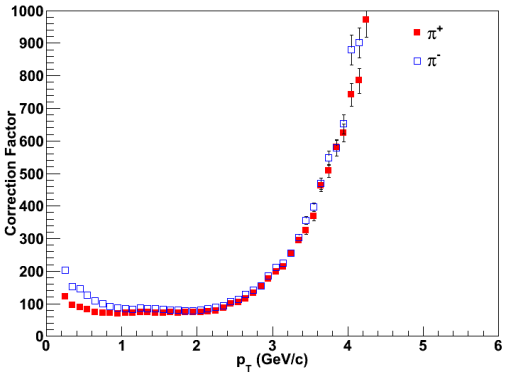

Figure 3.44: The correction factors of π in the $++$ field as a function of p_T.

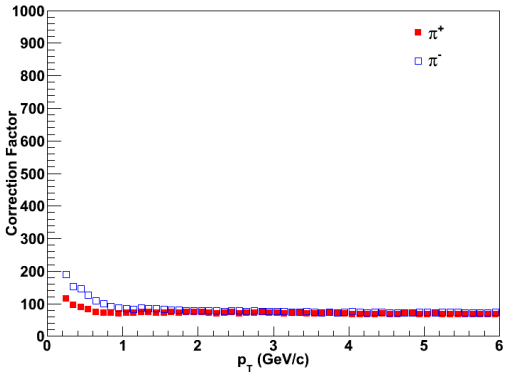

Figure 3.45: The correction factors with symmetric m^2 cut only of π in the $++$ field as a function of p_T.

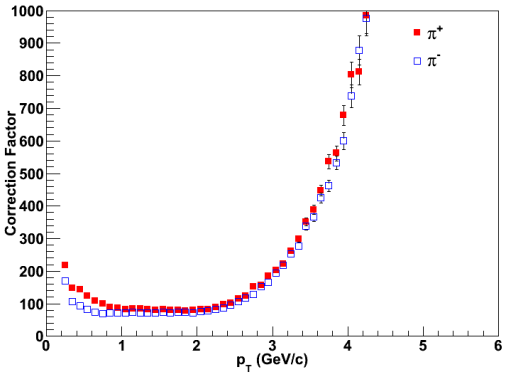

Figure 3.46: The correction factors of π in the $--$ field as a function of p_T.

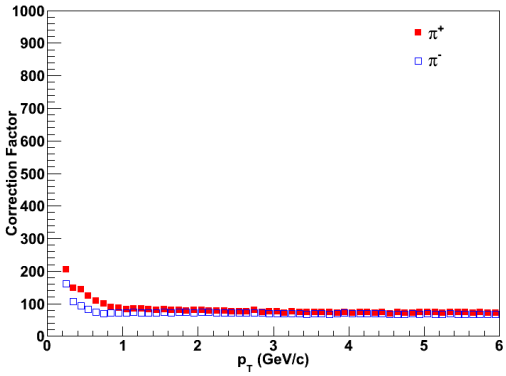

Figure 3.47: The correction factors with symmetric m^2 cut only of π in the $--$ field as a function of p_T.

Here again we plot both charges of pions for each DC alpha value field together.

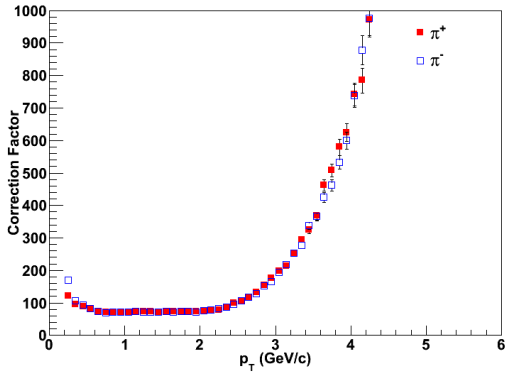

Figure 3.48: The correction factors of π with $\alpha < 0$ as a function of p_T.

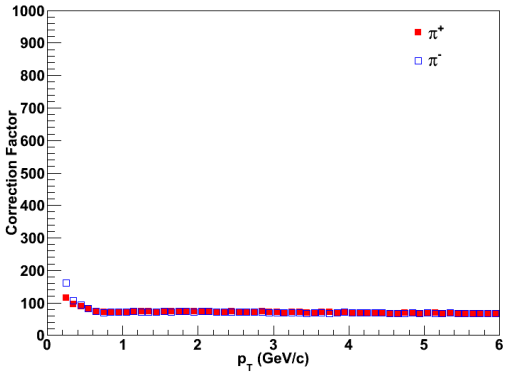

Figure 3.49: The correction factors with symmetric m^2 cut only of π with $\alpha < 0$ as a function of p_T.

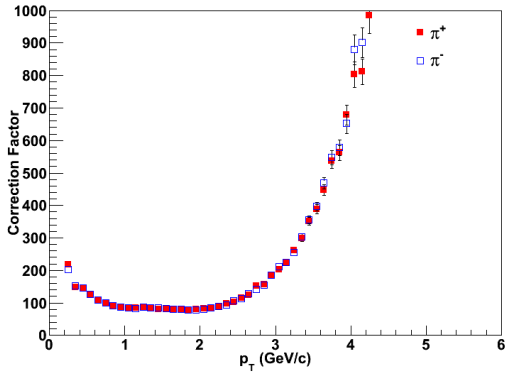

Figure 3.50: The correction factors of π with $\alpha > 0$ as a function of p_T.

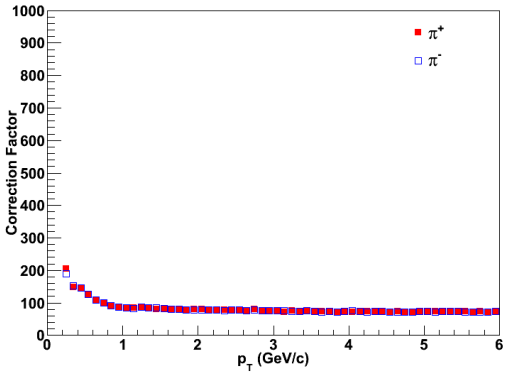

Figure 3.51: The correction factors with symmetric m^2 cut only of π with $\alpha > 0$ as a function of p_T.

In the proceeding 4 pages, we reiterate the above process for kaons on the next two pages protons for the two pages following that.

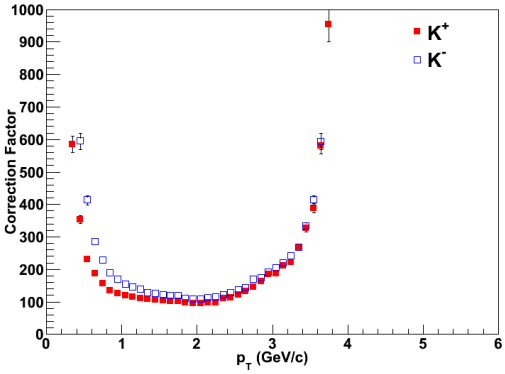

Figure 3.52: The correction factors of K in the $++$ field as a function of p_T.

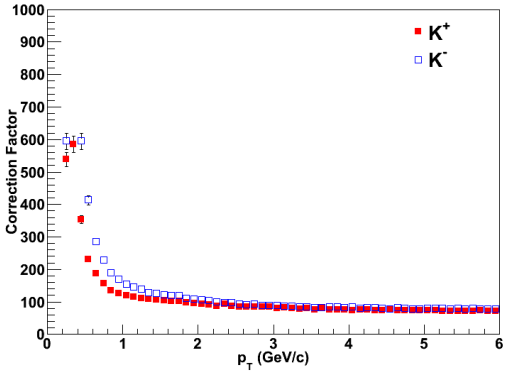

Figure 3.53: The correction factors with symmetric m^2 cut only of K in the $++$ field as a function of p_T.

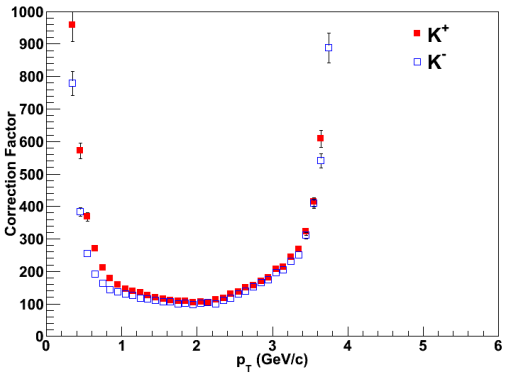

Figure 3.54: The correction factors of K in the $--$ field as a function of p_T.

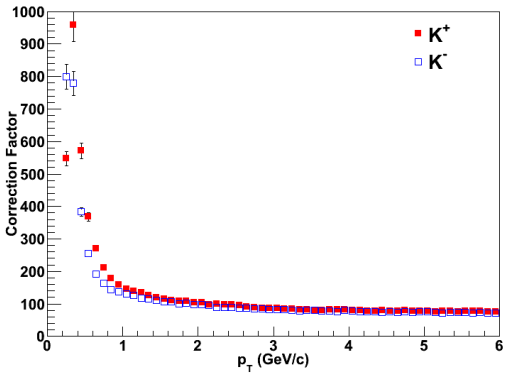

Figure 3.55: The correction factors with symmetric m^2 cut only of K in the $--$ field as a function of p_T.

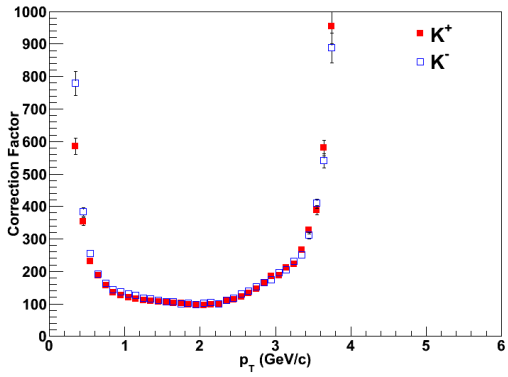

Figure 3.56: The correction factors of K with $\alpha < 0$ as a function of p_T.

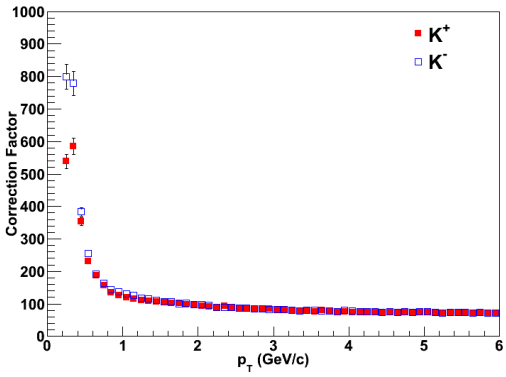

Figure 3.57: The correction factors with symmetric m^2 cut only of K with $\alpha < 0$ as a function of p_T.

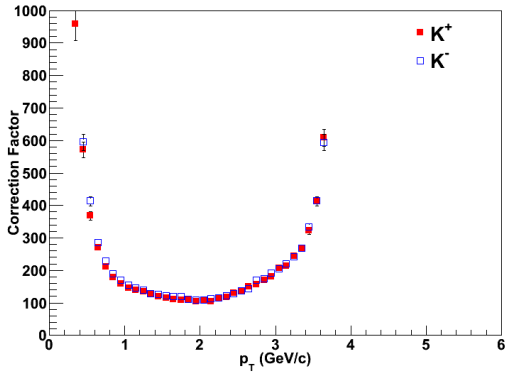

Figure 3.58: The correction factors of K with $\alpha > 0$ as a function of p_T.

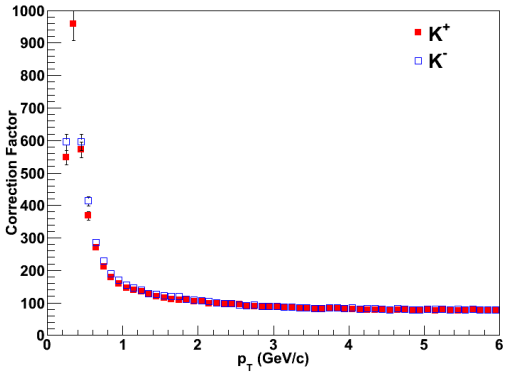

Figure 3.59: The correction factors with symmetric m^2 cut only of K with $\alpha > 0$ as a function of p_T.

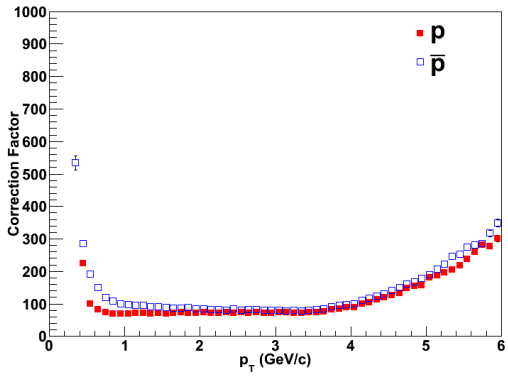

Figure 3.60: The correction factors of p and $\bar{p}$ in the $++$ field as a function of p_T.

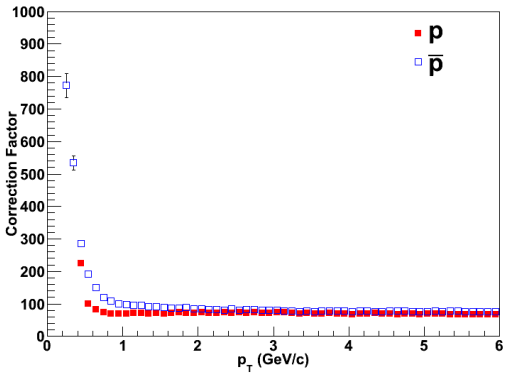

Figure 3.61: The correction factors with symmetric m^2 cut only of p and $\bar{p}$ in the $++$ field as a function of p_T.

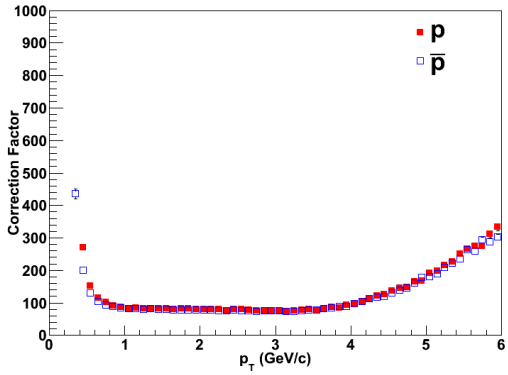

Figure 3.62: The correction factors of p and $\bar{p}$ in the $--$ field as a function of p_T.

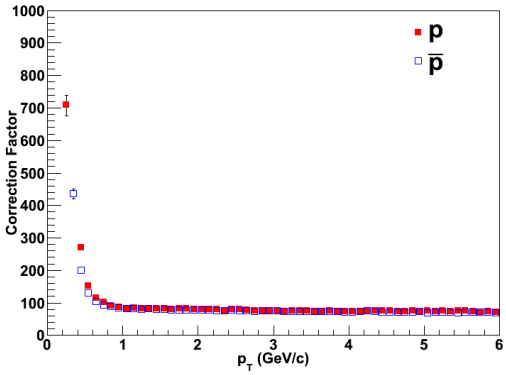

Figure 3.63: The correction factors with symmetric m^2 cut only of p and $\bar{p}$ in the $--$ field as a function of p_T.

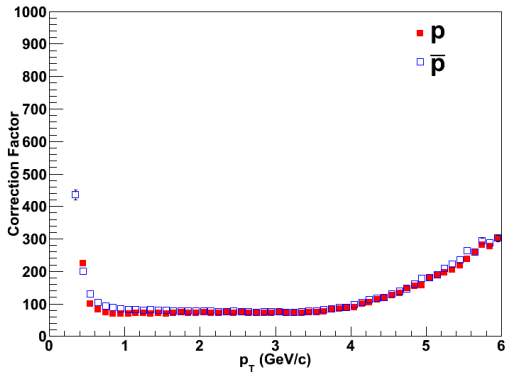

Figure 3.64: The correction factors of p and $\bar{p}$ with $\alpha < 0$ as a function of p_T.

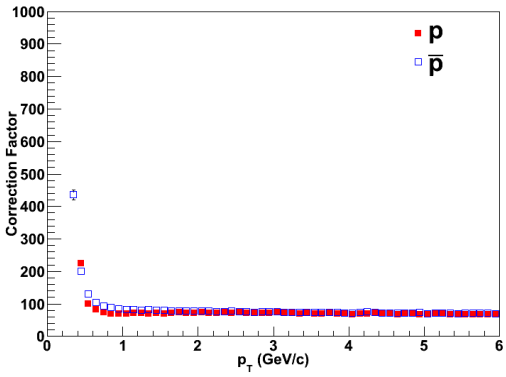

Figure 3.65: The correction factors with symmetric m^2 cut only of p and $\bar{p}$ with $\alpha < 0$ as a function of p_T.

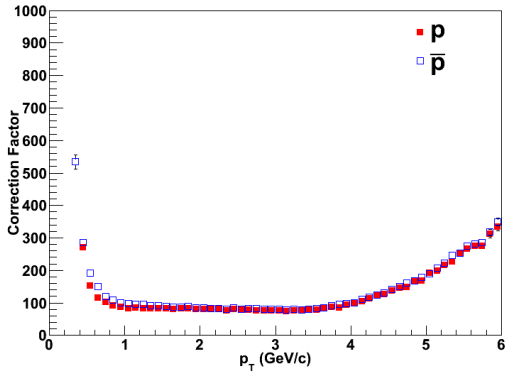

Figure 3.66: The correction factors of p and $\bar{p}$ with $\alpha > 0$ as a function of p_T.

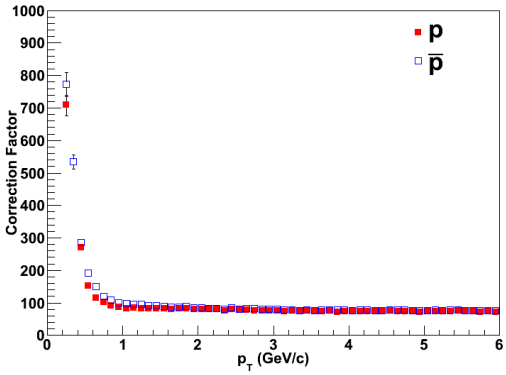

Figure 3.67: The correction factors with symmetric m^2 cut only of p and $\bar{p}$ with $\alpha > 0$ as a function of p_T.

3.2.2 Comparisons Between Simulated and Real Data

To ensure an accurate evaluation of the efficiencies, especially those of the tracking cuts, it is necessary to verify that the simulation software is working as expected, and to accommodate any unexpected behavior.

We find that the DC acceptance is poorly described in the simulations. Even small differences in DC acceptance can cause significant differences in the evaluation of the p_T dependence of the acceptance and cut efficiencies, so a detailed DC fiducial cut is need. We find that the PC acceptance is reasonably well-described in the simulations but there is room for improvement. These are p_T-independent and contribute only to the overall normalization. Additionally, the TOFW dead strip map is not in the simulations, so a strip cut is applied to both real and simulated tracks. This too is p_T-independent and contributes only to the overall normalization. Fortunately, we find the TOFW timing performance is extremely well described in the simulated data, which is very beneficial for the evaluation of asymmetric PID cuts.

Since the final subsection of the preceding section was about the PID functions in the real data, we begin our treatment of simulated and real comparisons with the PID functions for the sake of continuity. This is also the most important comparison for this analysis. The PID functions for simulated data are determined in the exact same manner as for real data.

3.2.2.1 PID functions in simulated and real data in Run7

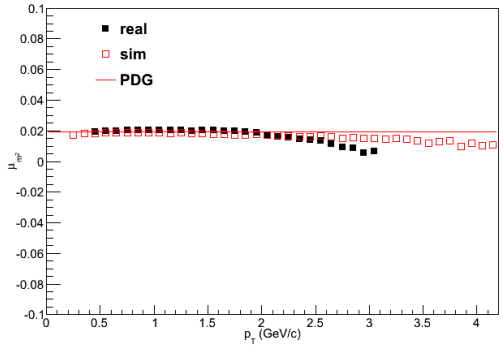

Figure 3.68: The mean of the m^2 distribution for π as a function of p_T, Run7.

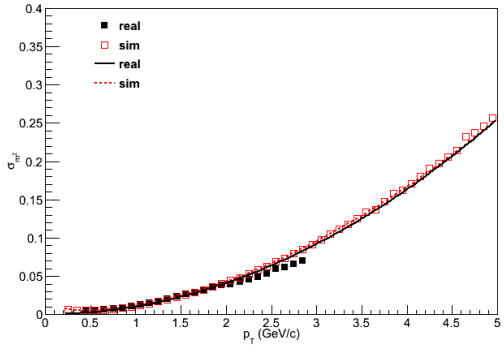

Figure 3.69: The standard deviation of the m^2 distribution for π as a function of p_T, Run7.

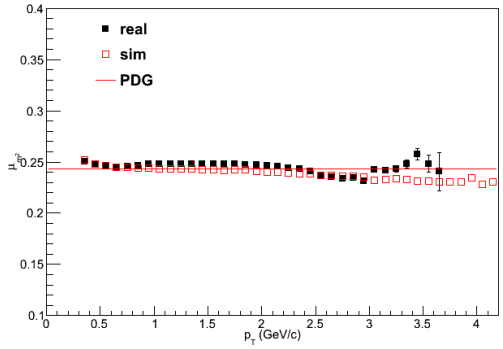

Figure 3.70: The mean of the m^2 distribution for K as a function of p_T, Run7.

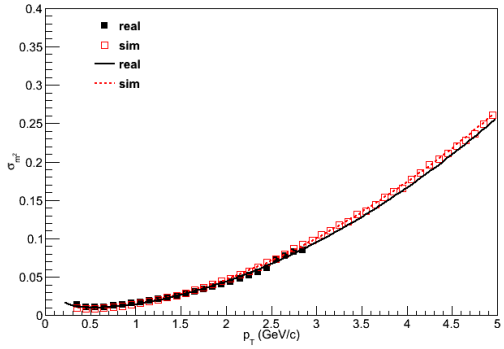

Figure 3.71: The standard deviation of the m^2 distribution for K as a function of p_T, Run7.

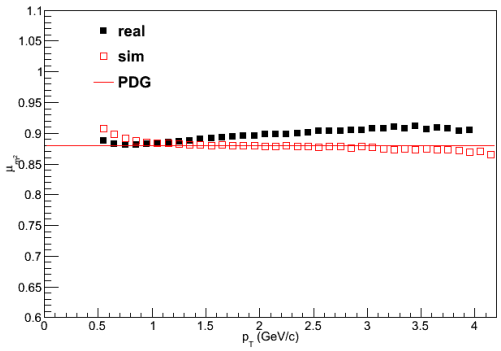

Figure 3.72: The mean of the m^2 distribution for p as a function of p_T, Run7.

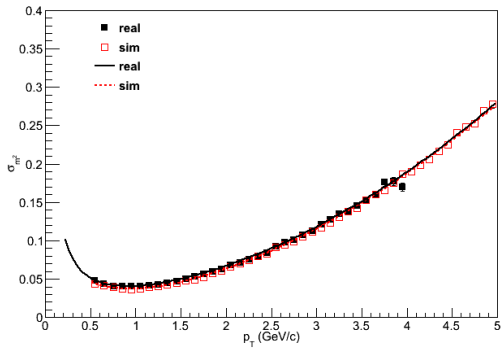

Figure 3.73: The standard deviation of the m^2 distribution for p as a function of p_T, Run7.

3.2.2.2 PID functions in simulated and real data in Run8

In order to match the real data, the $ttofw$ variable (representing the time-of-flight, which is the difference between the time measured in the TOFW and the start time determined by the BBC) in the simulated data is smeared with a Gaussian distribution using gRandom and then the m^2 is recalculated with the adjusted timing variable. To address the apparent discrepancy in the momentum resolution, the standard deviations of the m^2 distributions in the simulated data are additionally widened by a small constant multiplicative factor for the heavier particles (5% for kaons and 10% for protons).

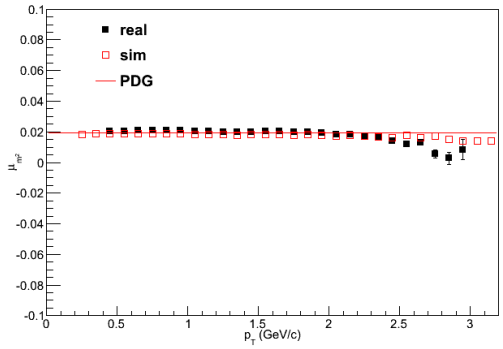

Figure 3.74: The mean of the m^2 distribution for π as a function of p_T, Run8.

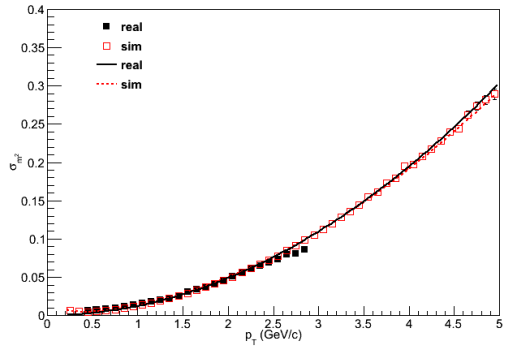

Figure 3.75: The standard deviation of the m^2 distribution for π as a function of p_T, Run8.

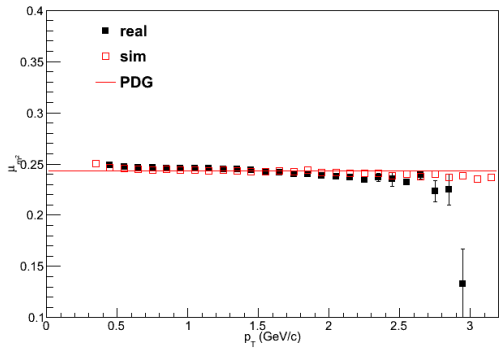

Figure 3.76: The mean of the m^2 distribution for K as a function of p_T, Run8.

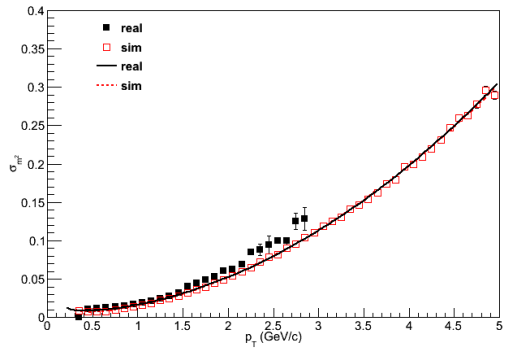

Figure 3.77: The standard deviation of the m^2 distribution for K as a function of p_T, Run8.

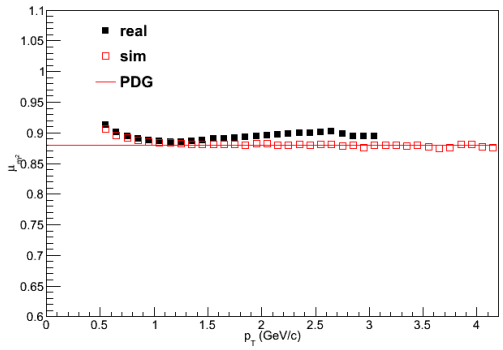

Figure 3.78: The mean of the m^2 distribution for p as a function of p_T, Run8.

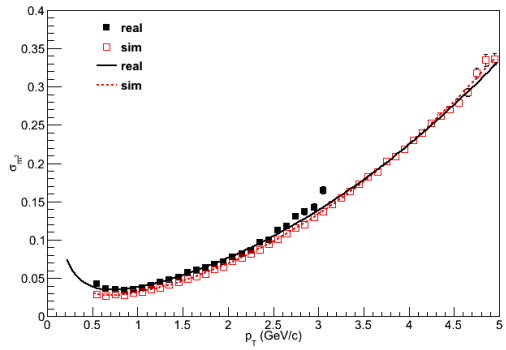

Figure 3.79: The standard deviation of the m^2 distribution for p as a function of p_T, Run8.

3.2.2.3 Drift chamber fiducial maps for Run7

These plots show the DC fiducial map for negative DC zed in the $+-$ field.

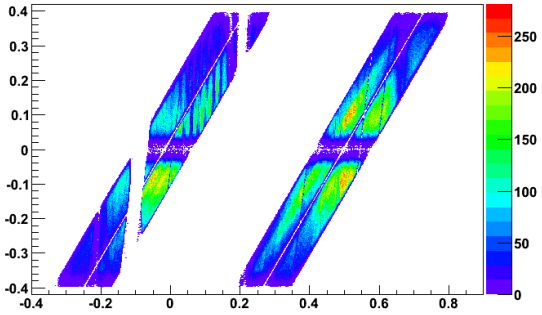

Figure 3.80: DC alpha vs DC phi, negative DC zed, $+-$ field. Real data, no fiducial cut applied.

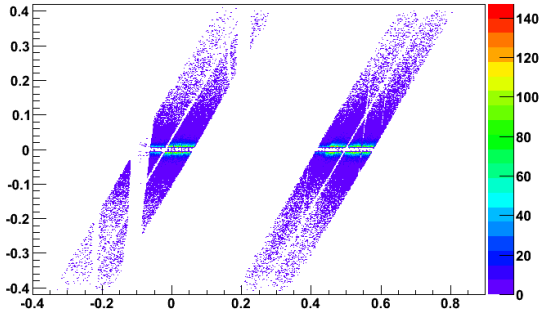

Figure 3.81: DC alpha vs DC phi, negative DC zed, $+-$ field. Simulated data, no fiducial cut applied.

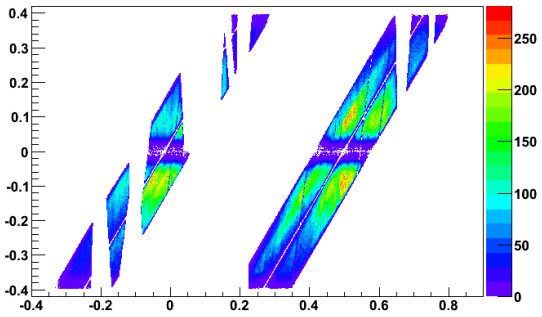

Figure 3.82: DC alpha vs DC phi, negative DC zed, $+-$ field. Real data, fiducial cut applied.

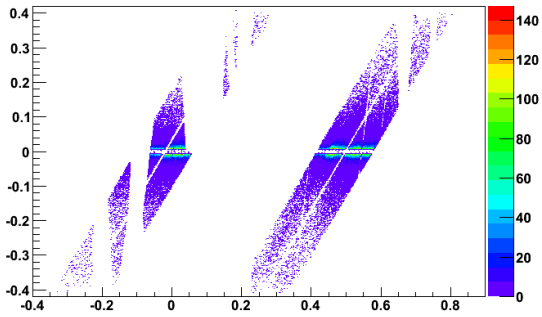

Figure 3.83: DC alpha vs DC phi, negative DC zed, $+-$ field. Simulated data, fiducial cut applied.

These plots show the DC fiducial map for positive DC zed in the $+-$ field.

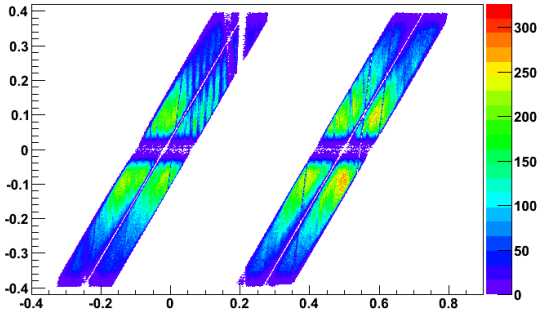

Figure 3.84: DC alpha vs DC phi, positive DC zed, $+-$ field. Real data, no fiducial cut applied.

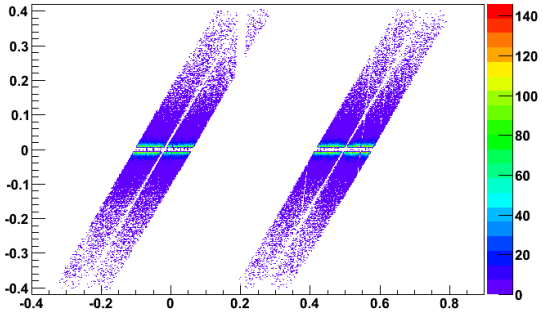

Figure 3.85: DC alpha vs DC phi, positive DC zed, $+-$ field. Simulated data, no fiducial cut applied.

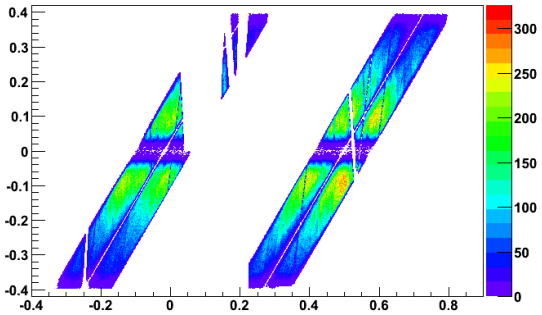

Figure 3.86: DC alpha vs DC phi, positive DC zed, $+-$ field. Real data, fiducial cut applied.

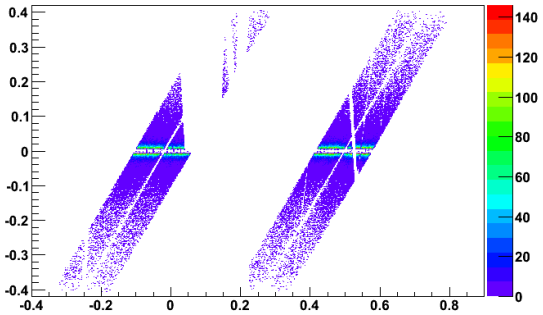

Figure 3.87: DC alpha vs DC phi, positive DC zed, $+-$ field. Simulated data, fiducial cut applied.

These plots show the DC fiducial map for negative DC zed in the $-+$ field.

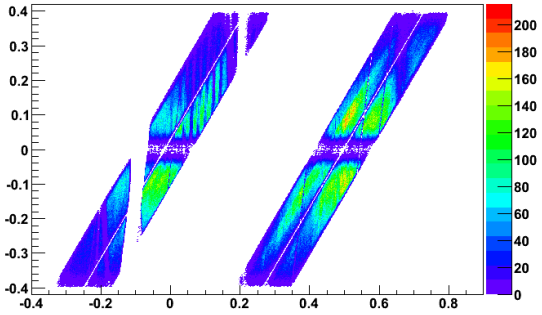

Figure 3.88: DC alpha vs DC phi, negative DC zed, $-+$ field. Real data, no fiducial cut applied.

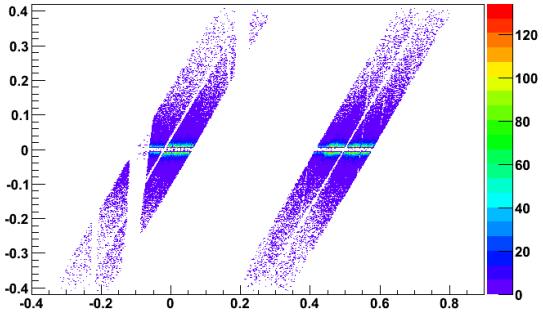

Figure 3.89: DC alpha vs DC phi, negative DC zed, $-+$ field. Simulated data, no fiducial cut applied.

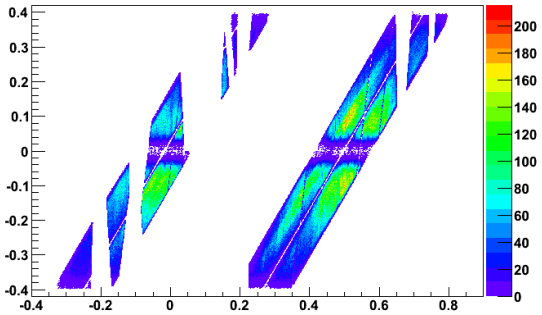

Figure 3.90: DC alpha vs DC phi, negative DC zed, $-+$ field. Real data, fiducial cut applied.

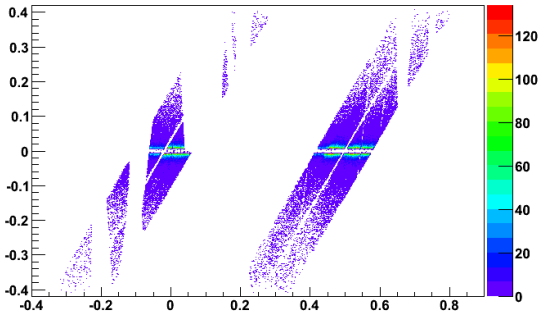

Figure 3.91: DC alpha vs DC phi, negative DC zed, $-+$ field. Simulated data, fiducial cut applied.

These plots show the DC fiducial map for positive DC zed in the $-+$ field.

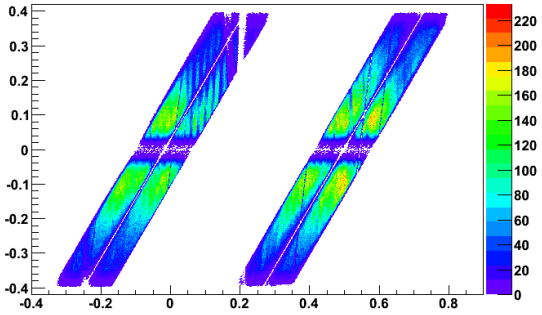

Figure 3.92: DC alpha vs DC phi, positive DC zed, $-+$ field. Real data, no fiducial cut applied.

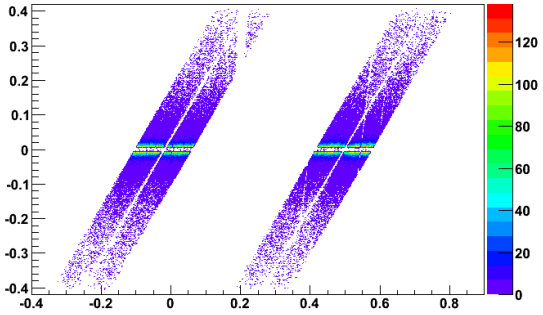

Figure 3.93: DC alpha vs DC phi, positive DC zed, $-+$ field. Simulated data, no fiducial cut applied.

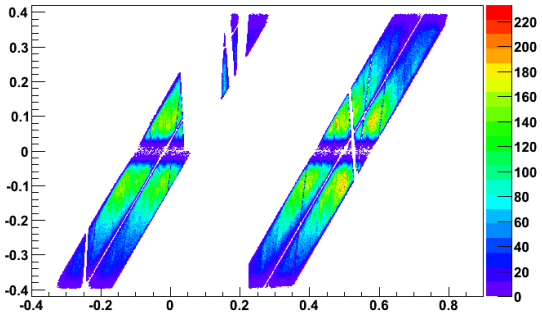

Figure 3.94: DC alpha vs DC phi, positive DC zed, $-+$ field. Real data, fiducial cut applied.

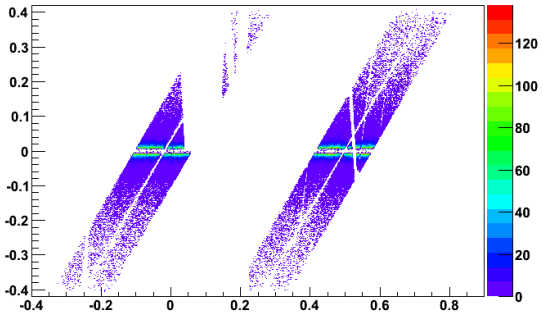

Figure 3.95: DC alpha vs DC phi, positive DC zed, $-+$ field. Simulated data, fiducial cut applied.

3.2.2.4 Drift chamber fiducial maps for Run8

These plots show the DC fiducial map for negative DC zed in the ++ field.

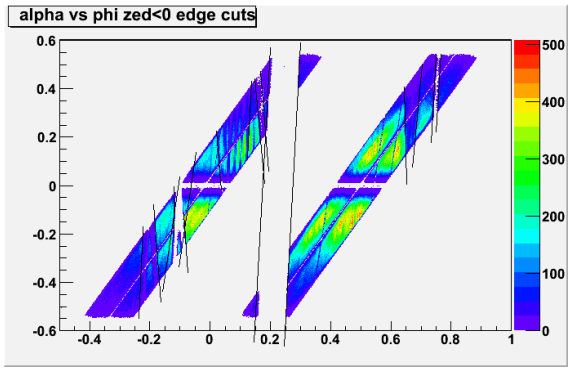

Figure 3.96: DC alpha vs DC phi, negative DC zed, ++ field. Real data, no fiducial cut applied.

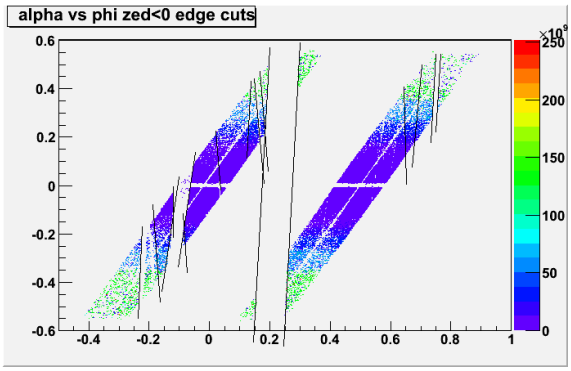

Figure 3.97: DC alpha vs DC phi, negative DC zed, ++ field. Simulated data, no fiducial cut applied.

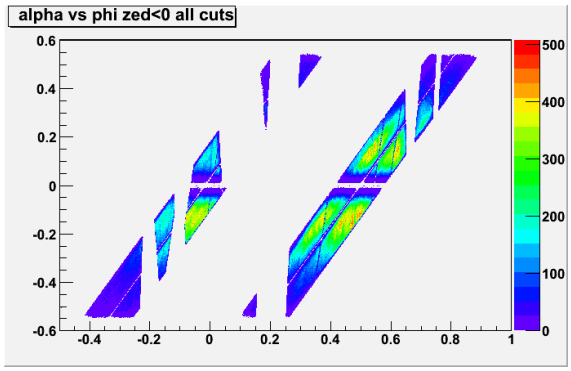

Figure 3.98: DC alpha vs DC phi, negative DC zed, ++ field. Real data, fiducial cut applied.

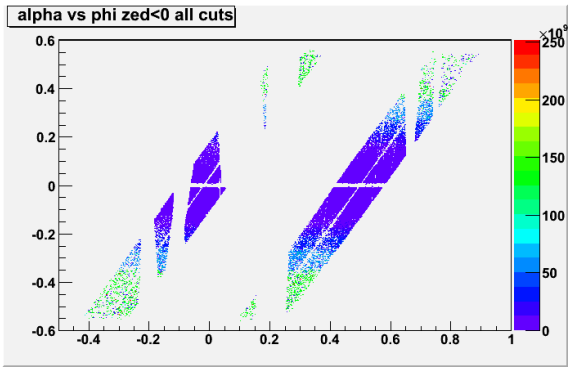

Figure 3.99: DC alpha vs DC phi, negative DC zed, ++ field. Simulated data, fiducial cut applied.

These plots show the DC fiducial map for positive DC zed in the ++ field.

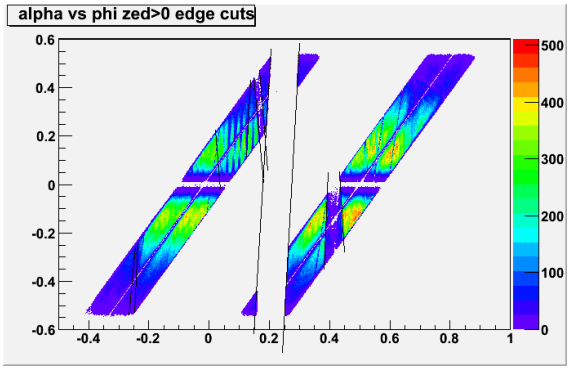

Figure 3.100: DC alpha vs DC phi, positive DC zed, ++ field. Real data, no fiducial cut applied.

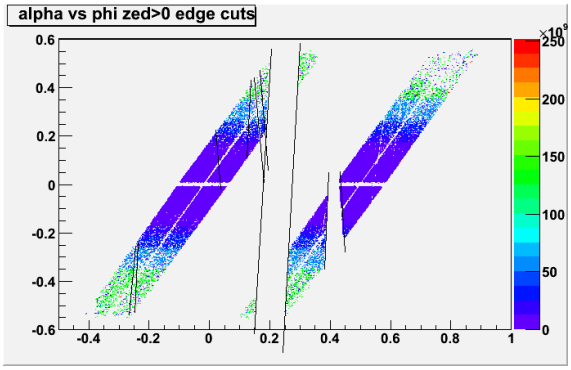

Figure 3.101: DC alpha vs DC phi, positive DC zed, ++ field. Simulated data, no fiducial cut applied.

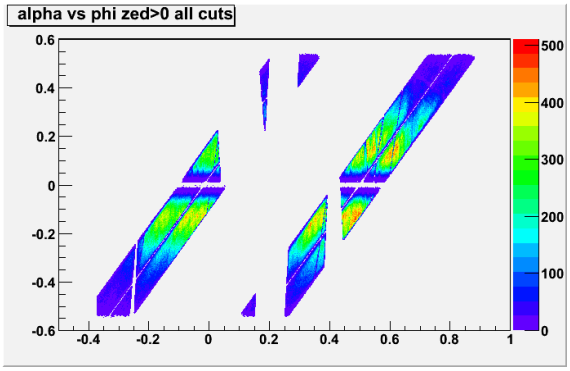

Figure 3.102: DC alpha vs DC phi, positive DC zed, ++ field. Real data, fiducial cut applied.

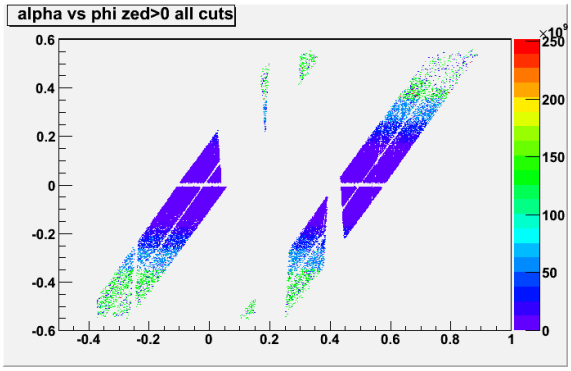

Figure 3.103: DC alpha vs DC phi, positive DC zed, ++ field. Simulated data, fiducial cut applied.

These plots show the DC fiducial map for negative DC zed in the −− field.

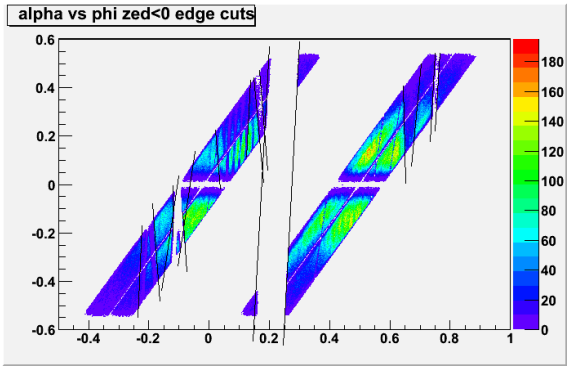

Figure 3.104: DC alpha vs DC phi, negative DC zed, −− field. Real data, no fiducial cut applied.

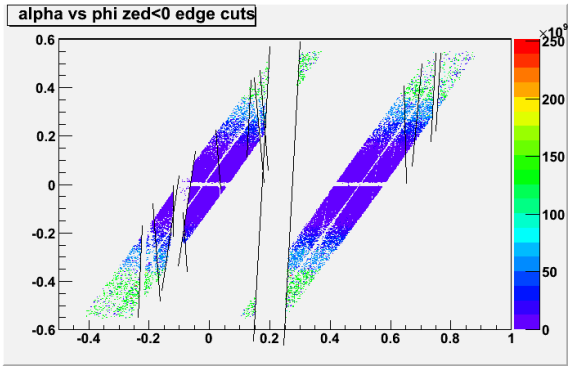

Figure 3.105: DC alpha vs DC phi, negative DC zed, −− field. Simulated data, no fiducial cut applied.

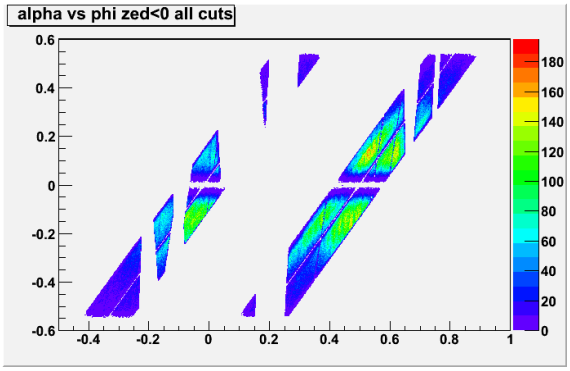

Figure 3.106: DC alpha vs DC phi, negative DC zed, −− field. Real data, fiducial cut applied.

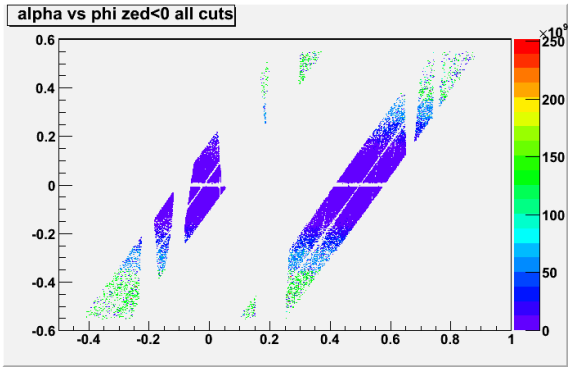

Figure 3.107: DC alpha vs DC phi, negative DC zed, −− field. Simulated data, fiducial cut applied.

These plots show the DC fiducial map for positive DC zed in the −− field.

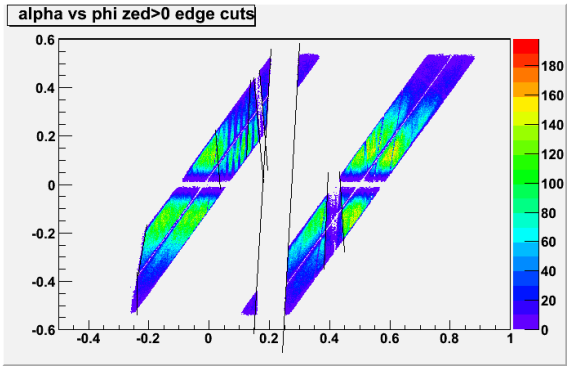

Figure 3.108: DC alpha vs DC phi, positive DC zed, −− field. Real data, no fiducial cut applied.

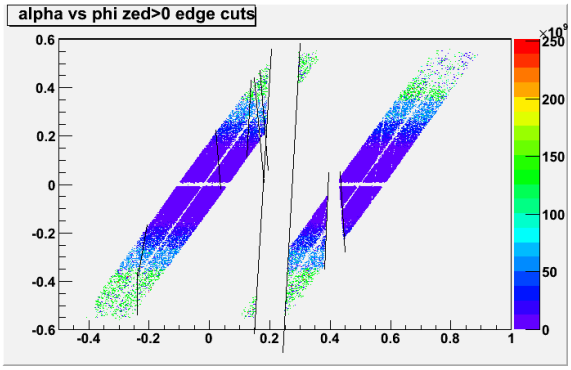

Figure 3.109: DC alpha vs DC phi, positive DC zed, −− field. Simulated data, no fiducial cut applied.

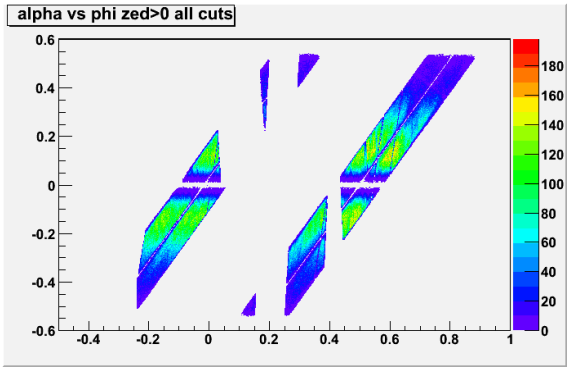

Figure 3.110: DC alpha vs DC phi, positive DC zed, −− field. Real data, fiducial cut applied.

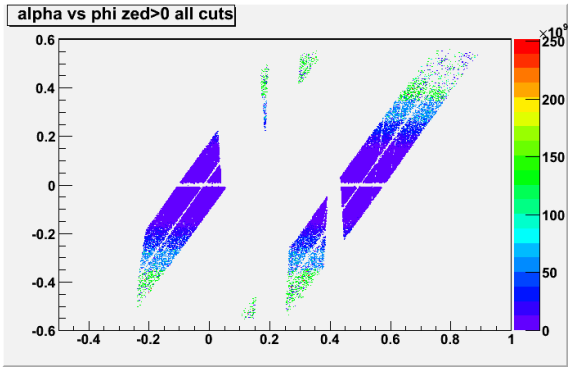

Figure 3.111: DC alpha vs DC phi, positive DC zed, −− field. Simulated data, fiducial cut applied.

3.2.2.5 Drift chamber 1-d phi distributions in Run7

In this section we show the 1-d DC phi distributions. We use the narrowest p_T bins possible to get the closest possible match between the simulated and DC alpha distributions. Even so, there are some slight observable shifts in phi coordinates between real and simulated data. We show each possible combination of charge, field, TOFW sector, and DC side (North and South). Only a single p_T bin, zed selection, and field configuration are shown, for a total of four figures. This is for brevity, as the various possible combinations yield 832, 960, or more figures depending on the p_T range.

Here we show the 1-d DC phi distributions for 0.5 GeV/c $< p_T <$ 0.6 GeV/c, positive zed, $+-$ field, sector W1.

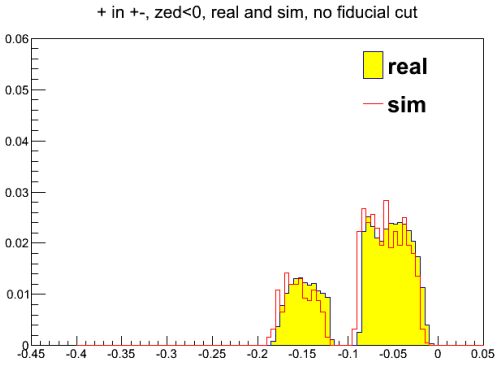

Figure 3.112: DC phi, positive DC zed, positive charge, $+-$ field. Real and sim data, no fiducial cut applied.

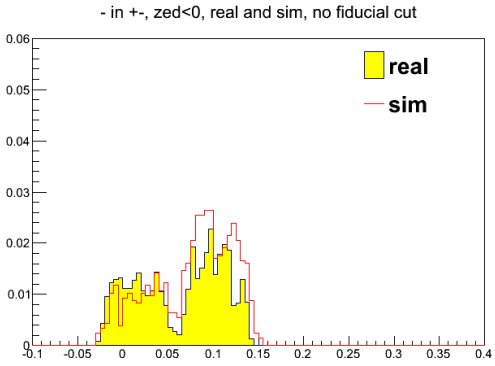

Figure 3.113: DC phi, positive DC zed, negative charge, $+-$ field. Real and sim data, no fiducial cut applied.

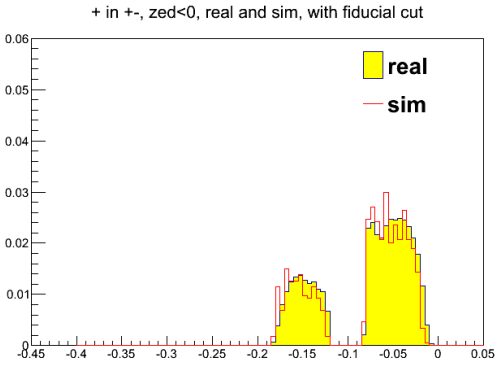

Figure 3.114: DC phi, positive DC zed, positive charge, $+-$ field. Real and sim data, fiducial cut applied.

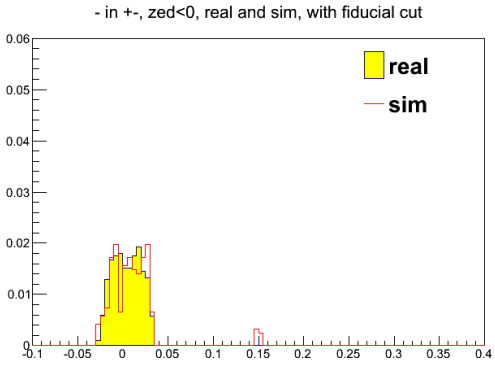

Figure 3.115: DC phi, positive DC zed, negative charge, $+-$ field. Real and sim data, fiducial cut applied.

3.2.2.6 Drift chamber 1-d phi distributions in Run8

In this section we show the 1-d DC phi distributions for a few selected p_T bins. We use the narrowest p_T bins possible to get the closest possible match between the simulated and DC alpha distributions. Even so, there are some slight observable shifts in phi coordinates between real and simulated data. We show each possible combination of charge, field, TOFW sector, and DC side (North and South). Only a single p_T bin, zed selection, and field configuration are shown, for a total of four figures. This is for brevity, as the various possible combinations yield 832, 960, or more figures depending on the p_T range.

Here we show the 1-d DC phi distributions for 0.5 GeV/c $< p_T <$ 0.6 GeV/c, negative zed, $++$ field, sector W1.

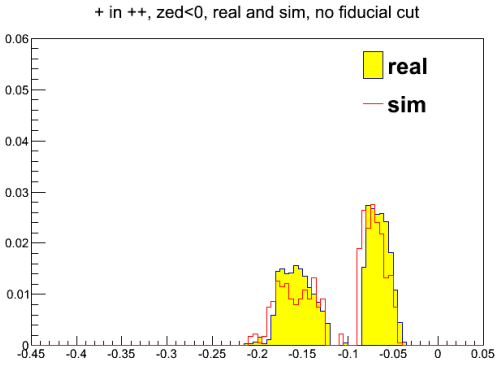

Figure 3.116: DC phi, positive DC zed, positive charge, $++$ field. Real and sim data, no fiducial cut applied.

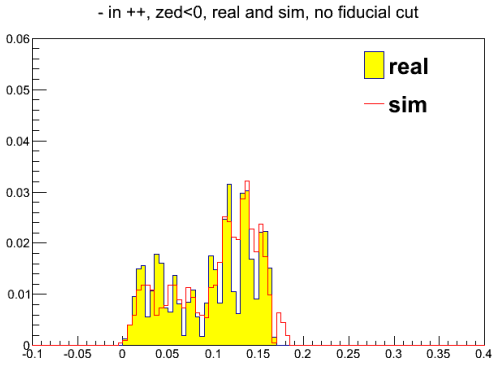

Figure 3.117: DC phi, positive DC zed, negative charge, $++$ field. Real and sim data, no fiducial cut applied.

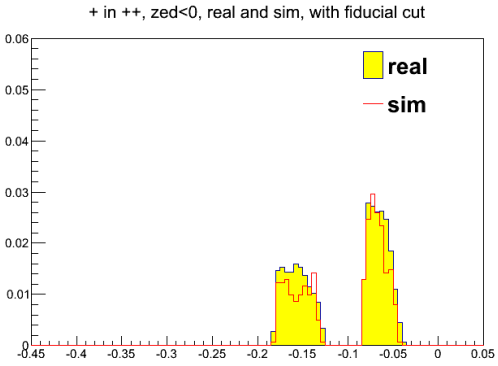

Figure 3.118: DC phi, positive DC zed, positive charge, $++$ field. Real and sim data, fiducial cut applied.

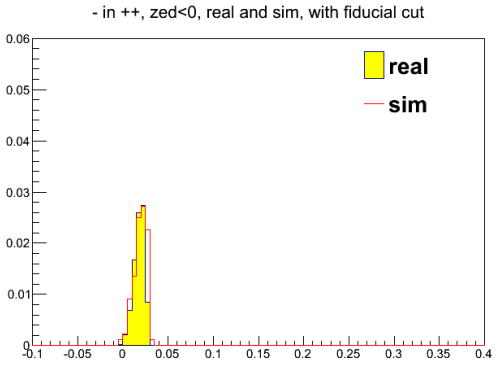

Figure 3.119: DC phi, positive DC zed, negative charge, $++$ field. Real and sim data, fiducial cut applied.

3.2.2.7 Particle yield ratios as a test of the DC fiducial cuts

Positive and negative charges occupy different regions of the DC parameter space (the alpha-phi plane), and their respective regions are reversed when the magnetic field is reversed. Therefore, the ratio of the corrected spectrum of a certain particle in one field to the corrected spectrum of the same particle in the other field should be identically one if the the acceptance is made uniform by the application of the DC fiducial cuts. The next set of plots shows the ratio of each particle.

Generally speaking, we find that the acceptance is worse for positive alpha than for negative alpha. For consistency, we present the ratios as negative alpha over positive alpha; that is, $(-$ in $+-)/(-$ in $-+)$ and $(+$ in $-+)/(+$ in $+-)$.

Figure 3.120 shows these ratios for Run7 Au+Au. As can be seen, the ratios generally show good agreement with unity, indicating uniform acceptance. However, the lowest few p_T points for the kaons and protons show a ratio somewhat divergent from unity, indicating a possible mass dependence of the non-uniformity in the acceptance, likely due to the multiple scattering in the drift chamber.

Now we use the same ratios to examine the acceptance in Run8. As with Run7, we find that the acceptance is worse for positive alpha than for negative alpha. We also observe some additional degradation of the fiducial acceptance when comparing to Run7. For consistency, we present the ratios as negative alpha over positive alpha; that is, $(-$ in $++)/(-$ in $--)$ and $(+$ in $--)/(+$ in $++)$.

Figure 3.121 shows these ratios for Run8 d+Au. As can be seen, the ratios generally show good agreement with unity, indicating uniform acceptance. At the very highest p_T

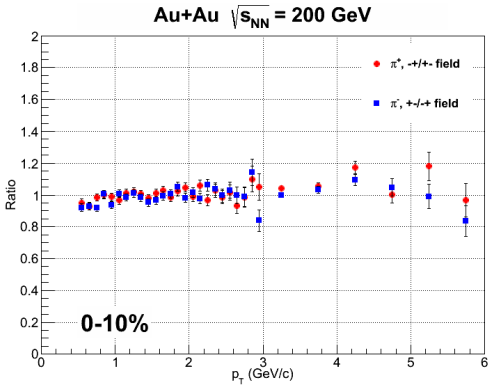

3.120 (a)

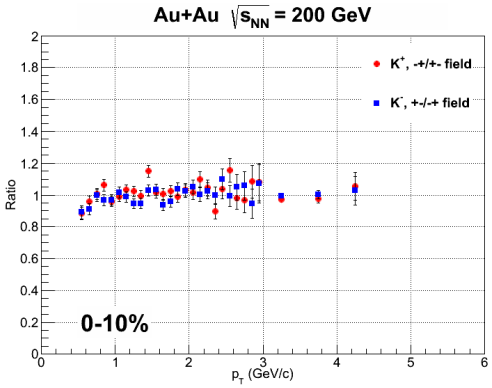

3.120 (b)

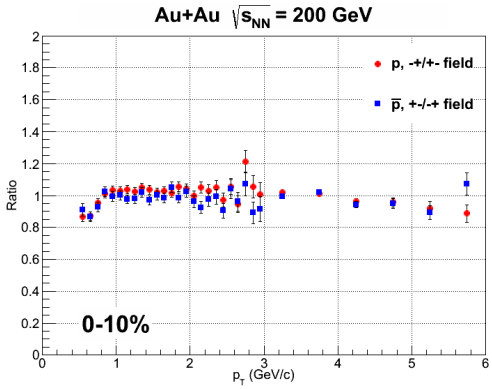

3.120 (c)

Figure 3.120: (a) Ratio of corrected $\pi^{\pm}$ in one field to the other. (b) Ratio of corrected $K^{\pm}$ in one field to the other. (c) Ratio of corrected p and $\bar{p}$ in one field to the other.

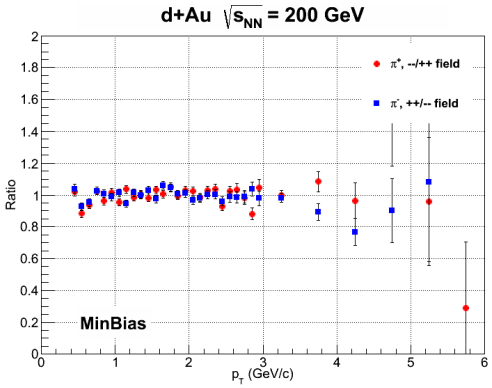

3.121 (a)

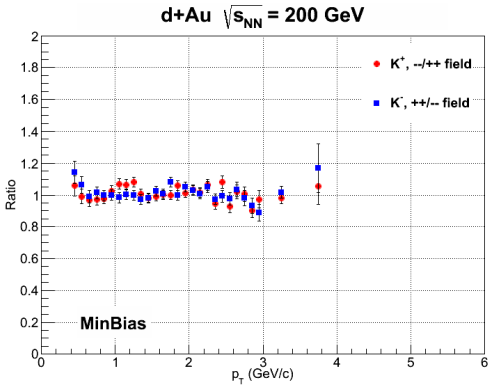

3.121 (b)

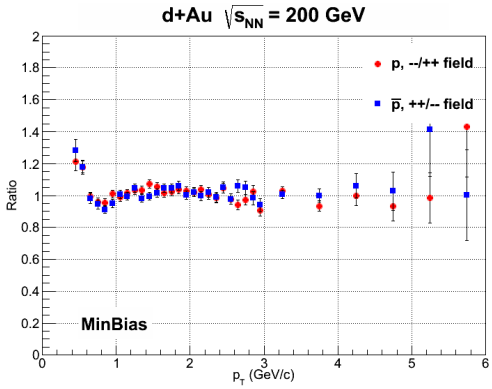

3.121 (c)

Figure 3.121: (a) Ratio of corrected $\pi^{\pm}$ in one field to the other. (b) Ratio of corrected $K^{\pm}$ in one field to the other. (c) Ratio of corrected p and $\bar{p}$ in one field to the other.

points the pions show some disagreement although these are likely due to statistical fluctuations, as the $--$ field data set is much smaller than the $++$ data set. Additionally, the lowest p_T point for the kaons and the lowest two p_T points for the protons show a ratio divergent from unity, indicating a possible mass dependence of the non-uniformity in the acceptance, likely due to the multiple scattering in the drift chamber. Because the multiple scattering also makes PID difficult in this p_T region, these points are excluded from the final results anyway.

3.2.2.8 Pad chamber fiducial maps for Run7

These plots show the PC1 fiducial map. Note that the momentum distribution is different in real data and simulated data, and therefore the tracks appear more spread out on the left than the right. This is because there are many low p_T with large bending angle in the DC and therefore the PC1 phi coordinate has a wider distribution. The only concern with these figures is to examine the dead areas.

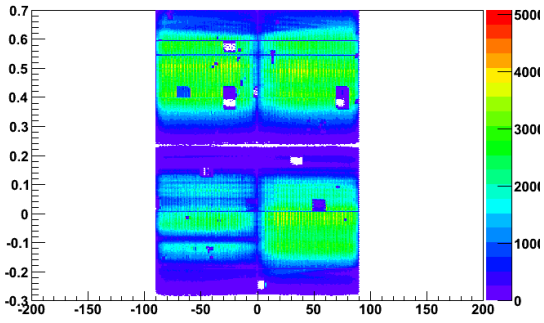

Figure 3.122: PC1 phi vs PC1 zed. Real data, no fiducial cut applied, Run7.

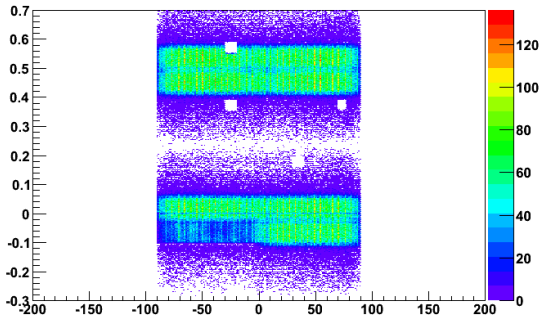

Figure 3.123: PC1 phi vs PC1 zed. Simulated data, no fiducial cut applied, Run7.

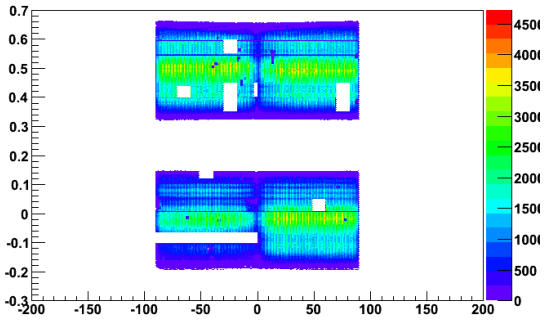

Figure 3.124: PC1 phi vs PC1 zed. Real data, fiducial cut applied, Run7.

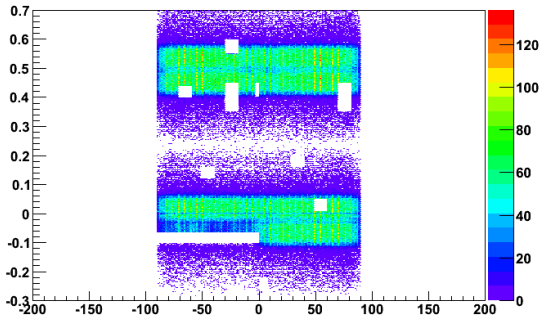

Figure 3.125: PC1 phi vs PC1 zed. Simulated data, fiducial cut applied, Run7.

These plots show the PC3 fiducial map.

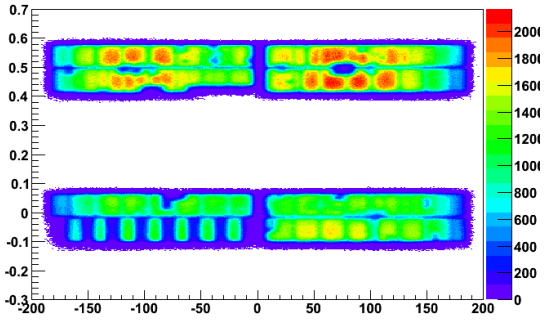

Figure 3.126: PC3 phi vs PC3 zed. Real data, no fiducial cut applied, Run7.

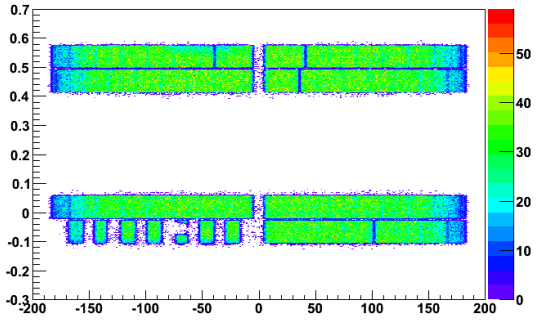

Figure 3.127: PC3 phi vs PC3 zed. Simulated data, no fiducial cut applied, Run7.

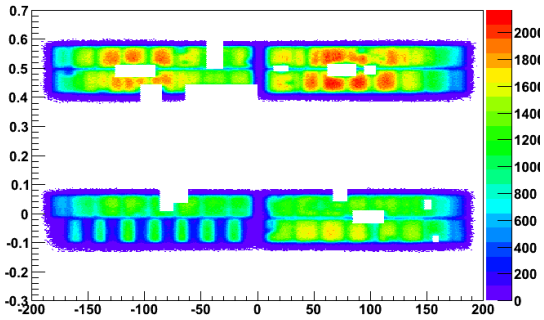

Figure 3.128: PC3 phi vs PC3 zed. Real data, fiducial cut applied, Run7.

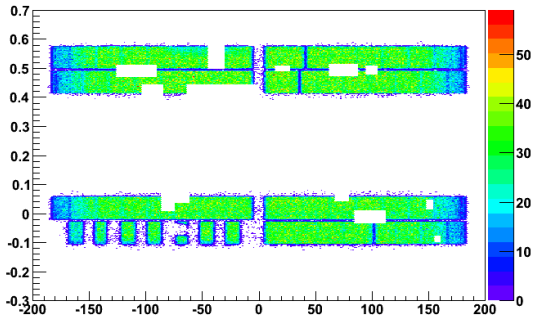

Figure 3.129: PC3 phi vs PC3 zed. Simulated data, fiducial cut applied, Run7.

3.2.2.9 Pad chamber fiducial maps for Run8

These plots show the PC1 fiducial map. As with the Run7 case, the PC1 phi distribution is wider for the real data. The only concern here is to examine the dead areas.

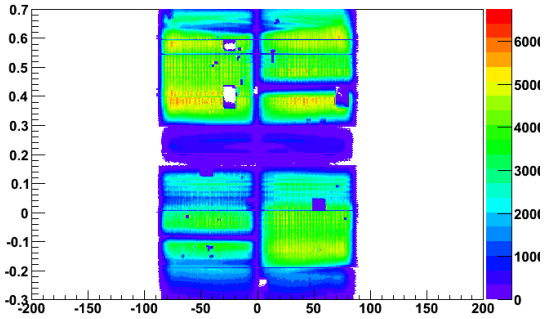

Figure 3.130: PC1 phi vs PC1 zed. Real data, no fiducial cut applied, Run8.

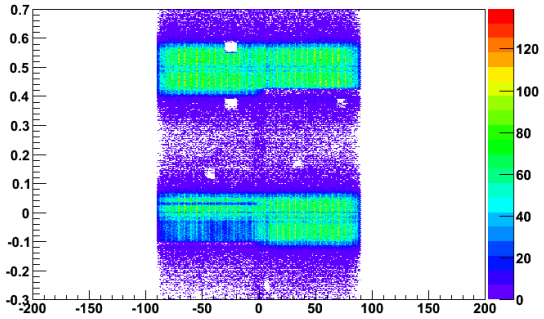

Figure 3.131: PC1 phi vs PC1 zed. Simulated data, no fiducial cut applied, Run8.

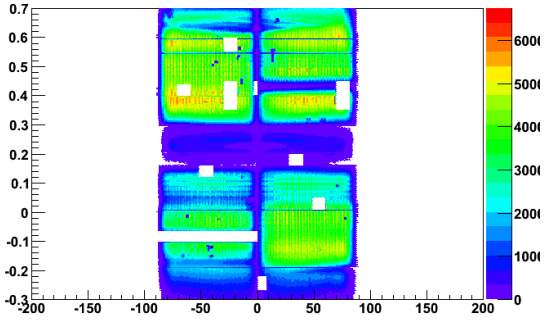

Figure 3.132: PC1 phi vs PC1 zed. Real data, fiducial cut applied, Run8.

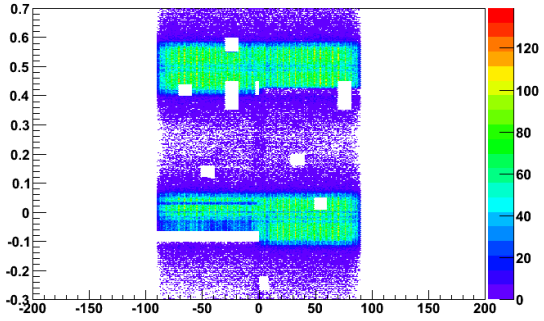

Figure 3.133: PC1 phi vs PC1 zed. Simulated data, fiducial cut applied, Run8.

These plots show the PC3 fiducial map.

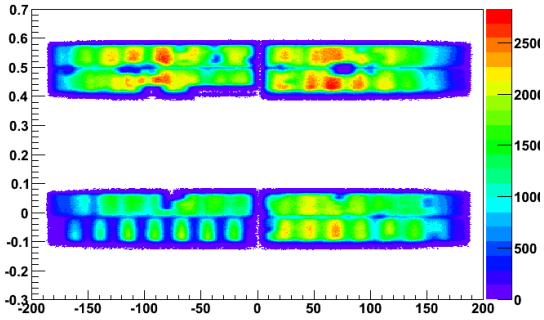

Figure 3.134: PC3 phi vs PC3 zed. Real data, no fiducial cut applied, Run8.

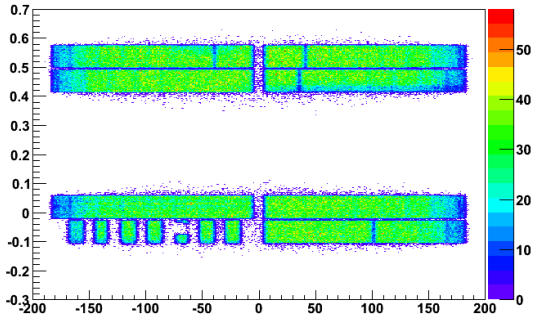

Figure 3.135: PC3 phi vs PC3 zed. Simulated data, no fiducial cut applied, Run8.

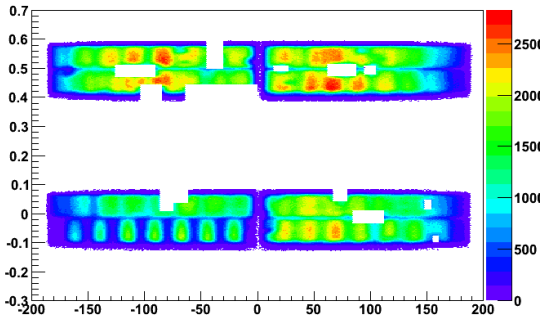

Figure 3.136: PC3 phi vs PC3 zed. Real data, fiducial cut applied, Run8.

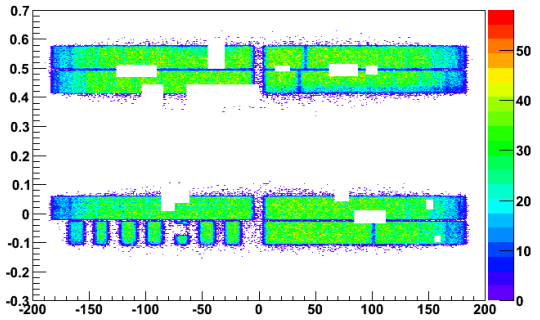

Figure 3.137: PC3 phi vs PC3 zed. Simulated data, fiducial cut applied, Run8.

3.2.2.10 Track matching residuals in simulations

The TOFW sigmalized residuals aren't outputted by PISA into the simDSTs, so it's necessary to use the dimensional residuals to calculate the sigmalized residuals. The PC3 sigmalized residuals, on the other hand, are outputted by PISA. However, they were analyzed and found not to be correct, so we calculate the sigmalized residuals for the PC3 using the same method as for the TOFW. Since the tracks in real data are dominated by pions, we use the track matching parameters fitted to the pions for all particles in simulation. We fill a 2-d histogram of each individual residual, separated by charge and field, as a function of p_T. We fit each p_T bin with a Gaussian distribution to determine the mean and standard deviation. We then fit those data points, both mean and sigma, with a function of the form

$$f(x) = p_0 + p_1/x + p_2/x^2 + p_3/\sqrt{x}, \tag{3.6}$$

and use the parameters from the fit to define a function in the simulation analysis code that calculates the sigmalized residuals from the raw ones. While all four charge and field combinations are analyzed independently in each run, only π^+ in the $+-$ field is shown for Run7 and only π^+ in the $++$ field is shown for Run8, and only a single residual is selected. This is only for brevity, showing 16 figures instead of 256.

Mean of tofwdz for π^+ in the $+-$ field

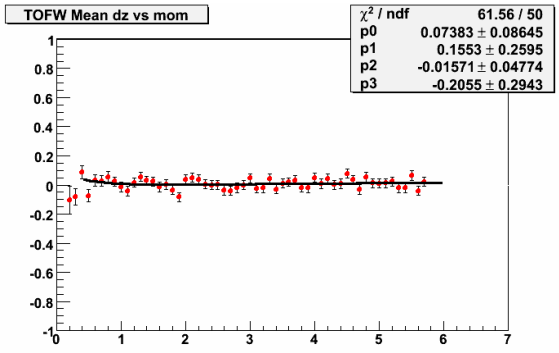

Figure 3.138: Mean of tofwdz for π^+ in the $+-$ field, sector W1

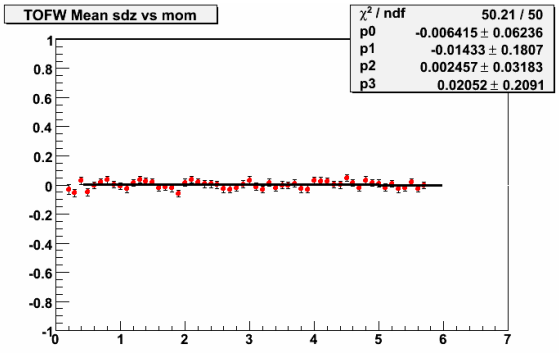

Figure 3.139: Mean of tofwsdz for π^+ in the $+-$ field, sector W1

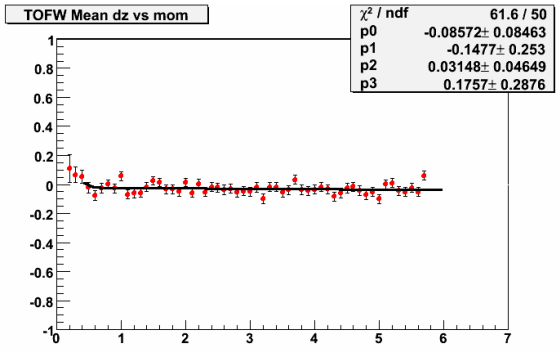

Figure 3.140: Mean of tofwdz for π^+ in the $+-$ field, sector W2

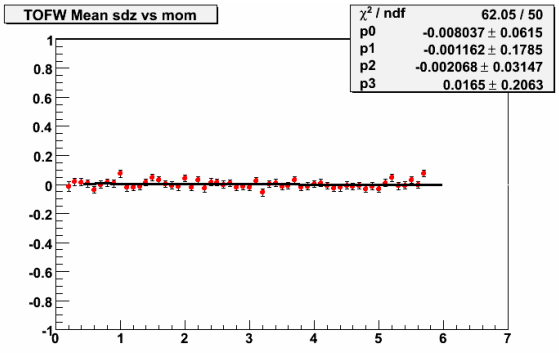

Figure 3.141: Mean of tofwsdz for π^+ in the $+-$ field, sector W2

Sigma of tofwdz for π^+ in the $+-$ field

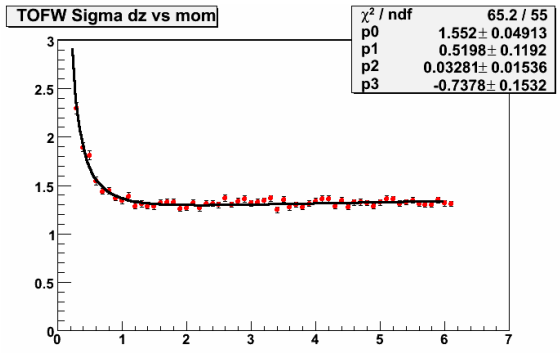

Figure 3.142: Sigma of tofwdz for π^+ in the $+-$ field, sector W1

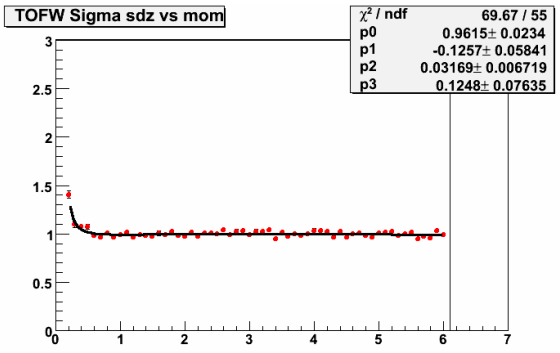

Figure 3.143: Sigma of tofwsdz for π^+ in the $+-$ field, sector W1

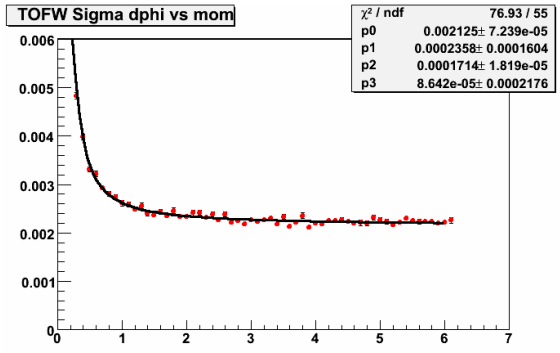

Figure 3.144: Sigma of tofwdz for π^+ in the $+-$ field, sector W2

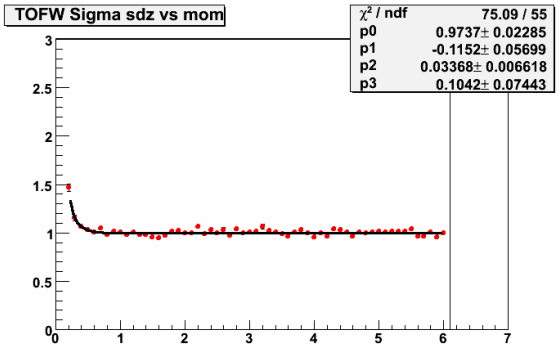

Figure 3.145: Sigma of tofwsdz for π^+ in the $+-$ field, sector W2

Mean of pc3dphi for π^+ in the ++ field

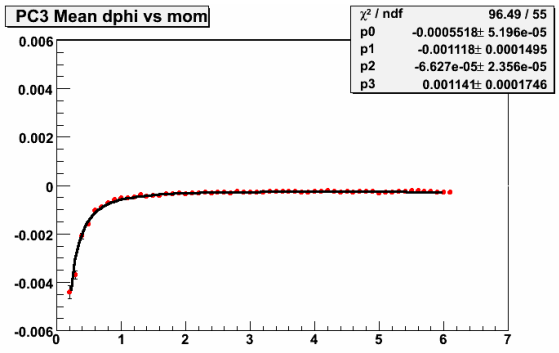

Figure 3.146: Mean of pc3dphi for π^+ in the ++ field, sector W1

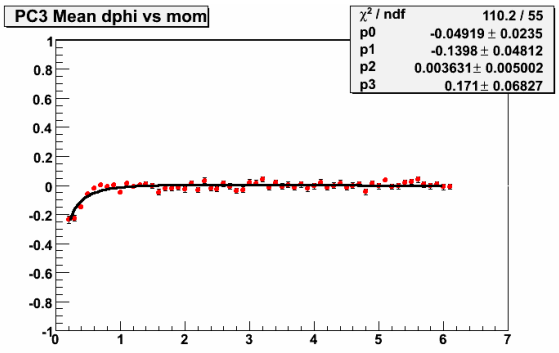

Figure 3.147: Mean of pc3sdphi for π^+ in the ++ field, sector W1

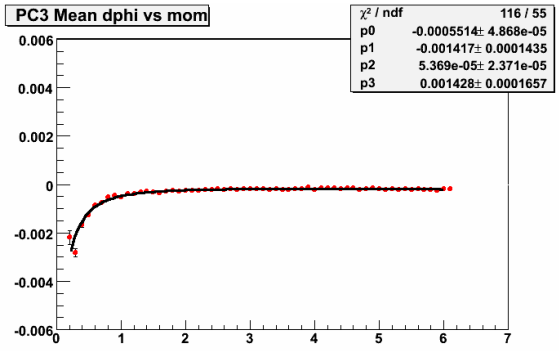

Figure 3.148: Mean of pc3dphi for π^+ in the ++ field, sector W2

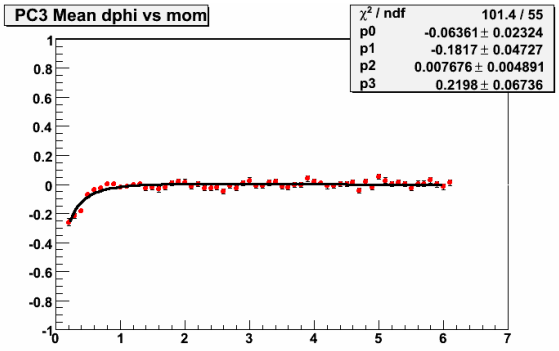

Figure 3.149: Mean of pc3sdphi for π^+ in the ++ field, sector W2

Sigma of pc3dphi for π^+ in the $++$ field

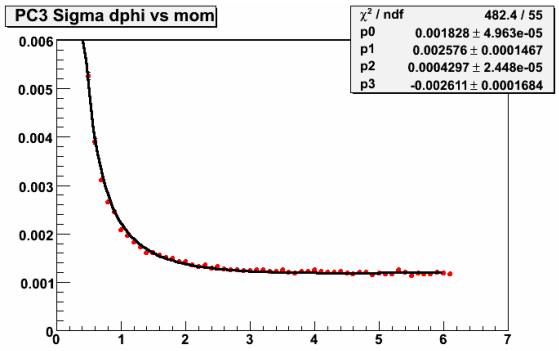

Figure 3.150: Sigma of pc3dphi for π^+ in the $++$ field, sector W1

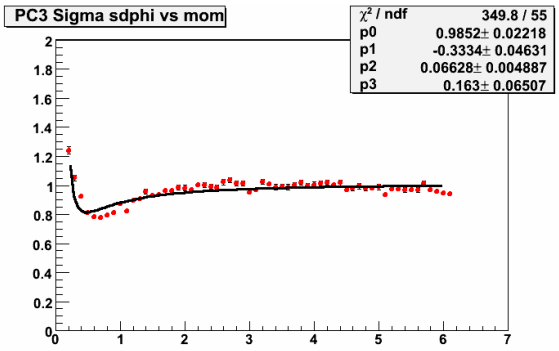

Figure 3.151: Sigma of pc3sdphi for π^+ in the $++$ field, sector W1

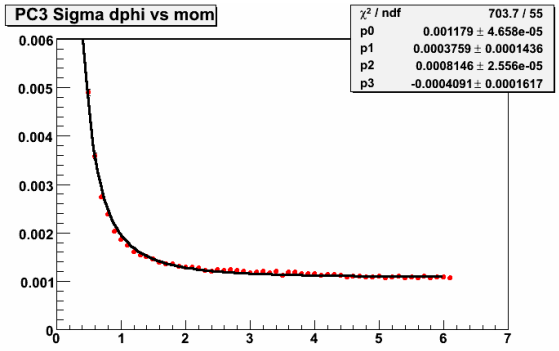

Figure 3.152: Sigma of pc3dphi for π^+ in the $++$ field, sector W2

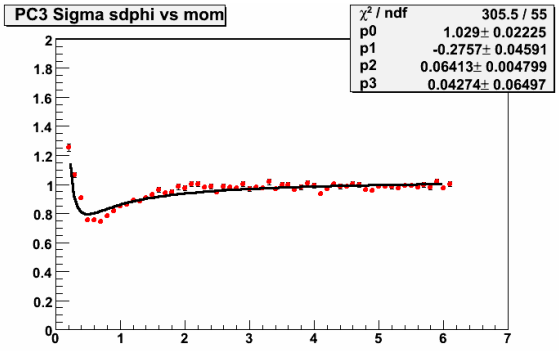

Figure 3.153: Sigma of pc3sdphi for π^+ in the $++$ field, sector W2

As can be seen from the preceding figures, the tuned means are consistent with zero. The standard deviations are consistent with unity at intermediate and high p_T but require a small amount of retuning at low p_T. The retuning is not shown but brings the standard deviations to within a few percent of unity. The uncertainty from this small deviation is extremely small, since a variation of 10% on the standard deviation would result in variation of roughly 1% of the confidence level for an integral over 2 standard deviations. To be specific, the confidence level for 2.0 standard deviations is 95.45%; the confidence level for 1.9 standard deviations is 94.26%; and the confidence level for 2.1 standard deviations is 96.43%. Therefore, if the standard deviation of our sigmalized residual is off by 10%, our yield is only affected by about 1%. If the standard deviation of our sigmalized residual is off by a few percent, the effect on our yield is negligible.

3.2.3 Detector Occupancy Correction

The high multiplicity of particle production in central heavy ion interactions creates a phenomenon called detector occupancy, a state in which the final state particle density exceeds the detector segmentation. This excess, of course, leads to a loss in reconstruction efficiency, and it must be modeled using simulations with precisely known conditions to be corrected properly. The embedding procedure consists of taking a single MC track and merging it with, or embedding it in, a real event. One can then reconstruct the embedded event and compute the probability of recovering the embedded track; this probability is the embedding efficiency.

The TOFW embedding algorithm has been tested extensively and matches expectations for efficiencies. The results are consistent for different charges and magnetic field configurations, which is expected and has been seen in previous embedding studies, such as those done for the Run2 spectra. Additionally, the embedding efficiency slightly decreases with increasing particle mass but is consistent within errors, which also matches previous results.

Occupancy corrections are only needed for the Run7 Au+Au data. In d+Au collisions the event multiplicity is much, much lower, and no correction is needed.

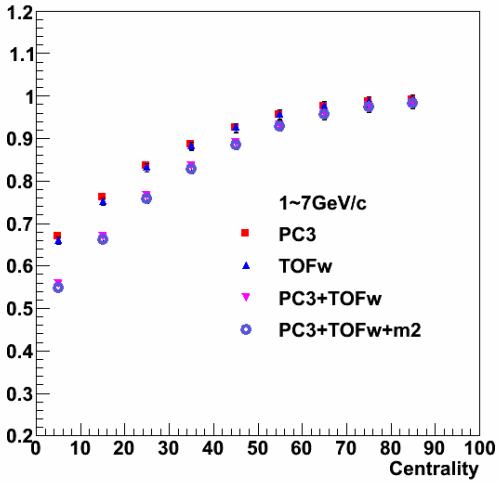

3.154 (a)

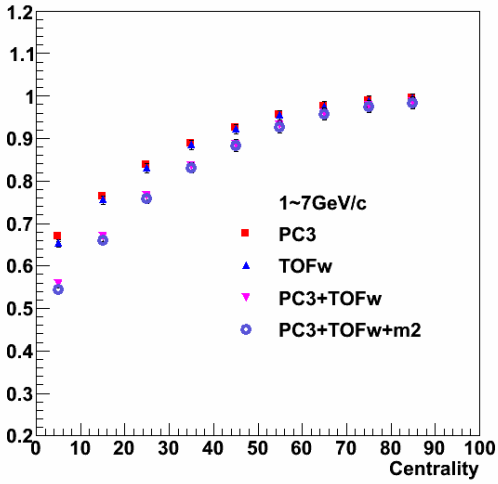

3.154 (b)

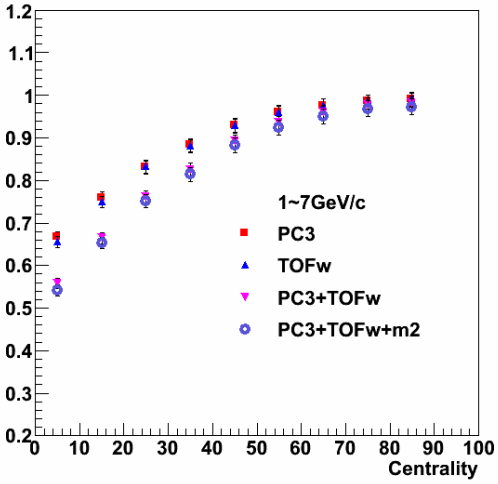

3.154 (c)

Figure 3.154: Embedding efficiencies for (a) pions, (b) kaons, (c) protons.

(a)

Cent	Eff	Err
0-10%	0.548893	0.00880221
10-20%	0.662735	0.00953364
20-30%	0.757962	0.0104718
30-40%	0.827697	0.011157
40-50%	0.88489	0.0117064
50-60%	0.929192	0.0121206
60-70%	0.956425	0.0124386
70-80%	0.974488	0.0124835
80-92%	0.982327	0.0126812

(b)

Cent	Eff	Err
0-10%	0.544422	0.00927691
10-20%	0.659825	0.0100399
20-30%	0.758137	0.0111331
30-40%	0.830143	0.0119109
40-50%	0.881734	0.0124252
50-60%	0.926603	0.0128705
60-70%	0.956888	0.0133055
70-80%	0.975305	0.013201
80-92%	0.982729	0.0133438

(c)

Cent	Eff	Err
0-10%	0.542065	0.0126423
10-20%	0.653215	0.0137354
20-30%	0.751339	0.0150791
30-40%	0.81413	0.0161309
40-50%	0.882178	0.0170243
50-60%	0.924843	0.0175984
60-70%	0.949757	0.0179427
70-80%	0.968341	0.0181093
80-92%	0.972655	0.0182228

Table 3.7: Embedding efficiencies for (a) pions, (b) kaons, (c) protons

3.2.4 TOFW Efficiency and ADC Cut Correction

The functionality of the TOFW is highly dependent on the high voltage between the electrodes of each MRPC. Because GEANT cannot simulate high electric fields in materials, neither the efficiency nor the ADC distribution in the TOFW can be adequately described by the simulations. Therefore, it is necessary to study these parameters using the real data. To estimate the ADC cut, we fill a 1-d histogram with the ADC value and take the ratio of the value integrated from 60 to 600 to the value integrated from 0 to 1000, including overflow but not underflow. To estimate the efficiency, we simply take the ratio of the number of tracks measured in the TOFW to the number of tracks passing through the TOFW. To estimate the number of tracks passing through the TOFW, we use a coincidence measurement of a hit in both the PC3 and PC2 with 3σ spatial track matching in each and hit locations overlapping with the TOFW fiducial volume. For the TOFW tracks, we further require the 4σ spatial track matching in the TOFW. As both a sanity check and a quick way to evaluate the systematics, we can compare the product of these two values to the efficiency measurement with the additional requirement of the standard ADC cut on the TOFW tracks. We find these two methods are quite consistent.

Table 3.8: TOFW efficiency and ADC cut estimates from in situ studies

Quantity	Value
Efficiency	90.9%
ADC cut	87.6%
Product	79.6%
Simultaneous	79.9%

3.2.5 Weak Decay Feeddown Correction

In order to ensure a fair comparison to other results, it is necessary correct the proton data for feeddown from hyperon decays. Due to the different acceptance for TOFE and TOFW, as well as effects caused by different magnetic field configurations (i.e. the field configuration was $+0$ and -0 for Run2 and Run3 while $+-$ and $-+$ for Run7 and $++$ and $--$ for Run8), the non-feeddown-corrected spectra will not have the same shape. To estimate the feeddown fraction, we analyzed 20 million simulated Λ events and determined the fraction of protons from the decay that fall into our PID cut window. To accurately account for the p_T shift, we fill the histograms with the reconstructed track p_T and with a weight of the form

$$W(p_T^{\text{track}}) = p_T e^{(m_T - m_0)/T}, \tag{3.7}$$

where all quantities on the R.H.S. are those of the parent Λ, so that the weight of a given track p_T is determined using the parent p_T as taken from the GEANT information in the TTree. This form is chosen to give the most accurate representation possible of what the actual input Λ spectrum would be. This fraction is then corrected for the branching ratio and the Λ/p ratio, which is taken to be 0.89 with m_T scaling [38, 130]. For the feeddown to antiprotons, we use the same data points but scale by the $\bar{p}/p$ and $\bar{\Lambda}/\Lambda$ ratios. In both Au+Au and d+Au the $\bar{p}/p$ ratio is taken to be 0.74 and the $\bar{\Lambda}/\Lambda$ ratio is taken to be 0.8 in Au+Au and 0.845 in d+Au, as prescribed in [135].

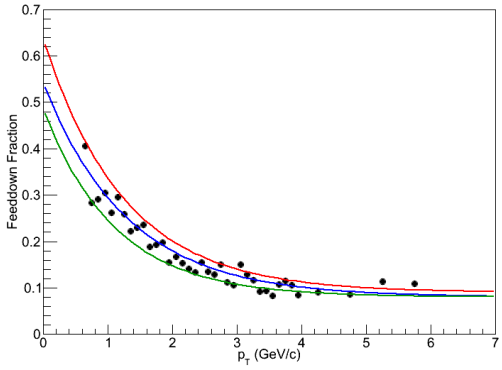

Figure 3.155: Feeddown fraction for Run7 acceptance

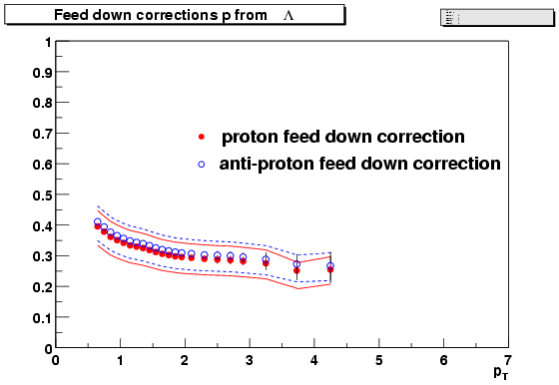

Figure 3.156: Feeddown fraction for Run2 acceptance

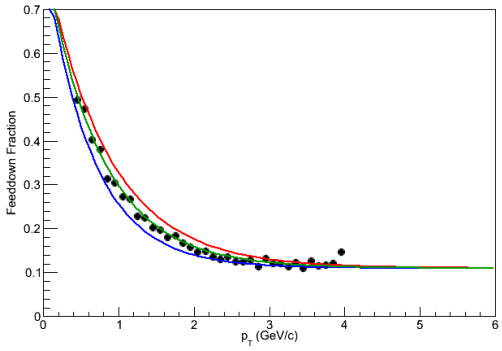

Figure 3.157: Feeddown fraction for Run8 acceptance

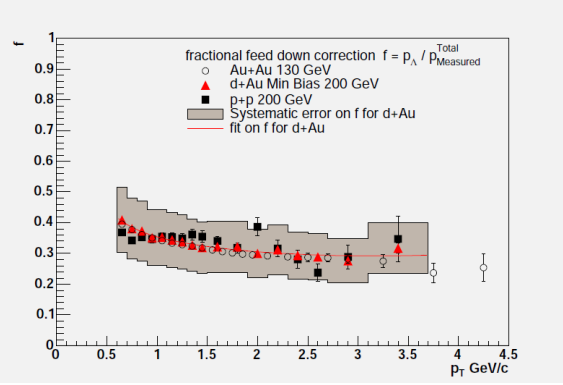

Figure 3.158: Feeddown fraction for Run3 acceptance

3.3 Systematic Uncertainty Estimations

To estimate the systematic uncertainty introduced by various cuts, one varies the cuts and examines the effect of the variations. The absolute value of the deviation of the ratio from unity is the percent difference between the two cuts, which can be used to assess the systematic uncertainty. In our case we are examining various quantities as a function of p_T, so we evaulate the uncertainty as a function of p_T as well.

In addition to analysis cuts, there are additional corrections applied to the data. The uncertainty introduced with these corrections can be evaluated in a variety of ways, depending on the method used to obtain the correction.

There are three basic types of systematic uncertainties: point-to-point uncorrelated; point-to-point correlated, which can change the shape of the spectrum in a smooth way as a function of p_T; and global or normalization, which can only move each point up or down by the same amount. In the PHENIX jargon, these are referred to as Type A, Type B, and Type C systematic uncertainties, respectively.

Because of the nature of analysis cuts, in that they affect the raw spectrum as a function of p_T, the systematic uncertainty associated with these is dominantly Type B. The same is true for any p_T dependent corrections. In this analysis, the only p_T dependendent correction is the weak-decay feeddown correction applied to the protons. In fact, these types of cuts and corrections can contribute to all three types of systematic uncertainties, although the effects on Type A and Type C uncertainties are both small and difficult to extract.

The p_T independent corrections, which are the various normalization correction terms, have Type C uncertainty only. It is conceivable for such a correction to have no associated

uncertainty. For example, we normalize to the number of events. The number of events for each magnetic field configuration in Run7 is in fact very slightly below the machine capacity of a 32 bit integer, which is 2,147,483,647 (compare to 2,136,153,235 events in the $+-$ field and 2,132,453,794 in the $-+$ field). The number of events for each magnetic field configuration in Run8 (1,378,825,610 for $++$ and 469,047,088 for $--$) is comfortably below the machine limit of 2,147,483,647 for a 32-bit integer. Moreover, the 9-10 significant figures in these numbers far exceeds the precision of the physical quantities being measured. Therefore the event number normalization is not considered to contribute systematic uncertainty. The same is true of the event normalization in the analysis of the simulations, which is likewise accurately countable to what is effectively arbitrary precision.

The rest of normalization corrections, such as the trigger efficiency and corrections for the TOFW efficiency and ADC distributions, do have associated uncertainty.

What about the Type A uncertainties? While in principle these are quite different from statistical uncertainties, in practice they have an indistinguishable effect and are therefore very difficult to determine using standard methods.

In previous studies of charged hadron yields (see AN187 [130] for PPG026 [38] and AN231 [131] for PPG030 [132]), the type of the sytematic uncertainties was not discussed. In that sense, our type determination is without precedent. The same is true of AN776 [133], although PPG101 [134] briefly mentions the uncertainty type: there, the uncertainties are described as Type B for the feeddown and PID uncertainties, and Type C for the others. However, the Type B and C uncertainties are summed in quadrature and presented as a single value. While the PID and feeddown corrections obviously have the strongest p_T dependence, the other analysis cuts do also affect the p_T shape. Therefore in

this study we describe all analysis cut correction uncertainties (as well as the feeddown) as Type B, and we quote the Type C uncertainties separately.

3.3.1 Executive Summary of Cuts and Corrections

The cuts and corrections are presented with the types of systematic uncertainties they present are given in Table 3.9.

Table 3.9: Uncertainties from Cuts and Corrections

Cut or Correction	Global	Point-to-point corr	Point-to-point uncorr
Trigger	Yes	No	No
Event Vertex	Yes	No	No
Detector Efficiencies	Yes	No	No
Detector Occupancy	Yes	No	No
Analysis cuts	Small	Yes	Small
Weak decay feed-down for p	Small	Yes	Small
TOFW specific			
Strip ID	Yes	No	No
Efficiency	Yes	No	No
ADC	Yes	No	No
PID	Small	Yes	Small

3.3.2 Systematic Uncertainty Estimates for Run7

3.3.2.1 DC fiducial cuts

Because of the severity of the drift chamber fiducial cuts, one needs to exercise great caution when assessing the associated systematic uncertainty. First we examine the effect of tightening the cuts by 5 mrad on each side of the active areas.

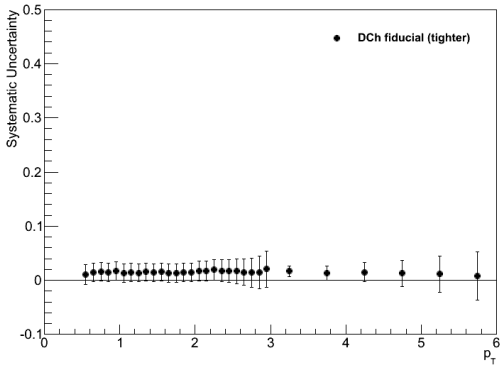

Figure 3.159: Relative uncertainty in DC fiducial cuts for π^+

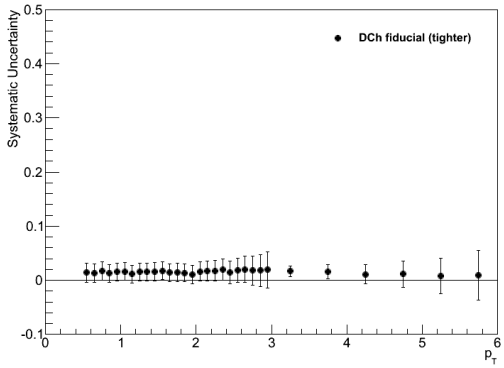

Figure 3.160: Relative uncertainty in DC fiducial cuts for π^-

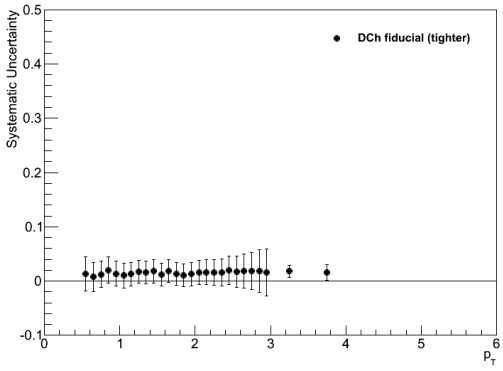

Figure 3.161: Relative uncertainty in DC fiducial cuts for K^+

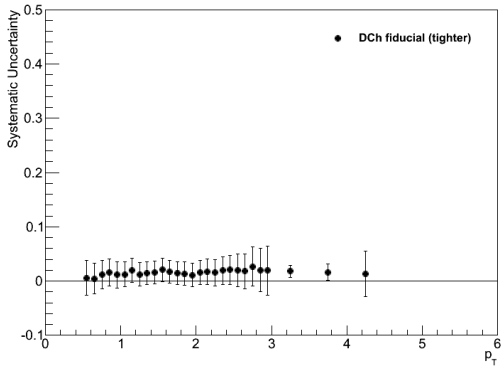

Figure 3.162: Relative uncertainty in DC fiducial cuts for K^-

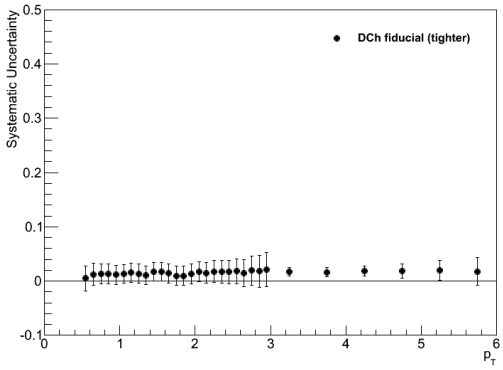

Figure 3.163: Relative uncertainty in DC fiducial cuts for p

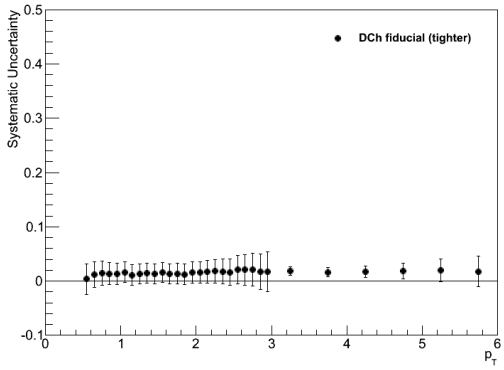

Figure 3.164: Relative uncertainty in DC fiducial cuts for $\bar{p}$

One clearly sees the apparent uncertainty is extremely small, despite a drastic increase in the severity of the cut. We see what appears to be a 2% uncertainty for all particles at all p_T. Next, as an additional check, we examine the affect of not making any fiducial cut at all while noting that the exact effect is reduced roughly by a factor of two owing to the fact that the active areas are reversed for each charge when the magnetic field is in the reverse configuration, which is true for approximately 50% of the data.

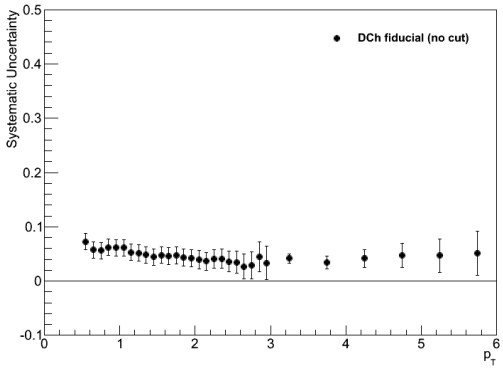

Figure 3.165: Relative uncertainty (maximal) in DC fiducial cuts for π^+

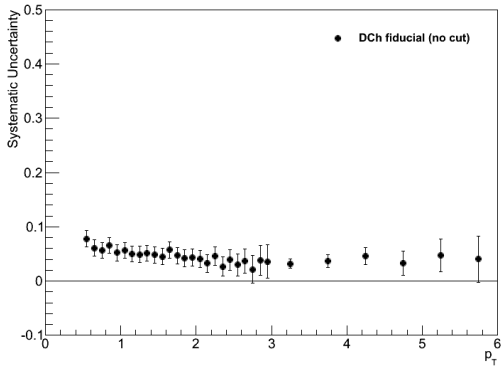

Figure 3.166: Relative uncertainty (maximal) in DC fiducial cuts for π^-

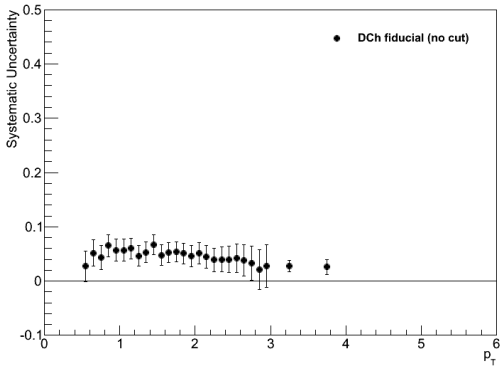

Figure 3.167: Relative uncertainty (maximal) in DC fiducial cuts for K^+

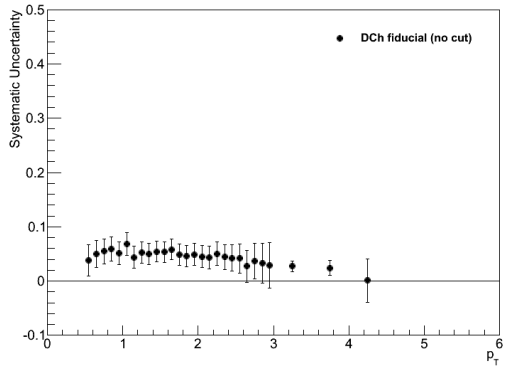

Figure 3.168: Relative uncertainty (maximal) in DC fiducial cuts for K^-

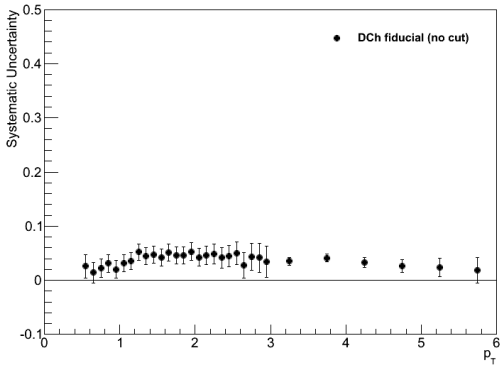

Figure 3.169: Relative uncertainty (maximal) in DC fiducial cuts for p

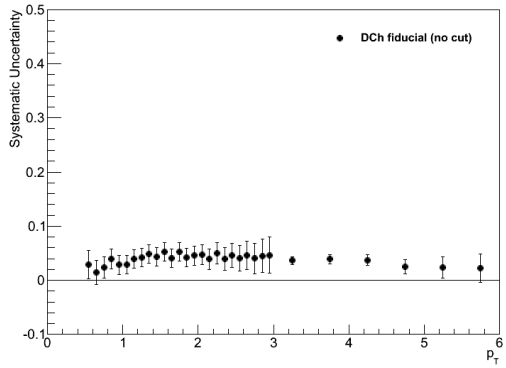

Figure 3.170: Relative uncertainty (maximal) in DC fiducial cuts for $\bar{p}$

Here we see the very significant effects of the cut, which makes the small uncertainty all the more remarkable. In the interest of caution we assign a 5% uncertainty for all particles at all p_T.

3.3.2.2 DC Zed cut

To estimate the uncertainty introduced by the DC zed cut, we compared our 3 cm $<$ $|z_{DC}|$ $<$ 70 cm cut used in the analysis to a 3 cm $<$ $|z_{DC}|$ $<$ 40 cm.

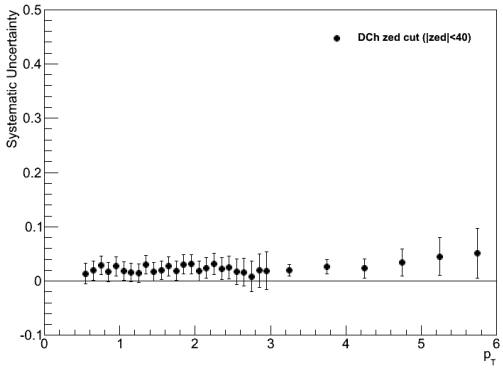

Figure 3.171: Relative uncertainty in DC Zed cut for π^+

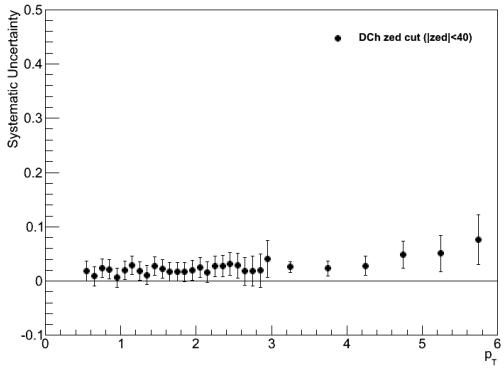

Figure 3.172: Relative uncertainty in DC Zed cut for π^-

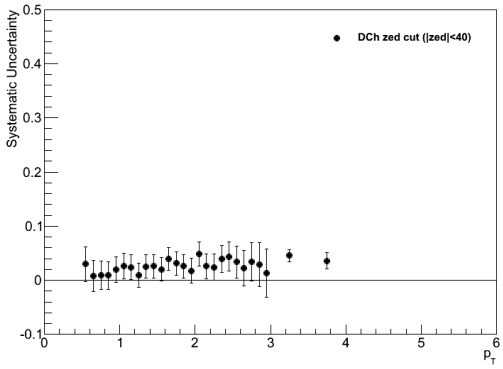

Figure 3.173: Relative uncertainty in DC Zed cut for K^+

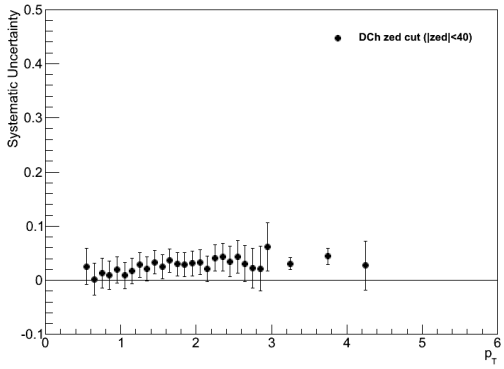

Figure 3.174: Relative uncertainty in DC Zed cut for K^-

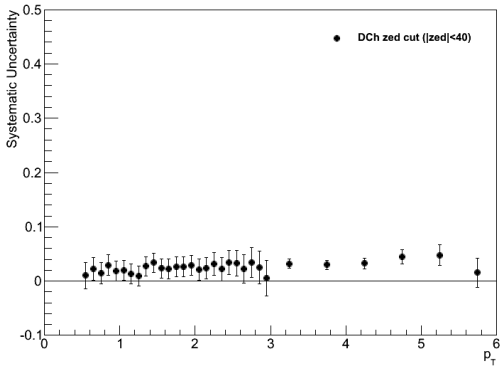

Figure 3.175: Relative uncertainty in DC Zed cut for p

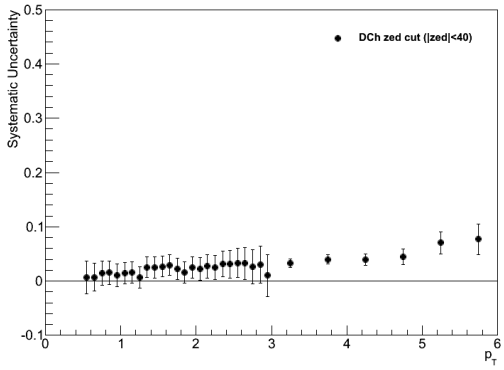

Figure 3.176: Relative uncertainty in DC Zed cut for $\bar{p}$

The uncertainty associated with the DC zed cut appears to be fairly small and largely indepent of particles species. While in unidentified charged hadron analyses a very tight DC zed cut has been found to significantly reduce background, that does not appear to be the case here. The systematic uncertainty for this cut is rolled into the DC fiducial cut, to which it is strongly related.

3.3.2.3 Track Matching cuts

To estimate the uncertainty introduced by the track matching cuts, we compared our 2σ cuts used in the analysis to 1.5σ cuts.

First we look at the PC3 track matching.

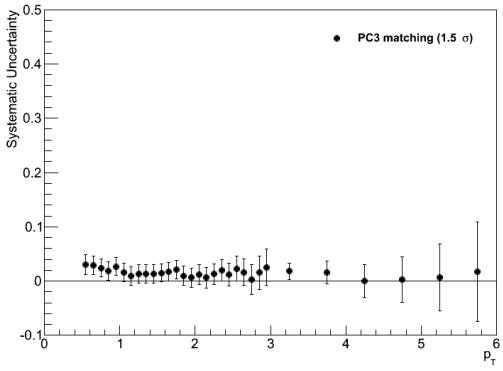

Figure 3.177: Relative uncertainty in PC3 track matching cut for π^+

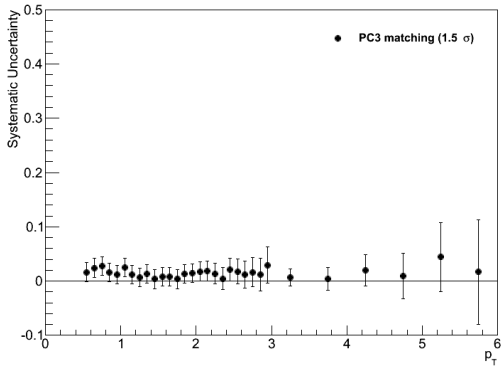

Figure 3.178: Relative uncertainty in PC3 track matching cut for π^-

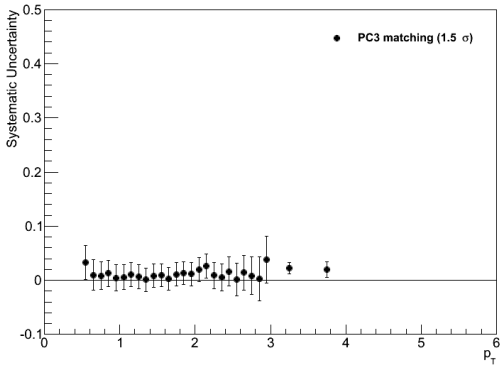

Figure 3.179: Relative uncertainty in PC3 track matching cut for K^+

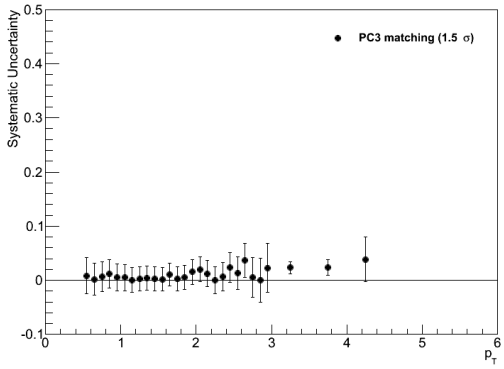

Figure 3.180: Relative uncertainty in PC3 track matching cut for K^-

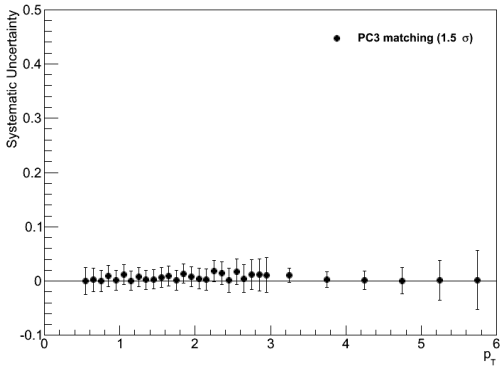

Figure 3.181: Relative uncertainty in PC3 track matching cut for p

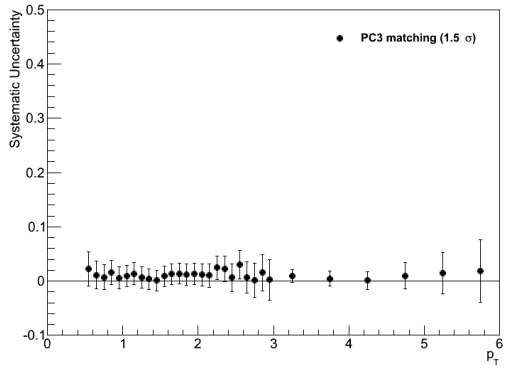

Figure 3.182: Relative uncertainty in PC3 track matching cut for $\bar{p}$

The uncertainty associated with the PC3 track matching appears to be quite small for all particles at all p_T. The uncertainty is assessed to be 2% for all particle species at all p_T.

Now we look at the TOFW track matching.

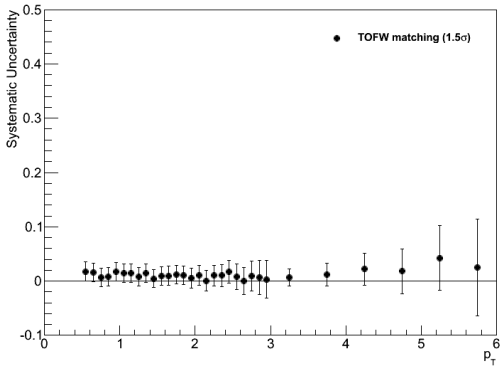

Figure 3.183: Relative uncertainty in TFW track matching cut for π^+

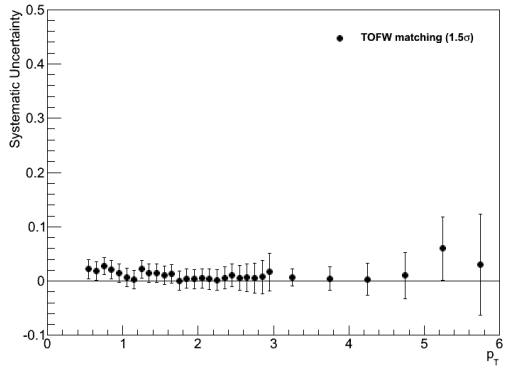

Figure 3.184: Relative uncertainty in TFW track matching cut for π^-

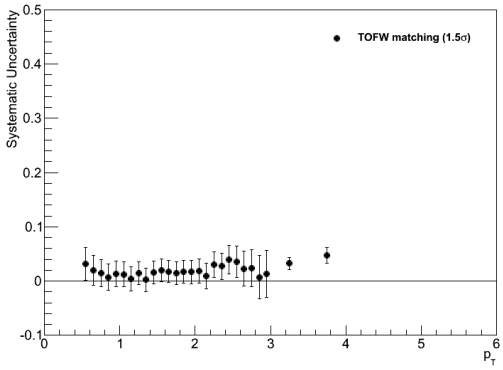

Figure 3.185: Relative uncertainty in TFW track matching cut for K^+

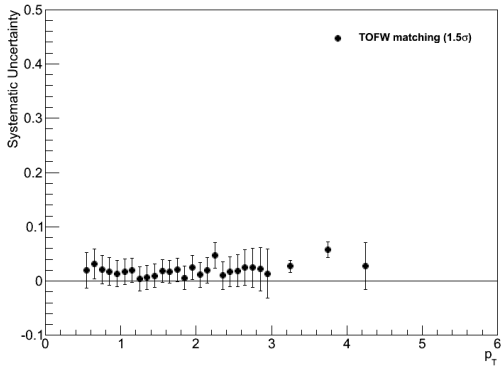

Figure 3.186: Relative uncertainty in TFW track matching cut for K^-

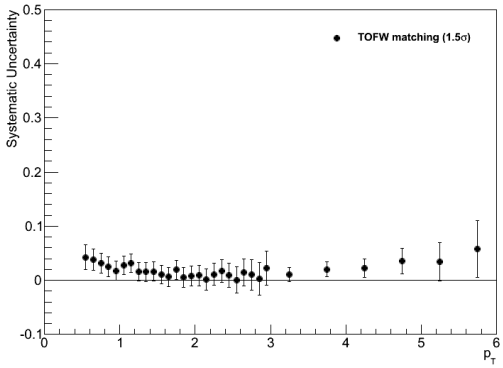

Figure 3.187: Relative uncertainty in TFW track matching cut for p

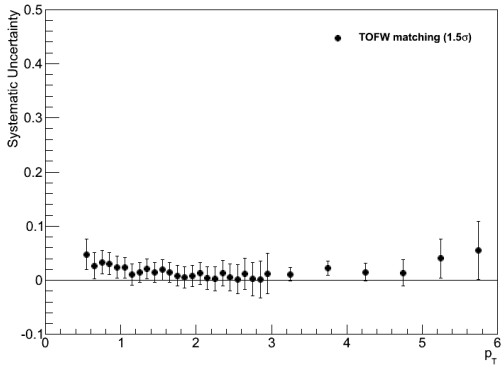

Figure 3.188: Relative uncertainty in TFW track matching cut for $\bar{p}$

The uncertainty associated with the TOFW track matching is somewhat more pronounced. The uncertainty is assessed to be 5% for all particles at all p_T.

3.3.2.4 PC fiducial cuts

To estimate the uncertainty associated with the PC1 and PC3 fiducial cuts, we examine the effect of tightening the cuts by 5 mrad in the ϕ-direction and 2 cm in the z-direction.

First we look at PC1.

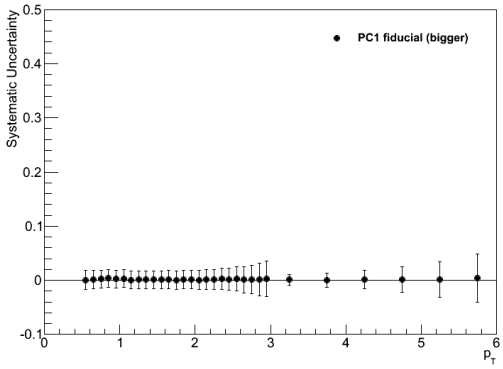

Figure 3.189: Relative uncertainty in PC1 fiducial cut for π^+

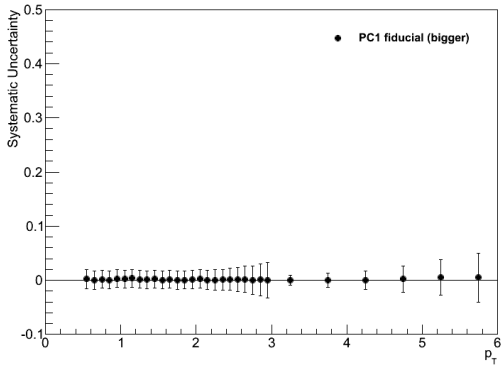

Figure 3.190: Relative uncertainty in PC1 fiducial cut for π^-

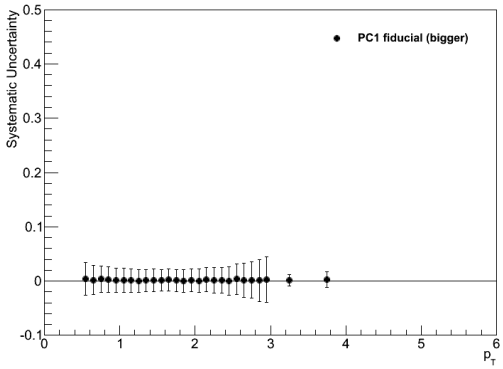

Figure 3.191: Relative uncertainty in PC1 fiducial cut for K^+

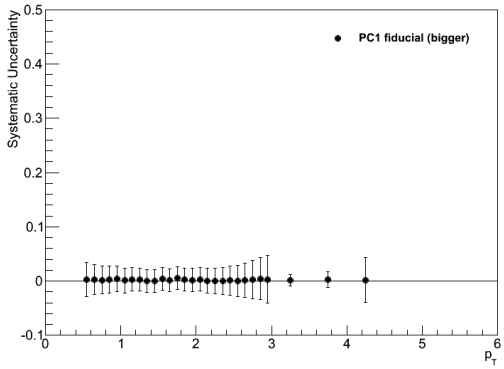

Figure 3.192: Relative uncertainty in PC1 fiducial cut for K^-

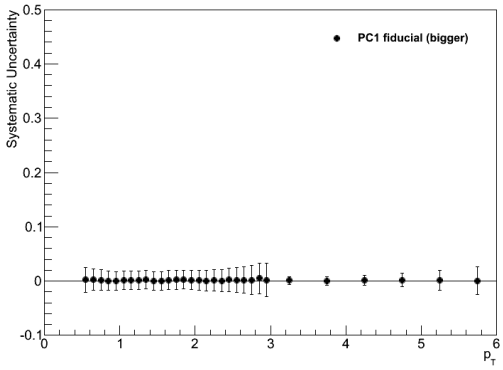

Figure 3.193: Relative uncertainty in PC1 fiducial cut for p

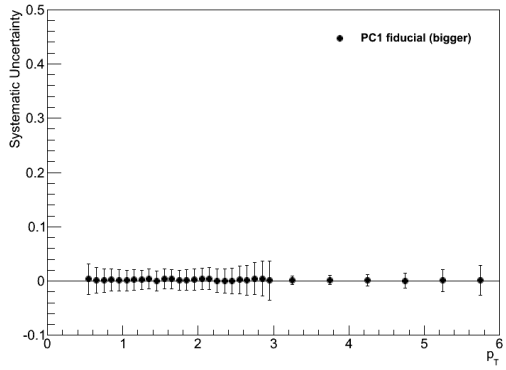

Figure 3.194: Relative uncertainty in PC1 fiducial cut for $\bar{p}$

Now we look at PC3.

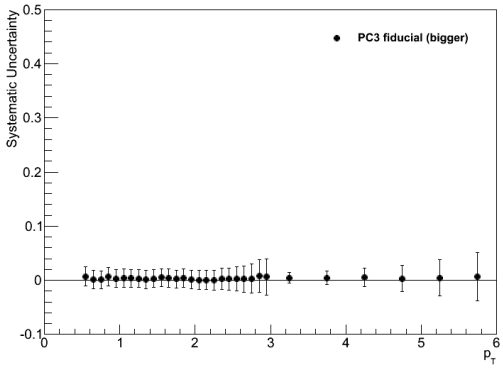

Figure 3.195: Relative uncertainty in PC3 fiducial cut for π^+

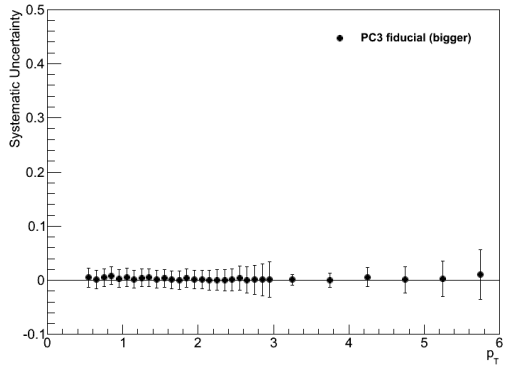

Figure 3.196: Relative uncertainty in PC3 fiducial cut for π^-

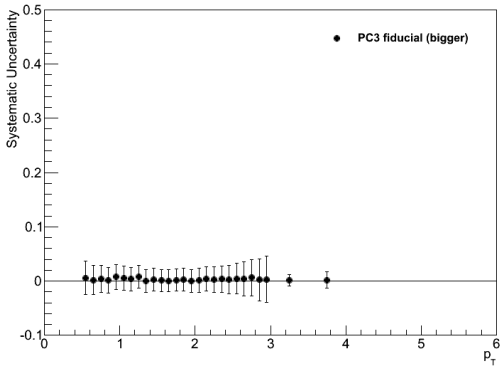

Figure 3.197: Relative uncertainty in PC3 fiducial cut for K^+

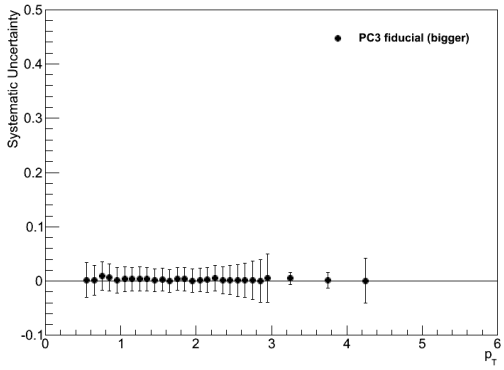

Figure 3.198: Relative uncertainty in PC3 fiducial cut for K^-

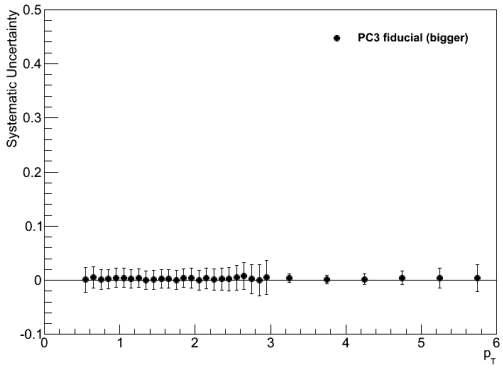

Figure 3.199: Relative uncertainty in PC3 fiducial cut for p

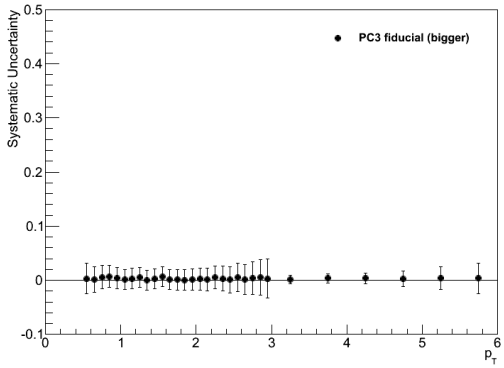

Figure 3.200: Relative uncertainty in PC3 fiducial cut for $\bar{p}$

For both PC1 and PC3 we find the systematic uncertainty associated with the fiducial cuts is not only completely independent of particle species, it is almost completely negligible altogether. It is assessed to be 1% for each cut.

3.3.2.5 PID functions, part I

To estimate the systematic uncertainty associated with the PID functions, first we vary the parameters of the analytical parametrization as discussed in the section on the PID functions.

First we look at the set of parameters from the fit.

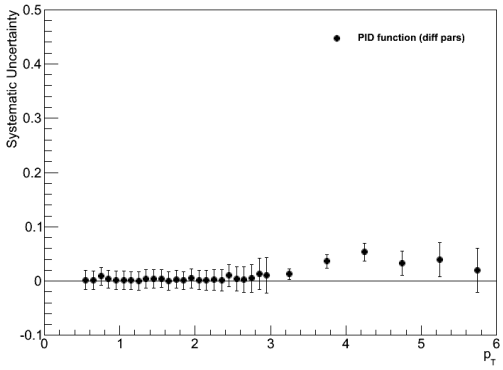

Figure 3.201: Relative uncertainty in PID cut for π^+

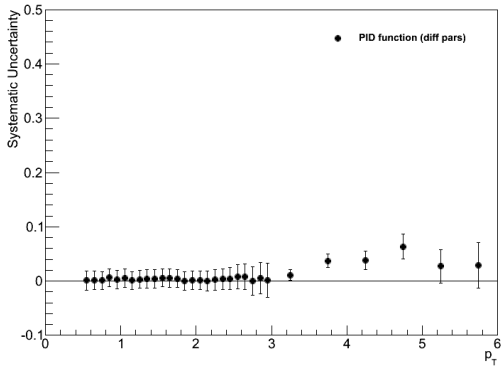

Figure 3.202: Relative uncertainty in PID cut for π^-

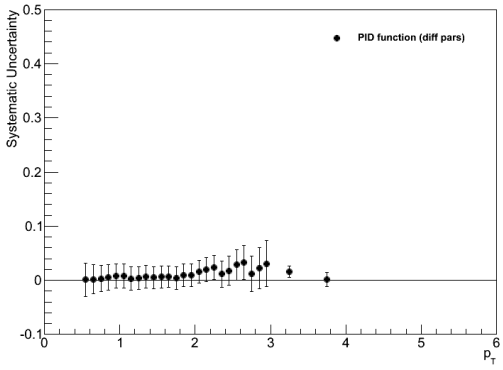

Figure 3.203: Relative uncertainty in PID cut for K^+

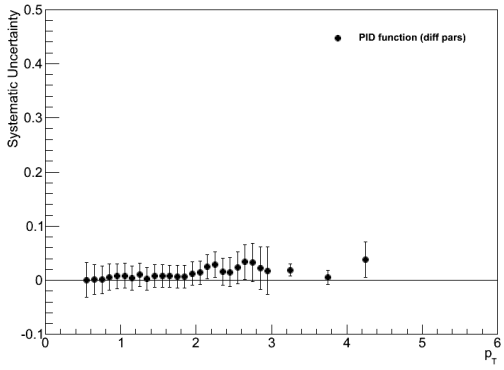

Figure 3.204: Relative uncertainty in PID cut for K^-

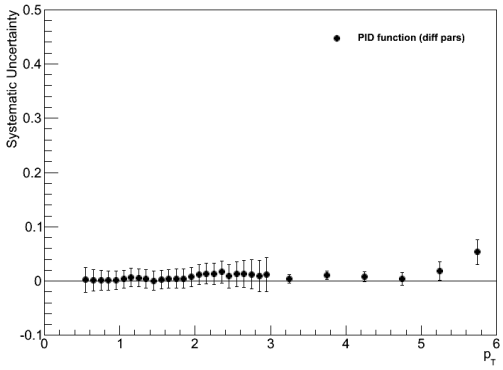

Figure 3.205: Relative uncertainty in PID cut for p

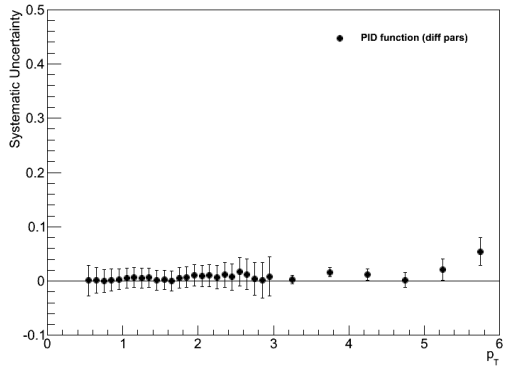

Figure 3.206: Relative uncertainty in PID cut for $\bar{p}$

Now we look at the alternate set of parameters.

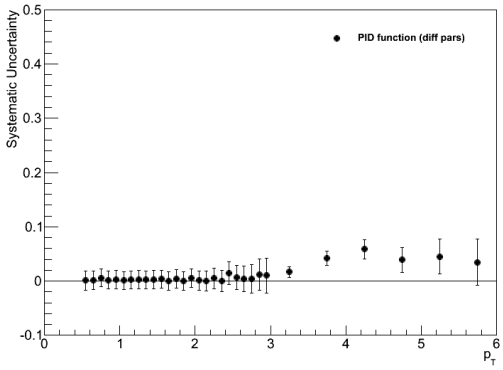

Figure 3.207: Relative uncertainty in PID cut for π^+

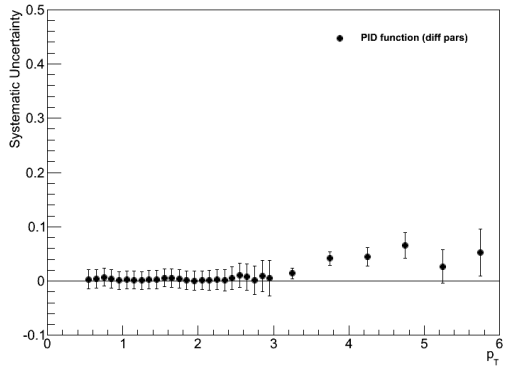

Figure 3.208: Relative uncertainty in PID cut for π^-

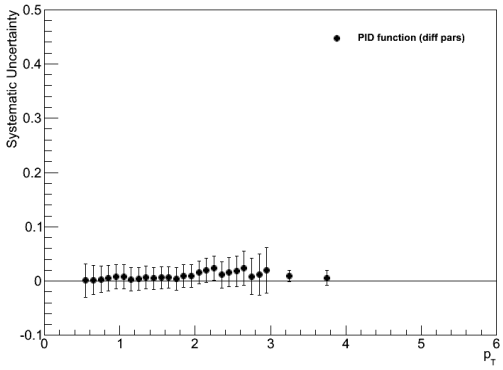

Figure 3.209: Relative uncertainty in PID cut for K^+

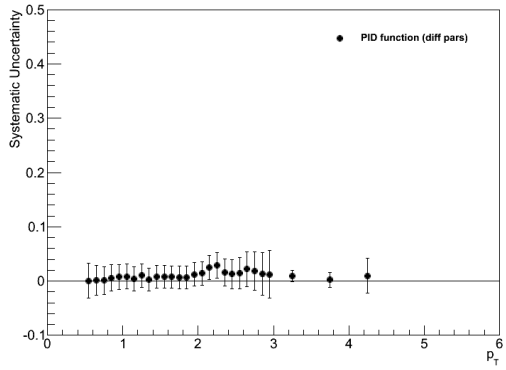

Figure 3.210: Relative uncertainty in PID cut for K^-

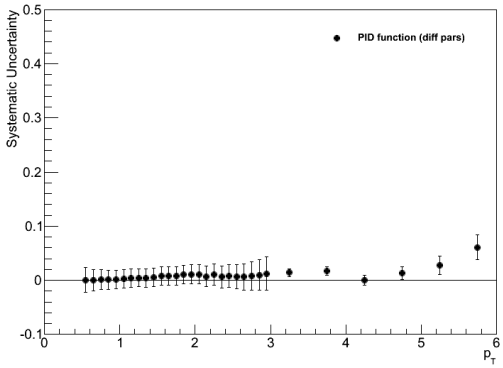

Figure 3.211: Relative uncertainty in PID cut for p

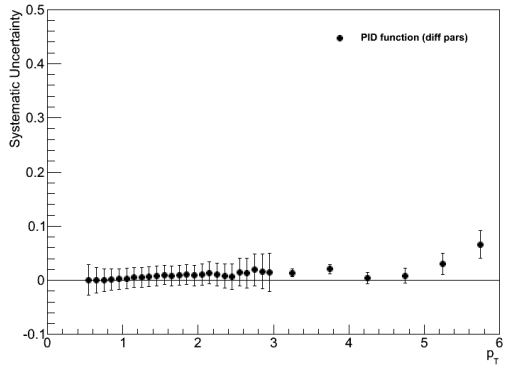

Figure 3.212: Relative uncertainty in PID cut for $\bar{p}$

For both sets of parameters we find reasonable consistency with the default set. For the moment we do not assess any uncertainty in the PID function based on the parameters, instead we alter the cut itself and examine the effects of doing so in the next section.

3.3.2.6 PID functions, part II

To estimate the systematic uncertainty associated with the PID functions, we tighten the cut in one of two ways. First, we change the window from 2 to 1.5 sigma but leave the veto alone at 2 sigma. Second, we leave the window alone at 2 sigma but change the veto from 2 to 2.5 sigma.

First the change in window.

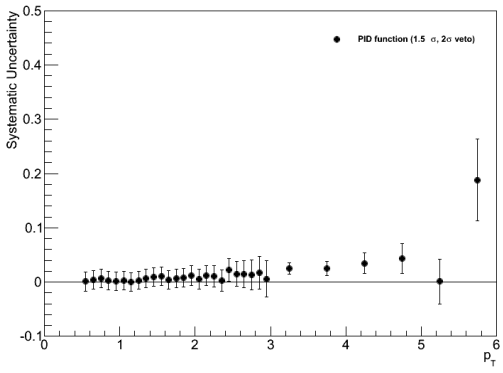

Figure 3.213: Relative uncertainty in PID cut for π^+

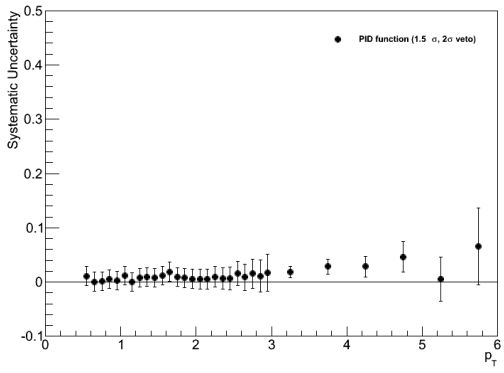

Figure 3.214: Relative uncertainty in PID cut for π^-

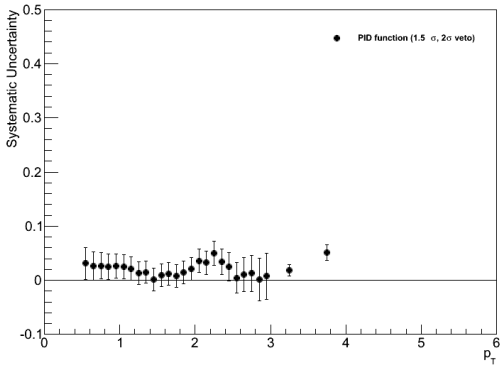

Figure 3.215: Relative uncertainty in PID cut for K^+

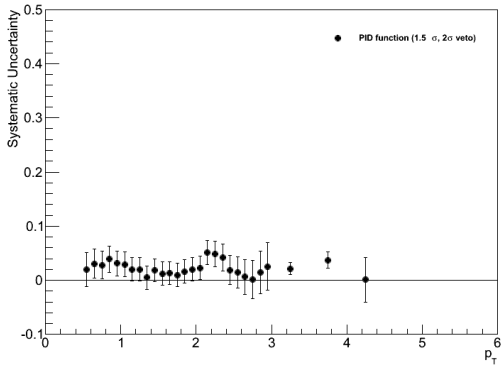

Figure 3.216: Relative uncertainty in PID cut for K^-

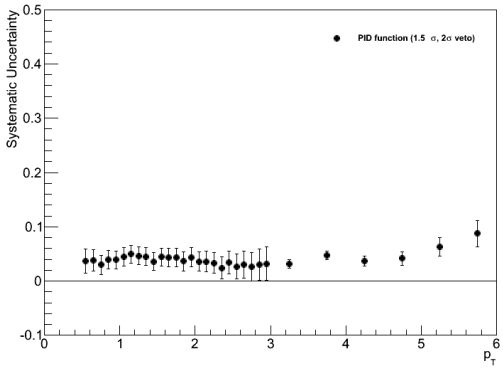

Figure 3.217: Relative uncertainty in PID cut for p

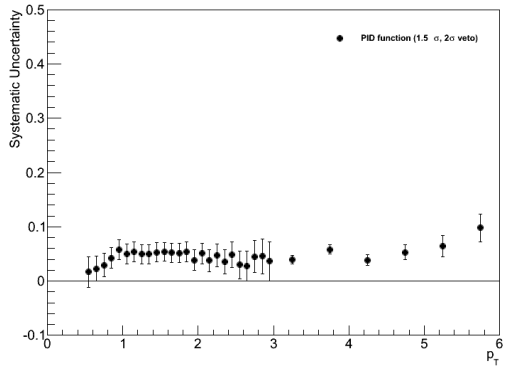

Figure 3.218: Relative uncertainty in PID cut for $\bar{p}$

For the change in PID window we find some mass dependent effects, with the protons exhibiting more apparent uncertainty than the kaons and pions. Additionally, the uncertainty in the window appears to be higher at high p_T above the PID crossover point. The uncertainty above the crossover point is likely influenced by the veto, indicating these two effects may be difficult to disentangle.

We assess a 2% uncertainty for pions for 0–3 GeV/c, a 5% uncertainty for kaons at all p_T, and a 5% uncertainty for protons at 0–3 GeV/c. The PID uncertainty for pions and protons at high p_T will be considered when examining the change in veto.

Next the change in veto.

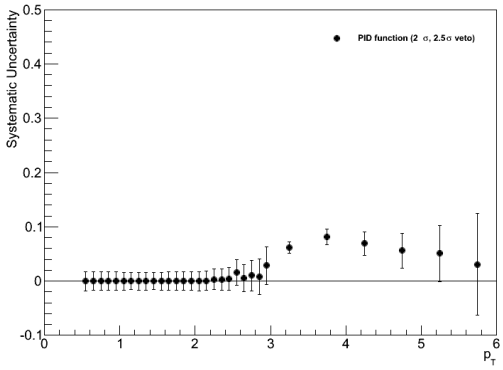

Figure 3.219: Relative uncertainty in PID cut for π^+

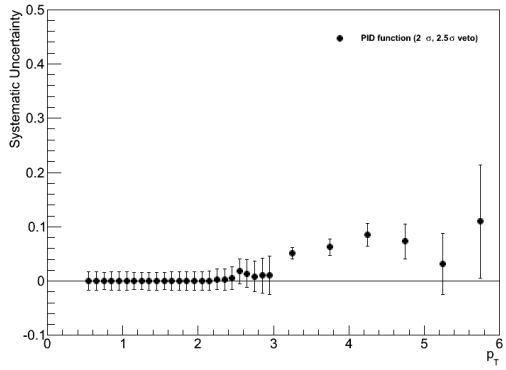

Figure 3.220: Relative uncertainty in PID cut for π^-

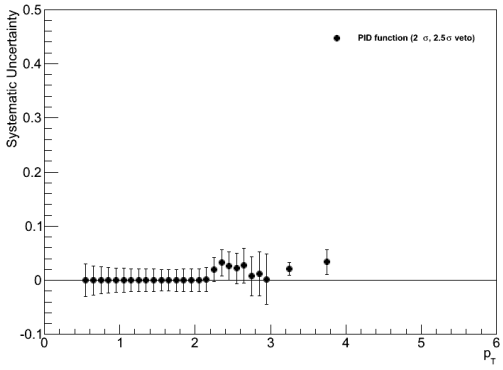

Figure 3.221: Relative uncertainty in PID cut for K^+

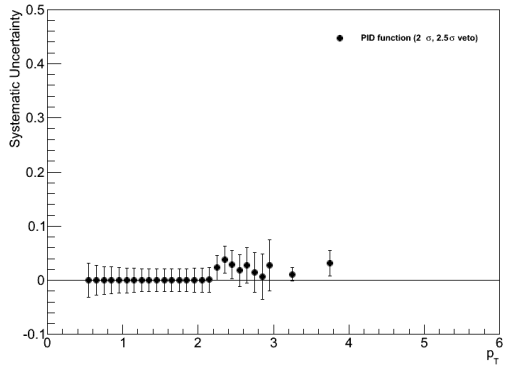

Figure 3.222: Relative uncertainty in PID cut for K^-

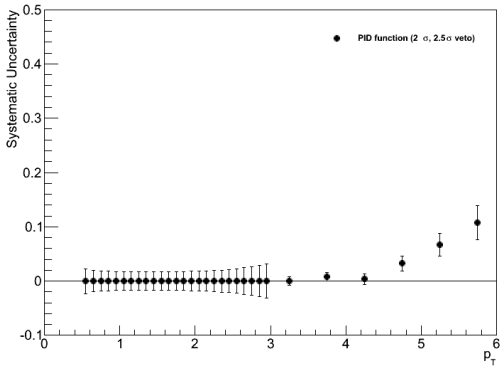

Figure 3.223: Relative uncertainty in PID cut for p

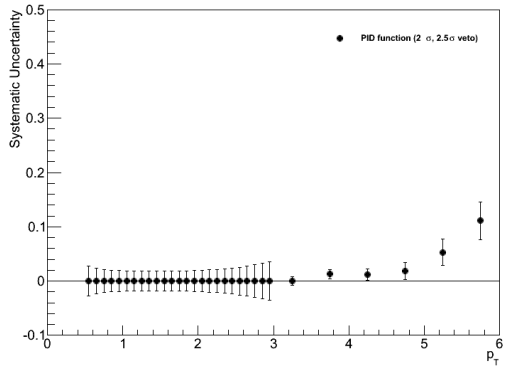

Figure 3.224: Relative uncertainty in PID cut for $\bar{p}$

In this comparision, we find absolutely no deviations below the pid crossover bands, which is to be expected. We also find significant deviatons above these points. We assess the uncertainty to be 5% for all particles.

Taking into consideration now both the window and veto together, we can assess final PID uncertainties. For pions the uncertainty is assessed to be 2% for 0–3 GeV/c and 5% for 3–6 GeV/c. For kaons the uncertainty is assessed to be 7%. For protons the uncertainty is assessed to be 5% for 0–3 GeV/c and 7% for 3–6 GeV/c.

3.3.2.7 EP cut

To estimate the systematic uncertainty associated with the $ecore/p_T > X$ cut, we vary the cut from $X = 0.2$ to 0.15 in one case and 0.25 in the other case.

First we look at $X = 0.15$.

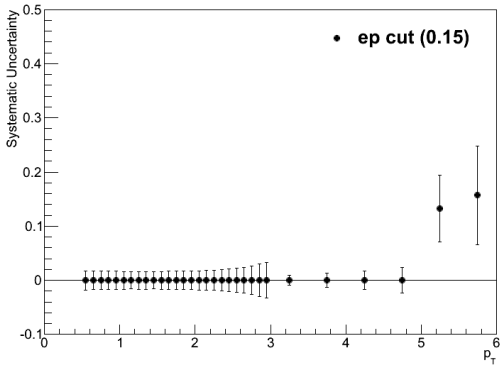

Figure 3.225: Relative uncertainty in EP cut for π^+

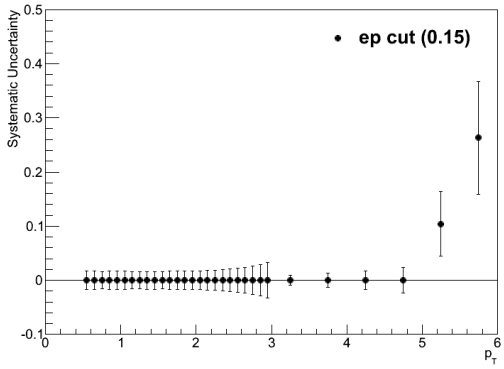

Figure 3.226: Relative uncertainty in EP cut for π^-

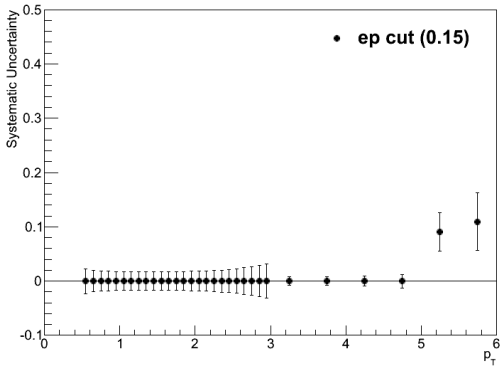

Figure 3.227: Relative uncertainty in EP cut for p

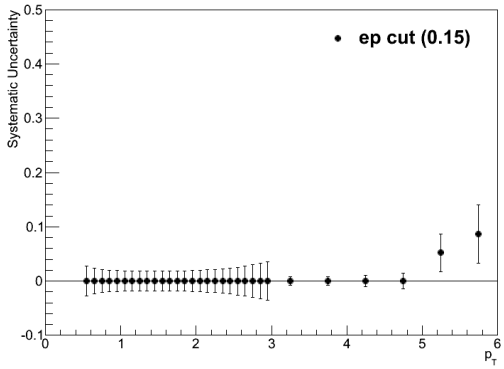

Figure 3.228: Relative uncertainty in EP cut for $\bar{p}$

In this comparison we see large differences, which could be due to a variety of factors,

including the uncertainty of the EMCal response in GEANT.

Next we look at $X = 0.25$.

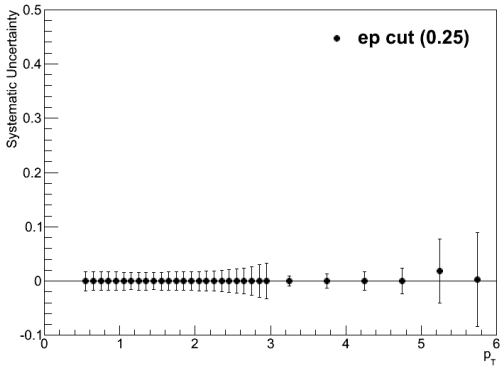

Figure 3.229: Relative uncertainty in EP cut for π^+

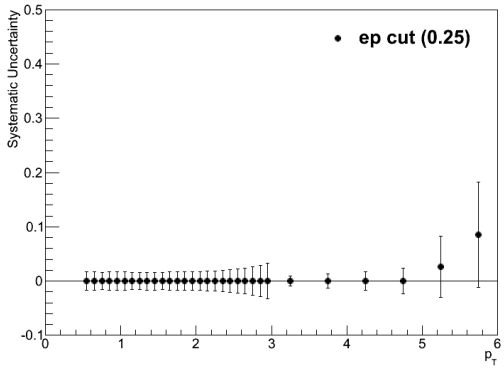

Figure 3.230: Relative uncertainty in EP cut for π^-

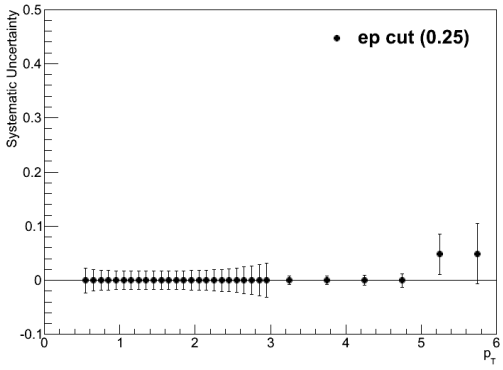

Figure 3.231: Relative uncertainty in EP cut for p

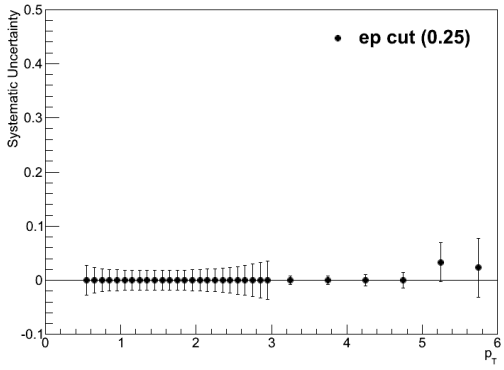

Figure 3.232: Relative uncertainty in EP cut for $\bar{p}$

Again we see fairly large differences. In the interest of caution we assess a 10% uncertainty for all $p_T > 5.0$ GeV/c for pions and protons. The cut is not applied to kaons for the final analysis and therefore no uncertainty is assessed.

3.3.3 Systematic Uncertainty Estimates for Run8

3.3.3.1 DC fiducial cuts

Because of the severity of the drift chamber fiducial cuts, one needs to exercise great caution when assessing the associated systematic uncertainty. First we examine the effect of tightening the cuts by 5 mrad on each side of the active areas.

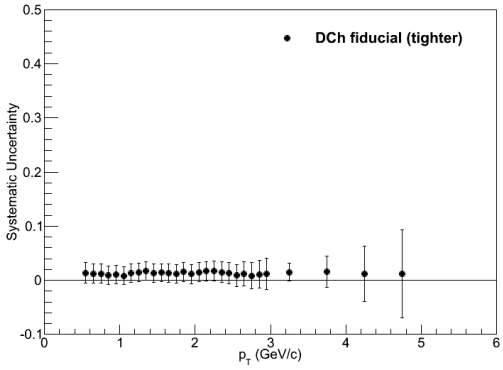

Figure 3.233: Relative uncertainty in DC fiducial cuts for π^+

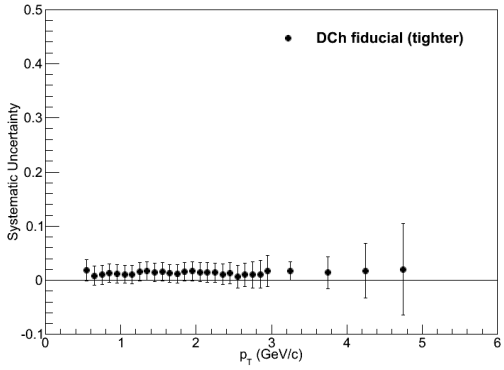

Figure 3.234: Relative uncertainty in DC fiducial cuts for π^-

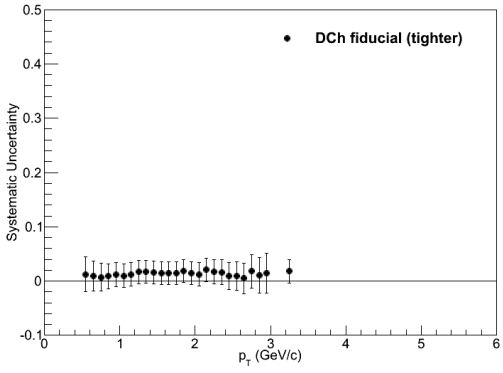

Figure 3.235: Relative uncertainty in DC fiducial cuts for K^+

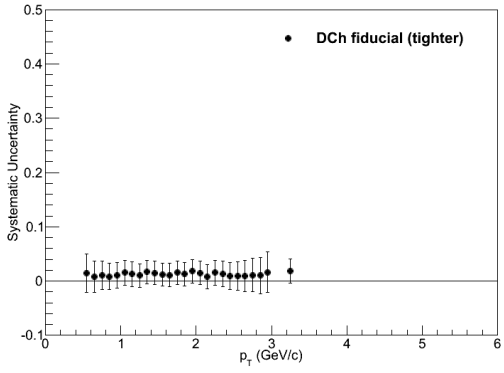

Figure 3.236: Relative uncertainty in DC fiducial cuts for K^-

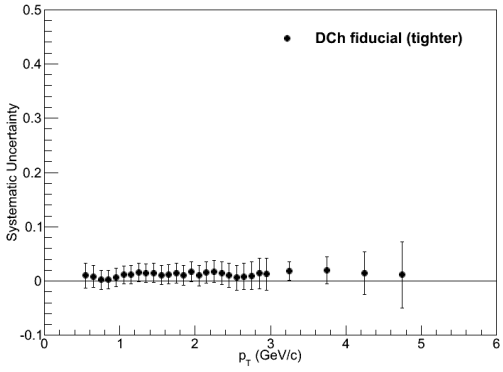

Figure 3.237: Relative uncertainty in DC fiducial cuts for p

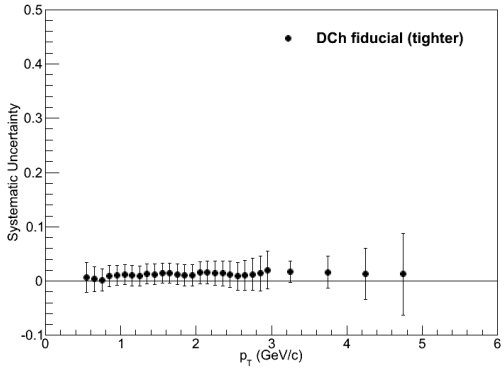

Figure 3.238: Relative uncertainty in DC fiducial cuts for $\bar{p}$

One clearly sees the apparent uncertainty is extremely small. There is no apparent p_T dependence but there is a systematic offset. Discretion suggests that, given the severity of the DC fiducial cuts, this may be an understatement of the uncertainty. Next we examine the affect of not making any fiducial cut at all. For the Run8dAu, roughly 75% of the data is in the $++$ magnetic field configuration with the remaining 25% being in the $--$ configuration. This results in a small but non-negligible reduction in the appearance of the lack of DC fiducial cuts in the succeeding figures.

Here we see very significant deviations, which are of course systematic effects, not systematic uncertainties. However, we can definitely now see that there is some significant p_T dependence to the correction. In addition to the aforementioned 2% global systematic uncertainty, we assign a 5% systematic uncertainty for all species at all p_T.

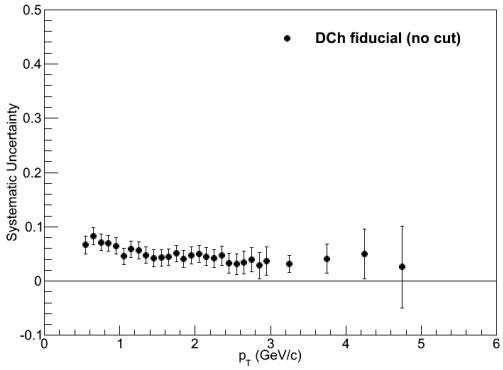

Figure 3.239: Relative uncertainty (maximal) in DC fiducial cuts for π^+

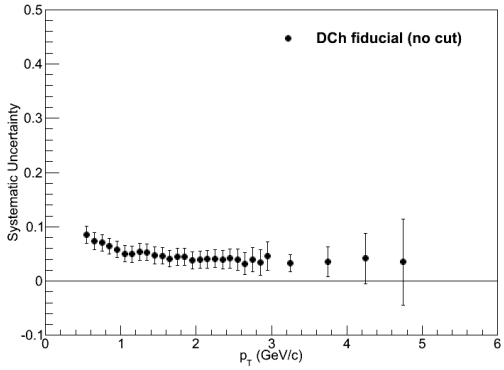

Figure 3.240: Relative uncertainty (maximal) in DC fiducial cuts for π^-

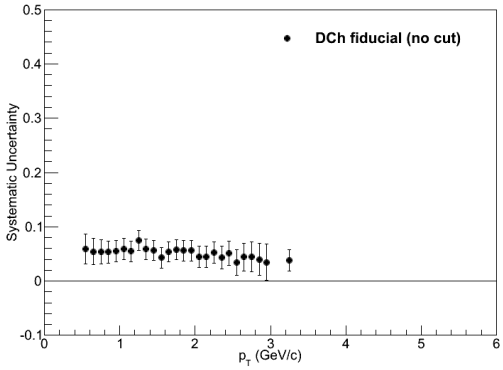

Figure 3.241: Relative uncertainty (maximal) in DC fiducial cuts for K^+

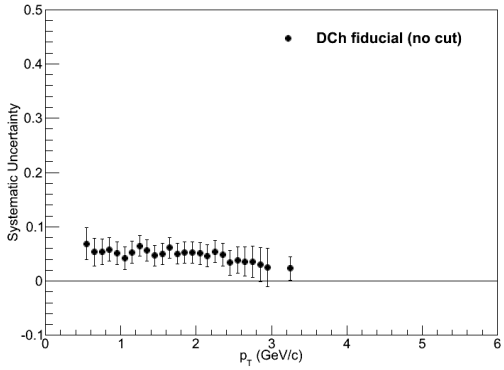

Figure 3.242: Relative uncertainty (maximal) in DC fiducial cuts for K^-

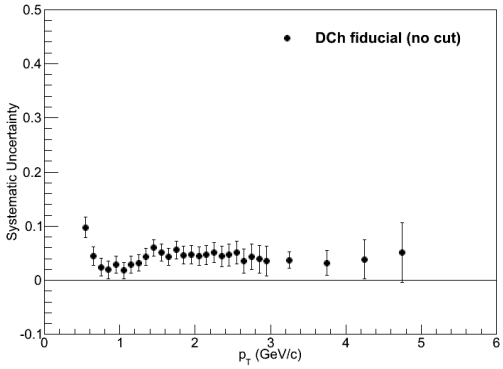

Figure 3.243: Relative uncertainty (maximal) in DC fiducial cuts for p

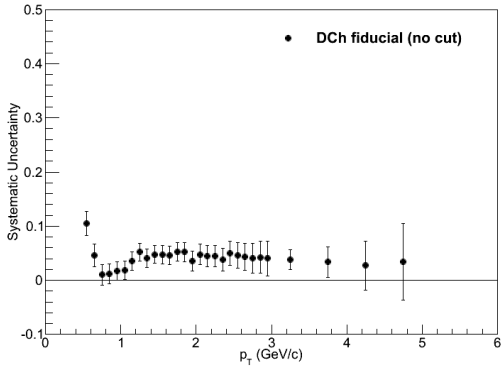

Figure 3.244: Relative uncertainty (maximal) in DC fiducial cuts for $\bar{p}$

3.3.3.2 DC Zed cut

To estimate the uncertainty introduced by the DC zed cut, we compared our 70 cm cut used in the analysis to a 40 cm cut.

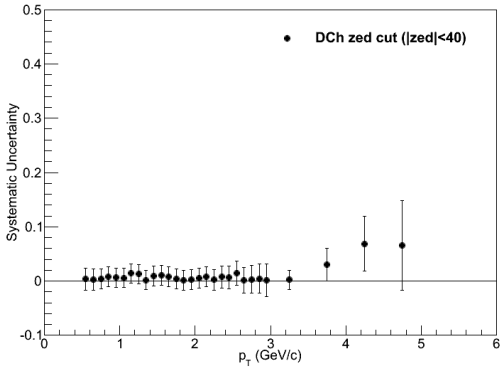

Figure 3.245: Relative uncertainty in DC Zed cut for π^+

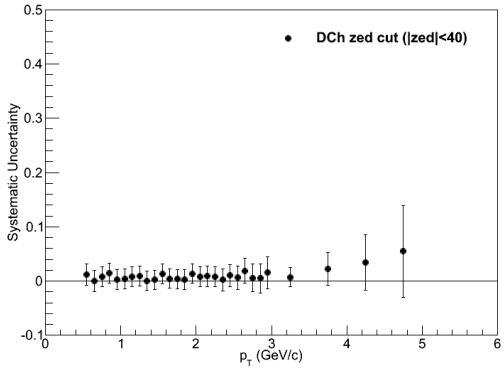

Figure 3.246: Relative uncertainty in DC Zed cut for π^-

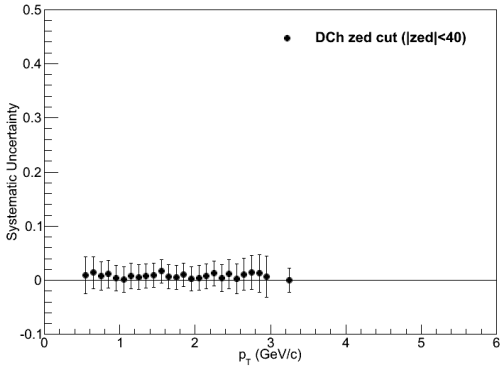

Figure 3.247: Relative uncertainty in DC Zed cut for K^+

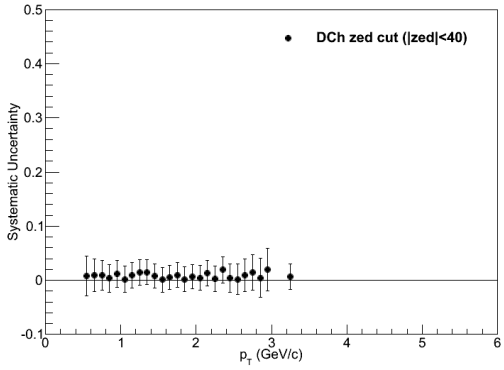

Figure 3.248: Relative uncertainty in DC Zed cut for K^-

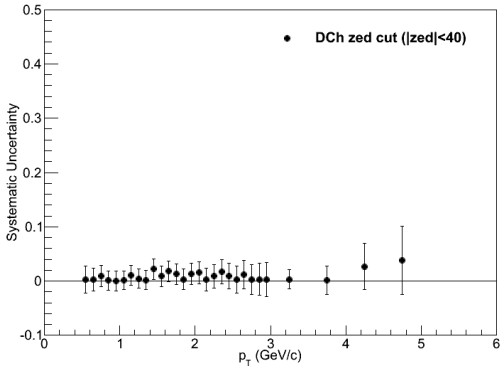

Figure 3.249: Relative uncertainty in DC Zed cut for p

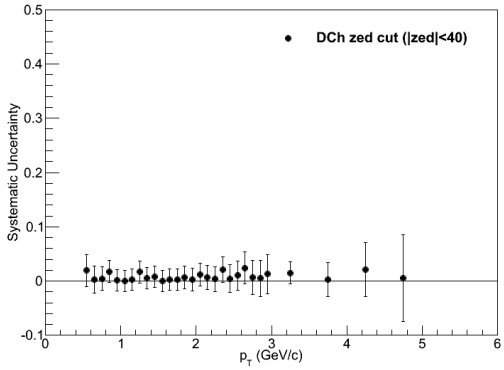

Figure 3.250: Relative uncertainty in DC Zed cut for $\bar{p}$

The uncertainty associated with the DC zed cut appears to be fairly small and largely indepent of particles species. At lower p_T the uncertainty is almost vanishing while at higher p_T there are some small but appreciable deviations. While in unidentified charged hadron analyses a very tight DC zed has been found to significantly reduce background, that does not appear to be the case here. The systematic uncertainty for this cut is rolled into the DC fiducial cut, to which it is strongly related.

3.3.3.3 Track Matching cuts

To estimate the uncertainty introduced by the track matching cuts, we compared our 2σ cuts used in the analysis to 1.5σ cuts.

First we look at the PC3 track matching.

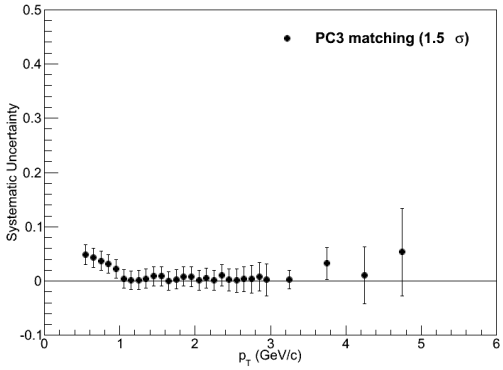

Figure 3.251: Relative uncertainty in PC3 track matching cut for π^+

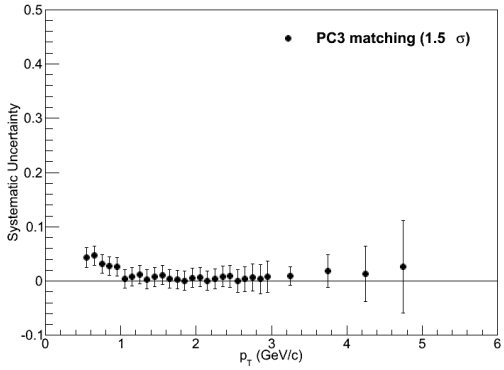

Figure 3.252: Relative uncertainty in PC3 track matching cut for π^-

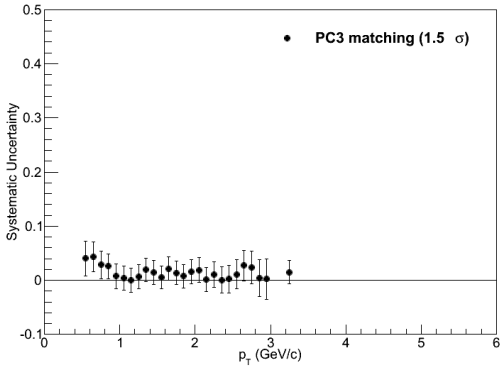

Figure 3.253: Relative uncertainty in PC3 track matching cut for K^+

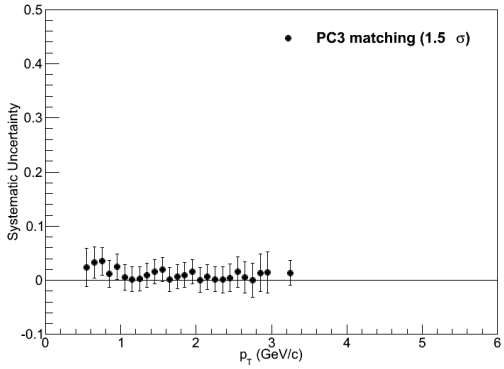

Figure 3.254: Relative uncertainty in PC3 track matching cut for K^-

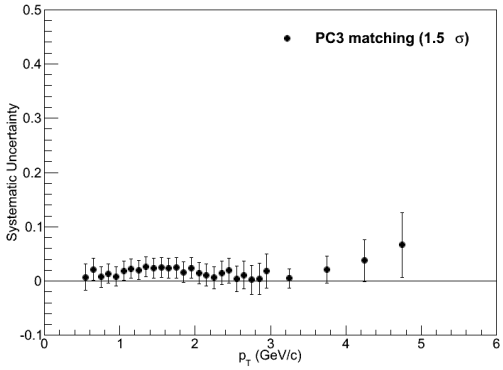

Figure 3.255: Relative uncertainty in PC3 track matching cut for p

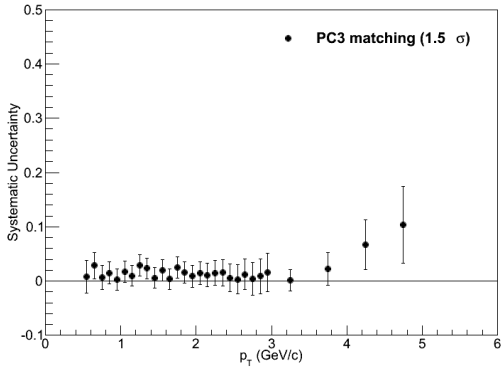

Figure 3.256: Relative uncertainty in PC3 track matching cut for $\bar{p}$

For pions and kaons, we see some fairly significant deviations at low p_T while this trend is absent for the protons. We additionally see a slight increase in the uncertainty at high p_T for all particle species where the background isolation effect of the track matching cuts are increasingly significant. We assign a 5% systematic uncertainty for all particle species at all p_T.

Now we look at the TOFW track matching.

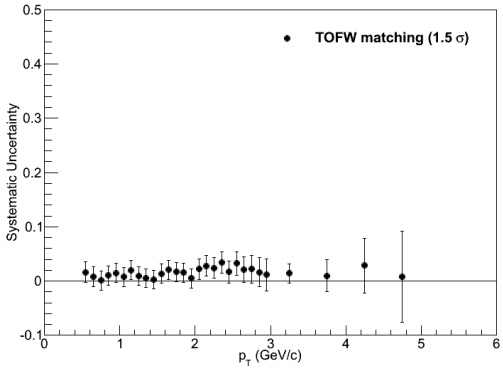

Figure 3.257: Relative uncertainty in TFW track matching cut for π^+

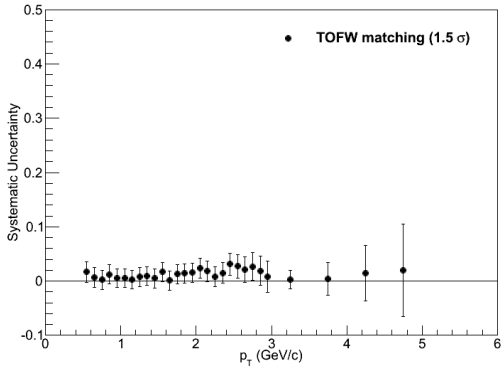

Figure 3.258: Relative uncertainty in TFW track matching cut for π^-

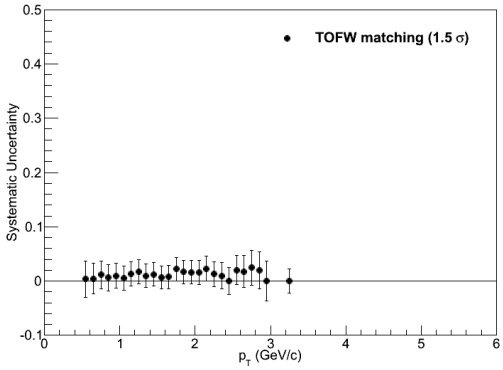

Figure 3.259: Relative uncertainty in TFW track matching cut for K^+

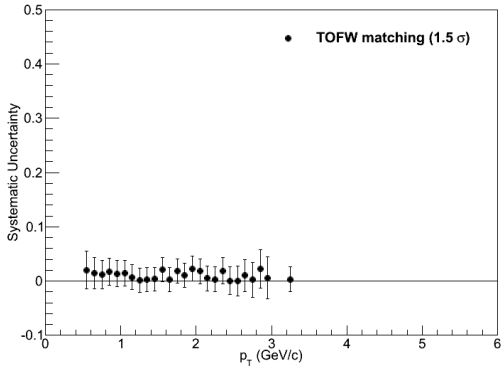

Figure 3.260: Relative uncertainty in TFW track matching cut for K^-

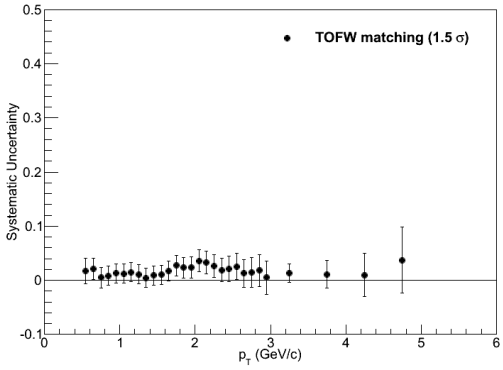

Figure 3.261: Relative uncertainty in TFW track matching cut for p

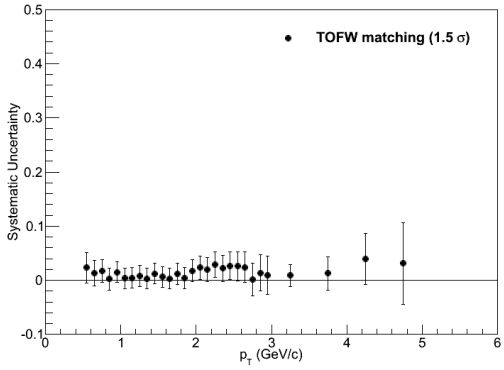

Figure 3.262: Relative uncertainty in TFW track matching cut for $\bar{p}$

There appears to be significant less systematic variation for the TOFW matching. We assign a 2% systematic uncertainty for all particle types for all p_T.

We will now look at a the comparisons with 2.5σ cut instead of a 1.5σ cut.

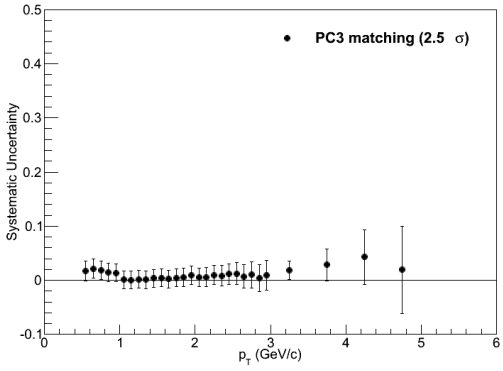

Figure 3.263: Relative uncertainty in PC3 track matching cut for π^+

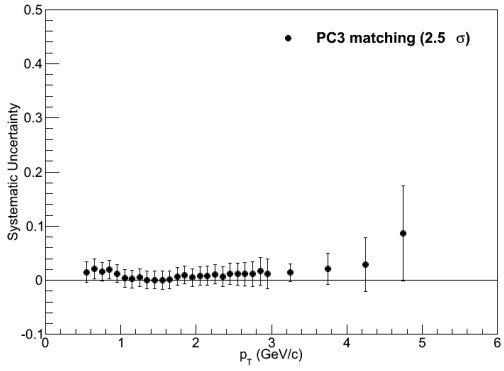

Figure 3.264: Relative uncertainty in PC3 track matching cut for π^-

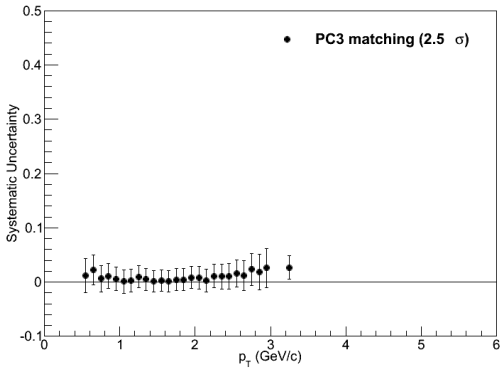

Figure 3.265: Relative uncertainty in PC3 track matching cut for K^+

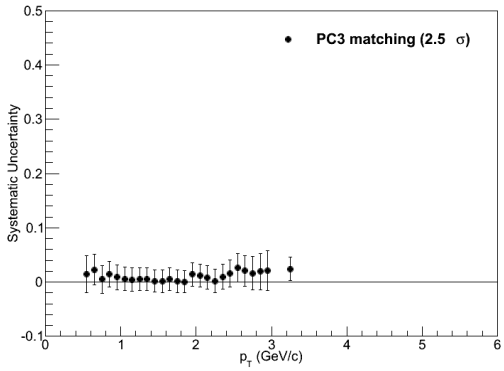

Figure 3.266: Relative uncertainty in PC3 track matching cut for K^-

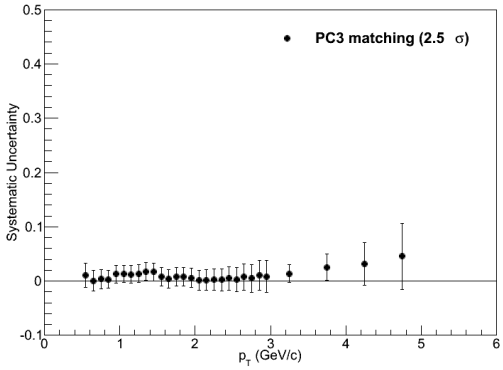

Figure 3.267: Relative uncertainty in PC3 track matching cut for p

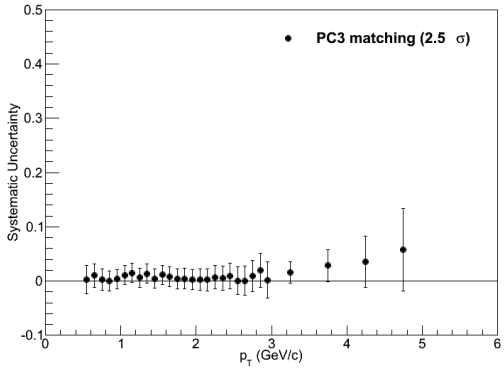

Figure 3.268: Relative uncertainty in PC3 track matching cut for $\bar{p}$

Now we look at the TOFW track matching.

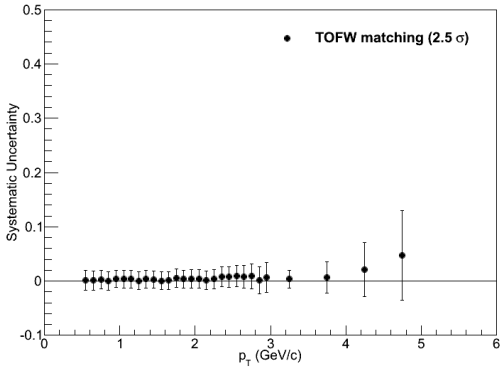

Figure 3.269: Relative uncertainty in TFW track matching cut for π^+

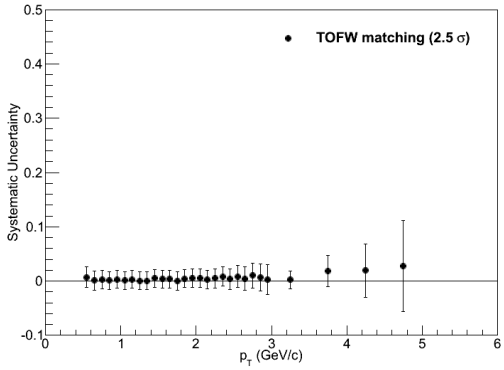

Figure 3.270: Relative uncertainty in TFW track matching cut for π^-

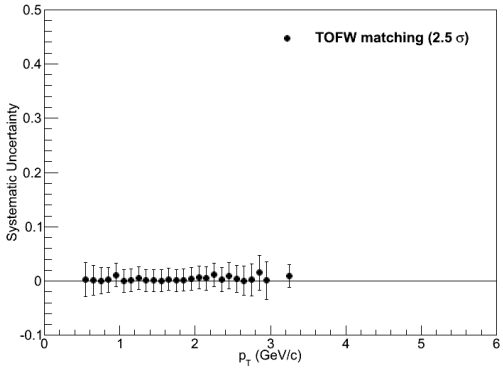

Figure 3.271: Relative uncertainty in TFW track matching cut for K^+

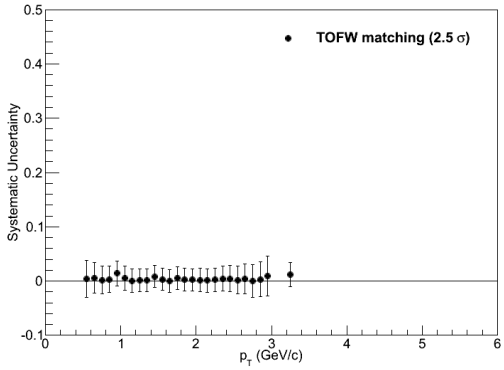

Figure 3.272: Relative uncertainty in TFW track matching cut for K^-

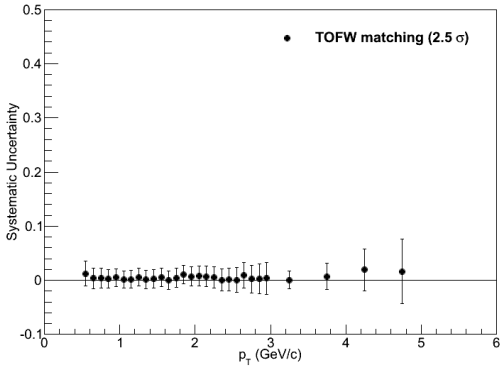

Figure 3.273: Relative uncertainty in TFW track matching cut for p

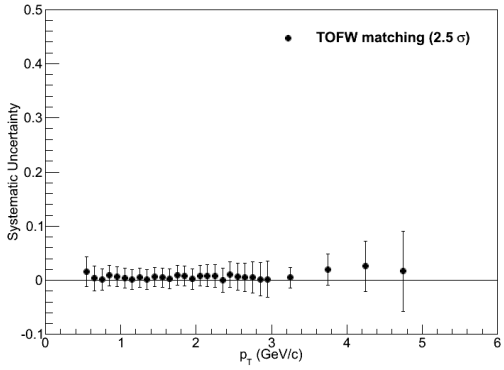

Figure 3.274: Relative uncertainty in TFW track matching cut for $\bar{p}$

Clearly the systematic variation with respect to the looser cut is somewhat diminised. A tighter cut is much more sensitive so small variations in the mean and standard deviation of the tracking variables than is a looser one. We note that the previous precedent (AN187, AN231) has been to look at looser track matching cuts and not wider ones. If we followed this path we could reduce the uncertainty associated with these cuts; however, we leave our assessments as they are.

3.3.3.4 PC fiducial cuts

To estimate the uncertainty associated with the PC1 and PC3 fiducial cuts, we examine the effect of tightening the cuts by 5 mrad in the ϕ-direction and 2 cm in the z-direction.

First we look at PC1.

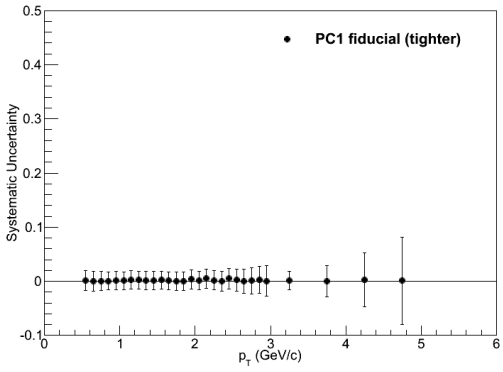

Figure 3.275: Relative uncertainty in PC1 fiducial cut for π^+

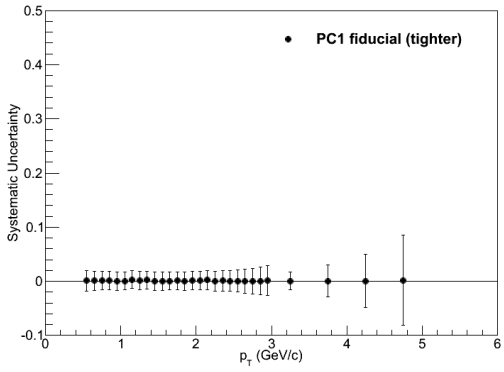

Figure 3.276: Relative uncertainty in PC1 fiducial cut for π^-

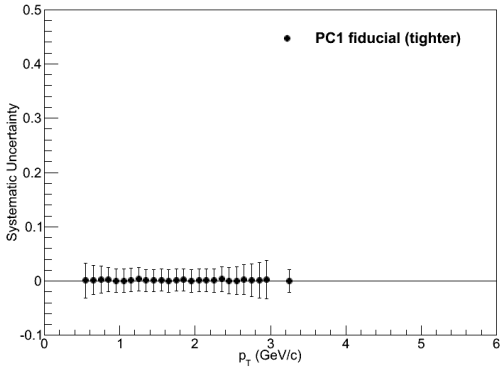

Figure 3.277: Relative uncertainty in PC1 fiducial cut for K^+

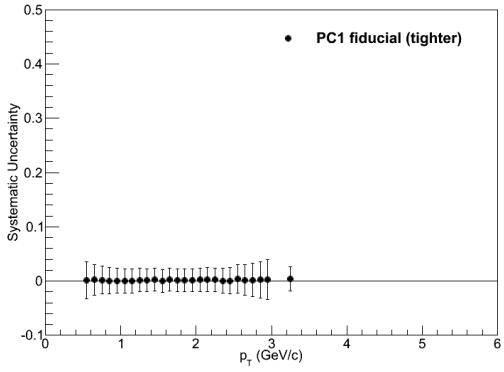

Figure 3.278: Relative uncertainty in PC1 fiducial cut for K^-

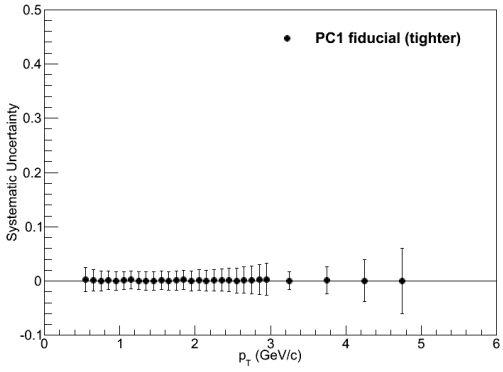

Figure 3.279: Relative uncertainty in PC1 fiducial cut for p

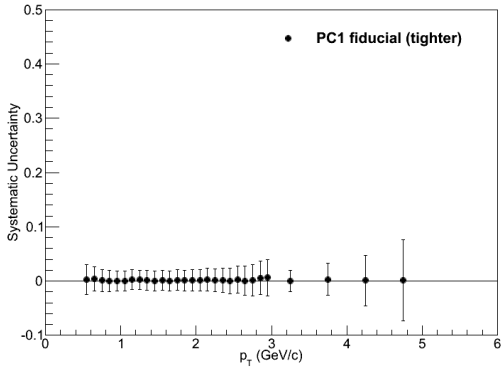

Figure 3.280: Relative uncertainty in PC1 fiducial cut for $\bar{p}$

Now we look at PC3.

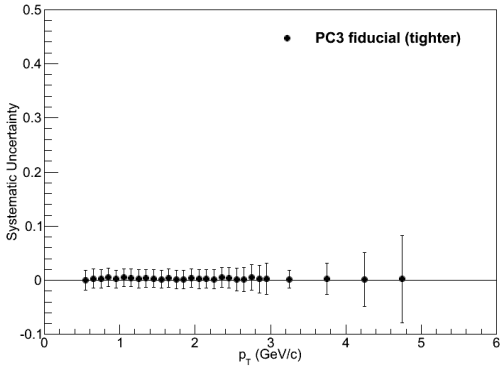

Figure 3.281: Relative uncertainty in PC3 fiducial cut for π^+

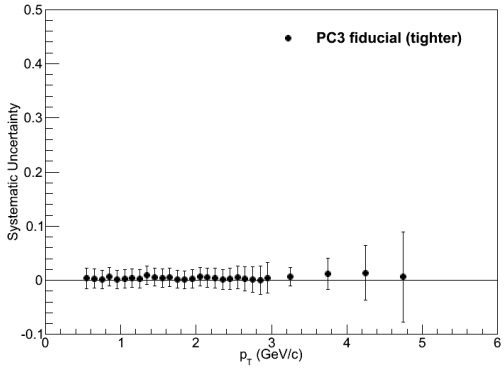

Figure 3.282: Relative uncertainty in PC3 fiducial cut for π^-

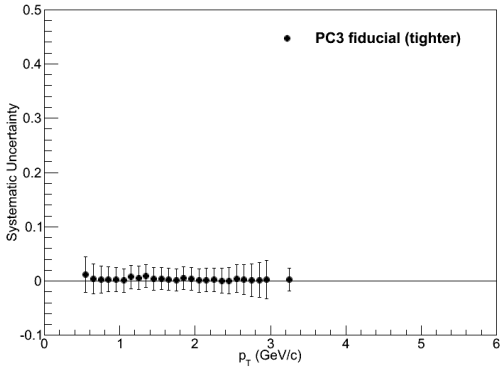

Figure 3.283: Relative uncertainty in PC3 fiducial cut for K^+

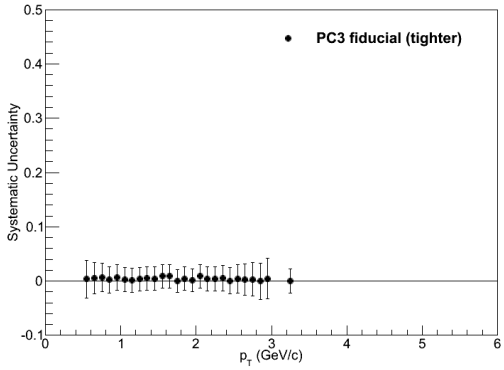

Figure 3.284: Relative uncertainty in PC3 fiducial cut for K^-

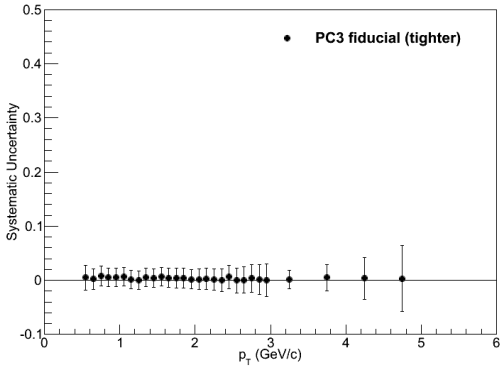

Figure 3.285: Relative uncertainty in PC3 fiducial cut for p

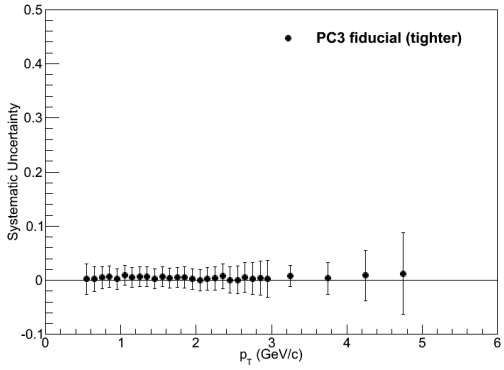

Figure 3.286: Relative uncertainty in PC3 fiducial cut for $\bar{p}$

For both PC1 and PC3 we find the systematic uncertainty associated with the fiducial cuts is not only completely independent of particle species, it is almost completely negligible altogether. It is assessed to be 1% for each cut.

3.3.3.5 PID functions, part I

To estimate the systematic uncertainty associated with the PID functions, first we vary the parameters of the analytical parametrization as discussed in the section on the PID functions.

First we look at the best fit set of parameters.

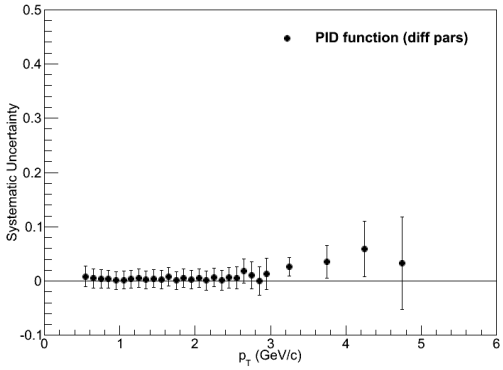

Figure 3.287: Relative uncertainty in PID cut for π^+

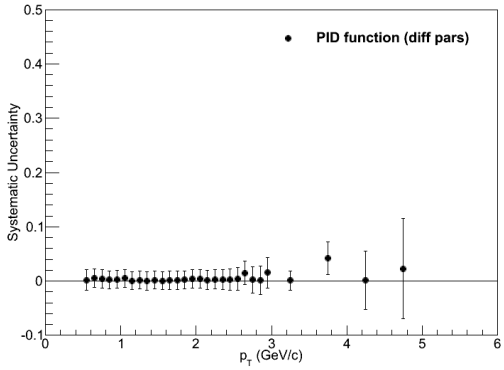

Figure 3.288: Relative uncertainty in PID cut for π^-

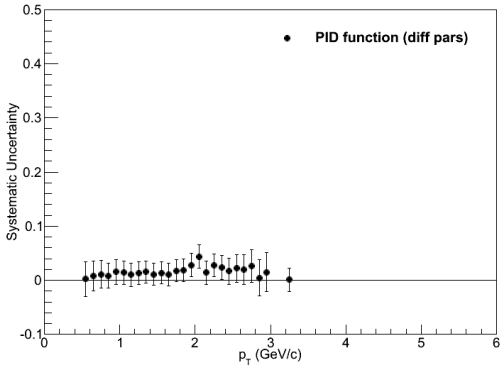

Figure 3.289: Relative uncertainty in PID cut for K^+

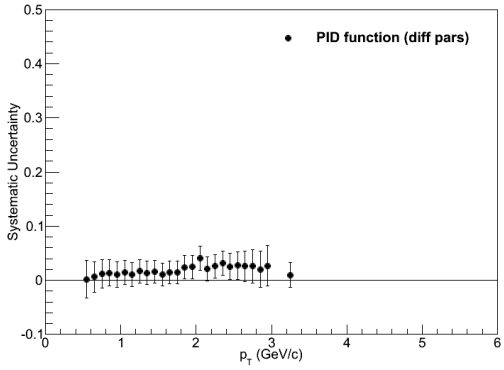

Figure 3.290: Relative uncertainty in PID cut for K^-

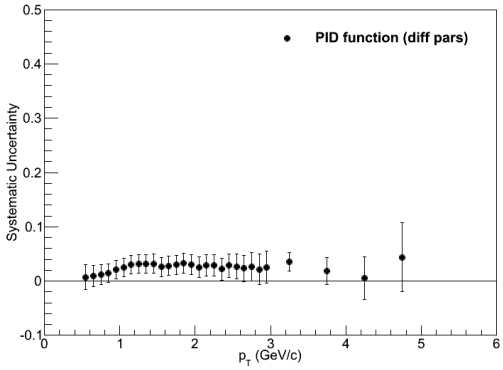

Figure 3.291: Relative uncertainty in PID cut for p

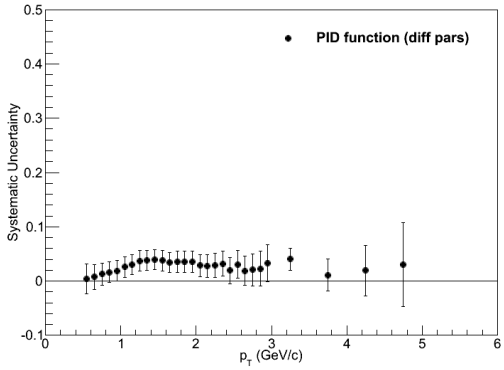

Figure 3.292: Relative uncertainty in PID cut for $\bar{p}$

We see increasing difference with particle mass, reflecting the significant difference in the angular resolution (and therefore the momentum uncertainty).

Now we look at the alternate set of parameters.

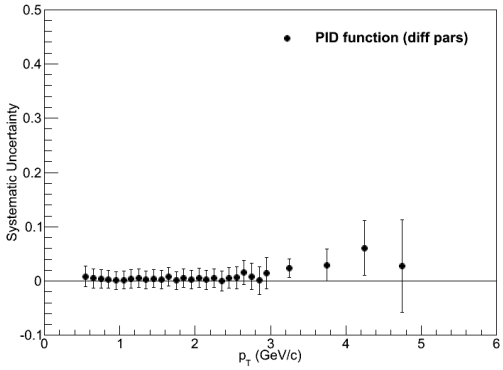

Figure 3.293: Relative uncertainty in PID cut for π^+

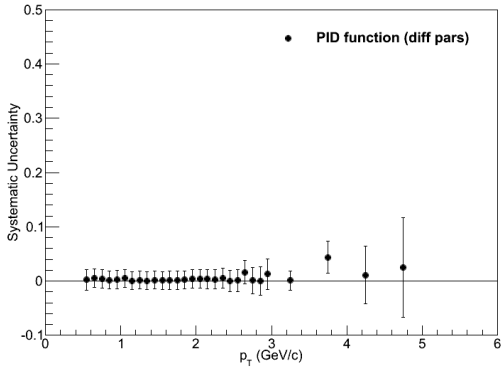

Figure 3.294: Relative uncertainty in PID cut for π^-

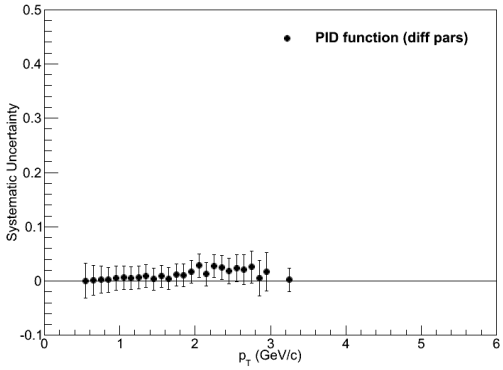

Figure 3.295: Relative uncertainty in PID cut for K^+

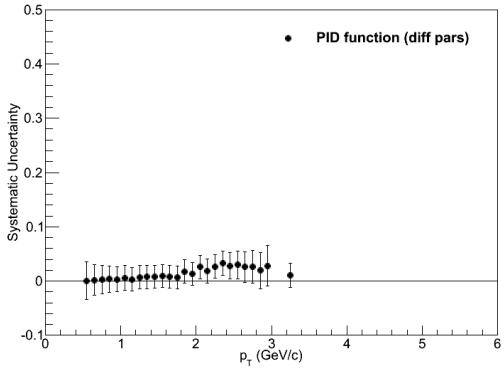

Figure 3.296: Relative uncertainty in PID cut for K^-

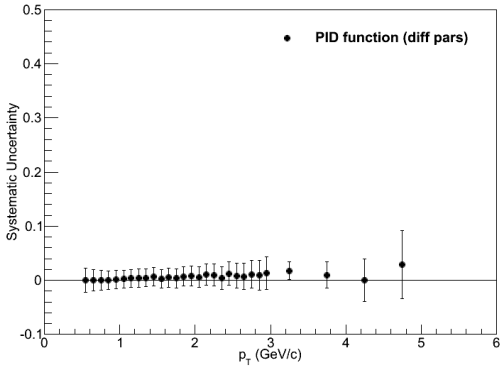

Figure 3.297: Relative uncertainty in PID cut for p

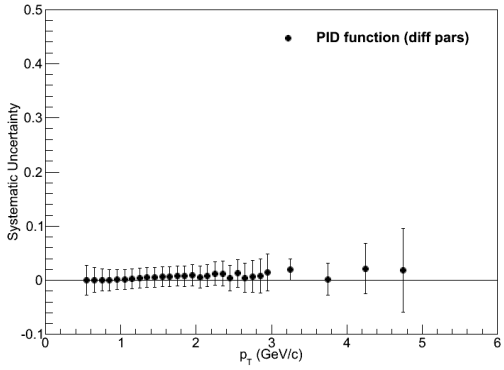

Figure 3.298: Relative uncertainty in PID cut for $\bar{p}$

For the alternate set of parameters, the differences are quite small for all particles species.

3.3.3.6 PID functions, part II

To estimate the systematic uncertainty associated with the PID functions, we tighten the cut in one of two ways. First, we change the window from 2 to 1.5 sigma but leave the veto alone at 2 sigma. Second, we leave the window alone at 2 sigma but change the veto from 2 to 2.5 sigma.

First the change in window.

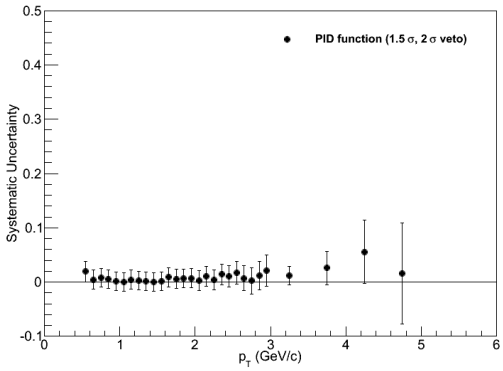

Figure 3.299: Relative uncertainty in PID cut for π^+

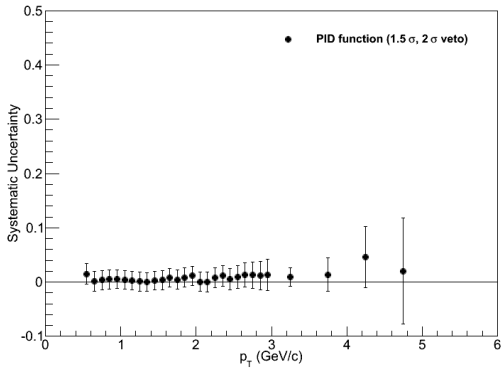

Figure 3.300: Relative uncertainty in PID cut for π^-

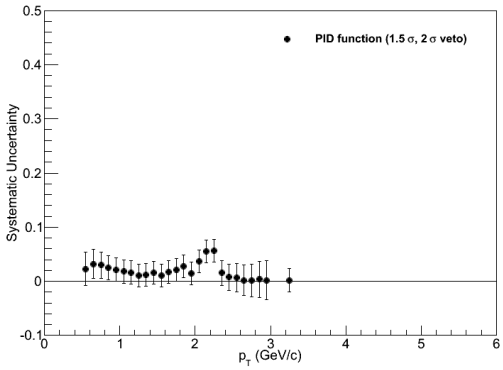

Figure 3.301: Relative uncertainty in PID cut for K^+

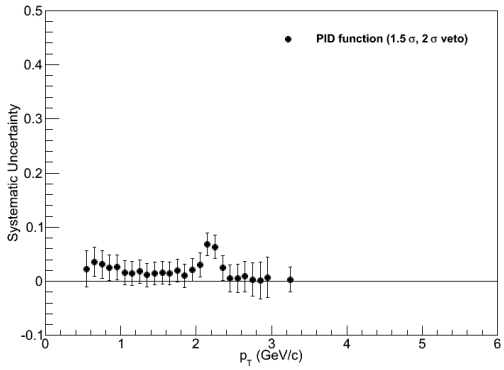

Figure 3.302: Relative uncertainty in PID cut for K^-

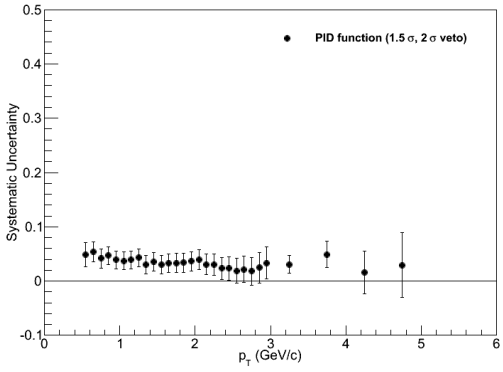

Figure 3.303: Relative uncertainty in PID cut for p

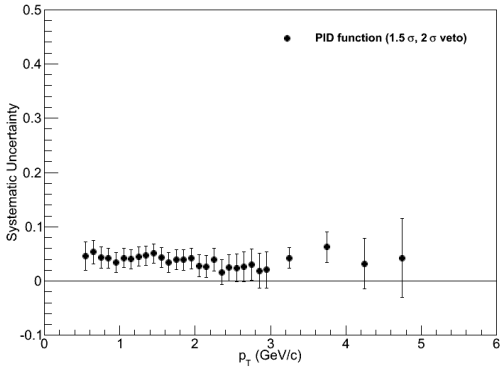

Figure 3.304: Relative uncertainty in PID cut for $\bar{p}$

Here again we see increasing differences with increasing particle mass, reflecting the effect of the momentum uncertainty.

Next the change in veto.

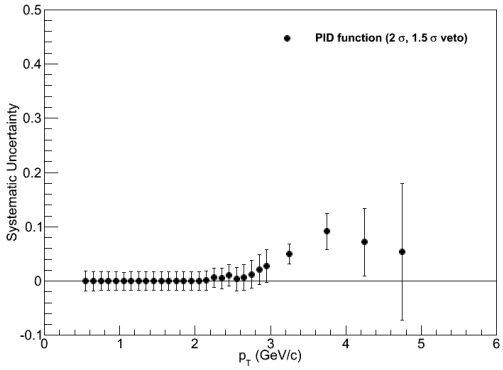

Figure 3.305: Relative uncertainty in PID cut for π^+

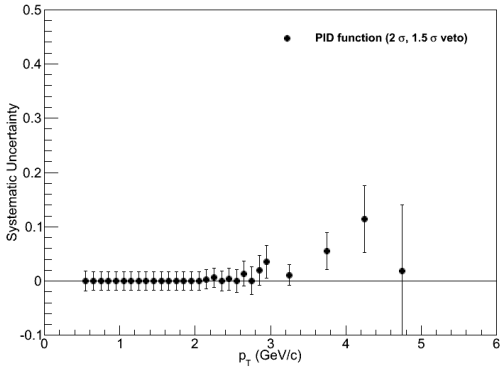

Figure 3.306: Relative uncertainty in PID cut for π^-

In this comparision, we find no deviations below the pid crossover bands, which is to be expected.

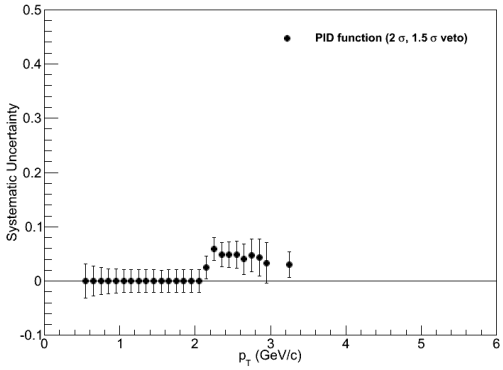

Figure 3.307: Relative uncertainty in PID cut for K^+

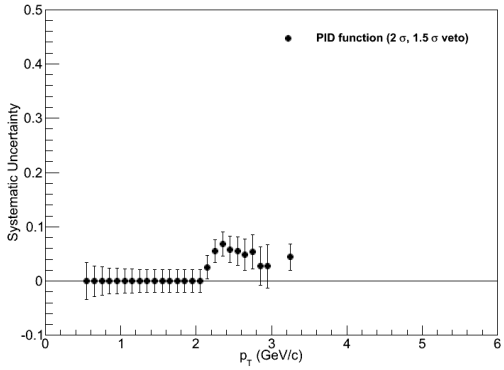

Figure 3.308: Relative uncertainty in PID cut for K^-

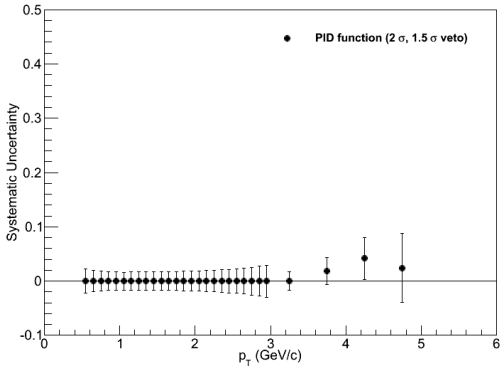

Figure 3.309: Relative uncertainty in PID cut for p

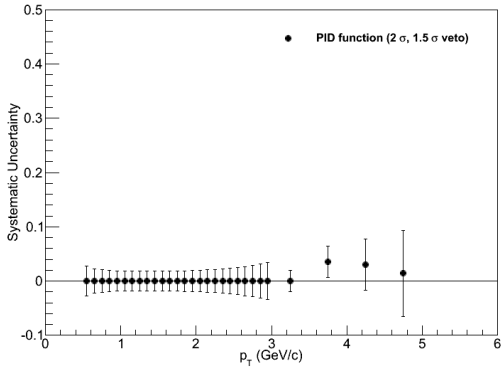

Figure 3.310: Relative uncertainty in PID cut for $\bar{p}$

Taking both the window and veto comparisons into account, we assess the following uncertainties. For the pions we assign a systematic uncertainty of 2% for 0–3 GeV/c and 5% for 3–5 GeV/c. For the kaons we assign a systematic uncertainty of 10% for all p_T. For protons we assign a systematic uncertainty of 5% for 0–3 GeV/c and 7% for 3–5 GeV/c.

3.3.4 Summary of Uncertainties from Cuts

Table 3.10: Summary of systematic uncertainties from analysis cuts for Run7.

Cut	π^+	π^-	K^+	K^-	p	$\bar{p}$
DC Fiducial	5%	5%	5%	5%	5%	5%
PC3 Matching	2%	2%	2%	2%	2%	2%
TOFW Matching	5%	5%	5%	5%	5%	5%
PC1 Fiducial	1%	1%	1%	1%	1%	1%
PC3 Fiducial	1%	1%	1%	1%	1%	1%
Subtotal	8%	8%	8%	8%	8%	8%
PID	2,5%	2,5%	7%	7%	5,7%	5,7%
EP Cut	10%	10%	-	-	10%	10%
Total, $p_T < 3$ GeV/c	8%	8%	11%	11%	8%	8%
Total, $p_T > 3$ GeV/c	9%	9%	11%	11%	9%	9%
Total, $p_T > 5$ GeV/c	14%	14%	-	-	14%	14%

Table 3.11: Summary of systematic uncertainties from analysis cuts for Run8.

Cut	π^+	π^-	K^+	K^-	p	$\bar{p}$
DC Fiducial	5%	5%	5%	5%	5%	5%
PC3 Matching	5%	5%	5%	5%	5%	5%
TOFW Matching	2%	2%	2%	2%	2%	2%
PC1 Fiducial	1%	1%	1%	1%	1%	1%
PC3 Fiducial	1%	1%	1%	1%	1%	1%
Subtotal	8%	8%	8%	8%	8%	8%
PID	2,5%	2,5%	10%	10%	5,7%	5,7%
Total, $p_T < 3$ GeV/c	8%	8%	13%	13%	9%	9%
Total, $p_T > 3$ GeV/c	9%	9%	13%	13%	11%	11%

3.3.5 Weak Decay Feeddown Uncertainties

There is a significant amount of uncertainty associated with the feeddown correction, owing primarily to uncertainty in the actual value of the inclusive Lambda spectrum, which has not been measured in Au+Au collisions at $\sqrt{s_{NN}}$ = 200 GeV. Small changes in the input spectrum can have significant effects on the reconstructred spectrum. The feeddown itself significantly affects the shape of the proton and antiproton spectra at low p_T while having an additional small effect on the normalization at all p_T. The uncertainty on the feeddown fraction itself is 25%. For Run7 this results in an uncertainty of 9% at low p_T that continually decreases to an uncertainty of about 3% at high p_T. Quite similarly for the Run8, the uncertainty various continuously from about 11% at low p_T and 3% for high p_T.

3.3.6 Global Systematic Uncertainties

The occupancy correction for the Au+Au data does not affect the shape of the p_T spectra; it only affects the overall normalization, and it does this in a centrality dependent way. The most central collisions have the largest correction and the most peripheral collisions have the smallest correction, and the uncertainties vary accordingly.

The uncertainty is estimated to be 20% of the overall correction. For example, in the most central collisions, the embedding efficiency is roughly 50%, therefore the associated uncertainty is 10%. In the most peripheral collisions, the embedding efficiency is about 97% and the associated uncertainty is 0.5%

Table 3.12: Centrality dependent global uncertainties for Run7 Au+Au

Cent	Correction	Uncertainty.
0-10%	0.542	9.2%
10-20%	0.653	6.9%
20-30%	0.751	5.0%
30-40%	0.814	3.7%
40-50%	0.882	2.4%
50-60%	0.925	1.5%
60-70%	0.950	1.0%
70-80%	0.968	0.6%
80-92%	0.973	0.5%

While there is no embedding correction needed for d+Au collisions, there do exist small but measurable centrality dependent effects. There exists a trigger bias where tracks belonging to a certain qualitative class of centrality fall into a different numerical class than the one to which they should belong. This effect causes there to be more tracks in central collisions and fewer in peripheral collisions than there should be. The bias factors and the

associated uncertainties for Run8 d+Au were determined in AN900 [129]. These numbers are not too different from the Run3 d+Au numbers, which can be found in e.g. [132].

Table 3.13: Global Uncertainty with Centrality Bias Correction

Cent	Correction	Uncertainty
0-20%	0.94	1.1%
20-40%	1.00	0.6%
0-100%	0.89	0.1%
40-60%	1.03	1.6%
60-88%	1.03	5.3%

CHAPTER IV

RESULTS AND DISCUSSION

4.1 Brief Recapitulation of the Analysis

The observant reader will recognize that the preceding chapter is quite long. In this section we very briefly summarize the salient features of the analysis as a refresher prior to moving on to the results and discussion.

The identified charged hadron analysis makes use of both sectors of the Time-of-flight detector in the west arm (TOFW). The Au+Au data are from the 2007 data set and the d+Au data are from the 2008 data set. Event selection utilizes the standard minimum bias trigger of one or more phototubes fired in both the north and south beam-beam counters (BBC), and further a vertex cut of $|z| < 30$ cm is required. Track selection starts with tracks in the drift chamber (DC) and first layer of the pad chambers (PC1), and only the highest quality selected tracks with quality 63 or 31 are selected, meaning both X1 and X2 layers of the DC have fired and there is z-coordinate information in both DC and PC1 (63) or at least PC1 alone (31). This selection ensures the best possible momentum resolution as well as the narrowest possible residual distributions in the outer detectors. Tracks are required to have a residual of 2 standard deviations or better in both the third layer of the pad chambers (PC3) and the TOFW. This tight track association cut helps minimize background. In d+Au collisions, the event multiplicity is low enough that the track association cuts are enough to properly handle the backgrounds. At high p_T in Au+Au, however, an additional

cut is needed. The electromagnetic calorimeter is also used further isolate background. Tracks are required to have a core energy of at least 20% of the momentum of the track. This eliminates low p_T particles that are falsely reconstructed as high p_T tracks, such as conversion electrons. Particles are identified using the time-of-flight from the TOFW, the momentum from the DC, and the path length from the tracking algorithm to reconstruct the mass squared of the particle. At low p_T, where the mass squared distributions are relatively narrow, tracks are required to have a mass squared value of 2 standard deviations or less within the mean for each particle type. The mean is selected to be the centroid of the distribution; however, the difference between the mean and the PDG value is negligible. At higher p_T, the mass squared distributions of the particles begin to overlap, so additional cuts need to be made to prevent significant PID contamination. In addition to the 2 standard deviation cut, an additional 2 standard deviation veto on the other particles' distributions is also applied. For example, a pion is defined as being within 2 standard deviations of the pion mass squared and also outside of 2 standard deviations of the kaon and proton mass squared. Assuming Gaussian distributions, this procedure limits PID contamination to 3% or less.

4.2 Results and Discussion

4.2.1 Invariant Yield as a Function of Transverse Momentum p_T

The foundation of the identified charged hadron analysis is the invariant yield as a function of transverse momentum p_T in different centrality classes for each particle species. For the Au+Au, the centrality classes are 0–10% (the most central), 10–20%, 20–40%, 40–

60%, and 60–92% (the most peripheral). For the d+Au, the centrality classes are 0–20% (the most central), 20–40%, 0–88% (Minimum Bias), 40–60%, and 60–88% (the most peripheral). From these quantities, all other observables are derived, such as particle ratios, nuclear modification factors, etc. Shown in Figure 4.1 are the invariant yields of charged pions (left panel), kaons (middle panel), and protons and antiprotons (right panel). They are plotted in order of the number of binary collisions N_{coll} as determined in the Glauber model, except for the most peripheral Au+Au (14.8) and most central d+Au (15.1), which are reversed for the sake of keeping the collision species together. We note however that the difference between the N_{coll} values is smaller than the systematic uncertainty in the Glauber calculation. Additionally, the difference in the N_{coll} values is also very small compared to the average, $(15.1 - 14.8)/\frac{1}{2}(15.1 + 14.8) \approx 2.0\%$.

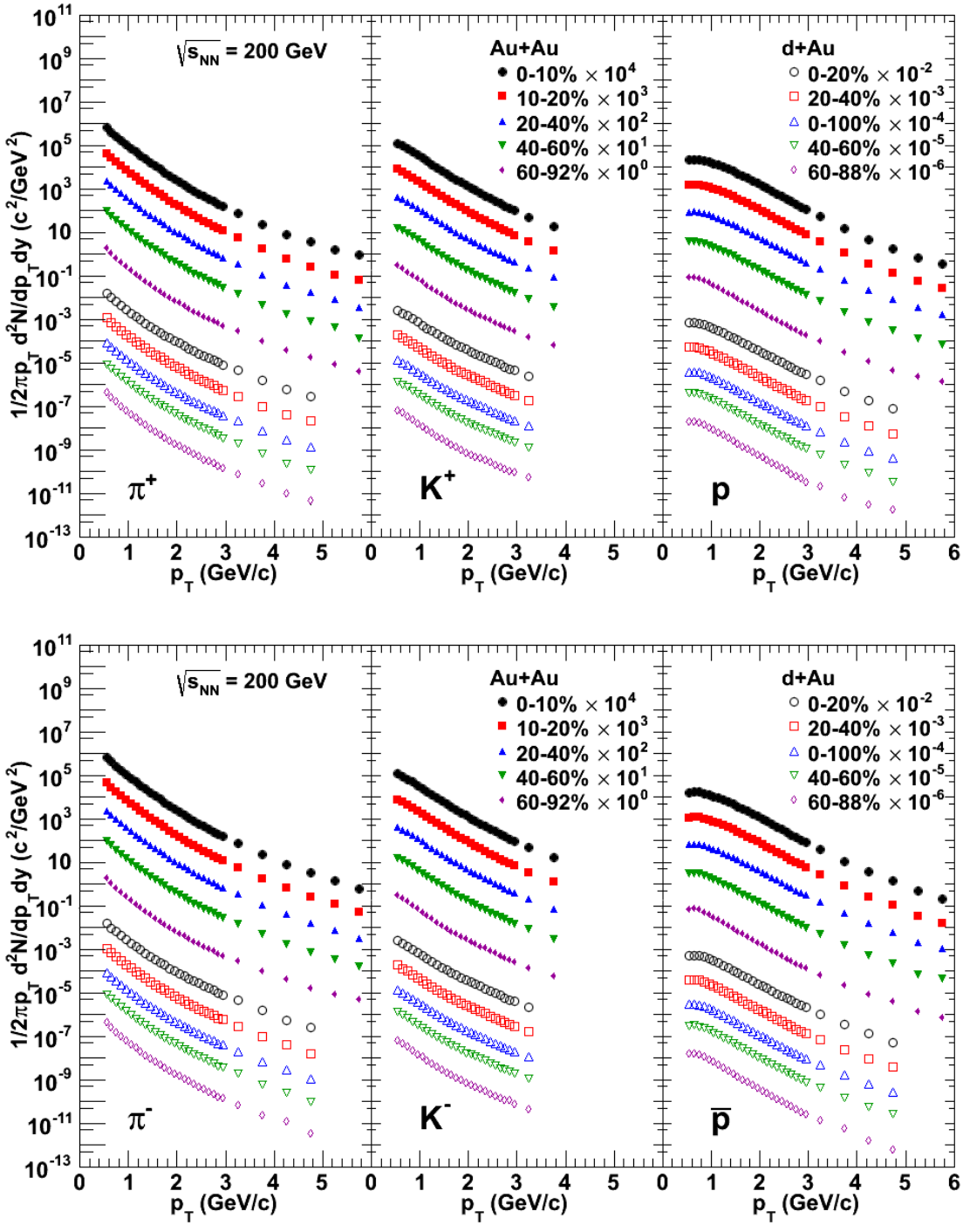

Figure 4.1: Invariant yield of charged pions as a function of p_T in Au+Au collisions and d+Au collisions. The yields are scaled by the arbitrary factors indicated in the legend for the sake of legibility. They are plotted in order of N_{coll}, except for the most peripheral Au+Au and most central d+Au, which are reversed for the sake of keeping collisions species grouped together.

4.2.2 Particle Ratios as a Function of Transverse Momentum

One of the simpler classes of derived quantities is the so-called homogeneous ratio, where one takes the ratio of charges of a single particle species. In the present analysis those ratios are π^-/π^+, K^-/K^+, and $\bar{p}/p$, which are plotted as a function of p_T in Figures 4.2, respectively. In each plot, the Au+Au data are on the left and the d+Au data are on the right. Drawn as a visual aid are thin black lines with value 1.0 for the pions, 0.93 for the kaons, and 0.73 for the protons; these values are picked from the reported p_T integrated values from [38]. Remarkably, all the ratios are essentially independent of both p_T and centrality. Based on simple arguments about isospin conservation and the basics of the parton distribution functions and fragmentation functions, one would expect each of these ratios to vary as a function of p_T as discussed in [136]. That these ratios show no apparent p_T dependence in heavy ion collisions at mid-rapidity, as they do in p+p collisions at mid-rapidity [134, 137], may indicate that while in elementary nucleon-nucleon collisions very high p_T produced hadrons are likely to have a valence quark from the initial reactants, this is not necessarily the case in nucleus-nucleus collisions or even perhaps nucleon-nucleus collisions (assuming d+Au is not materially different from p+Au).

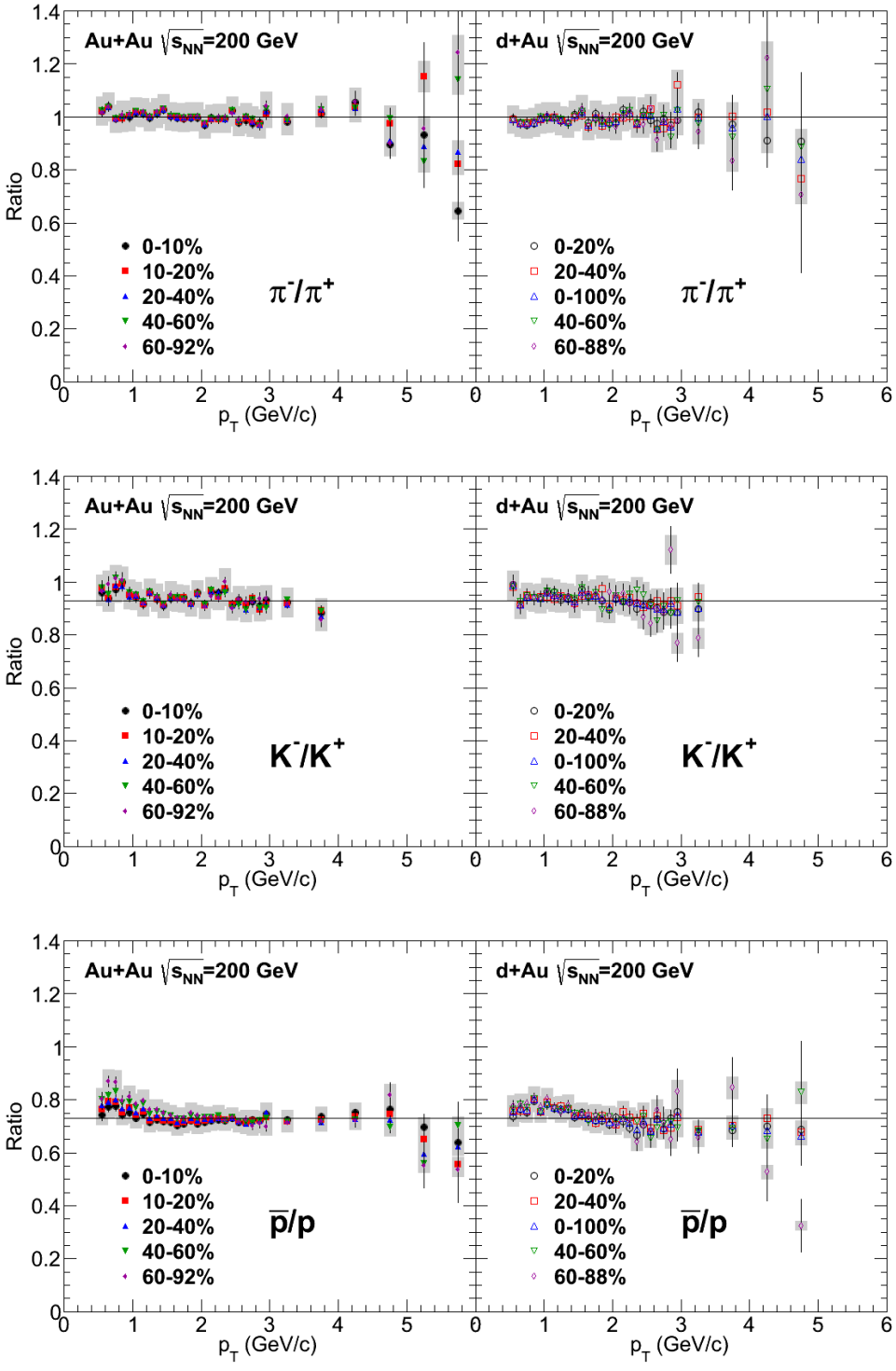

Figure 4.2: Ratio of invariant yield of π^-/π^+ (top), K^-/K^+ (middle), and $\bar{p}/p$ (bottom) as a function of p_T in Au+Au collisions (left panels) and d+Au collisions (right panels) in each centrality bin. Thin lines are drawn as a visual aid.

Shown in Figures 4.3 and 4.4 are the kaon to pion ratios as a function of p_T (K^+/π^+ on the left, K^-/π^- on the right) in Au+Au collisions and d+Au collisions, respectively. The ratios in Au+Au collisions show a small increase with increasing centrality. The enhancement of the integrated K/π ratio in more central collisions is attributed to strangeness equilibration in various thermal models [31, 32]. This is reflected in the differential ratio, although the differential ratio may include additional information about the differences in the fragmentation functions and/or the phase space distribution functions used in the recombination models. As discussed in a previous PHENIX publication [138], the strangeness enhancement present in the hot and dense nuclear medium has an effect on certain recombination models [139]. Specifically, the thermal component of thermal+shower recombination is dominant to higher p_T for strange hadrons (like kaons) than it is for non-strange hadrons (like pions). Therefore, the ratio will not only show an enhancement, but will show a larger enhancement at intermediate p_T relative to lower p_T where the strange particles have a larger thermal component than the non-strange particles. At sufficiently high p_T where the shower component begins to dominate for both strange and non-strange particles, this ratio is expected turn over and begin to lower again. However, this turnover point is beyond the p_T reach available for kaons in this study. The K/π ratios in d+Au collisions are essentially identical for all centrality classes, indicating that the mechanism for strangeness production in d+Au collisions is the same for all centrality classes.

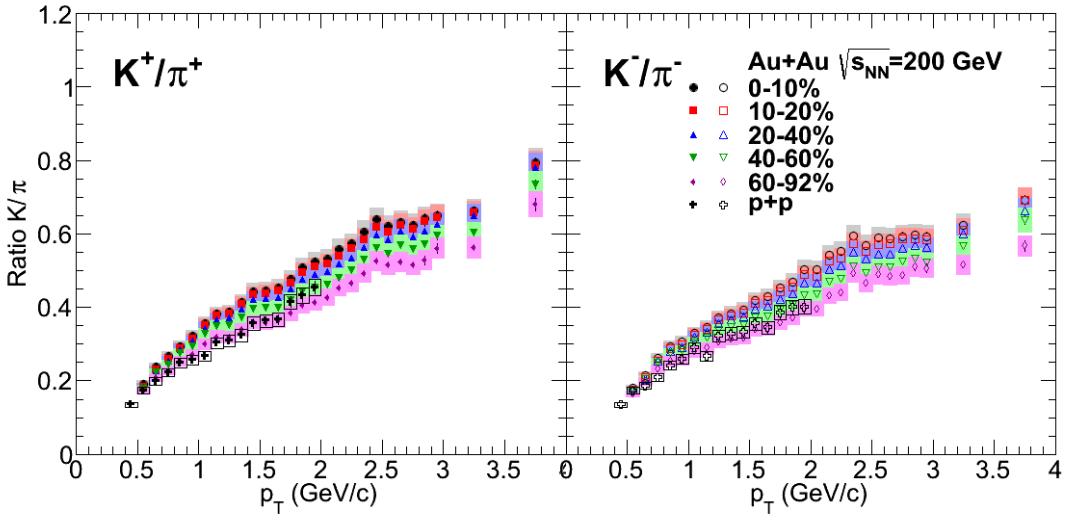

Figure 4.3: Ratio of invariant yield of positive kaons to positive pions (left panel) and negative kaons to negative pions (right panel) as a function of p_T in Au+Au collisions in each centrality bin.

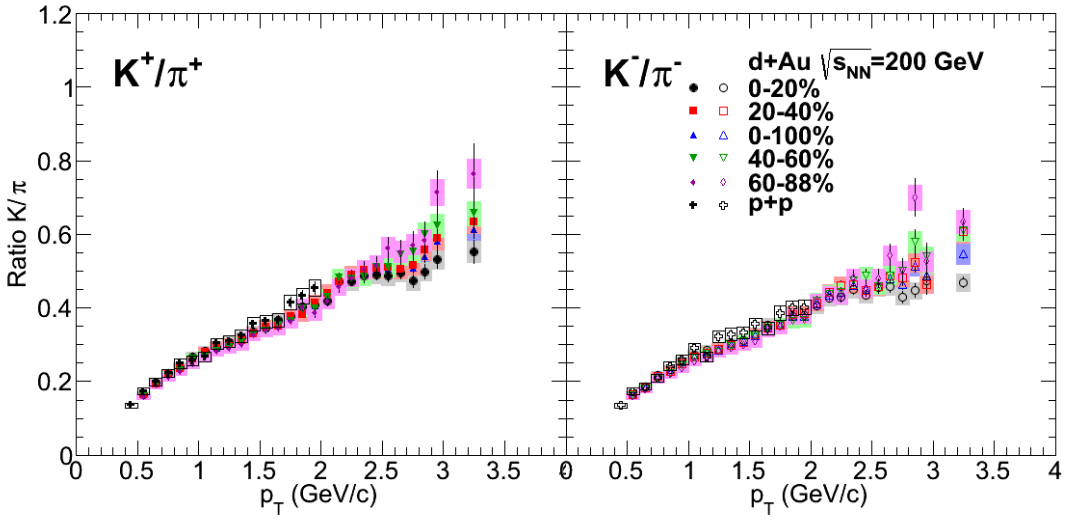

Figure 4.4: Ratio of invariant yield of positive kaons to positive pions (left panel) and negative kaons to negative pions (right panel) as a function of p_T in d+Au collisions in each centrality bin.

Shown in Figures 4.5 and 4.6 are the proton to pion ratios as a function of p_T (p/π^+ on the left, $\bar{p}/\pi^-$ on the right) in Au+Au collisions and d+Au collisions, respectively. The ratios in central Au+Au collisions show a strong enhancement over the values in p+p collisions, which is widely attributed to the parton recombination mechanism of hadronization, which gives rise to significant enhancement of baryon yields relative to meson yields in heavy ion collisions. The p/π ratios in the other centralities in Au+Au show a clear and consistent trend with decreasing enhancement as the collisions become more peripheral. In d+Au collisions, on the other hand, the enhancement is much smaller in central collisions relative to peripheral, but it is still significant. The p/π ratio in the most central d+Au collisions appears consistent with the ratio in the most peripheral Au+Au collisions. Additionally, the p/π ratio is enhanced over p+p collisions in each d+Au centrality class except for the most peripheral.

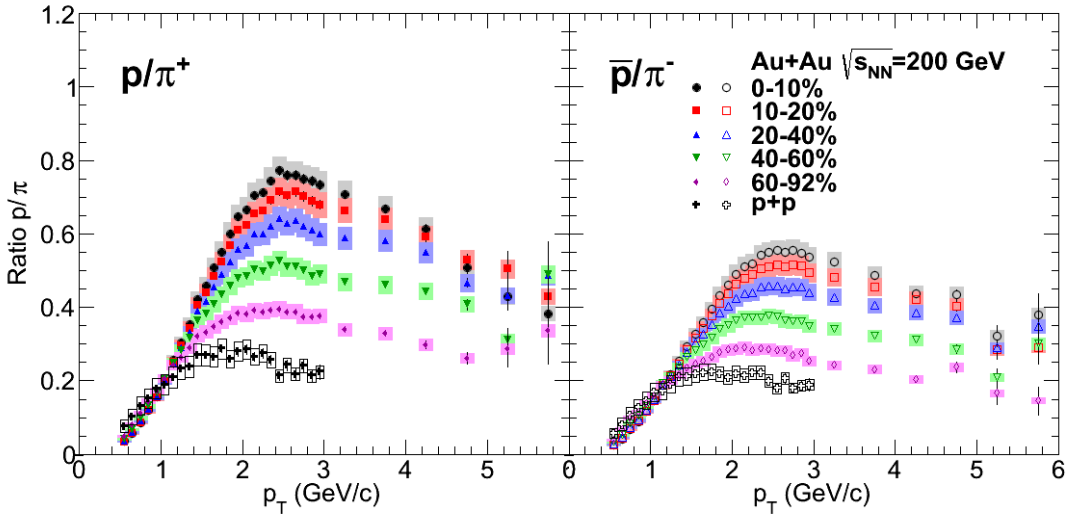

Figure 4.5: Ratio of invariant yield of protons to positive pions (left panel) and antiprotons to negative pions (right panel) as a function of p_T in Au+Au collisions in each centrality bin.

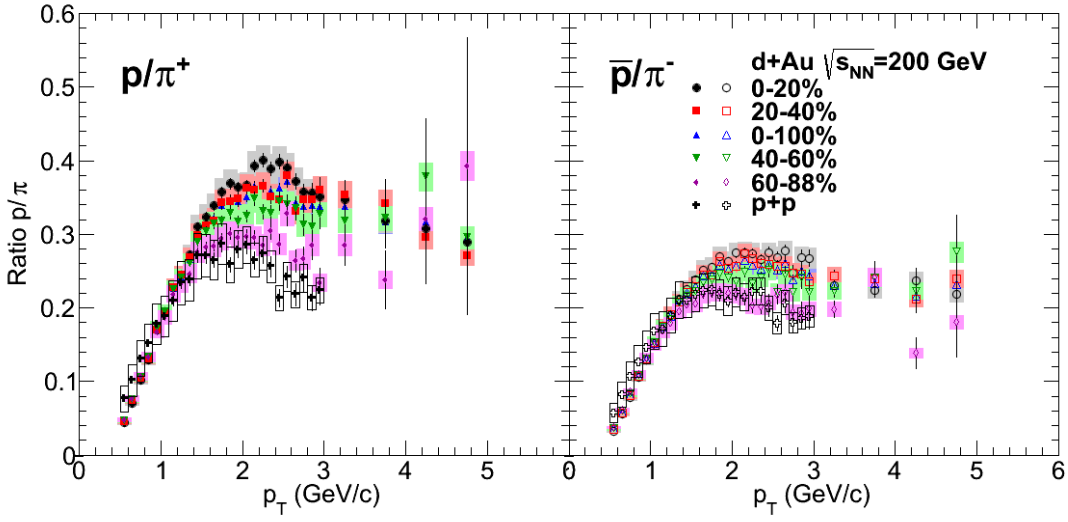

Figure 4.6: Ratio of invariant yield of protons to positive pions (left panel) and antiprotons to negative pions (right panel) as a function of p_T in d+Au collisions in each centrality bin.

4.2.3 Nuclear Modification Factors as a Function of Transverse Momentum

To measure the modification of the spectrum of produced particles in heavy ion collisions relative to the spectrum in p+p collisions, nuclear modification factors are employed. The nuclear modification factor R_{AA} is defined as the yield in Au+Au collisions divided by the yield in p+p collisions, normalized by the number of binary nucleon+nucleon collisions N_{coll} as determined from the Glauber model. The nuclear modification factor R_{CP} is defined as the yield in central Au+Au collisions divided by the yield in peripheral Au+Au collisions, normalized to the respective number of binary nucleon+nucleon collisions. These can be expressed mathematically as:

$$R_{AA} = \frac{Yield^{Au+Au}}{N_{coll}^{Au+Au} Yield^{p+p}}, \tag{4.1}$$

$$R_{CP} = \frac{Yield^{central}}{Yield^{peripheral}} \frac{N_{coll}^{peripheral}}{N_{coll}^{central}}. \tag{4.2}$$

Figure 4.7 shows R_{CP} for 0-10%/40-60% (left panel) and 0-10%/60-92% (right panel) as a function of p_T for charge averaged pions, kaons, and protons from the present study, neutral pions from [93], and the ϕ meson from [138]. One observes a modest rise in the low to intermediate p_T region but an overall significant suppression for both pions and kaons. Also observed is a slightly larger value for kaons in both cases compared to pions, indicating the additional role of strangeness enhancement in the particle production mechanism. The observed enhancement of kaons relative to pions appears to be lower for the 0-10%/40-60% as compared to the 0-10%/60-92%, suggesting a centrality dependence of the strangeness enhancement, which is consistent with the K/π ratios shown above. Fig-

ure 4.8 shows R_{AA} as a function of p_T in different centrality classes for charge averaged pions, kaons, and protons, as well as again the π^0 and ϕ. For all pions and the charged kaons, decreasing suppression with decreasing centrality is observed. This has been previously reported in analyses of the neutral pion R_{AA} [91, 93].

The R_{CP} and central R_{AA} both show significant baryon enhancement relative to mesons in the intermediate p_T region, 2–3 GeV/c. This is further evidence, along with the large proton to pion ratio, of the dominance of parton recombination as the dominant mode of hadronization in this region. For p_T above 3 GeV/c the enhancement starts to diminish and at the highest p_T points are similar for baryons and mesons. Observe however that the central R_{AA} falls off much more quickly than the R_{CP}, suggesting that the recombination dynamics may play a significant role even in the peripheral collisions where collective effects should be relatively small. The proton R_{AA} shows a very similar pattern with respect to centrality as the pion R_{AA}, in that the shape is very similar but that the overall level of the points keeps rising as the collisions become more peripheral. However, while this trend continues with the most peripheral bin for pions, the situation is quite different for the protons. The shape of the most peripheral R_{AA} curve for protons is much flatter. It starts at the highest level at low p_T, preserving the trend seen in the pions. However, the value increases much more slowly with p_T, crossing the other centralities around 1.5 GeV/c and having a maximum value very similar to the most central bin. Additionally, above 3.0 GeV/c it falls off much more slowly than the other centralities and ends up at the same level as the next most peripheral bin (40–60%) at the highest p_T points.

As with Au+Au collisions, nuclear modification factors are employed with d+Au colli-

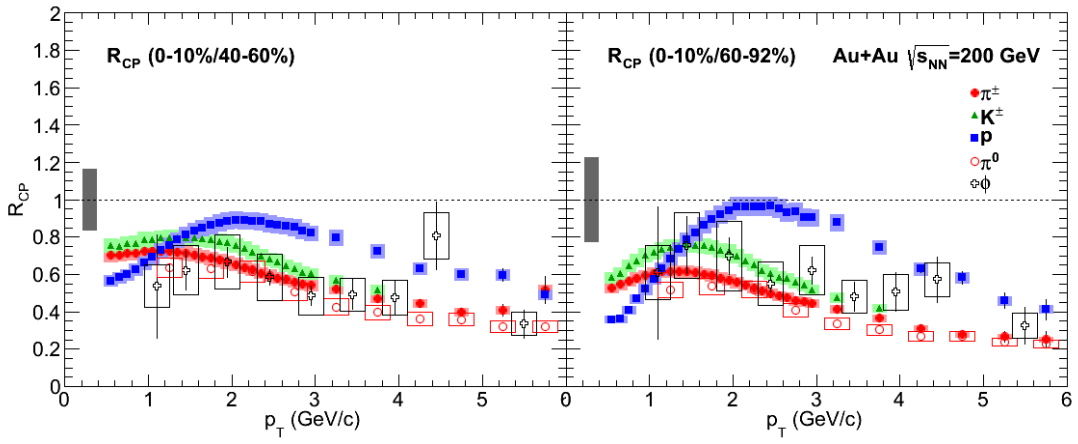

Figure 4.7: R_{CP} for 0-10%/40-60% (left panel) and 0-10%/60-92% (right panel) as a function of p_T for charge averaged pions, kaons, and protons, π^0 [93], and ϕ [138]. A thin black line is drawn at unity indicating non-modification as a visual aid. The shaded boxes indicate the associated uncertainty on N_{coll} from the Glauber model.

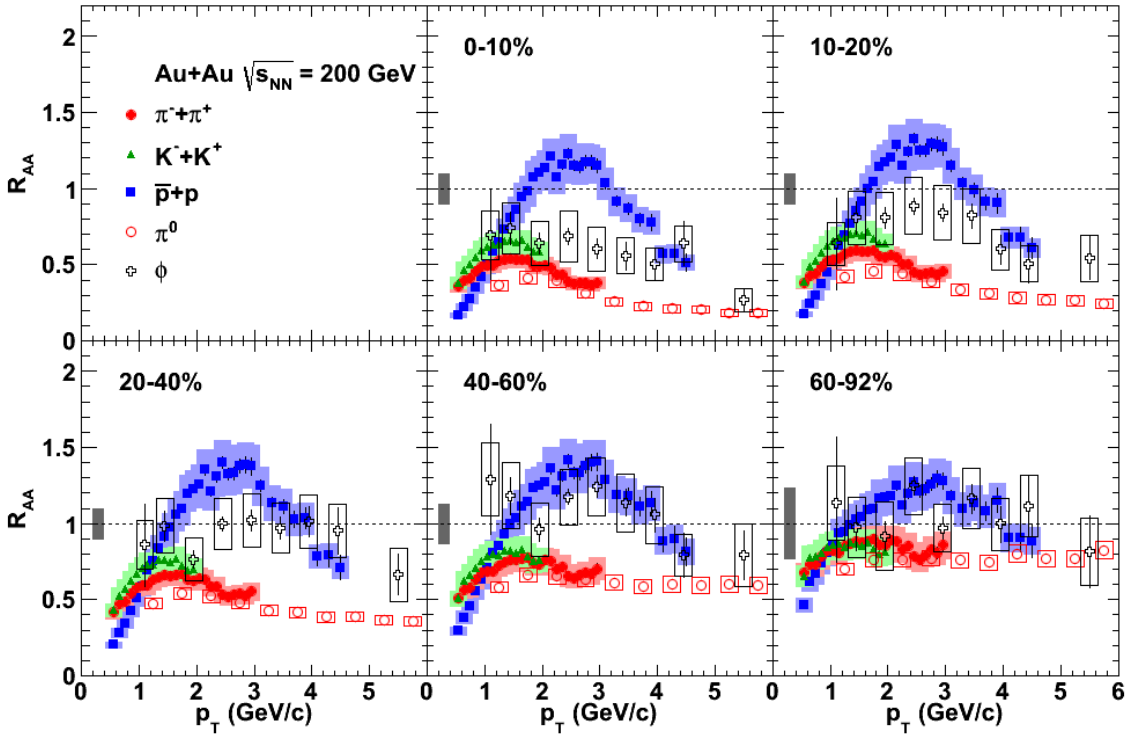

Figure 4.8: Nuclear modification factor R_{AA} as a function of p_T in different centrality classes of charge averaged pions, kaons, and protons, π^0 [93], and ϕ [138]. A thin black line is drawn at unity indicating non-modification as a visual aid.

sions as well. Instead of R_{AA}, R_{dA} is used instead and is defined as

$$R_{dA} = \frac{Yield^{d+Au}}{N_{coll}^{d+Au} Yield^{p+p}}; \tag{4.3}$$

the quantity R_{CP} is defined in exactly the same way as before.

Figure 4.9 shows R_{dA} as a function of p_T in different centrality classes for charged averaged pions particles. We use previously published PHENIX data on identified hadron in p+p collisions [134] to calculate the R_{dA}. A small Cronin enhancement above 1.0 GeV/c is observed in all centrality classes except for the most peripheral where no modification is observed. This is consistent with previous measurements of neutral pions [13, 140].

The most central R_{dA} show a small Cronin enhancement for pions and a much stronger Cronin enhancement for protons, reaching a value of roughly a factor of 2 enhancement at intermediate p_T. The most peripheral the R_{dA} is similar for all particles, with each particle showing essentially no modification above 1.0 GeV/c. There is a small but still noticeable centrality dependence in the proton R_{dA}, with the most central showing the greatest enhancement and the enhancement decreasing as the collisions become more peripheral, in contrast the completely negligible differences in the other centralities for the pions. This pattern is in fact very similar to the small but significant centrality dependence of the p/π ratio, and these two observables can be taken to be driven by the same mechanism. Also apparent in the R_{dA} is that the enhancement for protons begins to fall off at 3.0 GeV/c and steadily drops with increasing p_T, appearing nearly unmodified at the highest p_T points.

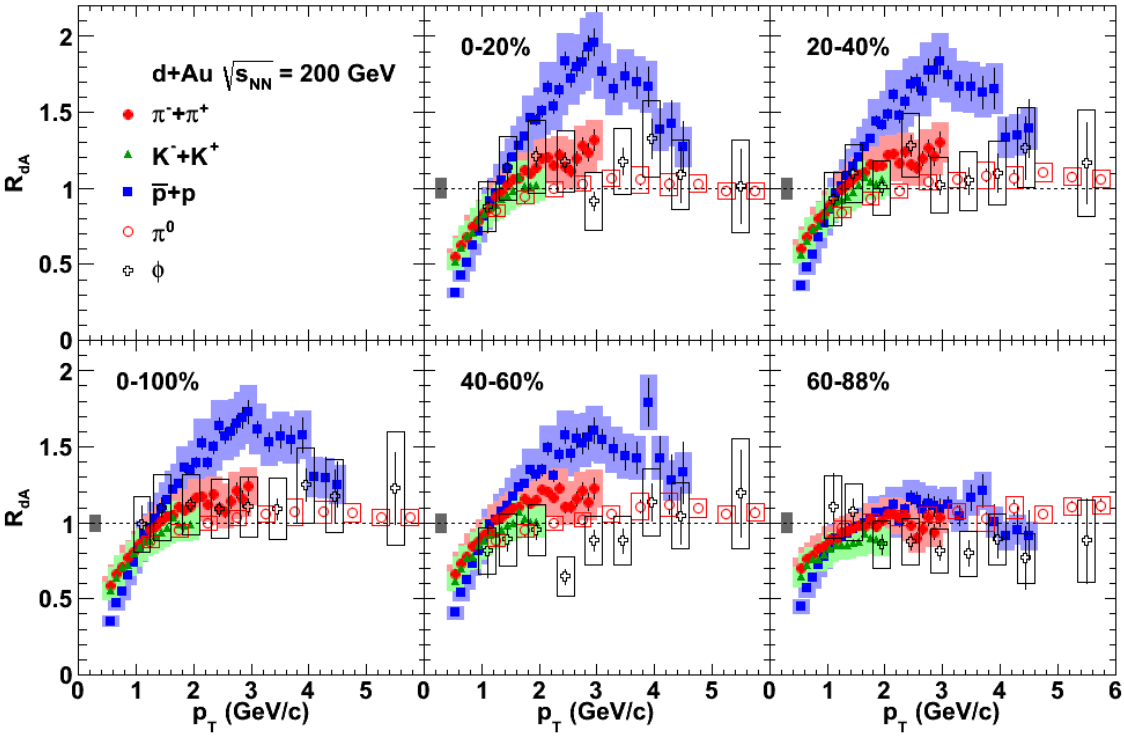

Figure 4.9: Nuclear modification factor R_{dA} as a function of p_T in different centrality classes of charge averaged pions, kaons, and protons, π^0 [140], and ϕ [138]. A thin black line is drawn at unity indicating non-modification as a visual aid.

4.2.4 Comparison of Peripheral Au+Au to Central d+Au

Given the remarkable similarities between peripheral Au+Au and central d+Au, it is tempting to compare the two directly.

Figure 4.10 shows the K/π ratio and Figure 4.11 shows the p/π ratio in peripheral Au+Au and central d+Au plotted together. In both cases the ratios are completely consistent with each other between the different collision species, suggesting that the particle production mechanisms in peripheral Au+Au and central d+Au are quite similar. Moreover, the previous plots showing the essentially negligible centrality dependence of particle ratios in d+Au suggests that the particle production in peripheral Au+Au is comparable to to the particle production in all d+Au collisions, regardless of centrality.

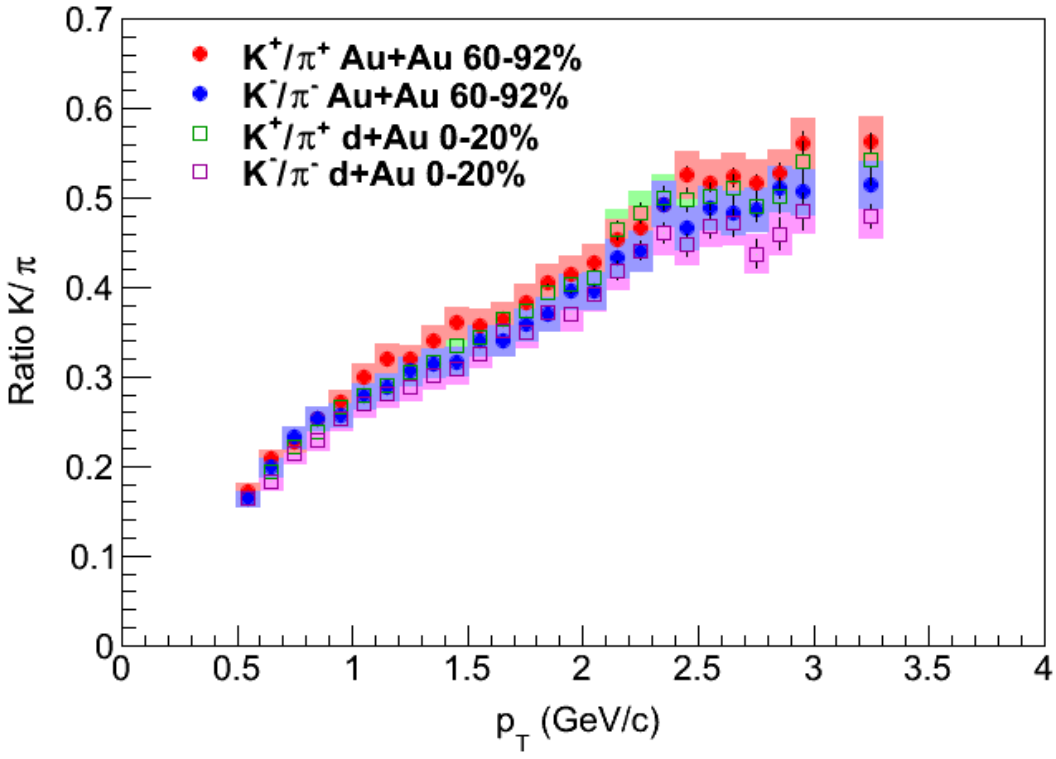

Figure 4.10: Ratio of K^+/π^+ and K^-/π^- as a function of p_T in peripheral Au+Au and central d+Au plotted together.

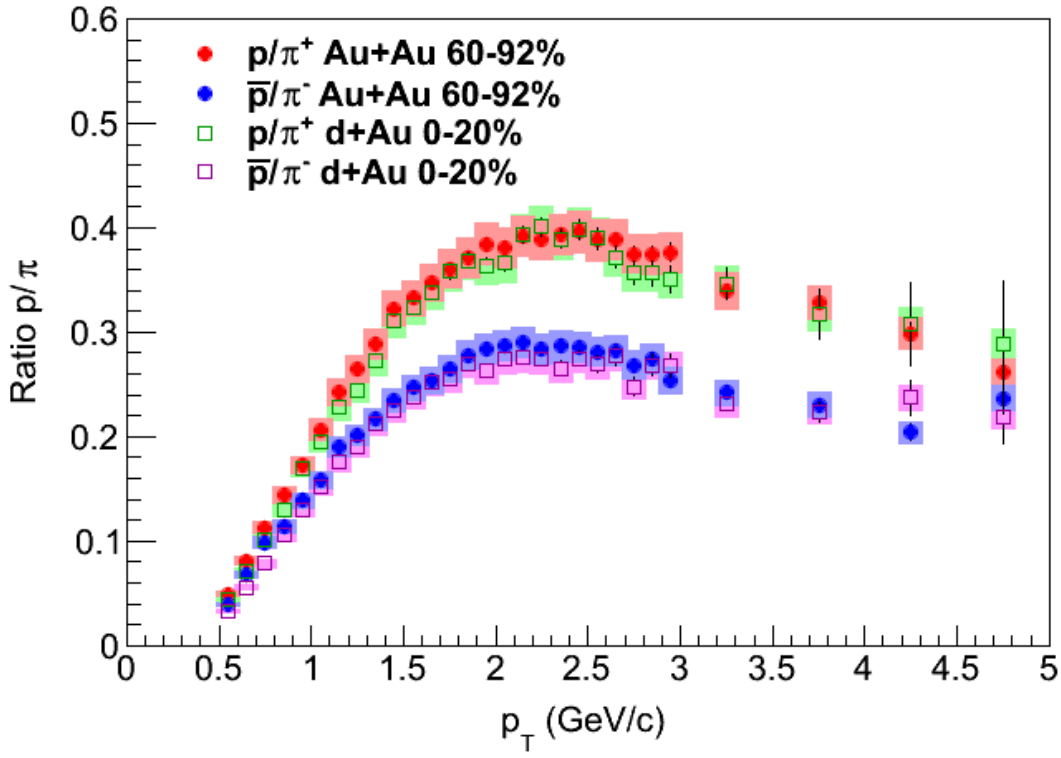

Figure 4.11: Ratio of p/π^+ and $\bar{p}/\pi^-$ as a function of p_T in peripheral Au+Au and central d+Au plotted together.

Figure 4.12 shows the ratio of the spectra in peripheral Au+Au to central d+Au, scaled by the ratio of the respective N_{coll} values, for pions, kaons, and protons. We note that the N_{coll} values for peripheral Au+Au (14.8) and central d+Au (15.1) are within 2% of each other and therefore consistent within the associated uncertainty from the Glauber model. The ratios are essentially identical for positive and negative charges. Moreover, the ratios tend to same value of roughly 0.7 for each particle species at and above 3 GeV/c. Below this p_T value, the ratio steadily increases with decreasing p_T. Moreover, there is an apparent ordering, with the protons exhibiting the largest ratio at the lowest p_T points, followed by the the kaons and then the pions. The ratios for kaons and pions are consistent within the

uncertainties while the ratio of the protons appears to be systematically above. This may be a manifestation of a baryon vs. meson effect. The apparent universal scaling above 2.5–3 GeV/c suggests a common particle production mechanism between peripheral Au+Au and central d+Au. It has already been discussed that particle production in central d+Au exhibits a Cronin enhancement while the particle production in peripheral Au+Au exhibits a small amount of suppression, hence it is not surprising this ratio is less than unity.

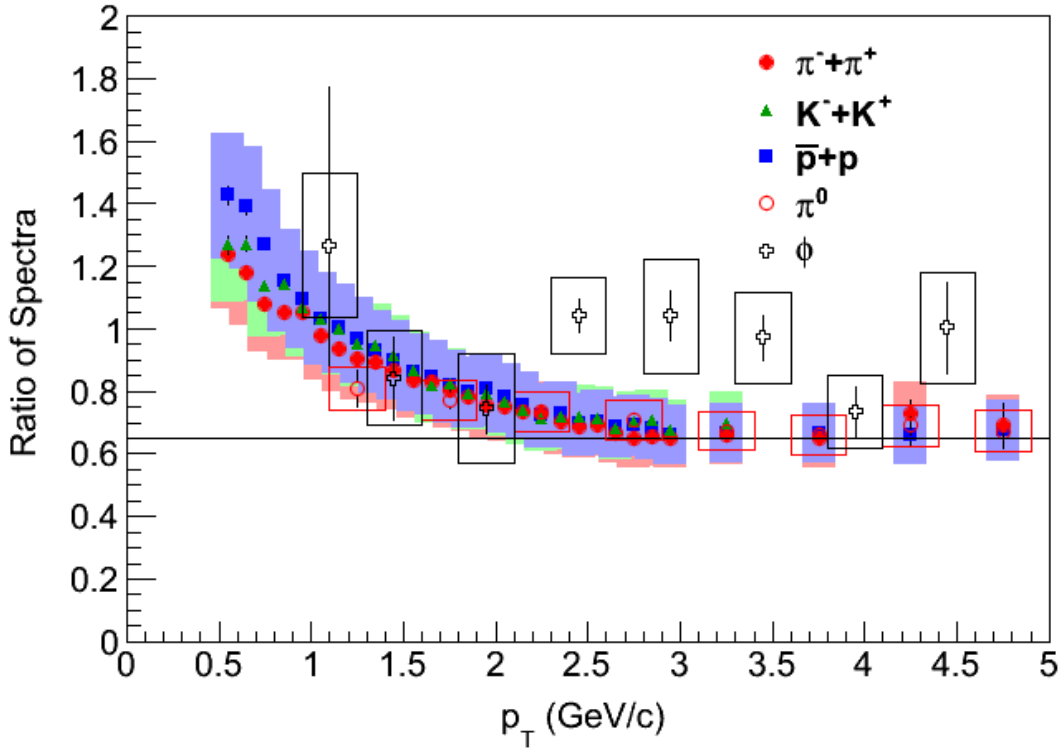

Figure 4.12: Ratio of invariant yield of particles in peripheral Au+Au collisions to central d+Au collisions as a function of p_T.

CHAPTER V

SUMMARY AND PERSPECTIVE

5.1 Infinite Time and Infinite Money

Some years ago, in the summer of 2007, I was at Brookhaven National Lab working with my good friend and then-production manager Carla Vale. One Tuesday afternoon (it was 22 May), we were already in the counting house so we decided to attend the PHENIX focus seminar for that day. The speaker was the inimitably energetic Peter Steinberg, who was, at the time, a collaborator in the already decommissioned PHOBOS, PHENIX, and ATLAS at the LHC. His talk was about the heavy ion program in the ATLAS collaboration.

It was quite clear during his presentation that the very large and highly sophisticated ATLAS was very well suited to most (though not quite all) measurements of interest for heavy ion physics. During the post-talk discussion, Carla said something that has stuck with me to this day: "this looks like the kind of detector you would build with infinite time and infinite money." Peter casually responded that she was in fact completely correct, as the LHC project had been in planning since the mid-1980s and that the total cost of ATLAS alone was approximately 1 billion CHF (1.1 billion USD).

It is all too tempting for a scientist to wonder what one might do without the arbitrary constraints imposed by academic calendars and fickle politicians. I will now very briefly explore this possibility. First I will discuss what kind of detector I would build for the measurements presented in this thesis, then I will discuss its integration into a more general

purpose design.

5.1.1 Geometrical Acceptance

What PHENIX most obviously lacks is acceptance. In the analysis presented in this thesis, the main detector subsystem used has an azimuthal coverage of 22° in azimuth and a total of 0.7 units of pseudorapidity. The coverage of the general purpose detectors at the LHC [141], ATLAS [142] and CMS [143] (the latter of which both the HEP and RHI groups at Vanderbilt are members) have full azimuthal coverage and central component coverage of at about 5 units of pseudorapidity as well forward component coverage of at about 4 more units of pseudorapidity. But even ignoring the forward coverage for the moment, the factor of roughly 16 increase in azimuthal coverage and factor of roughly 7 increase in pseudorapidity acceptance gives a factor of more than 100 increased acceptance.

Therefore, step 1 is to build a detector with TOF coverage in full azimuth and 5 units of pseudorapidity. Obviously, all other things being equal, a larger detector means larger event sizes and therefore slower event recording rates. The event recording rate bottleneck(s) maybe the things like network bandwith or hard disk write speeds. During recent operational periods in PHENIX, the main minimum bias trigger, BBCLL1 (BBC local level 1) has measured rates of up to 15 kHz. Since this is larger than what can be written to disk, it is necessary to use a prescale. A prescale is simply a numerical factor by which the number of raw triggers is reduced to the number of live triggers, i.e. the number are recorded. If we wish only to record MB events, we set the BBCLL1 prescale to 0.333. If we have additional triggers we'd also like to record, such as a trigger for a rare process, we reduce the

prescale further to accomodate that. Given that we have infinite time in addition to infinite money, we can simply run our accelerator 10 times longer to achieve the same recorded integrated luminosity to recover the factor of 100 if we wish. On the other hand, we could also develop a trigger for high p_T charged tracks. We could then record a mix of MB triggered data and high p_T triggered data. The MB triggered data will have adequate statistics for low p_T particles where the yield is high, and the triggered data will select only the very rare events that have the high p_T hadrons.

The analysis presented in this thesis is primarily not limited by statistics. However, a simple rule of thumb is that for every 1 GeV/c in p_T, the yield is reduced by an order of magnitude. Obviously one can actually look at the observed spectrum and determine the exact amounts, but for our present purposes this approximation is adequate. If we seek to extend our p_T reach by a factor of 2 from 6 GeV/c to 12 GeV/c, we need 10^6 as many MB events to preserve the same statisitical significance for the highest p_T bin. In fact, this is as strong an argument for using a special high p_T trigger as any. Let's suppose at the moment we trigger on charged tracks with $p_T > 6$ GeV/c. If N MB events gives adequate statistical significance at 6 GeV/c, It makes much more sense to record an additional N triggered events, rather than $N \times 10^6$ MB events. This is especially when N is large; in the present case, N is of order 10^7 (since the analysis in this thesis makes use of 10^9 events and we are suggesting a detector with a factor 10^2 greater acceptance), and recording 10^{13} MB events is simply not practicable.

Of course, increased statistical precision is certainly not the only advantage of better coverage. Looking at particle production differentially with respect to pseudorapidity (or, even better, rapidity) is a potentially very interesting measurement, in A+A collisions and

especially in d+A or p+A collisions.

5.1.2 Timing Resolution

Ignoring the issue of background for the moment, the main limitation on PID by TOF is the timing resolution. The TOFW used in this analysis has excellent intrinsic timing resolution of 75 ps for a total in situ resolution of 84 ps when run in conjunction with the BBC for the start time measurement. Although this is very good and is well ahead of the original design specification of 100 ps, recent developments [144, 145] in TOF technology have shown a TOF with as low as 10 ps timing resolution. If this technology were used for both the start time measurement and the track flight time measurement, total in situ resolution of order 14 ps could be achieved.

As can be seen in Figure 5.1, the configuration used in this analysis has 4σ π/K separation up to about 2.5 GeV/c and K/p separation up to about 4.0 GeV/c, and the kaon band crosses the pion centroid at about 3.2 GeV/c and the it crosses the proton centroid at about 6.0 GeV/c.

What happens if we change the in situ timing resolution from 84 ps to 14 ps, all other things being equal? We end up with something like what we see in Figure 5.2. This configuration has 4σ π/K separation up to about 5.5 GeV/c and K/p separation up to about 8.0 GeV/c, and the kaon band crosses the pion centroid at about 7.7 GeV/c and the it crosses the proton centroid at about 13.0 GeV/c.

This is a very impressive change, and we haven't even played with any other parameters yet.

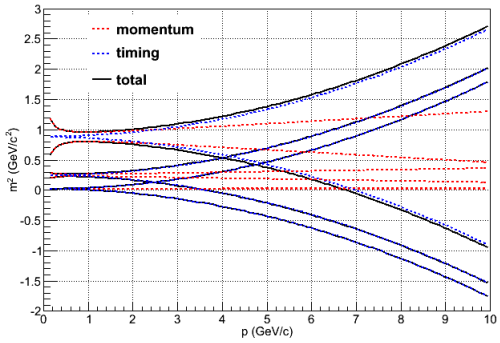

Figure 5.1: PID bands representing 2σ for pions, kaons, and protons with the standard parameter set.

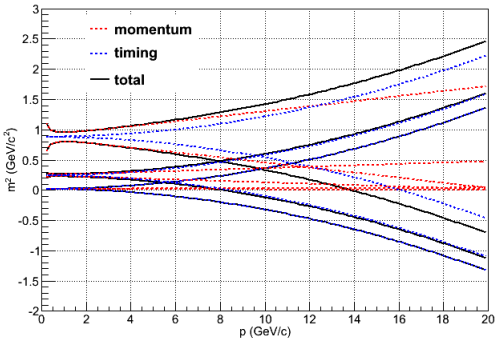

Figure 5.2: PID bands representing 2σ for pions, kaons, and protons with $\sigma_t = 14$ ps .

5.1.3 Momentum Determination and Tracking

In fact the momentum resolution does not so strongly affect the m^2 distributions, see Figure 5.3 for a compliment to Figure 5.1 and Figure 5.2 for a compliment to Figure 5.4. It does however very strongly affect how high in p_T the measurements can be regarded as meaningful. With the uncertainty in the momentum determination at high p_T being roughly $1\% \times p_T$, the uncertainty reaches 100% at 100 GeV/c. But CMS and ALICE have already shown results with unidentified hadrons going to up 100 GeV/c in p_T.

Even at 20 GeV/c with a 20% uncertainty, the minimum reasonable binwidth would be 8 GeV/c (4 GeV/c on either side of the bin width). Clearly, then, a factor of, say, 8 improvement in the momentum uncertainty is an extremely useful feature in terms of obtaining a reasonably differential measurement. This would allow us to have a 1 GeV/c bin width, which is not so unreasonable; in fact a 2 GeV/c bin width is presently used in the PHENIX π^0 analyses in this momentum range.

The momentum resolution can be improved even using the existing DC technology.

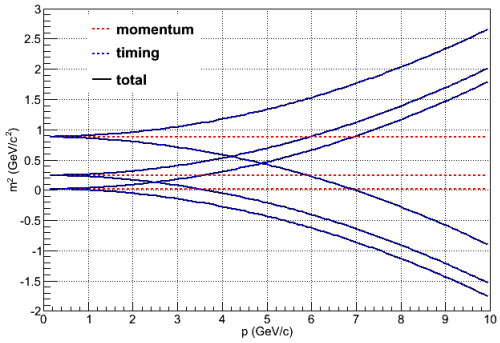

Figure 5.3: PID bands representing 2σ for pions, kaons, and protons with perfect momentum determination.

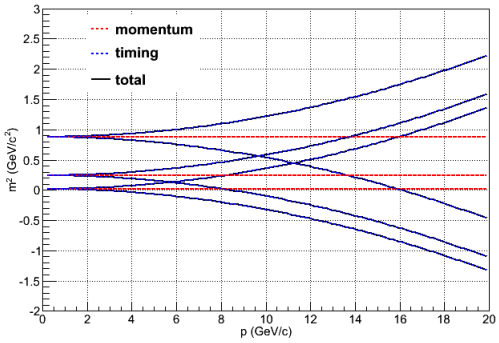

Figure 5.4: PID bands representing 2σ for pions, kaons, and protons with $\sigma_t = 14$ ps and perfect momentum determination.

The DC has a spatial resolution of roughly 150 μm in the $r - \phi$ plane, which translates to an angular resolution of order 1 mrad.

Assuming a physically larger detector can be constructed with the same spatial resolution, the angular resolution can reduced linearly with an increase in distance from the vertex to the detector, as long as adequate uniformity of the magnetic field can be maintained. Problematically an increase in distance will adversely affect the low p_T. However, this problem can easily be solved by a silicon pixel and strip detector that lies very close to the vertex. In fact we will discuss using a vertex tracker for the momentum reconstruction shortly, but first we continue our order of magnitude problem.

The momentum resolution can be further improved by increasing the strength of the magnetic field. The track bending can be approximately represented as $\alpha \approx K_1/p_T$, where K_1 is the field integral term. Since we've already doubled the distance to the DC, we've also already doubled the field integral (assuming perfectly uniform field strength, which is not the case in PHENIX, but which can be the case for our ideal detector and which will serve

us well enough for the purposes at hand). In the previous section I showed results using the Run7 reversed coil configuration, which has a field integral of 75 mrad GeV/c. In the normal configuration, the field integral is a much larger 104 mrad GeV/c. This is achieved with a roughly uniform axial field with a maximum field strength of 0.9 T. A uniform field with a much higher strength is an entirely reasonable proposition. In fact CMS has a maximum field strength of approximately 4 T with excellent uniformity. Doubling the field to 1.8 T, well below currently achievable field strengths, will give an overall increase in the field integral by a factor of 4. Too high a field can cause significant problems with low p_T tracking, but CMS can reconstruct tracks with a p_T as low as 0.3 GeV/c with good efficiencies and reasonable fake rates using only the three inner most layers of their silicon vertex detector (the three pixel layers). In fact, the first implementation of this tracking method for heavy ion data in CMS was done by current Vanderbilt University graduate student Eric Appelt.

To recapitulate, simply by doubling the distance and the magnetic field, we gain the factor of 8 improvement in momentum resolution we sought. We could further increase the field strength if so desired. However, let us now explore a better possibility: the aforementioned silicon vertex tracker. CMS employs an inner tracking system with 3 layers of pixels followed by 10 layers of strips. Using this configuration, CMS achieves remarkable momentum resolution of no worse than 3% at 100 GeV/c. This can be seen in Figure 5.5. Contrast this with the momentum resolution achieved by the DC configuration used in PHENIX seen in Figure 5.6.

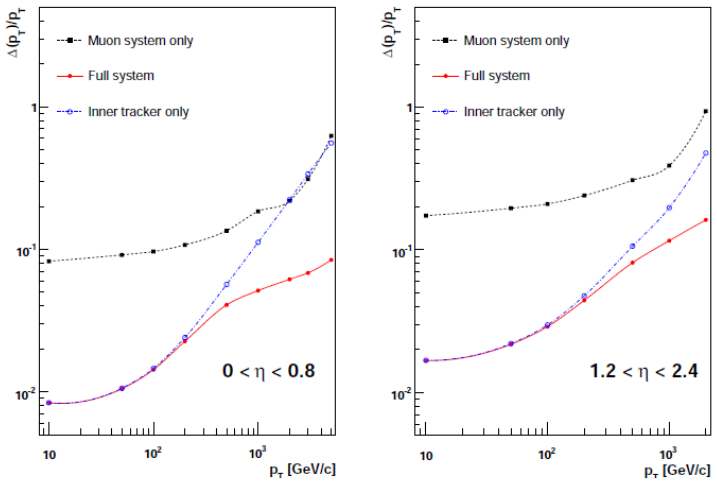

Figure 5.5: Momentum uncertainty for CMS inner tracking system, as reported in [143].

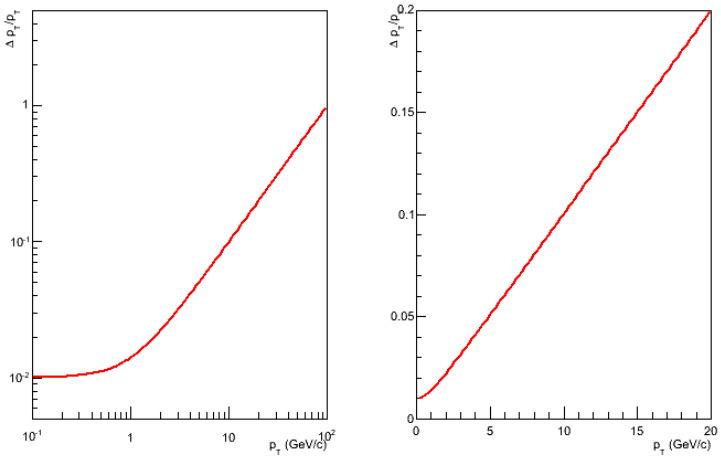

Figure 5.6: Momentum uncertainty for PHENIX DC.

There are many other advantages. For example, one can determine the location of the vertex of the track with excellent precision. Therefore, one can easily reduce or perhaps eliminate the background almost entirely by requiring a tight vertex cut. This alone gives the additional advantage of removing the weak-decay feeddown from the baryons without making any assumptions about the hyperon spectra, thereby reducing the systematic uncertainty. In addition, the hyperons themselves are also very interesting to study, and they can be identified through secondary vertex reconstruction, which can also be employed to identify certain strange mesons. For example, the baryon vs. meson dynamics could be studied using the Λ baryon and the K^0_S meson in addition to protons and pions.

5.1.4 Other methods of PID

Of course, PID by TOF is not the only means of identifying particles. Both STAR at RHIC and ALICE at the LHC do PID by TOF at low to interemediate p_T but rely on PID by the relativistic rise of dE/dx in a time projection chamber (TPC) to do PID at high p_T. A time projection chamber is a large gas volume used to construct three dimenstional tracks. The tracks are essentially continuously imaged as the TPC collects a large number of samples (typically 100 samples per meter of gas). The curvature of the track gives the momentum and the ionization of the gas gives the dE/dx [146].

Figure 5.7 shows dE/dx as a function of momentum for all tracks, with the different particle species labeled [147]. As can be seen, the dE/dx for various particles starts at a local maximum, decreases to a global minimum, and then slow starts to rise again as p_T increases. This final rise is called the relativistic rise. For $p_T > 3.0$ GeV/c or so,

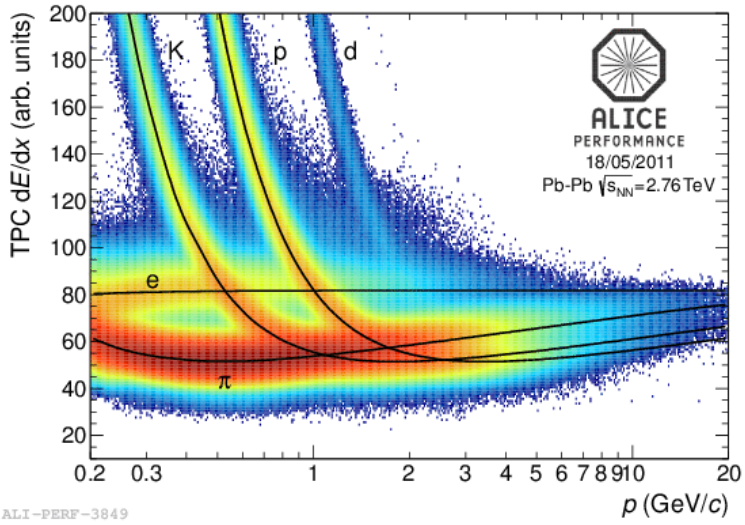

Figure 5.7: The distribution of dE/dx for all particles in a TPC [147].

all three hadrons $\pi/K/p$ are in the relativistic rise and have essentially the same slope. In this region, the the dE/dx centroids are close together and thus the distributions have considerable overlap. Therefore, PID extraction requires a statistical separation based on a simultaneous fit of multiple Gaussian distribution functions which is shown in Figure 5.8.

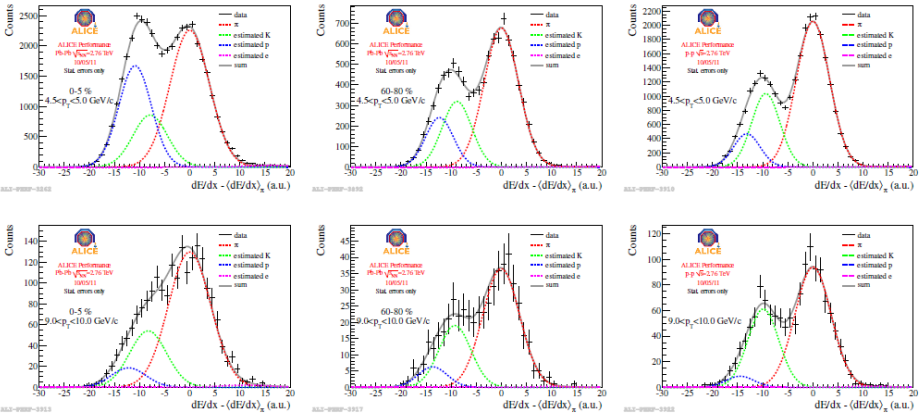

Figure 5.8: Several 1-dimensional projections of the dE/dx distribution for all particles in a TPC [147].

5.1.5 What might we learn?

The idea of course is to get pions, kaons, and protons identified the highest p_T possible so as to examine the flavor dynamics, as discussed at the end of Chapter 1. We show some results on high p_T identified particles from STAR [137, 148] and ALICE [147] in Figures 5.9, 5.10, and 5.11.

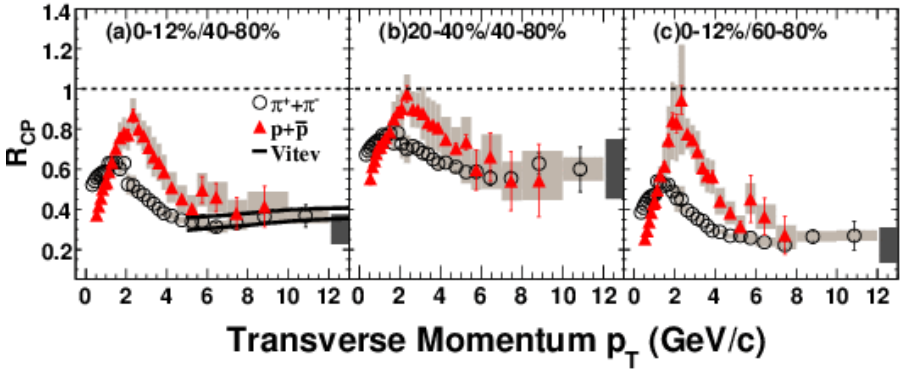

Figure 5.9: Nuclear modification factor R_{CP} for pions and protons measured by STAR [148].

It is interesting to note that in 2006 STAR published protons independently, but in 2012 they published only kaons and protons together (not fully separated). The ALICE data follow the same method as the latter STAR paper. The ALICE results are prelminary only and none have been published so far. The STAR data from 2006 suggest that the modification of protons and pions is very similar, meaning the color charge effects might be completely washed out. However, we must note that the systematic uncertainties are large. The ALICE data however show a similar trend, which is especially compelling given their additional measurement of Λ and K^0_S as shown in Figure 5.11. While we obviously

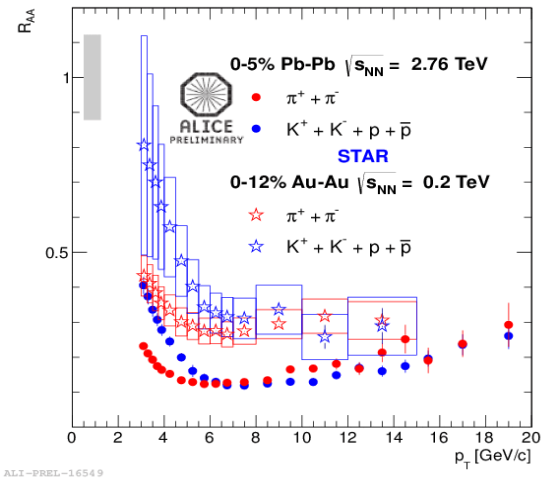

Figure 5.10: Nuclear modification factor R_{AA} of $\pi^{\pm}$ and $K^{\pm} + p$ as measured by ALICE [147] shown with similar measurements done by STAR [137].

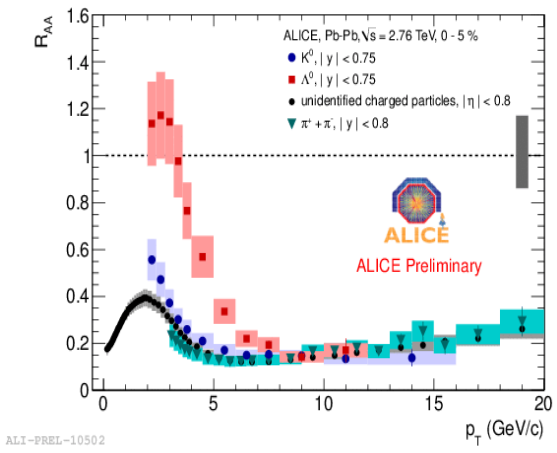

Figure 5.11: Nuclear modification factor R_{AA} various identified hadrons as measured by ALICE [147].

can't definitively conclude that baryons and mesons have the same modification, it does seem clear that if flavor dependent effects are present at all, they must be fairly small. While jet flavor conversions [110] do offer a natural and intuitive explanation for how the color charge effect would be washed out, more observables specific to the model need to be calculated and measured to make any definitive statements about it.

5.2 Summary

In summary we have presented identified charged hadron spectra and ratios as a function of p_T and centrality for Au+Au and d+Au collisions at $\sqrt{s_{NN}} = 200$ GeV. We find that the homogeneous ratios are largely independent of p_T, centrality, and collisions species. We find that the kaon to pion ratios exhibit a p_T dependent enhancement as a function of centrality in Au+Au collisions, and this ratio is centrality independent in d+Au collisions and consistent with peripheral Au+Au collisions. We further find that the kaon nuclear

modification factors in Au+Au exhibit a suppression pattern that is not quite as strong as that of the pions, while in d+Au they exhibit essentially the same Cronin enhancement. For protons, we find a significant and strongly centrality dependent enhancement in Au+Au collisions. In d+Au collisions, there is a weak centrality dependence, and the most central d+Au is consistent with the most peripheral Au+Au. We further find that the nuclear modification factors in Au+Au for protons show no apparent suppression and in fact a slight enhancement at intermediate p_T, while this enhancement disappears at higher p_T with the nuclear modification factor of protons approaching that of pions at the highest p_T available. The nuclear modification factors of protons in d+Au exhibit a strong Cronin enhancement, much stronger than that of either the pion or kaon. Finally, in addition to many similarities between peripheral Au+Au and central d+Au observed in the particle ratios, we find that the direct ratio of of the spectra in peripheral Au+Au and central d+Au is independent of particle species and p_T above a certain threshold (2.5–3.0 GeV/c).

5.3 Final Thoughts

It has been a long journey to this point. For you, reader, but especially for me. This has been a long 200-some-odd pages for you but an infinitely longer 7 years for me. Regardless, it was in graduate school that I met my wife, and that alone has made the entire experience worth doing. Would I do it again? I would.

APPENDIX A

ABBREVIATIONS

- AGS - Alternating Gradient Synchrotron
- BNL - Brookhaven National Laboratory
- CERN - Organisation européene pour la recherche nucléaire (French: European Organization for Nuclear Research)
- GSI - Gesellschaft für Schwerionenforschung (German: Institute for Heavy Ion Research)
- ISR - Intersecting Storage Ring
- LBNL - Lawrence Berkeley National Laboratory
- LHC - Large Hadron Collider
- QCD - Quantum Chromodynamics
- QED - Quantum Electrodynamics
- QGP - Quark Gluon Plasma
- RHIC - Relativistic Heavy Ion Collider
- SIS - Schwerionensynchrotron (German: Heavy Ion Synchrotron)
- SLAC - Stanford Linear Accelerator Center
- SPS - Super Proton Synchrotron

APPENDIX B

UNITS

It is quite common, especially in high energy physics, to adopt a system of units that naturally lends itself to the field of study. In this dissertation, as is customary in high energy physics, I use the so-called "natural units" in which $\hbar = c = 1$. Because high energy nuclear physics is frequently interested in thermodynamics, the Boltzmann constant, k_B, is also taken to be unity. In this system, temperature, mass, momentum, and energy all have the same units, reported in decadal multiples of eV, usually MeV and GeV. In addition, time and length have the same units, usually reported in fm or cm. Lastly, mass and length are inversely proportional to each other, and the following relation gives a convenient relationship between the two: $\hbar c$ = 197.3 MeV fm.

APPENDIX C

COORDINATE SYSTEMS AND KINEMATIC VARIABLES

The natural symmetry of most high energy experiments is cylindrical. The beam pipe defines the z-axis, and the plane normal to the z-axis is the transverse (xy) plane. The definitions of the x- and y-axes are with y pointing up and x pointing to a side, and the directions are usually chosen in keeping with a right-handed coordinate system. Lorentz boosts are restricted to be along the z-axis, the boost parameter is usually called y. This restriction gives the rapidity a fairly simple definition:

$$y = \frac{1}{2} \ln \frac{E + p_z}{E - p_z}. \tag{C.1}$$

Sometimes, when the mass of the particle is not known (i.e. only the charge and momentum of the track have been determined), pseudo-rapidity is used instead, which can be defined as

$$\eta = \frac{1}{2} \ln \frac{p + p_z}{p - p_z}. \tag{C.2}$$

This definition illustrates the connection to rapidity; however, it belies its simplicity and hence the reason for its common use. It can also be defined as $\eta = -\ln(\tan(\theta/2))$, which demonstrates its immediate connection to a direct observable, the angle of emission with respect to the z-axis (the zenith angle). However, rapidity is preferred by theoretical calculations and so is a better variable to use when possible (i.e. when particle identification is

available).

Instead of total momentum, transverse momentum, p_T, is usually used; since boosts are restricted to the z-axis, this is a Lorentz invariant (by construction). Indeed, by this construction, all transverse quantities are Lorentz invariant. Another useful variable is the transverse mass, which could also be called the transverse energy; it is defined as

$$m_T = \sqrt{p_T^2 + m^2}. \tag{C.3}$$

Clearly, the transverse kinetic energy is simply $KE_T = m_T - m$.

APPENDIX D

A SKIRMISH WITH QCD

In order to get a glimpse at the depth and richness of QCD, let us take a brief look at the Lagrangian. In this section, I borrow heavily from graduate level survey texts on QFT [149, 150], as well as more specialized texts on QCD [1, 2]. I do not present any original work, I merely catalog the various important ideas and results in a systematic way.

Quarks are fermions with an extra degree of freedom called color. This can be motivated by examining the wave function of the Δ^{++} baryon:

$$|\Delta^{++}\rangle = |u,\uparrow\rangle \otimes |u,\uparrow\rangle \otimes |u,\uparrow\rangle \tag{D.1}$$

or, as a shorthand,

$$|\Delta^{++}\rangle = |u,\uparrow;u,\uparrow;u,\uparrow\rangle. \tag{D.2}$$

Clearly, this is not allowed by the Pauli Exclusion Principle. Therefore, there must be some hidden degree of freedom or internal symmetry at work. To properly anti-symmetrize this wavefunction, we can make a shrewd use of the Levi-Civita tensor:

$$|\Delta^{++}\rangle = \sum_{i,j,k=1}^{3} \epsilon^{ijk} |u,i,\uparrow;u,j,\uparrow;u,k,\uparrow\rangle. \tag{D.3}$$

We interpret this extra degree of freedom as color. With this in mind, we can write a quark

spinor as a triplet of spinors, one for each color:

$$\psi = \begin{pmatrix} \psi_r \\ \psi_g \\ \psi_b \end{pmatrix}. \tag{D.4}$$

Let us now examine quantum field theoretic formulation of the celebrated Dirac equation, which describes a free fermion:

$$i\partial\!\!\!/\psi - m\psi = 0. \tag{D.5}$$

The Dirac conjugate of this equation, which describes a free anti-fermion, is

$$i\partial\!\!\!/\bar{\psi} + m\bar{\psi} = 0. \tag{D.6}$$

These equations are in fact simply the Euler-Lagrange equations of the Dirac Lagrangian,

$$\mathcal{L} = \bar{\psi}(i\partial\!\!\!/ - m)\psi. \tag{D.7}$$

Since the color degree of freedom is hidden, an arbitrary phase rotation between the three components of the color triplet should leave the Lagrangian invariant. To mix the components of a column vector with three components, one needs a 3×3 matrix. We make the following transformation: $\psi \to \psi' = V\psi$ and $\bar{\psi} \to \bar{\psi}' = \bar{\psi}V^\dagger$. Clearly, this leaves the Dirac Lagrangian invariant if V is unitary. We also make the further restriction that the

determinant is unity, and so $V \in SU(3)$.

Let us now consider the case where we promote the global phase rotation to a local one, i.e. $V \to V(x)$. This process of promoting a global transformation to a local one is called gauging, and the invariance of the Lagrangian under these symmetries is called gauge invariance. To ensure invariance of the Lagrangian, new fields have to be introduced, and these are called the gauge fields; these fields are always vector fields and so the quantized states are always vector particles, and thus are called the gauge bosons. Here, since there are eight generators of $SU(3)$, we have eight gluons. Since the new term introduced contains both the fermion fields and the gauge fields, it is called the interaction term. This means we can interpret the gauge fields as the fields which mediate the interaction. On the quantum level, we have quarks interacting by exchanging gluons. Unfortunately, the mathematical formulation of all of this is much too complex to treat here, so I'll just give the results.

The gauge covariant derivative is constructed in such a way that it leaves the Dirac Lagrangian invariant under the minimal substitution $\partial_\mu \to D_\mu$. The gauge covariant derivative is:

$$D_\mu = \partial_\mu + igA^a_\mu t_a. \tag{D.8}$$

The free gauge field strength tensor can be determined by the commutator of the gauge covariant derivative with itself:

$$[D_\mu, D_\nu] = -igF^a_{\mu\nu} t_a, \tag{D.9}$$

so the definition of the gluon field strength tensor is

$$F^a_{\mu\nu} = \partial_\mu A^a_\nu - \partial_\nu A^a_\mu + C^a_{bc} A^b_\mu A^c_\nu. \tag{D.10}$$

The first two terms look just like the field strength tensor for the free photon field, but the third term here is truly remarkable. As a consequence of the non-commutativity of the generators, there is a coupling between two gluon fields. This means that, unlike the photon of QED, the gluons of QCD can interact with each other. Since this is a consequence of the fact that the gauge symmetry is described by a non-Abelian group, QCD is called a non-Abelian gauge field theory.

If we put this all together, we can write the QCD Lagrangian in a very terse way:

$$\mathcal{L}_{\mathrm{QCD}} = -\frac{1}{4} F^a_{\mu\nu} F^{\mu\nu}_a + \bar{\psi}(i\not{D} - m)\psi. \tag{D.11}$$

We can also write it in a more revealing manner:

$$\mathcal{L}_{\mathrm{QCD}} = -\frac{1}{4} F^a_{\mu\nu} F^{\mu\nu}_a + \bar{\psi}(i\not{\partial} - m)\psi - g\bar{\psi}\not{A}^a t_a \psi, \tag{D.12}$$

where the first term is the free gauge field term, the second term is the free fermion field term, and the last term is the interaction term.

REFERENCES

[1] T. Muta. *Foundations of Quantum Chromodynamics*. World Scientific, River Edge, NJ, USA, 1998.

[2] W. Greiner, S. Schramm, and E. Stein. *Quantum Chromodynamics*. Springer-Verlag, Berlin, Germany, 2007.

[3] Edward V. Shuryak. Quantum Chromodynamics and the Theory of Superdense Matter. *Phys. Rept.*, 61:71–158, 1980.

[4] K. Adcox et al. Formation of dense partonic matter in relativistic nucleus-nucleus collisions at RHIC: Experimental evaluation by the PHENIX collaboration. *Nucl.Phys.*, A757:184–283, 2005.

[5] C.-Y. Wong. *Introduction to High-Energy Heavy-Ion Collisions*. World Scientific, River Edge, NJ, USA, 1994.

[6] J. Bartke. *Introduction to Relativistic Heavy Ion Physics*. World Scientific, Hackensack, NJ, USA, 2009.

[7] W. Florkowski. *Phenomenology of Ultra-Relativistic Heavy-Ion Collisions*. World Scientific, Hackensack, NJ, USA, 2010.

[8] Michele Arneodo. Nuclear effects in structure functions. *Phys.Rept.*, 240:301–393, 1994.

[9] L.V. Gribov, E.M. Levin, and M.G. Ryskin. Semihard Processes in QCD. *Phys.Rept.*, 100:1–150, 1983.

[10] Edmond Iancu and Raju Venugopalan. The color glass condensate and high energy scattering in QCD. *arXiv:hep-ph/0303204*, 2003.

[11] E. F. Mattathias. Identifed Particle Production in p+p and d+Au Collisions at RHIC Energies. Doctoral Dissertation in Physics, Stony Brook University, Stony Brook, December 2004.

[12] Dmitri Kharzeev, Eugene Levin, and Larry McLerran. Parton saturation and N(part) scaling of semihard processes in QCD. *Phys.Lett.*, B561:93–101, 2003.

[13] S.S. Adler et al. Absence of suppression in particle production at large transverse momentum in $\sqrt{s_{NN}}$ = 200 GeV d+Au collisions. *Phys.Rev.Lett.*, 91:072303, 2003.

[14] J.W. Cronin, Henry J. Frisch, M.J. Shochet, J.P. Boymond, R. Mermod, et al. Production of Hadrons with Large Transverse Momentum at 200-GeV, 300-GeV, and 400-GeV. *Phys.Rev.*, D11:3105, 1975.

[15] D. Antreasyan, J.W. Cronin, Henry J. Frisch, M.J. Shochet, L. Kluberg, et al. Production of Hadrons at Large Transverse Momentum in 200-GeV, 300-GeV and 400-GeV p p and p n Collisions. *Phys.Rev.*, D19:764–778, 1979.

[16] Alberto Accardi. Cronin effect in proton nucleus collisions: A Survey of theoretical models. 2002.

[17] Rudolph C. Hwa and C.B. Yang. Final state interaction as the origin of the Cronin effect. *Phys.Rev.Lett.*, 93:082302, 2004.

[18] R.J. Glauber and G. Matthiae. High-energy scattering of protons by nuclei. *Nucl.Phys.*, B21:135–157, 1970.

[19] Prashant Shukla. Glauber model for heavy ion collisions from low energies to high energies. *arXiv:nucl-th/0112039*, 2001.

[20] L. D. Landau. On the multiparticle production in high-energy collisions. *Izv. Akad. Nauk SSSR Ser. Fiz.*, 17:51–64, 1953.

[21] P. Carruthers and Minh Doung-van. Rapidity and angular distributions of charged secondaries according to the hydrodynamical model of particle production. *Phys. Rev.*, D8:859–874, 1973.

[22] J. D. Bjorken. Highly Relativistic Nucleus-Nucleus Collisions: The Central Rapidity Region. *Phys. Rev.*, D27:140–151, 1983.

[23] I. G. Bearden et al. Nuclear stopping in Au+Au collisions at $\sqrt{s_{NN}}$ = 200 GeV. *Phys. Rev. Lett.*, 93:102301, 2004.

[24] K. Adcox et al. Measurement of the mid-rapidity transverse energy distribution from $\sqrt{s_{NN}}$ = 130 GeV Au+Au collisions at RHIC. *Phys.Rev.Lett.*, 87:052301, 2001.

[25] S.S. Adler et al. Systematic studies of the centrality and $\sqrt{s_{NN}}$ dependence of the $dE_T/d\eta$ and $dN_{ch}/d\eta$ in heavy ion collisions at mid-rapidity. *Phys.Rev.*, C71:034908, 2005.

[26] F. Karsch, E. Laermann, and A. Peikert. Quark mass and flavor dependence of the QCD phase transition. *Nucl. Phys.*, B605:579–599, 2001.

[27] Frithjof Karsch. Lattice results on QCD thermodynamics. *Nucl. Phys.*, A698:199–208, 2002.

[28] Peter F. Kolb, Josef Sollfrank, and Ulrich W. Heinz. Anisotropic transverse flow and the quark hadron phase transition. *Phys.Rev.*, C62:054909, 2000.

[29] A. Andronic, P. Braun-Munzinger, and J. Stachel. Hadron production in central nucleus nucleus collisions at chemical freeze-out. *Nucl. Phys.*, A772:167–199, 2006.

[30] V. Koch. Lecture notes on global observables. Public lecture, http://oldsite.to.infn.it/qgp/School07/koch.pdf.

[31] Masashi Kaneta and Nu Xu. Centrality dependence of chemical freeze-out in Au+Au collisions at RHIC. *nucl-th/0405068*, 2004.

[32] J. Cleymans, Burkhard Kampfer, M. Kaneta, S. Wheaton, and N. Xu. Centrality dependence of thermal parameters deduced from hadron multiplicities in Au+Au collisions at $\sqrt{s_{NN}}$ = 130 GeV. *Phys. Rev.*, C71:054901, 2005.

[33] Frithjof Karsch. Lattice QCD at high temperature and density. *Lect. Notes Phys.*, 583:209–249, 2002.

[34] Peter Braun-Munzinger, Krzysztof Redlich, and Johanna Stachel. Particle production in heavy ion collisions. *nucl-th/0304013*, 2003.

[35] M. Stephanov. Plenary Talk at Quark Matter 2008.

[36] Berndt Muller. Hadronic signals of deconfinement at RHIC. *arXiv:nucl-th/0404015*, 2004.

[37] John Adams et al. Experimental and theoretical challenges in the search for the quark gluon plasma: The STAR Collaboration's critical assessment of the evidence from RHIC collisions. *Nucl.Phys.*, A757:102–183, 2005.

[38] S.S. Adler et al. Identified charged particle spectra and yields in Au+Au collisions at $\sqrt{s_{NN}}$ = 200 GeV. *Phys.Rev.*, C69:034909, 2004.

[39] N. Herrmann, J. P. Wessels, and T. Wienold. Collective flow in heavy-ion collisions. *Ann. Rev. Nucl. Part. Sci.*, 49:581–632, 1999.

[40] S. Huang. Measurements of high p_T identified particles v_2 and v_4 in $\sqrt{s_{NN}}$ = 200 GeV Au+Au collisions by PHENIX. *J.Phys.G*, G35:104105, 2008.

[41] Burak Han Alver, Clement Gombeaud, Matthew Luzum, and Jean-Yves Ollitrault. Triangular flow in hydrodynamics and transport theory. *Phys. Rev.*, C82:034913, 2010.

[42] Hannah Petersen, Guang-You Qin, Steffen A. Bass, and Berndt Muller. Triangular flow in event-by-event ideal hydrodynamics in Au+Au collisions at $\sqrt{s_{\rm NN}} = 200A$ GeV. *Phys. Rev.*, C82:041901, 2010.

[43] A. Adare et al. Measurements of Higher-Order Flow Harmonics in Au+Au Collisions at $\sqrt{s_{NN}} = 200$ GeV. *Phys.Rev.Lett.*, 107:252301, 2011.

[44] John Adams et al. Directed flow in Au+Au collisions at $\sqrt{s_{NN}}$ = 62- GeV. *Phys. Rev.*, C73:034903, 2006.

[45] M. Issah. Private communication.

[46] Xin-Nian Wang. Effect of jet quenching on high p_T hadron spectra in high-energy nuclear collisions. *Phys. Rev.*, C58:2321, 1998.

[47] J. Velkovska. P(t) distributions of identified charged hadrons measured with the PHENIX experiment at RHIC. *Nucl.Phys.*, A698:507–510, 2002.

[48] Ivan Vitev and Miklos Gyulassy. Jet quenching and the anti-p greater than or equal to pi- anomaly at RHIC. *Phys.Rev.*, C65:041902, 2002.

[49] K. Adcox et al. Centrality dependence of pi+ / pi-, K+ / K-, p and anti-p production from s(NN)**(1/2) = 13-=GeV Au+Au collisions at RHIC. *Phys.Rev.Lett.*, 88:242301, 2002.

[50] Stephen Scott Adler et al. Scaling properties of proton and anti-proton production in $\sqrt{s_{NN}}$ = 200 GeV Au+Au collisions. *Phys. Rev. Lett.*, 91:172301, 2003.

[51] Stephen Scott Adler et al. Production of Phi mesons at mid-rapidity in $\sqrt{s_{NN}}$ = 200 GeV Au+Au collisions at RHIC. *Phys. Rev.*, C72:014903, 2005.

[52] C. Adler et al. Mid-rapidity Lambda and Antilambda production in Au+Au collisions at $\sqrt{s_{NN}}$ = 130 GeV. *Phys. Rev. Lett.*, 89:092301, 2002.

[53] Rudolph C. Hwa and C. B. Yang. Scaling behavior at high p_T and the p/pi ratio. *Phys. Rev.*, C67:034902, 2003.

[54] K.P. Das and Rudolph C. Hwa. Quark - anti-Quark Recombination in the Fragmentation Region. *Phys.Lett.*, B68:459, 1977.

[55] Rudolph C. Hwa. Clustering and Hadronization of Quarks: A Treatment of the Low p(t) Problem. *Phys.Rev.*, D22:1593, 1980.

[56] Rudolph C. Hwa and C. B. Yang. Fragmentation or recombination at high p_T? *J. Phys.*, G30:S1117–S1120, 2004.

[57] R. J. Fries, Berndt Muller, C. Nonaka, and S. A. Bass. Hadronization in heavy ion collisions: Recombination and fragmentation of partons. *Phys. Rev. Lett.*, 90:202303, 2003.

[58] R. J. Fries, Berndt Muller, C. Nonaka, and S. A. Bass. Hadron production in heavy ion collisions: Fragmentation and recombination from a dense parton phase. *Phys. Rev.*, C68:044902, 2003.

[59] V. Greco, C. M. Ko, and P. Levai. Parton coalescence and antiproton/pion anomaly at RHIC. *Phys. Rev. Lett.*, 90:202302, 2003.

[60] V. Greco, C. M. Ko, and P. Levai. Parton coalescence at RHIC. *Phys. Rev.*, C68:034904, 2003.

[61] S. Huang. Private communication.

[62] Denes Molnar and Sergei A. Voloshin. Elliptic flow at large transverse momenta from quark coalescence. *Phys.Rev.Lett.*, 91:092301, 2003.

[63] Paul Sorensen. Particle dependence of elliptic flow in Au + Au collisions at s(NN)**(1/2) = 200-GeV. *J.Phys.G*, G30:S217–S222, 2004.

[64] Rudolph C. Hwa and C.B. Yang. Azimuthal Anisotropy: Ridges, Recombination and Breaking of Quark Number Scaling. *Phys.Rev.*, C78:044903, 2008.

[65] A. Adare et al. Deviation from quark-number scaling of the anisotropy parameter v_2 of pions, kaons, and protons in Au+Au collisions at $\sqrt{s_{NN}}$ = 200 GeV. 2012.

[66] Peter F. Kolb, Lie-Wen Chen, Vincenzo Greco, and Che Ming Ko. Momentum anisotropies in the quark coalescence model. *Phys.Rev.*, C69:051901, 2004.

[67] S. A. Bass, B. Mueller, and W. A. Zajc. Virtual journal on qcd matter. http://qgp.phy.duke.edu/.

[68] Berndt Muller, R. J. Fries, and S. A. Bass. Thermal recombination: Beyond the valence quark approximation. *Phys. Lett.*, B618:77–83, 2005.

[69] David A. Appel. JETS AS A PROBE OF QUARK - GLUON PLASMAS. *Phys.Rev.*, D33:717, 1986.

[70] A. Majumder. A Comparative study of Jet-quenching Schemes. *J.Phys.G*, G34:S377–388, 2007.

[71] Urs Achim Wiedemann. Jet Quenching in Heavy Ion Collisions. 2009.

[72] S. A. Bass et al. Systematic Comparison of Jet Energy-Loss Schemes in a 3D hydrodynamic medium. *J. Phys.*, G35:104064, 2008.

[73] Steffen A. Bass et al. Systematic Comparison of Jet Energy-Loss Schemes in a realistic hydrodynamic medium. *Phys. Rev.*, C79:024901, 2009.

[74] W. A. Horowitz and B. A. Cole. Systematic theoretical uncertainties in jet quenching due to gluon kinematics. *Phys. Rev.*, C81:024909, 2010.

[75] R. Baier, Yuri L. Dokshitzer, Alfred H. Mueller, S. Peigne, and D. Schiff. Radiative energy loss of high energy quarks and gluons in a finite-volume quark-gluon plasma. *Nucl. Phys.*, B483:291–320, 1997.

[76] R. Baier, Yuri L. Dokshitzer, Alfred H. Mueller, S. Peigne, and D. Schiff. Radiative energy loss and p_T-broadening of high energy partons in nuclei. *Nucl. Phys.*, B484:265–282, 1997.

[77] B. G. Zakharov. Radiative energy loss of high energy quarks in finite-size nuclear matter and quark-gluon plasma. *JETP Lett.*, 65:615–620, 1997.

[78] Urs Achim Wiedemann. Gluon radiation off hard quarks in a nuclear environment: Opacity expansion. *Nucl. Phys.*, B588:303–344, 2000.

[79] Carlos A. Salgado and Urs Achim Wiedemann. Calculating quenching weights. *Phys.Rev.*, D68:014008, 2003.

[80] Nestor Armesto, Carlos A. Salgado, and Urs Achim Wiedemann. Medium induced gluon radiation off massive quarks fills the dead cone. *Phys.Rev.*, D69:114003, 2004.

[81] Miklos Gyulassy, Peter Levai, and Ivan Vitev. Jet quenching in thin quark gluon plasmas. 1. Formalism. *Nucl.Phys.*, B571:197–233, 2000.

[82] M. Gyulassy, P. Levai, and I. Vitev. NonAbelian energy loss at finite opacity. *Phys.Rev.Lett.*, 85:5535–5538, 2000.

[83] Xin-Nian Wang and Xiao-feng Guo. Multiple parton scattering in nuclei: Parton energy loss. *Nucl.Phys.*, A696:788–832, 2001.

[84] Peter Brockway Arnold, Guy D. Moore, and Laurence G. Yaffe. Transport coefficients in high temperature gauge theories. 1. Leading log results. *JHEP*, 0011:001, 2000.

[85] Peter Brockway Arnold, Guy D. Moore, and Laurence G. Yaffe. Photon emission from ultrarelativistic plasmas. *JHEP*, 0111:057, 2001.

[86] Peter Brockway Arnold, Guy D. Moore, and Laurence G. Yaffe. Photon and gluon emission in relativistic plasmas. *JHEP*, 0206:030, 2002.

[87] J. D. Bjorken. Energy Loss of Energetic Partons in Quark - Gluon Plasma: Possible Extinction of High p(t) Jets in Hadron - Hadron Collisions. 1982. FNAL internal code FERMILAB-PUB-82-059-THY.

[88] Munshi G. Mustafa and Markus H. Thoma. Quenching of hadron spectra due to the collisional energy loss of partons in the quark gluon plasma. *Acta Phys. Hung.*, A22:93–102, 2005.

[89] Simon Wicks, William Horowitz, Magdalena Djordjevic, and Miklos Gyulassy. Elastic, Inelastic, and Path Length Fluctuations in Jet Tomography. *Nucl. Phys.*, A784:426–442, 2007.

[90] Thorsten Renk. The Phenomenology of Elastic Energy Loss. *Phys. Rev.*, C76:064905, 2007.

[91] S.S. Adler et al. A Detailed Study of High p_T Neutral Pion Suppression and Azimuthal Anisotropy in Au+Au Collisions at $\sqrt{s_{NN}}$ = 200 GeV. *Phys.Rev.*, C76:034904, 2007.

[92] A. Adare et al. Quantitative Constraints on the Opacity of Hot Partonic Matter from Semi-Inclusive Single High Transverse Momentum Pion Suppression in Au+Au collisions at $\sqrt{s_{NN}}$ = 200 GeV. *Phys.Rev.*, C77:064907, 2008.

[93] A. Adare et al. Suppression pattern of neutral pions at high transverse momentum in Au+Au collisions at $\sqrt{s_{NN}}$ = 200 GeV and constraints on medium transport coefficients. *Phys.Rev.Lett.*, 101:232301, 2008.

[94] S. Afanasiev et al. High p_T π^0 Production with Respect to the Reaction Plane in Au+Au Collisions at $\sqrt{s_{NN}}$ = 200 GeV. *Phys.Rev.*, C80:054907, 2009.

[95] A. Adare et al. Azimuthal anisotropy of neutral pion production in Au+Au collisions at $\sqrt{(s_N N)}$ = 200 GeV: Path-length dependence of jet quenching and the role of initial geometry. *Phys.Rev.Lett.*, 105:142301, 2010.

[96] S.S. Adler et al. Dense-Medium Modifications to Jet-Induced Hadron Pair Distributions in Au+Au Collisions at $\sqrt{s_{NN}}$ = 200 GeV. *Phys.Rev.Lett.*, 97:052301, 2006.

[97] A. Adare et al. System Size and Energy Dependence of Jet-Induced Hadron Pair Correlation Shapes in Cu+Cu and Au+Au Collisions at $\sqrt{s_{NN}}$ = 200 and 62.4 GeV. *Phys.Rev.Lett.*, 98:232302, 2007.

[98] A. Adare et al. Transverse momentum and centrality dependence of dihadron correlations in Au+Au collisions at $\sqrt{s_{NN}}$ = 200 GeV: Jet-quenching and the response of partonic matter. *Phys.Rev.*, C77:011901, 2008.

[99] A. Adare et al. Dihadron azimuthal correlations in Au+Au collisions at $\sqrt{s_{NN}}$ = 200 GeV. *Phys.Rev.*, C78:014901, 2008.

[100] A. Adare et al. Suppression of away-side jet fragments with respect to the reaction plane in Au+Au collisions at $\sqrt{s_{NN}}$ = 200 GeV. *Phys.Rev.*, C84:024904, 2011.

[101] A. Adare et al. Trends in Yield and Azimuthal Shape Modification in Dihadron Correlations in Relativistic Heavy Ion Collisions. *Phys.Rev.Lett.*, 104:252301, 2010.

[102] A. Adare et al. Photon-Hadron Jet Correlations in p+p and Au+Au Collisions at $\sqrt{s_{NN}}$ = 200 GeV. *Phys.Rev.*, C80:024908, 2009.

[103] Zhangbu Xu. High p_T Identified Particle Spectra. 2008.

[104] S. Albino, B.A. Kniehl, and G. Kramer. Fragmentation functions for light charged hadrons with complete quark flavor separation. *Nucl.Phys.*, B725:181–206, 2005.

[105] S. Albino, B.A. Kniehl, and G. Kramer. AKK Update: Improvements from New Theoretical Input and Experimental Data. *Nucl.Phys.*, B803:42–104, 2008.

[106] Daniel de Florian, Rodolfo Sassot, and Marco Stratmann. Global analysis of fragmentation functions for pions and kaons and their uncertainties. *Phys.Rev.*, D75:114010, 2007.

[107] Daniel de Florian, Rodolfo Sassot, and Marco Stratmann. Global analysis of fragmentation functions for protons and charged hadrons. *Phys.Rev.*, D76:074033, 2007.

[108] Daniel de Florian, Rodolfo Sassot, and Marco Stratmann. Fragmentation functions for pions, kaons, protons and charged hadrons. *J.Phys.Conf.Ser.*, 110:022045, 2008.

[109] W. Liu, C.M. Ko, and B.W. Zhang. Jet conversions in a quark-gluon plasma. *Phys.Rev.*, C75:051901, 2007.

[110] W. Liu and R.J Fries. Probing nuclear matter with jet conversions. *Phys.Rev.*, C77:054902, 2008.

[111] H. Hahn et al. The RHIC design overview. *Nucl. Instrum. Meth.*, A499:245–263, 2003.

[112] K. Adcox et al. PHENIX detector overview. *Nucl. Instrum. Meth.*, A499:469–479, 2003.

[113] K. H. Ackermann et al. STAR detector overview. *Nucl. Instrum. Meth.*, A499:624–632, 2003.

[114] B. B. Back et al. The PHOBOS detector at RHIC. *Nucl. Instrum. Meth.*, A499:603–623, 2003.

[115] M. Adamczyk et al. The BRAHMS experiment at RHIC. *Nucl. Instrum. Meth.*, A499:437–468, 2003.

[116] M. Allen et al. PHENIX inner detectors. *Nucl. Instrum. Meth.*, A499:549–559, 2003.

[117] K. Adcox et al. PHENIX central arm tracking detectors. *Nucl. Instrum. Meth.*, A499:489–507, 2003.

[118] M. Aizawa et al. PHENIX central arm particle ID detectors. *Nucl. Instrum. Meth.*, A499:508–520, 2003.

[119] L. Aphecetche et al. PHENIX calorimeter. *Nucl. Instrum. Meth.*, A499:521–536, 2003.

[120] H. Akikawa et al. PHENIX muon arms. *Nucl. Instrum. Meth.*, A499:537–548, 2003.

[121] Stephen Scott Adler et al. PHENIX on-line systems. *Nucl. Instrum. Meth.*, A499:560–592, 2003.

[122] S. H. Aronson et al. PHENIX magnet system. *Nucl. Instrum. Meth.*, A499:480–488, 2003.

[123] K. Ikematsu et al. A start-timing detector for the collider experiment PHENIX at RHIC-BNL. *Nucl. Instrum. Meth.*, A411:238–248, 1998.

[124] C. Adler et al. The RHIC zero-degree calorimeters. *Nucl. Instrum. Meth.*, A499:433–436, 2003.

[125] V. G. Ryabov. Drift chambers for the PHENIX central tracking system. *Nucl. Instrum. Meth.*, A419:363–369, 1998.

[126] J. Barrette et al. The pixel readout system for the PHENIX pad chambers. *Nucl. Phys.*, A661:665–668, 1999.

[127] B. Love et al. The implementation and performance of the phenix time-of-flight west detector subsystem. In preparation.

[128] Arkadij Taranenko Jiangyong Jia Maya Shimomura ShinIchi Esumi Rui Wei, Roy Lacey. PHENIX Analysis Note 768 Glauber Calculations of Centrality Dependent Variables in Au+Au collisions at $\sqrt{s_{NN}}$ = 200 GeV (Run 7). Internal PHENIX Collaboration documentation.

[129] Jamie Nagle. PHENIX Analysis Note 900 PHENIX Run-8 d-Au at 200 GeV Centrality Categorization. Internal PHENIX Collaboration documentation.

[130] T. Chujo, A. Kiyomichi, and J. Velkovska. PHENIX Analysis Note 187 Identified Charged Single Particle Spectra and Yield at $\sqrt{s_{NN}}$ = 200 GeV Au+Au for PPG015/026. Internal PHENIX Collaboration documentation.

[131] F. Matathias, T.K. Hemmick, B. Jacak, T. Chujo, and J. Velkovska. PHENIX Analysis Note 231 Identified Charged Particle Spectra, Ratios and Nuclear Modification Factors at $\sqrt{s_{NN}}$ = 200 GeV d+Au collisions. Internal PHENIX Collaboration documentation.

[132] S.S. Adler et al. Nuclear effects on hadron production in d+Au and p+p collisions at $\sqrt{s_{NN}}$ = 200 GeV. *Phys.Rev.*, C74:024904, 2006.

[133] M. Konno and T. Chujo. PHENIX Analysis Note 776 Identied Charged Hadron p_T Spectra in p+p Collisions at $\sqrt{s}$ = 200 and 62.4 GeV. Internal PHENIX Collaboration documentation.

[134] A. Adare et al. Identified charged hadron production in p+p collisions at $\sqrt{s}$ = 200 and 62.4 GeV. *Phys.Rev.*, C83:064903, 2011.

[135] F. Matathias. PHENIX Analysis Note 339 Feeddown corrections to protons and antiprotons in p+p and d+Au collisions at $\sqrt{s}$ = 200 GeV. Internal PHENIX Collaboration documentation.

[136] Xin-Nian Wang. Effect of jet quenching on high p_T hadron spectra in high-energy nuclear collisions. *Phys. Rev.*, C58:2321, 1998.

[137] G. Agakishiev et al. Identified hadron compositions in p+p and Au+Au collisions at high transverse momenta at $\sqrt{s_{NN}} = 200$ GeV. *Phys.Rev.Lett.*, 108:072302, 2012.

[138] A. Adare et al. Nuclear modification factors of phi mesons in d+Au, Cu+Cu and Au+Au collisions at $\sqrt{s_{NN}}$=200 GeV. *Phys.Rev.*, C83:024909, 2011.

[139] Rudolph C. Hwa and C.B. Yang. Production of strange particles at intermediate pT in central Au+Au collisions at high energies. *Phys.Rev.*, C75:054904, 2007.

[140] S.S. Adler et al. Centrality dependence of pi0 and eta production at large transverse momentum in s(NN)**(1/2) = 200-GeV d+Au collisions. *Phys.Rev.Lett.*, 98:172302, 2007.

[141] (ed.) Evans, Lyndon and (ed.) Bryant, Philip. LHC Machine. *JINST*, 3:S08001, 2008.

[142] G. Aad et al. The ATLAS Experiment at the CERN Large Hadron Collider. *JINST*, 3:S08003, 2008.

[143] S. Chatrchyan et al. The CMS experiment at the CERN LHC. *JINST*, 3:S08004, 2008.

[144] M. Chiu. A Design for a Novel TOF Detector with 10 ps Resolution.

[145] M. Chiu, S. White, T. Tsang, W. Powell, R. Dix, K. Drummond, and C.Y. Chi. PHENIX Technical Note 445 Electronics Feasibility Study Using Waveform Digitizers for a 10 ps Time-of-Flight Detector.

[146] A. Oskarsson. Private communication.

[147] Peter Christiansen. High pt identified particle production in ALICE. 2012.

[148] B.I. Abelev et al. Identified baryon and meson distributions at large transverse momenta from Au+Au collisions at s(NN)**(1/2) = 200-GeV. *Phys.Rev.Lett.*, 97:152301, 2006.

[149] M. E. Peskin and D. V. Schroeder. *Introduction to Quantum Field Theory*. Westview Press, Boulder, CO, USA, 1995.

[150] A. Lahiri and P. B. Pal. *A First Book of Quantum Field Theory*. Alpha Science International, Pangbourne, UK, 2001.